

University of Windsor

## Scholarship at UWindor

---

Electronic Theses and Dissertations

Theses, Dissertations, and Major Papers

---

2014

### Stress and Strain Distributions during Machining of Ti-6Al-4V at Ambient and Cryogenic Temperatures

Md. Fahim Rahman  
*University of Windsor*

Follow this and additional works at: <https://scholar.uwindsor.ca/etd>



Part of the [Mechanical Engineering Commons](#)

---

#### Recommended Citation

Rahman, Md. Fahim, "Stress and Strain Distributions during Machining of Ti-6Al-4V at Ambient and Cryogenic Temperatures" (2014). *Electronic Theses and Dissertations*. 5048.  
<https://scholar.uwindsor.ca/etd/5048>

This online database contains the full-text of PhD dissertations and Masters' theses of University of Windsor students from 1954 forward. These documents are made available for personal study and research purposes only, in accordance with the Canadian Copyright Act and the Creative Commons license—CC BY-NC-ND (Attribution, Non-Commercial, No Derivative Works). Under this license, works must always be attributed to the copyright holder (original author), cannot be used for any commercial purposes, and may not be altered. Any other use would require the permission of the copyright holder. Students may inquire about withdrawing their dissertation and/or thesis from this database. For additional inquiries, please contact the repository administrator via email ([scholarship@uwindsor.ca](mailto:scholarship@uwindsor.ca)) or by telephone at 519-253-3000ext. 3208.

**Stress and Strain Distributions during Machining  
of Ti-6Al-4V at Ambient and Cryogenic  
Temperatures**

**By**

**MD. FAHIM RAHMAN**

**A Thesis**

**Submitted to the Faculty of Graduate Studies  
through Engineering Materials  
in Partial Fulfillment of the Requirements for  
the Degree of Master of Applied Science at the  
University of Windsor**

**Windsor, Ontario, Canada  
2014**

**© 2014 Md. Fahim Rahman**

# **Stress and Strain Distributions during Machining of Ti-6Al-4V at Ambient and Cryogenic Temperatures**

by

**Md. Fahim Rahman**

APPROVED BY:

**Outside Program Reader**

**D. Ting** (Mechanical Engineering),

Department of Mechanical, Automotive, and  
Materials Engineering

**Program Reader**

**D. Green** (Engineering Materials),

Department of Mechanical, Automotive, and  
Materials Engineering

**Advisor**

**A.T. Alpas** (Engineering Materials),

Department of Mechanical, Automotive, and  
Materials Engineering

**22 January 2014**

## **DECLARATION OF ORIGINALITY**

I hereby certify that I am the sole author of this thesis and that no part of this thesis has been published or submitted for publication.

I certify that, to the best of my knowledge, my thesis does not infringe upon anyone's copyright nor violate any proprietary rights and that any ideas, techniques, quotations, or any other material from the work of other people included in my thesis, published or otherwise, are fully acknowledged in accordance with the standard referencing practices. Furthermore, to the extent that I have included copyrighted material that surpasses the bounds of fair dealing within the meaning of the Canada Copyright Act, I certify that I have obtained a written permission from the copyright owner(s) to include such material(s) in my thesis and have included copies of such copyright clearances to my appendix.

I declare that this is a true copy of my thesis, including any final revisions, as approved by my thesis committee and the Graduate Studies office, and that this thesis has not been submitted for a higher degree to any other University or Institution.

## ABSTRACT

Dry and liquid nitrogen pre-cooled Ti-6Al-4V samples were machined at a cutting speed of 43.2 m/min and at low (0.1 mm/rev) to high (0.4 mm/rev) feed rates for understanding the effects of temperature and strain rate on chip microstructures. During cryogenic machining, it was observed that between feed rates of 0.10 and 0.30 mm/rev, a 25% pressure reduction on tool occurred. Smaller number of chips and low tool/chip contact time and temperature were observed (compared to dry machining under ambient conditions). An in-situ set-up that consisted of a microscope and a lathe was constructed and helped to propose a novel serrated chip formation mechanism when microstructures (strain localization) and surface roughness were considered. Dimpled fracture surfaces observed in high-speed-machined chips were formed due to stable crack propagation that was also recorded during in-situ machining. An instability criterion was developed that showed easier strain localization within the 0.10-0.30mm/rev feed rate range.

## DEDICATION

*To my parents,*

*Mr. Mizanur Rahman and Mrs. Tohomina Rahman,*

*and*

*to my brother, sister and their families*

*for the love, endless support and encouragement*

## **ACKNOWLEDGEMENTS**

I would like to express my sincere gratitude to my advisor Dr. A. T. Alpas for his constant supervision, encouragement, support and patience during my graduate studies. Working under his expert guidance has been a great learning experience.

I also would like to thank my committee members: Dr. D. Green and Dr. D. Ting for their invaluable discussions, suggestions and time. Special thanks to the Mr. S. Bhattacharya for his constant encouragement and support. I also wish to thank Technical Support Centre crew for providing assistance with the set-up, for their invaluable suggestions and for coordinating the tests. I also would like to thanks to Mr. P. Seguin for his invaluable help with the calibration of the force measurement system. Sincere thanks to Mrs. S. Lackie for her constant help related to SEM.

I appreciate all researchers of the Tribology of Lightweight Materials, for their help, constant support and encouragement.

Sincere thanks to Natural Sciences and Engineering Research Council of Canada (NSERC) through a Strategic Network (CANRIMT) for the financial support.

# TABLE OF CONTENTS

DECLARATION OF ORIGINALITY .....	iii
ABSTRACT.....	iv
DEDICATION .....	v
ACKNOWLEDGEMENTS.....	vi
LIST OF TABLES.....	xiv
LIST OF FIGURES.....	xv
LIST OF ABBREVIATIONS .....	xxxii
LIST OF SYMBOLS .....	xxxiii
CHAPTER 1: INTRODUCTION.....	1
1.1 Background of This Research.....	1
1.2 Objective of Current Research.....	2
CHAPTER 2: LITERATURE SURVEY .....	4
2.1 Titanium Alloys.....	4
2.1.1 Phases and Alloying Elements of Titanium .....	5
2.1.2 Deformation Mode of Titanium Alloys .....	5
2.1.3 Important Features of Ti-6Al-4V .....	6
2.1.3.1 Microstructure of Ti-6Al-4V .....	6
2.1.3.2 Phase Transformations of Ti-6Al-4V .....	6
2.1.3.3 Mechanical Properties of Ti-6Al-4V .....	7



2.2. Basics of Machining Process .....	9
2.2.1 Orthogonal Cutting .....	10
2.2.2 Forces and Stress during Orthogonal Cutting .....	10
2.2.3 Deformation Zones .....	11
2.2.4 Classification of Chips .....	11
2.2.5 Microstructural Deformation due to Orthogonal Cutting .....	13
2.2.5.1 Shear Angle Estimation .....	14
2.2.5.2 Effective Plastic Strain Estimation .....	14
2.2.5.3 Flow Stress Estimation .....	16
2.2.5.4 Energy Expended due to Plastic Deformation and Temperature Rise .....	17
2.3 Machining of Titanium Alloys .....	18
2.3.1 Machinability of Ti-6Al-4V.....	18
2.3.2 Serrated Chip Formation Mechanisms .....	20
2.3.2.1 Adiabatic Shear Mechanism .....	20
2.3.2.2 Periodic Crack Development Mechanism .....	21
2.3.2.3 Recent Clarifications on Adiabatic Shear Mechanism .....	22
2.3.3 Adiabatic Shear Band in Ti-6Al-4V .....	23

2.3.3.1 Instability Criteria.....	23
2.3.3.2 Types of Adiabatic Shear Band.....	26
2.3.3.3 Recrystallization and Phase Transformation in Adiabatic Shear Band .....	26
2.3.4 Fracture Surface of Ti-6Al-4V .....	29
2.3.4.1 Morphology of Fracture Surface .....	29
2.3.4.2 Mechanisms of Chip Fracture .....	30
2.3.5 Cryogenic Machining.....	31
2.3.6 Effect of Cutting Condition.....	32
2.3.6.1 Distance between Two Consecutive Shear Band.....	32
2.3.6.2 Chip Thickness and Shear Angle .....	33
2.3.6.3 Comparison of Different Force Components.....	33
2.3.6.4 Surface Roughness .....	34
2.3.6.5 Tool Wear.....	34
2.4 Summary of Literature Survey .....	35
TABLES.....	36
FIGURES.....	38
CHAPTER 3: EXPERIMENTAL PROCEDURE.....	72
3.1 Workpiece Geometry.....	72

3.2 In-Situ Machining .....	73
3.2.1 Schematic Design of In-Situ Set-Up.....	73
3.2.2 Components.....	74
3.2.3 Assembly of In-Situ Set-Up.....	75
3.2.4 Procedure of In-Situ Machining .....	76
3.3 High Speed Machining .....	76
3.3.1 Lathe for Orthogonal Cutting.....	76
3.3.2 Machining Parameters.....	76
3.3.3 Tool .....	77
3.4 Differences between the In-Situ and High Speed Set-Ups .....	77
3.5 Measurement System of Force Sensor .....	77
3.5.1 Design.....	78
3.5.2 Calibration.....	78
3.5.3 Data Acquisition.....	80
3.6 Cryogenic Machining Approach .....	80
3.7 Sample Preparation and Metallographic Approach .....	81
3.8 Surface Characterization.....	82

3.9 Microhardness Measurements .....	82
FIGURES.....	83
CHAPTER 4: EXPERIMENTAL RESULTS.....	98
4.1 In-Situ Machining .....	98
4.1.1 Average Cutting Speed and Feed Measurement for In-Situ Tests.....	98
4.1.2 Microstructural Interpretation of Serrated Chip Formation .....	99
4.1.3 Formation of Serrated Chips .....	100
4.1.4 Characteristics of Serrated Chip Formation during Cryogenic Machining.....	101
4.1.5 Difference between Serrated and Continuous Chips Formation Process .....	101
4.2 High Speed Machining of Ti-6Al-4V (Dry and Cryogenic).....	102
4.2.1 Microstructure of Material Ahead of Tool Tip.....	102
4.2.2 Chips Formed in Different Conditions.....	104
4.2.3 Adiabatic Shear Band and Crack Formation .....	105
4.2.4 Fracture Surface Morphology .....	107
4.2.5 Quantitative Analyses of Chip Characteristics from Microstructure .....	108
4.2.5.1 Chip Thickness Measurement.....	108
4.2.5.2 Variation of Distance between Shear Bands .....	108
4.2.5.3 Shear Displacement Variation .....	109

4.2.5.4 Shear Band Width .....	110
4.2.5.5 Shear Angle Variation .....	110
4.2.6 Force Measurements .....	112
4.2.6.1 Measured Cutting and Feed Force.....	112
4.2.6.2 Comparison of Forces .....	112
4.2.6.3 Variation of Resultant and Shear Force .....	114
4.2.7 Apparent Shear Stress in Shear Band .....	114
4.2.8 Variation of Shear Strain in Shear Band.....	115
4.2.9 Velocity Calculations .....	116
4.2.10 Variation of Strain Rate.....	116
4.2.10.1 Calculation of Bulk Strain Rate.....	117
4.2.10.2 Measurement of Strain Rate in Shear Plane.....	117
4.2.11 Subsurface Deformation State.....	117
4.2.12 Machined Surface Characteristics.....	118
4.2.13 Tool Wear and Adhesion.....	118
FIGURES.....	120
CHAPTER 5: DISCUSSION.....	167
5.1 Serrated Chip Formation Mechanism .....	167

5.2 Difference in Serrated Chip Characteristics during Slow and High Speed Machining .....	169
5.3 Schematic Models of Chips Based on Microstructural Quantitative Analyses .....	171
5.4 Tool Wear, Diffusion and Adhesion .....	172
5.5 Strain Rate, Shear Band Temperature and Flow Localization.....	175
5.6 Specific Cutting Energy and Bulk Deformation .....	176
5.7 Shear Strain in Shear Band and Instability Criteria .....	178
FIGURES.....	182
CHAPTER 6: CONCLUSIONS.....	202
6.1 Conclusions .....	202
6.2 Future Work .....	203
REFERENCES.....	205
APPENDICES .....	213
Appendix A.....	213
Appendix B.....	216
VITA AUCTORIS .....	217

## LIST OF TABLES

<b>Table 2.1</b> Classification of elements that form different types of titanium alloys [13].....	36
<b>Table 2.2</b> Important properties of different metals[15,93-97]. .....	36
<b>Table 2.3</b> Yield strength and ultimate tensile strength variation with temperature of Ti-6Al-4V alloy [19].....	37
<b>Table 2.4</b> Tool life for each cutting condition and improvement with cryogenic coolant [85].....	37

# LIST OF FIGURES

## CHAPTER 2

<b>Figure 2.1</b> Phase diagram of titanium showing different types of titanium alloys based on the alloying elements [13].	38
<b>Figure 2.2</b> Hexagonal close packed structure and body centered cubic structure of $\alpha$ and $\beta$ phase respectively [13].	38
<b>Figure 2.3</b> Optical image of Ti-6Al-4V [98].	39
<b>Figure 2.4</b> Phase diagram of Ti-6Al-4V [99].	39
<b>Figure 2.5</b> Different types of phase transformations in Ti-6Al-4V where $\omega$ phase requires very high rate of cooling, diffusion controlled process requires very slow cooling and martensitic transformation process requires intermediate rate of cooling and all these are dependent on the % of solute content as well.	40
<b>Figure 2.6</b> TEM bright-field images of: (a) fine (3 $\mu\text{m}$ ); and (b) coarse (11 $\mu\text{m}$ ) grained Ti-6Al-4V deformed at 600°C with a strain rate of $10^{-3}\text{s}^{-1}$ ( $\epsilon=0.3$ ) [18].	40
<b>Figure 2.7</b> Typical true stress-strain curves of Ti-6Al-4V alloys deformed at different strain rates and temperatures [19].	41
<b>Figure 2.8</b> At a true strain of 0.05 variations of strain rate sensitivity as a function of temperature for deformation under different strain rate range [19].	41
<b>Figure 2.9</b> Hardness of annealed Ti-6Al-4V at various temperatures [9].	42



**Figure 2.10** Temperature dependence of the yield stress of Ti-6Al-4V at low [100] and high [19] strain rates compared to  $\alpha$ -Ti [101]. At strain rate of  $10^{-3}s^{-1}$  and at a temperature of 0K, the flow stress of Ti-6Al-4V is 1600MPa which reaches a plateau of 600MPa at around 600K. At higher strain rate there is no such plateau. .... 42

**Figure 2.11** Schematic diagram of orthogonal cutting. .... 43

**Figure 2.12** Force diagram for orthogonal cutting where  $F_c$  is cutting force,  $F_f$  is feed force,  $F_s$  is the shear force on the shear plane,  $N_s$  is the normal force on the shear plane,  $F_p$  is shear force on rake face and  $N_p$  is the normal force on the rake face [10]. .... 43

**Figure 2.13** Deformation zones produced during orthogonal cutting [102]. .... 44

**Figure 2.14** Two main types of chips formed both for Ti 140A at different cutting conditions (a) Continues chips of Ti 140 A, Cutting speed = 30.5m/min, Feed = 0.13mm/rev, (b) Cyclic chips of Ti 140 A, Cutting speed = 45.7m/min, Feed = 0.26mm/rev [7]. .... 45

**Figure 2.15** Different types of cyclic chips (a) Wavy chips [27] (b) Segmental chips [27] (c) Catastrophic shear or serrated chips [27] (d) Discontinuous chips [103]. .... 45

**Figure 2.16** Cross-sectional optical micrograph of the material (hot extruded Cu) ahead of the tool tip formed during orthogonal cutting [31]. .... 46

**Figure 2.17** (a) Schematic illustration of microstructural evolution and grain refinement induced by plastic deformation ahead of the tool tip and (b) the sequence of grain refinement events shown on the cross-section of the sample [31]. .... 46

**Figure 2.18** (a) A computer generated image of the cross-section of the machined work piece with the chip still attached. The image was obtained by determining the location of each point

on the deformation lines and these were plotted to actual scale shown on the diagram, (b) Schematic diagram showing the measurement of shear angles from the slopes of the deformation lines [30]. ..... 47

**Figure 2.19** Model for true shearing of a sphere[34]. Ideal spherical crystal ABC turns into A'B'C after shearing.  $l_x$  and  $l_y$  are the distances at the X and Y directions respectively and  $\theta$  is the deformation angle. .... 48

**Figure 2.20** Strain distribution diagram showing the values of equivalent shear strains,  $\epsilon$ , in the material (Al 1100) ahead of the tool tip. Equivalent strains were estimated from the local shear angle values,  $\Phi$  using Eq. (2.13). The iso-strain contours are also shown [32]. ..... 48

**Figure 2.21**The cumulative stress-strain curve of commercial purity copper subjected to orthogonal cutting [33]. ..... 49

**Figure 2.22** Temperature distribution of the material ahead of the tool tip due to plastic deformation in 1100 Aluminum [32]. ..... 49

**Figure 2.23** Schematic diagram of a sequence of events, showing various stages involved in chip formation during machining titanium alloys[6]. ..... 50

**Figure 2.24** Mechanism of saw tooth chip formation by periodic crack formation process[54]. . 51

**Figure 2.25** (a) Free body diagram of chip, (b) Hodograph for gross cracked region of chip only [7]. ..... 52

**Figure 2.26** Model used to explain adiabatic shear theory of saw tooth chip formation where A is the segment that is going to be formed and B is a well developed segment. 1 and 2 are two

fractured surfaces and 3 shows contact area between A and B. 4 and 5 represent flattening and the path of strain localization respectively [62]. ..... 53

**Figure 2.27** Model for thermal analysis based on adiabatic shear theory where in (a) the strain localization path is initially straight, (b) shear force,  $S_2$  makes the path curve and (c) shear force,  $S_2$  acts on the material not along the strain localized region [63]. ..... 54

**Figure 2.28** Adiabatic transformed shear band in a chip of titanium alloy Ti-6Al-4V, obtained by orthogonal cutting at the velocity 13 m/s[87]. ..... 55

**Figure 2.29** Schematic illustration showing sequence of deformation-recrystallization steps in dynamic deformation [69]. ..... 55

**Figure 2.30** (a) A Very thin transparent section was taken from the chip produced during machining of Ti-6Al-4V alloy at a cutting speed of 10m/s and (b) XRD analyses on the transparent section showed no phase transformation [60]. ..... 56

**Figure 2.31** Saw tooth chip formation in Ti-6Al-4V at a constant feed rate of 0.21 mm/rev at different cutting speed (a) 30.2 m/min, (b) 59.6 m/min, (c) 81.4 m/min, (d) 126.6 m/min, (e) 178.4 m/min and (f) 281.3 m/min [74]. ..... 57

**Figure 2.32** At a constant feed rate of 0.21 mm/rev (a) Incipient separation of segments at a cutting speed of 30.2 m/min and (b) Complete separation of segments at a cutting speed of 59.6 m/min [74]. ..... 58

**Figure 2.33** TEM image of adiabatic shear band at a cutting speed of 59.6 m/min and feed rate 0.21mm/rev (Diffraction pattern was taken down  $[111]\beta$  and  $[0001]\alpha$ ) [74]. ..... 58

<b>Figure 2.34</b> TEM image of adiabatic shear band at cutting speed 126.6 m/min and feed rate 0.21mm/rev where (a) center of adiabatic shear band and (b) transitional region between matrix and center (Diffraction pattern was taken down [0001] $\alpha$ ) [74].	59
<b>Figure 2.35</b> Microhardness at different position including shear band of Ti-6Al-4V alloy [76].	59
<b>Figure 2.36</b> Voids within well developed shear zone of Ti-6Al-4V alloy [78].	60
<b>Figure 2.37</b> Dimple shear band fracture surface (a) Secondary image (b) Backscattered image [79].	61
<b>Figure 2.38</b> Relatively smooth shear band fracture surface (a) Secondary image (b) Backscattered image [79].	61
<b>Figure 2.39</b> Secondary image of shear band fracture surfaces partially covered with (a) Globular aggregate (b) Individual globules [79].	61
<b>Figure 2.40</b> Transmission electron micrographs of superplastically deformed specimens (3 $\mu\text{m}$ ) at 900°C: (a) an $\alpha$ surrounded by $\alpha$ ; and (b) an $\alpha$ surrounded by $\beta$ [18].	62
<b>Figure 2.41</b> Schematic illustration of evolution of void and fracture-surface morphologies in adiabatic shear bands; sequence a,b,c corresponds to increasing density of void nucleation sites[78].	63
<b>Figure 2.42</b> Measured and predicted tool temperature in different machining techniques [83].	64
<b>Figure 2.43</b> Schematic illustration of (a) generation and (b) delivery of cryogenic compressed air to the cutting edge [84].	65

<b>Figure 2.44</b> Photograph of liquid nitrogen coolant delivery system showing modified tool holder nozzle for rake face cooling with an additional flank face cooling nozzle [85].....	66
<b>Figure 2.45</b> Schematic representation of modified tool for cryogenic coolant delivery on rake and flank surfaces [86].....	66
<b>Figure 2.46</b> The variation of measured thickness of flow chip and the calculated shear angle with cutting speed obtained in cutting hardened Fe-9.7%Ni-0.1%C alloy where serrated chips formed at a constant feed of 0.259 mm and a positive rake angle of $\pm 5^\circ$ [88].....	67
<b>Figure 2.47</b> Measurement of shear band angle and chip thickness in dry and cryogenic condition at different feed rates [85]. .....	67
<b>Figure 2.48</b> Comparison of cutting and feed forces in wet and cryogenic machining [86].....	68
<b>Figure 2.49</b> Variation of surface roughness with cutting velocity in wet (using emulsion of cutting fluid) and cryogenic machining [86]. .....	69
<b>Figure 2.50</b> Different types of tool wear [104].....	69
<b>Figure 2.51</b> Rake wear during dry and cryogenic condition (cooling of tool flank face). Cutting speed-125m/min, Feed-0.15 mm/rev and width of cut-2.7mm [85].....	70
<b>Figure 2.52</b> Average wear of the primary flank and nose during dry cutting and using cryogenic coolant [85].....	71

### CHAPTER 3

<b>Figure 3.1</b> Microstructure of Ti-6Al-4V indicating $\alpha$ and $\beta$ phases.....	83
---	----

<b>Figure 3.2</b> In-situ machining design showing the direction of workpiece revolution and feed where (a) shows the tool, workpiece and chip are on the same plane and (b) presents the overall schematic where this plane can be focused with a microscope.....	84
<b>Figure 3.3</b> Components of in-situ set-up (a) Sherline lathe (4500/4530) (b) Proscope HR2 handheld digital microscope (c) Luxo 18730 microscope (d) milling table and (e)Uncoated tungsten carbide parting tool. ....	86
<b>Figure 3.4</b> In-situ set-up assembly and different parts.....	87
<b>Figure 3.5</b> Harrison M300 lathe for high speed machining. ....	88
<b>Figure 3.6</b> Uncoated tungsten carbide tool. ....	88
<b>Figure 3.7</b> Schematic presentation of the difference between high speed and in-situ machining set-up. ....	89
<b>Figure 3.8 (a)</b> A schematic of the force sensor used to measure force during high speed machining and (b) actual image of the force sensor. ....	90
<b>Figure 3.9</b> Calibration of the force sensor in cutting direction where (a) shows the curve during loading, (b) during unloading and (c) final calibration graph for cutting force. ....	92
<b>Figure 3.10</b> Calibration of the force sensor in feed direction where (a) shows the curve during loading, (b) during unloading and (c) final calibration graph for feed force. ....	94
<b>Figure 3.11</b> Data acquisition system of the force sensor where the electrical signal obtained during machining is transferred wirelessly to the base station and then via USB transferred to convert it in a readable format. ....	95

**Figure 3.12** Workpiece covered with ice where no ice on chips formed after cryogenic machining. .... 96

**Figure 3.13** (a) Schematic presentation of workpiece and tool assembly of high speed machining where chip produced during interrupted cutting, (b) section that was cut to obtain the required samples, (c) location of the samples, (d) and (e) polished and etched samples taken from (c). .. 97

#### CHAPTER 4

**Figure 4.1** Microstructure obtained during in-situ machining where (a) showed the path of strain localization and in (b) (in that same microstructure) some important features of the chips that was going to be formed were pointed out. .... 120

**Figure 4.2** Sequential microstructural observation of formation of a particular serrated chip during in-situ machining of Ti-6Al-4V where (a) reveals that the crack initiated at the tool tip, then (b) and (c) present the steps of stable propagation of the crack which was within the strain localized region formed in step 1 and finally in (d) the new chip B had formed by unstable crack propagation ( Average cutting speed- 0.06m/min, Feed- 0.07mm and width of cut 0.07mm). . 122

**Figure 4.3** Microstructure obtained during cryogenic machining of Ti-6Al-4V (Average cutting speed- 0.06m/min, Feed- 0.05mm and width of cut 0.07mm). .... 123

**Figure 4.4** Sequential microstructural observation of formation of a continuous chip during in-situ machining of 6061 Aluminum where (a) reveals that a plastic zone formed and it moved forward, (b) and (c) shows that the size of that plastic zone increased and kept moving forward and in (d) the whole plastically deformed portion got separated (Average cutting speed- 0.02m/min, Feed- 0.1mm and width of cut 0.07mm). .... 125

**Figure 4.5** Cross sectional optical image of material ahead of tool tip of Ti-6Al-4V alloy subjected to orthogonal cutting at a cutting speed of 43.2m/min where (a) in dry condition and at feed rates of 0.17mm/rev, (b) in dry condition and at feed rates of 0.22mm/rev (c) in cryogenic condition and at feed rates of 0.12mm/rev and (d) in cryogenic condition and at feed rates of 0.38 mm/rev. .... 127

**Figure 4.6** Serrated chips formed during machining of Ti-6Al-4V alloy at a cutting speed of 43.2m/min and at feed rates of (a) 0.12 mm/rev, (c) 0.18 mm/rev, (e) 0.24 mm/rev, (g) 0.26 mm/rev and (i) 0.38 mm/rev in cryogenic conditions and (b) 0.09 mm/rev, (d) 0.17 mm/rev, (f) 0.22 mm/rev, (h) 0.26 mm/rev and (j) 0.32 mm/rev in dry conditions where their differences in terms of cracking tendency is shown. .... 129

**Figure 4.7** Summary of cracking tendency of serrated chips formed during machining of Ti-6Al-4V alloy in dry and cryogenic condition, at a cutting speed of 43.2m/min and at comparable feed rates. .... 130

**Figure 4.8** Optical image showing (a) surfaces of serrated chip, formed during Ti-6Al-4V alloy machining in cryogenic condition at a cutting speed of 43.2m/min and at a feed rates of 0.38mm/rev where (b) and (c) are the SEM images of the corresponding regions shown with circles indicating that the surfaces are well within shear band..... 131

**Figure 4.9** (a) Optical image of wider cracked surface of serrated chip formed during Ti-6Al-4V alloy machining in cryogenic condition, at a cutting speed of 43.2m/min and at a feed rates of 0.38mm/rev (b) low magnification SEM images and (c) high magnification SEM images of the wider cracked region indicating that the crack tip shifted towards the edge of shear band..... 132



**Figure 4.10** (a) Optical image of wider cracked surface of serrated chip formed during Ti-6Al-4V alloy machining in dry condition, at a cutting speed of 43.2m/min and at a feed rates of 0.32mm/rev (b) backscattered SEM image of the wider cracked region indicating that the crack tip shifted towards the edge of shear band..... 133

**Figure 4.11** (a) Optical image of narrow cracked surface of serrated chip formed during Ti-6Al-4V alloy machining in cryogenic condition, at a cutting speed of 43.2m/min and at a feed rates of 0.38mm/rev (b) backscattered SEM image of the narrow cracked region indicating that the cracked surface is well within the shear band..... 134

**Figure 4.12** (a) Optical image of wider cracked surface of serrated chip formed during Ti-6Al-4V alloy machining in cryogenic condition, at a cutting speed of 43.2m/min and at a feed rate of 0.38mm/rev where (b) secondary and (c) backscattered SEM images of the corresponding region showing that the cracked surface moved out of the shear band and fractured beta particle. ... 135

**Figure 4.13** Different regions of interest indicated in the SEM image of serrated chips formed during Ti-6Al-4V alloy machining in cryogenic condition, at a cutting speed of 43.2m/min and at a feed rates of 0.24mm/rev. .... 136

**Figure 4.14** (a) SEM image of serrated chip of Ti-6Al-4V alloy machined in dry condition, at a cutting speed of 43.2m/min and at a feed rates of 0.32mm/rev showing the region of fracture surface from which higher magnification image was taken and (b) High magnification SEM image showing dimple type fractured surface..... 137

**Figure 4.15** SEM image showing elongated dimples as well as comparatively smooth regions in the fracture surface of Ti-6Al-4V alloy machined in dry condition, at a cutting speed of 43.2m/min and at a feed rates of 0.32mm/rev. .... 138

**Figure 4.16** (a) SEM image of serrated chip of Ti-6Al-4V alloy machined in cryogenic condition, at a cutting speed of 43.2m/min and at a feed rate of 0.24mm/rev showing the region of fracture surface from which higher magnification image was taken and (b) High magnification SEM image showing elongated dimples as well as comparatively smooth regions within the fractured surface of Ti-6Al-4V alloy. .... 139

**Figure 4.17** Optical image of serrated chips obtained during machining in cryogenic condition at a cutting speed of 43.2m/min and at a feed rate of 0.38mm/rev indicating the procedure of measuring maximum, minimum chip thickness and distance between shear bands. Maximum and minimum chip thickness lines are perpendicular to the rake face whereas the line representing the distance between the shear band is also perpendicular to the shear bands. . 140

**Figure 4.18** Variation of chip thickness with feed rates (measured from microstructures) at a cutting speed of 43.2m/min in dry and cryogenic conditions where (a) shows maximum chip thickness, (b) shows minimum chip thickness and (c) shows average chip thickness. .... 141

**Figure 4.19** Variation of average distance between two consecutive shear bands with feed rates (measured from microstructures) at a cutting speed of 43.2m/min in dry and cryogenic conditions. .... 142

**Figure 4.20** Optical image of serrated chips obtained during machining in cryogenic condition at a cutting speed of 43.2m/min and at a feed rate of 0.38mm/rev indicating the procedure of measuring shear displacement and width of shear bands. .... 142

**Figure 4.21** Variation of average shear displacement with feed rates (measured from microstructures) at a cutting speed of 43.2m/min in dry and cryogenic conditions. .... 143

<b>Figure 4.22</b> Variation of normalized displacement with feed rates (measured from microstructures) at a cutting speed of 43.2m/min in dry and cryogenic conditions. ....	143
<b>Figure 4.23</b> SEM image of serrated chips obtained during machining in cryogenic condition at a cutting speed of 43.2m/min and at a feed rate of 0.38mm/rev showing the variation of shear band width from free surface towards the rake face of the chip.....	144
<b>Figure 4.24</b> Variation of average shear band width with feed rates (measured from microstructures) at a cutting speed of 43.2m/min in dry and cryogenic conditions. ....	144
<b>Figure 4.25</b> Optical image of serrated chips obtained during machining in cryogenic condition at a cutting speed of 43.2m/min and at a feed rate of 0.38mm/rev indicating the procedure of measuring shear angle.....	145
<b>Figure 4.26</b> Variation of average shear angle with feed rates (measured from microstructures) at a cutting speed of 43.2m/min in dry and cryogenic conditions. ....	145
<b>Figure 4.27</b> Variation of average shear angle calculated from the formula with feed rates at a cutting speed of 43.2m/min in dry and cryogenic conditions. ....	146
<b>Figure 4.28</b> Variation of (a) average cutting force and (b) average feed force with feed rates at a cutting speed of 43.2m/min in dry and cryogenic conditions. ....	147
<b>Figure 4.29</b> Direction of different types of forces that act on material during orthogonal cutting. ....	148
<b>Figure 4.30</b> Comparison of different type of forces of dry and cryogenic conditions at cutting speed of 43.2m/min and at various feed rates.....	153

**Figure 4.31** Variation of (a) average resultant force and (b) average shear force with feed rates at a cutting speed of 43.2m/min in dry and cryogenic conditions. .... 154

**Figure 4.32** Schematic diagram to demonstrate shear plane. .... 155

**Figure 4.33** Variation of apparent shear stress in shear band with feed rates at a cutting speed of 43.2m/min in dry and cryogenic conditions. .... 155

**Figure 4.34** Variation of apparent normalized shear stress in shear band [normalized with respect to feed] with feed rates at a cutting speed of 43.2m/min in dry and cryogenic conditions. .... 156

**Figure 4.35** Variation of average shear strain in shear band with feed rates at a cutting speed of 43.2m/min in dry and cryogenic conditions. .... 156

**Figure 4.36** Variation of (a) apparent velocity in shear band and (b) velocity of chip with feed rates at a cutting speed of 43.2m/min in dry and cryogenic conditions. .... 157

**Figure 4.37** Variation of bulk strain rate with feed rates at a cutting speed of 43.2m/min in dry and cryogenic conditions. .... 158

**Figure 4.38** Variation of (a) average resultant force and (b) average shear force with feed rates at a cutting speed of 43.2m/min in dry and cryogenic conditions. .... 158

**Figure 4.39** Optical image of subsurface deformation at a cutting speed of 43.2m/min where (a) in dry condition and at a feed rate of 0.17mm/rev and (b) in cryogenic condition and at a feed rate of 0.26mm/rev..... 159

**Figure 4.40** Variation of average depth of deformed zone (measured from microstructure) with feed rates at a cutting speed of 43.2m/min in dry and cryogenic conditions..... 160

**Figure 4.41** Variation of machined surface roughness,  $R_a$  and root mean squared roughness,  $R_q$  at comparable feed rates in dry and cryogenic conditions machined at a cutting speed of 43.2m/min. .... 162

**Figure 4.42** Variation of (a) average surface roughness,  $R_a$  and (b) average root mean squared roughness,  $R_q$  with feed rates at a cutting speed of 43.2m/min in dry and cryogenic conditions. .... 163

**Figure 4.43** Uncoated tungsten carbide tool after cryogenic machining at a cutting speed of 43.2 m/min and at feed rate of 0.26 mm/rev where (a) shows damaged cutting edge due to crater wear and (b) shows the EDS analysis that reveals high percentage of tungsten and carbon with some titanium due to adhesion..... 164

**Figure 4.44** Uncoated tungsten carbide tool after dry machining at a cutting speed of 43.2 m/min and at feed rate of 0.17 mm/rev where (a) shows crater wear and (b) shows the EDS analysis that reveals adhesion of titanium. .... 165

**Figure 4.45** Uncoated tungsten carbide tool after cryogenic machining at a cutting speed of 43.2 m/min and at feed rate of 0.26 mm/rev where (a) shows crater wear and (b) shows the EDS analysis that reveals adhesion of titanium. .... 166

## CHAPTER 5

**Figure 5.1** Stepwise features of serrated chip formation mechanism developed on the basis of microstructural evidences where (a) the first step is strain localization, (b) the second step

shows crack initiation, (c) the third step showing stable crack propagation and (d) the final step is unstable crack propagation.....	183
<b>Figure 5.2</b> Summary of the serrated chip formation mechanism developed through microstructural analyses that includes the gradual movement of the tool, strain localization, crack initiation/propagation, crack closure between two consecutive chips and generation of machined surface.....	184
<b>Figure 5.3</b> Characteristics of serrated chips formed during in-situ (a) dry and (b) cryogenic machining.....	185
<b>Figure 5.4</b> Distribution of forces along different faces of tool when the rake angle is $\alpha_r$ [102]..	186
<b>Figure 5.5</b> Optical image of serrated chip obtained during cryogenic machining at a cutting speed of 43.2m/min and at a feed rate of 0.38mm/rev indicating the procedure of measuring shear displacement in which crack formed. ....	186
<b>Figure 5.6</b> (a) Optical images of different types of serrated chips formed during cryogenic machining at a cutting speed of 43.2m/min and at a feed rate of 0.38mm/rev and (b) shows corresponding shear strain in shear band and strain rate in shear plane. ....	188
<b>Figure 5.7</b> (a) Optical images of different types of serrated chips formed during dry machining at a cutting speed of 43.2m/min and at a feed rate of 0.38mm/rev and (b) shows the corresponding shear strain in the shear band and the strain rate in the shear plane. ....	189
<b>Figure 5.8</b> Schematic model of chips based on microstructural quantitative analysis where (a) represents chips of dry condition and (b) of cryogenic condition in between 0.10mm/rev to 0.40mm/rev feed rates. ....	190

**Figure 5.9** Model for the wear of diamond by the diffusion of carbon through Titanium Carbide (TiC) reaction layer [47]. ..... 191

**Figure 5.10** Diffusion of Carbon from tool to the rake face of the workpiece where (a) shows the SEM image of the rake face and (b) shows the EDS spectra during dry machining at a cutting speed of 43.2 m/min and at a feed rate of 0.22mm/rev..... 192

**Figure 5.11** Diffusion of Carbon from the tool to the rake face of the workpiece where (a) shows the SEM image of the rake face and (b) shows the EDS spectra during cryogenic machining at a cutting speed of 43.2 m/min and at a feed rate of 0.24mm/rev..... 193

**Figure 5.12** Variation of the strain rate in the shear plane with the bulk strain rate at a cutting speed of 43.2m/min in dry and cryogenic conditions. .... 194

**Figure 5.13** Variation of temperature within the shear band with respect to the feed rate at a cutting speed of 43.2m/min in dry and cryogenic conditions. .... 194

**Figure 5.14** Variation of specific cutting energy with feed rates at a cutting speed of 43.2m/min in dry and cryogenic conditions. .... 195

**Figure 5.15** Optical image showing different deformation zones in a serrated chip formed during dry machining at a cutting speed of 43.2m/min and at feed rates of 0.32mm/rev..... 195

**Figure 5.16** (a) SEM image of indentation marks in front of the material ahead of the tool tip and (b) shows the same image at higher magnification indicating the average size of the diagonals that clearly depicts lower hardness at the tool tip which corresponds to concentrated deformation. .... 196

**Figure 5.17** Optical image of serrated chip showing no deformation in bulk region produced during dry machining at a cutting speed of 43.2m/min and at feed rates of 0.32mm/rev, (b) is a high magnification SEM image of the chips showed in (a) where the secondary deformation zone is separated from the undeformed bulk region. .... 197

**Figure 5.18** Variation of volume percent of a shear band in a single chip with feed rates at a cutting speed of 43.2m/min in dry and cryogenic conditions. .... 198

**Figure 5.19** Variation of (a) apparent shear stress in the shear band versus the shear strain in the shear band where  $R^2$  value for dry and cryogenic conditions are 0.98 and 0.97 respectively, (b) apparent shear stress in shear band with temperature within shear band where  $R^2$  value for dry and cryogenic conditions are 0.99 and 0.98 respectively and (c) temperature within shear band with shear strain in shear band where  $R^2$  value for dry and cryogenic conditions are 0.98 and 0.97 respectively at a cutting speed of 43.2m/min in dry and cryogenic conditions..... 200

**Figure 5.20** Instability during dry and cryogenic machining at a cutting speed of 43.2m/min at different feed rates..... 201



## LIST OF ABBREVIATIONS

COF	Coefficient of Friction
EDS	Energy Dispersive X-Ray Spectroscopy
OR	Orientation Relationship
SEM	Scanning Electron Microscope
TEM	Transmission Electron Microscope

## LIST OF SYMBOLS

$F_c$	Cutting Force
$F_f$	Feed Force
$F_s$	Shear Force
$N_s$	Normal Force on Shear Plane
$F_p$	Shear Force on Rake Face
$N_p$	Normal Force on Rake Face
$\mu$	Coefficient of Friction
$\tau$ or $\tau_s$	Shear Stress
$\sigma_m$	Mean Stress
$\bar{\sigma}_s$	Saturation Stress
$\bar{\sigma}_0$	Yield Flow Strength
$\bar{\sigma}$	Effective Flow Stress
$\bar{\epsilon}$	Effective Strain
$\epsilon_{x,y,z}$	Normal Strains
$\gamma_{ij}$	Shear Strains
$V$	Cutting Speed
$f$	Feed/Feed Rate
$w$	Width of Cut
$w_{sb}$	Shear Band Width
$\Phi$	Shear Angle
$\alpha$	Rake angle
$T_{sz}$	Temperature in Shear Band
$\Delta T$	Temperature Rise
$T_{amb}$	Ambient Temperature
$W$	Work of Plastic Deformation
$U$	Specific Cutting Energy
$J$	Mechanical Equivalent of Heat
$K$	Thermal Diffusivity

$\bar{C}$	Specific Heat Capacity
$\rho$	Density
$m$	Strain rate sensitivity
$\dot{\epsilon}$	Strain rate
$T$	Temperature
$\frac{\partial \tau}{\partial \gamma}$	Slope of shear stress-shear strain curve
$\frac{\partial \tau}{\partial \theta}$	Slope of temperature dependence of flow stress
$\frac{d\theta}{d\gamma}$	Slope of temperature vs. shear strain curve
$\dot{c}$	Rate of dissolution
$c$	Concentration of the dissolve material
$c_s$	Maximum solubility
$\nu$	Frequency of atomic oscillation
$\beta$	Number of atoms leaving and joining the solution
$\Delta G$	Activation energy for dissolution
$k$	Boltzmann constant
$T$	Absolute temperature at the interface
$U_{\text{total}}$	Total spent energy
$U_{\text{SB}}$	Energy spent in shear band
$U_{\text{Bulk}}$	Energy spent in bulk region
$U_{\text{SDZ}}$	Energy spent in the secondary deformation zone
$\frac{\partial \tau}{\partial T_{\text{SZ}}}$	Slope of shear band temperature dependence of flow stress
$\frac{\partial T_{\text{SZ}}}{\partial \gamma}$	Slope of shear band temperature vs. shear strain curve

# CHAPTER 1

## INTRODUCTION

### 1.1 Background of Research

Machining is a process that removes unwanted material in a controlled way from the workpiece, as chips, to give the desired shape. Most research in this field focuses on optimization of the process by producing products with better surface finish, consuming less power and increased tool life.

For ductile materials, chips are produced by deforming the workpiece in a certain way that most of the deformation takes place in a particular shear plane, which minimizes the plastic work. Merchant [1] proposed a model to predict the orientation of this shear plane. Lee and Shafer [2] predicted the shear angle and strain distribution whereas Oxley [3] proposed a formula to calculate the shear angle. These studies were based on homogeneous deformation where continuous chips form.

Ti-6Al-4V which is an  $\alpha$ - $\beta$  titanium alloy, has poor thermal properties and does not deform homogeneously. Under these circumstances if the rate of thermal softening is greater than that of strain hardening, then the deformation localizes into thin shear bands [4]. Shaw [5] has shown that in machining of certain materials, thermal energy concentration due to poor thermal properties causes localized deformation in a narrow band. This narrow band is called an adiabatic shear band.

At high cutting speeds, Ti-6Al-4V alloys form adiabatic shear bands and produce serrated chips because of inhomogenous deformation. The chip formation mechanism was studied by many researchers [6,7] but there is still a lack of understanding of crack initiation/propagation processes.

Ti-6Al-4V alloy is known as a difficult to cut material. High chemical reactivity with the tool along with poor thermal properties that cause heat entrapment at the tool/chip interface are responsible for severe tool wear [8]. To mitigate this problem, several environmentally safe cooling approaches were introduced. The effect of liquid nitrogen cooling on mechanical properties was studied [9]. In the field of machining, cryogenic approaches were widely evaluated in terms of how they improve the tool life. But the effect of cryogenic conditions on chip formation mechanisms has not been studied. These studies require detailed chip characterization. Then the roles of chip formation mechanisms on tool life can be analyzed.

## **1.2 Objective of Current Research**

In this work, liquid nitrogen precooled Ti-6Al-4V samples were machined at a cutting speed of 43.2 m/min and at low (0.1 mm/rev) to high (0.4 mm/rev) feed rates. The results were compared to those obtained at ambient conditions in order to understand the effect of low temperature on chip formation and workpiece deformation behaviour. Chips formed in all these conditions were characterized using metallographic methods. Quantitative analyses were performed on the microstructures of the chips. A machining set-up was designed and built for real-time observation of serrated chip formation mechanisms. During the chip formation process cracks were found to initiate from the tool tip and their propagation became unstable at locations closer to the surface. Based on microstructures, a novel mechanism of crack

initiation/propagation was proposed. Finally, the significance of cryogenic machining was analyzed considering the diffusion, adhesion/tool wear and energy efficiency of machining process. The conditions under which strain localization occur were determined and correlated with chip formation mechanism.

## CHAPTER 2

### LITERATURE SURVEY

Metal cutting or machining is a procedure that removes unwanted material and gives mechanical components the desired shape. Higher productivity, better efficiency with greater precision and the longevity of finished products have been the driving forces behind intensive research in this field. Improvements in machining require combined knowledge of not only physics, chemistry and material behaviour but also heat transfer, solid mechanics and tribology [10].

Titanium alloys are known to be difficult to cut. This section outlines the previous work done by researchers in the field of titanium alloy machining. The works reviewed were carried out to optimise the machining process. A limited amount of work has been performed to understand the mechanisms behind serrated chip formation.

#### **2.1 Titanium Alloys**

Titanium alloys are attractive materials especially for the aerospace industry designers because of their high strength-to-mass ratio, which is maintained at elevated temperatures. In addition, these materials demonstrate corrosion and fatigue resistance. Thus, they are used as biomedical implants and in other industrial and commercial applications, such as nuclear waste storage, food processing, electrochemical applications (including cathodic protection and extractive metallurgy), marine applications, petroleum refining and chemical processing [11,12].

The application of titanium alloys is dependent on particular properties, specifically microstructures, which are in turn dependent on alloying elements and details of the mechanical processing history.

### **2.1.1 Phases and Alloying Elements of Titanium**

There are mainly four different types of Ti alloys, which are classified in terms of alloying elements [13]:  $\alpha$  alloys, near  $\alpha$  alloys,  $\alpha$ - $\beta$  alloys and  $\beta$  alloys [12,14,15].  $\beta$  alloys are further classified as metastable and stable  $\beta$  alloys [13]. All these alloys are shown in the phase diagram of titanium in Figure 2.1.

The  $\alpha$  phase has a hexagonal, close-packed (HCP) structure. The  $\beta$  phase is body-centered cubic (BCC), as shown in Figure 2.2. The presence of  $\alpha$  stabilizers (aluminum, oxygen, nitrogen and carbon) helps form  $\alpha$  and near  $\alpha$  alloys where  $\beta$  stabilizers (vanadium, iron, manganese, etc.) form metastable and stable  $\beta$  titanium alloys. A mixture of these two types of alloying elements forms  $\alpha$ - $\beta$  titanium alloys. The alloying elements on which these alloys form are shown in Table 1.

### **2.1.2 Deformation Mode of Titanium Alloys**

The deformation mode of titanium alloys depends on the phases present. The main deformation mechanism is dislocation slip. Although the  $\alpha$  phase shows twinning, which is suppressed in an  $\alpha$ - $\beta$  alloy and in  $\beta$  Ti, the twinning is limited [13].

The  $\alpha$  phase has a close-packed plane (0001), which is the basal plane. The (0001) basal plane has only one closed-pack direction that is  $\langle 1120 \rangle$ . The  $\alpha$  phase has only three slip systems, whereas the  $\beta$  phase has 42 slip systems. Although the number of slip systems is higher



in the BCC  $\beta$  phase, it requires higher shearing stress for the dislocations to move because the planes are not close-packed [16]. Therefore, the  $\alpha$  phase can deform much more readily than the  $\beta$  phase in the Ti-6Al-4V alloy.

### **2.1.3 Important Features of Ti-6Al-4V**

Ti-6Al-4V is one of the most popular titanium-based alloys for aerospace applications. Titanium industries produce this alloy more than 50% of the total production of all other types of titanium alloys. Used in a variety of applications, from massive parts for aerospace industries to small parts used as biomedical implants, Ti-6Al-4V requires sophisticated machining operations. The difficulties found with this alloy arise from its properties, which depend on its microstructure.

#### **2.1.3.1 Microstructure of Ti-6Al-4V**

Containing 6% aluminum (Al) and 4% vanadium (V), this alloy is an  $\alpha$ - $\beta$  type Ti alloy. Aluminum and vanadium are added as  $\alpha$  and  $\beta$  stabilizers, respectively. Figure 2.3 shows the microstructure of Ti-6Al-4V, including the  $\alpha$  and  $\beta$  phases. This microstructure is composed of equiaxed  $\alpha$  grains along with a lamellar  $\beta$ . Therefore, it has a bimodal structure at room temperature. In this structure,  $\alpha$  (HCP) is the stable phase and  $\beta$  (BCC) is the metastable phase.

#### **2.1.3.2 Phase Transformations of Ti-6Al-4V**

Ti-6Al-4V alloys undergo a phase transformation ( $\alpha$  to  $\beta$ ) at  $995 \pm 15^\circ\text{C}$  [13]. A phase diagram of this alloy is shown in Figure 2.4. Two different types of phase transformation can occur in this alloy: martensitic and diffusion-controlled.

Two types of martensitic phase transformations are possible depending on the phase transformation temperature and the amount of alloying element. In cases with low martensitic transformation temperatures in alloys with higher amounts of solute content, the phase that forms is called acicular martensite. This phase has nearly parallel  $\alpha$  plates or laths belonging to the same variant of Burgers relationships. In the other cases, the massive martensite forms that show intimate mixtures of  $\alpha$  plates where each have different variants of Burgers relationships [13].

With the increasing amount of solute content, the martensite phase becomes distorted and takes the shape of an orthorhombic crystal, which is designated as  $\alpha''$ . If the martensitic transformation is suppressed, the  $\beta$  phase transforms into an athermal  $\omega$  phase that appears as a uniform dispersion of extremely fine particles. Upon annealing, an isothermal  $\omega$  phase forms [13].

Diffusion controlled phase transformation occurs in cases involving slow cooling, which is controlled by nucleation and growth process. As the cooling rate increases, the size and thickness of the  $\alpha$  plates decrease [13]. The different types of phase transformations are summarized in Figure 2.5.

### **2.1.3.3 Mechanical Properties of Ti-6Al-4V**

The widespread use of the Ti-6Al-4V alloy is due to its combination of excellent properties. It has lower density and higher yield strength compared to AISI-1045 steel and lower thermal conductivity compared to all other metals, such as AISI-1045, Aluminum 1100 and ETP copper. Table 2.2 compares the important properties of Ti-6Al-4V alloy, AISI 1045 steel, Aluminum 1100 and ETP copper.

It has been observed that both phases deform [17,18] in the Ti-6Al-4V alloy. However, the amount of deformation is not the same for both phases. The deformation of the phases in Ti-6Al-4V alloy is dependent on the size of the grains. The deformation of fine grains in the Ti-6Al-4V alloy is of the isostress type because most of the dislocations are found in the  $\beta$  phase (Figure 2.6), which means the amount of deformation in the  $\alpha$  and  $\beta$  phases are not same. For the same alloy with a higher grain size, the system is a mixture of the isostress and isostrain types because both phases experience strain. Because of the larger size of the  $\beta$  phase, a higher amount of stress is concentrated due to the larger slip distance that also deforms the adjacent  $\alpha$  grain [18].

The mechanical characteristics found in Ti-6Al-4V are very complex because of its strong sensitivity to processing parameters such as strain rate and temperature. It is vital to understand these in order to clarify its deformation modes as well as to properly interpret the relationship between its microstructure and processing variables along with its properties under different loading conditions. The typical true stress-strain curves of Ti-6Al-4V alloys deformed at different strain rates and temperatures are shown in Figure 2.7. It can be seen that true stress increases monotonously with true strain and reaches a maximum value before fracture. This depicts that plastic deformation of Ti-6Al-4V alloy is greatly dependent on strain rate and temperature. However, the effect of temperature is more pronounced [19]. The variation in yield strength and ultimate tensile strength with temperature seen in Figure 2.7 is summarized in Table 2.3.

Figure 2.8 shows the effect of temperature on strain rate sensitivity. Strain rate sensitivity ( $m$ ) is calculated using the following equation for constant temperature and strain [16]:

$$m = \left( \frac{\partial \ln \sigma}{\partial \ln \dot{\epsilon}} \right)_{\epsilon, T} \quad (2.1)$$

where  $m$  is strain rate sensitivity,  $\sigma$  is flow stress,  $\dot{\epsilon}$  is strain rate,  $\epsilon$  is strain and  $T$  is temperature. In all four strain rate regions, the sensitivity increases. Figures 2.7 and 2.8 show that when the strain rate is higher, the strain hardening decreases at a critical temperature. However, in cases with low temperatures, the effect of strain rate is not as significant. Because of this strain rate, the sensitivity increases at a very high rate when the temperature is sufficiently high (e.g. above 500°C) when deforming at a constant strain rate.

Collings [20] analyses of impact strength, percent elongation and reduction in area showed that Ti-6Al-4V could maintain its toughness and ductility at low temperature, even at liquid nitrogen temperatures. However, the hardness of this annealed Ti-6Al-4V 33.5 HRC alloy increases about 42 HRC at low temperatures, as shown in Figure 2.9 [9].

Titanium alloys experience an increase in strength at low temperatures [9]. Compared to  $\alpha$ -Ti, Ti-6Al-4V shows a sharp rise in flow stress below room temperature. At around 0K, the flow stress of Ti-6Al-4V is 1600MPa, whereas for  $\alpha$ -Ti, it is around 750MPa [21].

In the low-strain-rate deformation process, the flow stress of Ti-6Al-4V reaches a plateau at around 600K, and there is a well-defined discontinuity at temperatures between 400K and 800K. Within this temperature range, the flow stress of  $\alpha$ -Ti and Ti-6Al-4V are very close. This feature is not found in the high-strain-rate deformation process. Above this temperature range, strain hardening decreases drastically due to the dynamic recovery that results in a decrease in flow stress [21]. These characteristics are shown in Figure 2.10.

## 2.2. Basics of Machining Process

Among different types of machining processes turning, milling and drilling are the widely used ones [10]. In turning process a single point tool removes the unwanted material to produce

the desired shape. This process is carried out in a lathe which is one of the oldest and most versatile machine tools [22].

### 2.2.1 Orthogonal Cutting

Orthogonal cutting is a type of turning operation in which the cutting tool generates a surface parallel to the original one [10]. In this process, the cutting tool is placed perpendicular to the relative motion of the tool and workpiece, as shown in Figure 2.11. [10,22]. On the other hand, if the cutting edge is not perpendicular, the process is known as oblique cutting [22,23].

### 2.2.2 Forces and Stress during Orthogonal Cutting

During the machining process, force is applied to the tool to cut the materials and according to Merchant, in equilibrium conditions, the forces between the tool face and chip and between the workpiece and the chip along the shear plane are equal. A force diagram is shown in Figure 2.12. The relationship between various forces are as follows [10,24]:

$$F_s = F_c \cos \Phi - F_f \sin \Phi \quad (2.2)$$

$$N_s = F_c \cos \Phi + F_f \sin \Phi \quad (2.3)$$

$$F_p = F_c \sin \alpha + F_f \cos \alpha \quad (2.4)$$

$$N_p = F_c \cos \alpha - F_f \sin \alpha \quad (2.5)$$

where  $F_c$  and  $F_f$  are the cutting and feed forces,  $F_s$  and  $F_p$  are the shear forces on the shear plane and rake face and  $N_s$  and  $N_p$  are the normal forces on the shear plane and rake face respectively.  $\Phi$  and  $\alpha$  are the shear and rake angles respectively.

The shear and normal components of the forces on the rake face can be used to measure the coefficient of friction between the chip and the tool using the following equation:

$$\mu = F_p / N_p = (F_c \sin \alpha + F_f \cos \alpha) / (F_c \cos \alpha - F_f \sin \alpha) \quad (2.6)$$

To measure the shear stress on the shear plane, the following approach can be used [24,25]:

$$\tau_s = \frac{\text{shear force on shear plane}}{\text{Area of Shear plane}} = \frac{F_c \cos \Phi - F_f \sin \Phi}{\left[ \frac{w \cdot f}{\sin \Phi} \right]} \quad (2.7)$$

where  $w$  is the width of cut and  $f$  is the uncut chip thickness which is the same as feed rate.

### 2.2.3 Deformation Zones

As the tool advances and removes material from the workpiece, deformation takes place in three different zones. These zones are known as the primary, secondary and tertiary zones; they are shown in Figure 2.13. Most of the deformation takes place in the primary deformation zone and along a fixed shear plane [1,24,26], which makes a shear angle of  $\Phi$  with the cutting direction. The secondary deformation zone forms because the chip slides along the rake face of the tool. The tertiary deformation zone forms between the machined surface and the flank face of the tool due to friction as well.

### 2.2.4 Classification of Chips

The type of chip formed during machining is not only dependent on the cutting parameters but also on the material properties. Therefore, to ensure quality machining, optimization of both of these factors is important. Two types of chips primarily exist (Figure 2.14): Steady state continuous chips and cyclic chips.

Cyclic chips can be classified into four different types (Figure 2.15):

- wavy chips;
- segmental chips;
- catastrophic shear chips or serrated chips; and
- discontinuous chips.

Cyclic variations in undeformed chip thickness, rake angle and clearance angle variation, which mainly occurs due to chatter, are causes of wavy chip formation. Limited rigidity and low damping of tools causes oscillation; therefore, part of the machine tool system experiences resonance and consequently vibrates at large amplitudes [27].

The segmental chips are similar to continuous chips but with a periodic variation in thickness. This type of chip forms at certain machining conditions. The mechanism of this type of chip formation can be described as a slow, forward movement of the plastic zone that forms a ramp on the free surface of the chip. This is followed by a rapid return of that zone back towards the tool because of partial fracture, thus forming a step on the chip segment. The instability in the primary shear zone is associated with negative stress-strain material characteristics at large strains; the instability in the secondary shear zone arises from frictional relaxation oscillations leading to stick-slip friction on the tool [27].

Ti alloys form catastrophic shear chips even at very low cutting speeds. Two different theories concern the basic origin of this type of chip formation. One describes the chip formation process on the basis of thermal origin where the other considers the periodic development of cracks in the original surface of the workpiece [7]. The details of this kind of chip formation will be described in Section 2.3.2.

Discontinuous chip formation begins by upsetting the incoming work material ahead of the tool tip. During this process, strain concentrates in a narrow band followed by crack formation ahead of the tool tip due to stress concentration leading to rupture along the shear surface. The failure is brittle in nature, and no re-welding of the individual segments occurs to separate it from the serrated chip [27].

### **2.2.5 Microstructural Deformation due to Orthogonal Cutting**

Machining is a high-strain rate deformation process that generates large strains and strain gradients in the workpiece [28]. Systematic microstructural analyses can not only increase understanding of the effect of machining on the work material and chip formation but also quantify different factors, such as the amount of deformation, depth of deformed zone and chip thickness for the optimization of the machining process.

A cross-sectional optical micrograph showing the primary deformation zone in a copper workpiece that was subjected to orthogonal cutting is shown in Figure 2.16. Ramalingam and Black [28,29] analyzed the plastically deformed root of a steel chip SEM (Scanning electron microscopy) and TEM (Transmission electron microscopy) and observed lamellar chip morphology, which was due to heterogeneous plastic flow. Thus, they concluded that a dynamic equilibrium exists between strain hardening and recovery during chip formation. Zhang and Alpas [30] observed the deformed microstructure of aluminum alloy (6061 Al) and measured the shear angle from the displacement of the extrusion lines, which act as inherent microstructural markers. They also established a method to determine the plastic strain gradients in the material ahead of the tool tip through the measured shear angle. Ni et al. performed TEM investigations on copper [31] and aluminum [32] and observed grain refinement by plastic



deformation as the material ahead of the tool tip passed through the primary deformation zone. A schematic based on a TEM analysis of deformed copper at the primary deformation zone is shown in Figure 2.17.

### **2.2.5.1 Shear Angle Estimation**

The shear angle can be estimated from the chip thickness value and feed. However, it is important to measure shear angle from the microstructure because in cases involving heterogeneous or localized deformation, the above estimations could be incorrect. In addition, the shear angle at a fixed position within the workpiece cannot be measured with this formula.

Zhang and Alpas [30] used the extrusion lines of 6061 Al as a marker and from the change in orientation of these lines due to shearing, they measured the angle. A computer-generated, accurate representation of the flow lines they presented is shown in Figure 2.18a. The shear angle values were then computed from the slope of these lines (Figure 2.18 b) according to the following formula:

$$\phi = \tan^{-1} \left( \frac{\Delta Y}{\Delta X} \right) \quad (2.8)$$

Elmadagli and Alpas [33] used the same procedure to measure the angle in cases involving orthogonally machined, commercially pure copper samples. However, instead of flow lines, they used the deformed grains as the marker and found that the shear angle varied from  $9^\circ$  to  $21^\circ$  from tool tip to chip root.

### **2.2.5.2 Effective Plastic Strain Estimation**

The amount of plastic deformation generated in the workpiece due to machining can be estimated using the method described by Dautzenberg and Zaat [34]. In this method, they

considered an ideal spherical crystal deforming under true shearing, as shown in Figure 2.19. All the components of normal strains and shear strains were considered as zero except  $d\gamma_{yx}$ . Thus,

$$d\epsilon_x = d\epsilon_y = d\epsilon_z = d\gamma_{zy} = d\gamma_{zx} = 0 \quad (2.9)$$

and

$$d\gamma_{yx} \neq 0 \quad (2.10)$$

where  $d\epsilon_{x,y,z}$  and  $d\gamma_{ij}$  represent the components of normal and shear strains respectively.

According to Thomsen et al. [35], the effective plastic strain  $d\bar{\epsilon}$  can be defined as follows:

$$\frac{9}{4} (d\bar{\epsilon})^2 = \frac{1}{2} \left[ (d\epsilon_x - d\epsilon_y)^2 + (d\epsilon_y - d\epsilon_{zy})^2 + (d\epsilon_z - d\epsilon_{xy})^2 \right] + \frac{3}{4} [d\gamma_{yx}^2 + d\gamma_{zy}^2 + d\gamma_{xz}^2] \quad (2.11)$$

From Eq. 2.10 and Eq. 2.11, it can be shown that:

$$d\bar{\epsilon} = \frac{d\gamma_{yx}}{\sqrt{3}} = \frac{\sqrt{3}}{3} \frac{dl_x}{dl_y} \quad (2.12)$$

Integrating this Eq. 2.12 leads to:

$$\bar{\epsilon} = \frac{\sqrt{3}}{3} \frac{1}{l_y} \int_0^{l_x} dl_x = \frac{\sqrt{3}}{3} \frac{l_x}{l_y} \quad (2.13)$$

from Eq. 2.8 and Eq. 2.13 :

$$\phi = \tan^{-1} \left( \frac{\Delta Y}{\Delta X} \right) = \tan^{-1} \left( \frac{\sqrt{3}}{3\bar{\epsilon}} \right)$$

$$\bar{\epsilon} = \frac{\sqrt{3}}{3 \tan \phi}$$

$$\bar{\epsilon} = \frac{\sqrt{3}}{3} \tan \theta \quad (2.14)$$

where  $\theta = 90^\circ - \Phi$  and  $\Phi$  is the shear angle.

Eq. 2.14 has been successfully used by researchers [30,32,33] to estimate the effective plastic strains at different positions of workpieces subjected to machining, as shown in Figure 2.20.

### 2.2.5.3 Flow Stress Estimation

Chip formation in ductile materials can be considered a process of dynamic equilibrium between strain hardening and recovery [28]. Tabor [36] related the amount of deformation with the hardness, considering the fact that both these factors are related to elastic limit.

The criteria for plastic flow in a solid body subjected to principal stresses of  $\sigma_1$ ,  $\sigma_2$  and  $\sigma_3$  is [16]:

$$\sigma_0 = \frac{1}{\sqrt{2}} [(\sigma_1 - \sigma_2)^2 + (\sigma_2 - \sigma_3)^2 + (\sigma_3 - \sigma_1)^2]^{\frac{1}{2}}$$

$$2\sigma_0^2 = (\sigma_1 - \sigma_2)^2 + (\sigma_2 - \sigma_3)^2 + (\sigma_3 - \sigma_1)^2 \quad (2.15)$$

where  $\sigma_0$  can be measured by uniaxial tension experiments.

The mean pressure,  $\sigma_m$ , can be defined as follows:

$$\sigma_m = \frac{\sigma_1 + \sigma_2 + \sigma_3}{3} \quad (2.16)$$

Based on assumptions made by Hill et al. [37], this equation can be solved. They concluded that plastic yielding would occur when the mean pressure,  $\sigma_m$

$$\sigma_m = 3\sigma_0 \quad (2.17)$$

Marsh [38] proposed an equation that relates the Vickers hardness to the corresponding flow stress,  $\bar{\sigma}$  as-

$$\bar{\sigma} = \frac{H}{3} \quad (2.18)$$

This approximation is commonly used by researchers to predict the flow stress at different positions on work material subjected to cutting operations [31,32].

#### 2.2.5.4 Energy Expended due to Plastic Deformation and Temperature Rise

Material subjected to machining just ahead of the tool tip towards the un-deformed portion shows a gradual decrease in plastic strain and flow stress. A relationship was developed by plotting the effective plastic strain and the corresponding effective flow stress value [33]. A regression analysis, shown in Figure 2.20, indicates that the curve follows the Voce equation [39]:

$$\bar{\sigma} = \bar{\sigma}_s - (\bar{\sigma}_s - \bar{\sigma}_0) \exp\left(-\frac{\bar{\epsilon}}{\bar{\epsilon}_c}\right) \quad (2.19)$$

where  $\bar{\sigma}$  is the effective flow stress and  $\bar{\epsilon}$  is the corresponding effective strain.  $\bar{\sigma}_s$  represents the saturation stress at which the work hardening rate is zero,  $\bar{\sigma}_0$  is the yield flow strength of the material and  $\bar{\epsilon}_c$  is a constant.

The stress-strain curve shown in from Figure 2.21 was used to calculate the work done per unit volume due to plastic deformation, as the area under the stress-strain curve gives the value of energy expended during the process. For each increment of strain, the work of plastic deformation,  $W$  (per unit volume), is given as follows [33]:

$$W = \int_{\bar{\epsilon}_n}^{\bar{\epsilon}_{n+1}} \bar{\sigma} d\epsilon = \bar{\sigma}_s - (\bar{\sigma}_s - \bar{\sigma}_0) \exp\left(-\frac{\bar{\epsilon}}{\bar{\epsilon}_c}\right) d\epsilon \quad (2.20)$$

According to the energy conversion rule, a large portion of this work would be converted to heat. This will increase the temperature, which can be expressed as follows [32]:

$$\Delta T = \frac{\beta}{\rho C} \int_{\bar{\epsilon}_n}^{\bar{\epsilon}_{n+1}} \bar{\sigma} d\epsilon = \bar{\sigma}_s - (\bar{\sigma}_s - \bar{\sigma}_0) \exp\left(-\frac{\bar{\epsilon}}{\bar{\epsilon}_c}\right) d\epsilon \quad (2.21)$$

where  $\beta$  is the plastic work converted into heat,  $\rho$  is density of the material and  $C$  is the specific heat capacity of the material. The increase in temperature during 1100 aluminum machining calculated using Eq. 2.21 is shown in Figure 2.22.

## **2.3 Machining of Titanium Alloys**

Machinability is judged in terms of four different criteria: 1) chip formation, 2) cutting force or power requirement, 3) tool life and 4) surface condition of the finished product [40]. Research in this field started in the early 1950s and has continued for optimizing the machining operations.

### **2.3.1 Machinability of Ti-6Al-4V**

Properties such as high strength-to-weight ratio, strength at high temperature, ductility and fracture resistance make Ti-6Al-4V a suitable option for various industrial applications, although these properties make it difficult to machine. Many researchers have noted different problems that arise during Ti-6Al-4V machining and their relation to material properties [8,41-45].

1. Machining operation accumulates high amount of deformation within the material, and a large portion of this deformation converts into heat. As shown in Table 2.2, titanium alloys possess poor thermal properties. The heat becomes trapped, which causes high temperature generation within a narrow zone leading to further deformation occurring in that particular region. Strain localization (or heterogeneous deformation) results in cyclic chip formation.

2. Localized deformation and the low modulus of elasticity, which decreases even at moderate temperatures, cause oscillations in cutting and thrust components of forces that eventually result in chatter [8].
3. Approximately 80% of the generated heat is conducted into the tool during machining Ti-6Al-4V (due to low thermal conductivity), whereas in cases using steel, the absorbed heat is approximately 50%. This high amount of heat, along with the oscillation produced during machining titanium alloys, is thought to be the reason for wear on flank faces [9].
4. Chips come into contact with the tool as they form and slide on the rake face of the tool during machining. When two different materials slide against each other, a solid solution forms. Wear on the dissolving material occurs from solution wear, diffusion wear or delamination wear. All these wear processes are related to the chemical stability of the materials [46]. Titanium alloys show high chemical reactivity with tool materials. According to calculations by Hartung et al. [47], no potential materials are suitable for machining titanium. The freshly formed surface at high temperatures reacts vigorously with tools and causes wear.

In summary, material properties are the root cause of the difficulties machining titanium alloys. Chips possess material properties at certain machining conditions; therefore, a thorough understanding of chip formation mechanisms and comparing chip characteristics at different machining conditions are necessary to solve or minimize problems.

## **2.3.2 Serrated Chip Formation Mechanisms**

The Ti-6Al-4V alloy produces serrated chips not only under conventional, high-speed machining but also at low cutting speeds [48]. Two mechanisms for serrated chip formation are proposed by researchers. These mechanisms are described in detail in this section.

### **2.3.2.1 Adiabatic Shear Mechanism**

Metallic materials strain hardens when plastically deformed. Further deformation requires the application of extra amounts of stress. Due to heat entrapment in titanium alloys, two opposing effects, strain hardening and thermal softening, occur simultaneously to create an unstable condition. Researchers [4, 49-53] have proposed that thermoplastic shear instability is the root cause of serrated or catastrophic shear chip formation in titanium alloys.

Based on high-speed imaging, a mechanism for serrated chip formation in the Ti-6Al-4V alloy was proposed [6] and described with the help of a schematic, which is shown in Figure 2.23. According to Komanduri [6], serrated chip formation is a two-stage procedure. In the first stage, thermal softening and strain hardening results in instability which leads to strain localization along a shear surface (band). This shear surface originates from the tool tip and gradually curves upwards until it meets the free surface. Therefore, a concave surface is formed (Figure 2.23c). In the second stage, the tool's gradual advancement applies an increased amount of force, at which point a crack initiates at the tool tip and gradual flattening increases the contact between the tool and the material ahead. Until this stage, there is almost no relative velocity between the bottom surface of the chip segment being formed and the tool. The chip being formed pushes the previously formed chip by bulging and gradually flattening, thus shifting its contact towards the tool face. As the upsetting progresses, more and more stress is

generated, which causes intense shear between the segment being formed and the one before it. This leads to the formation of shear bands, which occurs at all cutting speeds. The intense shear at higher cutting speeds separates the individual segments due to the gradual decrease in contact between any two segments.

### **2.3.2.2 Periodic Crack Development Mechanism**

In Ti-6Al-4V, serrated chips are found even at very low cutting speeds. Because the cutting speed is low, the generated heat will be low as well. Therefore, the adiabatic shear theory of serrated chip formation may not prevail because the basis of this theory is of thermal origin. Nakayama et al. [54] developed a different theory for serrated chip formation. They ran tests on extremely cold-worked (brittle) brass and suggested that periodic crack development is the basis of chip serration rather than adiabatic shear. They explained their theory with the help of a schematic, which is shown in Figure 2.24. The figure shows that the material at point C moves upward along CD, which has the same applied load direction. A shear crack initiates at point D, which runs from the surface in a downward direction toward the tool tip along the path DO. As the tool advances, the chip glides outward along the cracked surface until the next crack forms at D'. The reason for the crack formation at point D is shown in the Figure 2.24a. As the tool advances, it provides compressive stress. Because D is on the surface, the compressive force along the  $\sigma_{\min}$  direction is zero. For being the crack arresting force zero, the shear force at D is the maximum that leads to crack initiation. As the crack propagates into the material, the value of the crack arresting force gradually rises. The crack is initially continuous, which is called gross crack, but it becomes discontinuous because of the arresting force, which creates microcracks.



The schematic developed by Nakayama et al. is a snapshot of the moment when a crack occurs at point D. Shaw and Vyas [7] developed a schematic showing a snapshot of an instant after crack formation. This schematic is shown in Figure 2.25.

Along with Nakayama et al. [54] and Vyas and Shaw [7], researchers such as Cook et al. [55], Elbestawi et al. [56] and Poulachon and Moisan [57] have suggested the same mechanism showing that cracks initiate periodically at the free surface and propagate towards the tool tip.

### **2.3.2.3 Recent Clarifications on Adiabatic Shear Mechanism**

Recent publications tend to support the adiabatic shear mechanism more than periodic crack development. A quick stop method was developed by Gente and Hoffmeister [58] to observe partially formed chips during high-speed machining of the Ti-6Al-4V alloy. They found localized shear in the chips, and they concluded the chips were different from those observed by Nakayama et al. [54] in cases involving brass. On the other hand, Cottrell and Brayne's [59] high-speed imaging observations during high-speed machining showed localized shear due to thermal instability. Metallurgical analyses of the chips from high-speed machining of the Ti-6Al-4V alloy [60] and hardened steel [61] led to the same findings. All these analyses were done in cases involving high-speed machining in which the contradiction of saw tooth chip formation mechanism persists.

Along with crack initiation/propagation mechanisms during saw tooth chip formation, some other aspects have gained recent attention as well. According to the adiabatic shear theory, strain is localized along a curved surface, which Recht [62] also mentioned in his proposed model (Figure 2.26). However, no particular reasons were provided for this. In addition, the reasons for the material extruding into this sharp point were not clarified. This

concept has been modified in a recent model based on thermal analysis [63], which is shown in Figure 2.27, but it still has some problems (see Shaw [10]).

### 2.3.3 Adiabatic Shear Band in Ti-6Al-4V

As mentioned previously, titanium alloys' poor thermal properties result in strain localization. The narrow section (band) away from the section of the material where deformation localizes becomes susceptible to failure much more than the material [64]. Thus, further deformation takes place within that narrow zone, which is known as the adiabatic shear band. This is because in the adiabatic shear process, no heat can be transferred, while in the isothermal process, heat transfer takes place so temperatures remain constant. The adiabatic shear band is one of the main distinct features of Ti-6Al-4V (Figure 2.28). In this section, some of the adiabatic shear band's important characteristics will be discussed.

#### 2.3.3.1 Instability Criteria

A sound knowledge about instability criteria is a must to predict in which particular condition the strain will be localized and an adiabatic shear band will form.

Recht [4] developed a criterion for those materials which are markedly affected by temperature distribution even at low strain rate deformation process. In these materials the shear strength depends on strain and temperature as follows:

$$\frac{d\tau}{d\gamma} = \frac{\partial\tau}{\partial\gamma} + \frac{\partial\tau}{\partial\theta} \cdot \frac{d\theta}{d\gamma} \quad (2.22)$$

Catastrophic shear occurs when the negative effect of the local rate of temperature change on strength is equal to or greater than the positive effect of strain hardening. At that moment, the slope of the true stress-true strain curve becomes zero, and the Eq. 2.22 becomes-

$$\frac{\partial \tau}{\partial \gamma} = - \frac{\partial \tau}{\partial \theta} \cdot \frac{d\theta}{d\gamma} \quad (2.23)$$

According to Recht [4], the criteria for catastrophic slip can be written as follows:

$$0 \leq \frac{\frac{\partial \tau}{\partial \gamma}}{-\frac{\partial \tau}{\partial \theta} \frac{d\theta}{d\gamma}} \leq 1 \quad (2.24)$$

where  $\theta$  is the temperature above ambient,  $\frac{\partial \tau}{\partial \gamma}$  is the slope of shear stress-shear strain curve,  $\frac{\partial \tau}{\partial \theta}$

is the slope of temperature dependence of flow stress and  $\frac{d\theta}{d\gamma}$  is the slope of temperature vs.

shear strain curve . This equation states that catastrophic shear will occur because the value of

the ratio  $\left(\frac{\frac{\partial \tau}{\partial \gamma}}{-\frac{\partial \tau}{\partial \theta} \frac{d\theta}{d\gamma}}\right)$  is between 0 and 1, where high positive value ( $> 1$ ) will cause uniform strain

throughout the material. A negative value indicates the material will become stronger with the increase in temperature.

Lemaire and Backofen [65] measured the temperature of the shear zone formed during machining. Although the material showed phase transformation, the measured temperature was below the phase transformation temperature. As a result, they considered machine stiffness that would be responsible for these differences and proposed the following formula as a criterion for plastic instability:

$$\frac{\partial \tau}{\partial \theta} \frac{\partial \theta}{\partial \gamma} < - \frac{C_{m\Gamma} \cdot b}{A} \quad (2.25)$$

where  $C_{m,r}$  is the stiffness of the machine,  $b$  is the shear zone thickness and  $A$  is the area of the shear plane.

Conventional instability analyses, in which the deformation rate is low, predict the occurrence of instability at maximum flow stress. Because the deformation rate is low, the effect of strain rate sensitivity is neglected for which the ratio,  $\alpha$  becomes [50]:

$$\alpha = \frac{\text{Softening rate}}{m} = 0 \quad (2.26)$$

where  $m$  is strain rate sensitivity. Because machining is a high-strain rate process, it is expected to have noticeable flow localization at strains beyond the shear stress maximum. Based on this idea, Semiatin and Rao [50] suggested the following:

$$\alpha = \frac{\text{Softening rate}}{m} \geq 5 \quad (2.27)$$

To determine the root cause of triggering an adiabatic shear band and to justify the validity of the above-mentioned ratio ( $\alpha$ ), two different models were proposed [66]. Among these two models, the flow localization that incorporated strain, strain rate hardening and thermal softening demonstrated that a critical value of strain concentration ( $\alpha$ ) is necessary to trigger the instability. However, this model predicted the ratio would be between 3 and 4 rather than 5.

Timothy and Hutchings [67] suggested the following formula to measure the critical instability strain:

$$\gamma_1 = \frac{n \cdot \rho \cdot C}{\beta \cdot \left(\frac{\partial \tau}{\partial \theta}\right)_{\epsilon, \dot{\epsilon}}} \quad (2.28)$$

where  $\rho$  is the density of the material,  $n$  is the strain hardening exponent,  $C$  is the specific heat capacity,  $\beta$  is the fraction of plastic work that appears as heat (generally between 0.9 and 1.0)

and  $\frac{\partial \tau}{\partial \theta}$  is the slope of the temperature dependence of flow stress taken at constant strain and strain rate.

### 2.3.3.2 Types of Adiabatic Shear Band

Two types of adiabatic shear band were reported in the literature on the extent of adiabatic strain localization and phase change [68,67,69]. Backman and Finnegan [70] originally proposed that shear bands could be deformed or transformed depending on the temperature within the shear band.

Deformed shear bands form within materials in which no phase change is possible or the temperature is below the phase transformation temperature even though the bands possess a high amount of modified grains than original. Metals with low thermal diffusivity and low resistance to adiabatic shear localization are prone to forming transformed shear bands. Deformed shear bands act as a precursor to transformed shear bands [71].

### 2.3.3.3 Recrystallization and Phase Transformation in Adiabatic Shear Band

The Ti-6Al-4V alloy can show both types of shear bands because it is a two-phase alloy. The phase transformation occurs at  $995 \pm 15^\circ\text{C}$ , as mentioned in Section 2.1.3.2. To identify the shear band morphology, it is important to determine the temperature within the shear band. The temperature can be estimated from the following equation [65]:

$$T_{sz} = \frac{\tau \gamma}{J \rho C} \left[ \frac{1}{1 + 1.328 \sqrt{\frac{K \gamma}{V f}}} \right] + T_{amb} \quad (2.29)$$

where  $T_{sz}$  is the shear band temperature,  $J$  is the mechanical equivalent of heat,  $\rho$  is density,  $C$  is the specific heat capacity,  $K$  is thermal diffusivity,  $V$  is cutting speed,  $f$  is feed and  $T_{amb}$  is ambient temperature. Along with the theoretical calculations, microstructural analyses were conducted to predict the type of bands.

Many researchers [67-69,72-75] observed equiaxed grains within the shear band. Meyers [69] noted a high angle boundary and low dislocation density along with equiaxed grains in Ti-6Al-4V alloys. These features were seen as indications of dynamic recrystallization occurring during plastic deformation. To nucleate the new recrystallized grains, a critical strain is needed. Due to the low specific heat ( $0.568 \text{ J/gm}^{\circ}\text{C}$ ) of Ti-6Al-4V alloys, heat generated due to deformation, will be trapped in the deformed zone, which increases the temperature to  $0.4 T_m$  or above, where  $T_m$  (around  $1800^{\circ}\text{C}$ ) is the melting temperature. At this temperature, the diffusional process is responsible for the occurrence of recrystallization. Consequently, each time the deformed material reaches a critical strain; new dislocation free grains nucleate and grow. A schematic of this process is shown in Figure 2.29.

A considerable amount of debate has taken place regarding the amount of heat generated within the shear band and whether the temperature rise is sufficient for phase transformation. Conducting XRD on the rake face of the chip has shown that no change in peaks occurs [73], which implies that no phase transformation occurred. Puerta et al. [60] cut a small transparent section, performed XRD analysis on the shear band and concluded that the shear band is of the deformed type (Figure 2.30).

The most efficient way to characterize the type of shear band is by conducting TEM analyses; some interesting features can be detected in this way [74]. Figure 2.31 shows the adiabatic shear band at different cutting speeds. Figures 2.31a and 2.31b clearly show that at a

cutting speed of 30.2m/min, the shear band was not as sharp and the chip showed incipient segmentation (Figure 2.32) which became completely segmented as the cutting speed was increased to 59.6m/min. The diffraction pattern in figure 2.33 shows that the  $\alpha$  and  $\beta$  phases were both present, which proves that this was a deformed type of shear band. Figure 2.34a shows the center region of the shear band and indicates the  $\alpha$  and  $\alpha''$  phases, where  $\alpha''$  is an orthorhombic crystal. Thus, there might be a phase transformation in the center region from  $\beta$  to  $\alpha''$ . However, at the same cutting condition (Figure 2.34b), the transition region was indexed only with  $\alpha$ , which indicated no phase transformation. The center and transition regions of the shear band formed at a cutting speed of 281.3m/min (Figure 2.31f) indicated complete transformation. The presence of the  $\alpha''$  phase indicates that the phase transformation is martensitic in nature. The orientation relationship (OR) found between the  $\alpha$  and  $\beta$  phases  $[0001]\alpha//[111]\beta$  and  $(0\bar{1}10)\alpha//(01\bar{1})\beta$  are not indicative of Burgers type. This type of OR is observed when hexagonal magnesium transforms into  $Mg_{17}Al_{12}$  through the diffusional process [74]. On the other hand, it was reported [75] that the phase transformation process in Ti-6Al-4V is a non-diffusional process.

In summary, the shear band type changes from a deformed band to a mixture of deformed and transformed bands to only a transformed band depending on the cutting speed (at a constant feed rate) [74]. A martensitic transformation takes place in all the transformed regions of the shear bands.

Another way of predicting the shear band type is by measuring the hardness of the band. In cases involving deformed bands, the hardness value should be higher due to a higher dislocation density in the deformed grains. However, for a transformed band, it should be lower because the BCC  $\beta$  phase transforms to  $\alpha'$  or  $\alpha''$ , which are allotropes (same chemical

composition but different structure) of  $\beta$ , and as mentioned [16] allotropic transformation of BCC phase is softer. Timothy and Hutchings noted that  $\alpha'$  in a transformed shear band was up to 10% softer than the adjacent deformed region [67]. Hardness has been measured by different researchers [69,76,77], who concluded that no substantial variation from the bulk region occurred (Figure 2.35).

### **2.3.4 Fracture Surface of Ti-6Al-4V**

Regardless of the crack initiation position or the type of shear band, fractures always occur within the strain localized region, which is the shear band. The observation of fracture surfaces is important because it can provide information about the phases present within the band and their mode of deformation.

#### **2.3.4.1 Morphology of Fracture Surface**

The presence of voids within the shear band has been reported by a number of researchers [67,69,72,78-80] and it was thought that the nucleation and growth is the cause of fracture of shear band. The void formed within a well-developed shear band is shown in Figure 2.36. Two types of cavities were found: spherical and elliptical cavities. The presence of elliptical cavities was thought to be formed only because of deformation, which in cases involving very high temperatures could take a spherical shape [72].

Three types of fracture surfaces were observed by Timothy and Hutchings [79]. These are shown in Figures 2.37–2.39. Figure 2.37 shows only the equiaxed type of dimples, but the elongated type of dimples can form as well [81]. The dimples were separated by comparatively smooth regions, as shown in Figure 2.38. Globules (Figure 2.39) may form due to local melting, which is attributed to very high-speed machining tests.



#### 2.3.4.2 Mechanisms of Chip Fracture

Some arguments have taken place regarding the nucleation of cavities within the shear band. Two types of theories are presented in the literature [78,80]. One considers the  $\alpha/\beta$  phase interface as a possible candidate for the formation of cavities due to sliding along the phase boundary. In cases involving super-plastic condition (fine grain and high temperature), most of the dislocations were observed in the  $\alpha/\beta$  phase boundaries but not in the core regions (Figure 2.40). The presence of the dislocations at the  $\alpha/\beta$  phase boundary proves phase boundary sliding because martensitic transformation does not increase dislocation density by volume expansion [18]. Since Ti-6Al-4V machining involves high temperatures in the shear band, thermal softening and local melting can also lead to high temperatures within the shear band and low tensile strength at the shear surface.

Three possible mechanisms are proposed for the growth of cavities [80]. One mechanism is based on the fact that the unloading establishes of a tensile stress state which causes the cavity to open. This could explain the cavities' spherical nature. Softening the shear band due to high temperatures may cause a tensile stress state, which could also cause cavities to grow. The third mechanism proposes that elongated shear cavities are formed but the high temperature within the shear band causes high atomic mobility, which helps the voids become spherical by reducing surface energy.

The possible reasons behind the formation of three different types of fracture surfaces were discussed by Timothy and Hutchings [78] which are shown in Figure 2.41. According to this model, the final shear fracture surface depends on the density of void formation. If the voids are formed at a certain critical distance, such as those shown in Figure 2.41b, the dimple type of fracture surface are formed (Figure 2.37). The knobbly type of fracture surface may form due to

tensile failure along a molten shear band (Figure 2.39b and Figure 2.41c). Subsequent rubbing between the two surfaces may produce a smoother texture.

Liao et al. [81] performed TEM analyses on the elongated dimple type of fracture surface and concluded that the dimples are formed in the  $\alpha$  phase because the size matches and that the comparatively smooth regions form in the  $\beta$  phase. They also mentioned that the  $\alpha$  phase showed an orientation change during deformation, which is attributed to twinning. As mentioned before, plastic deformation produced during metal cutting involves a dynamic equilibrium between strain hardening and recovery. Therefore, factors governing the kinetics of dynamic recovery, such as collision and dragging of dislocations (due to attraction and repulsion of dislocations), cross slip (movement of screw dislocation from one slip plane to another) and climb (movement of dislocation out of glide plane) must be considered for a better understanding of the possible reasons for chip fracture [82].

### **2.3.5 Cryogenic Machining**

Today, the Ti-6Al-4V alloy is machined using cryogenic techniques because heat entrapment and drastic temperature, which increases in a narrow zone, is a challenge for optimizing Ti-6Al-4V machining operation and cooling with liquid nitrogen helps attain lower temperatures quickly due to its low boiling point (-196°C). In addition, liquid nitrogen does not involve problems with disposal, which makes it environmentally safe.

Hong and Ding [83] showed measured and predicted temperatures of a tool used in different cutting approaches (Figure 2.42). Figure 2.42 shows that different types of cooling approaches are used, even in cryogenic machining. Cooling only the rake face or the flank face of the tool showed very similar temperatures as the pre-cooled workpiece. In case of cooling

both faces of the tool showed the lowest temperatures. Therefore, injecting liquid nitrogen during machining is very important for cryogenic machining.

Sun et al. [84] developed a cooling method in which liquid nitrogen was mixed with compressed air and passed over the rake and flank faces of the tool, as shown in Figure 2.43. In this type of coolant delivery system, it is possible that the coolant will not reach the exact cutting zone. To avoid this problem, modified tool holder was used by Bermingham et al. [85] which is shown in (Figure 2.44). In this method, the modified tool holder could efficiently cool only the rake face only. So an additional nozzle was used for flank face cooling. Dhananchezian et al. [86] modified the cutting tool so all the tool surfaces of the tool could be cooled without using any additional nozzles. A schematic of this modified tool is shown in Figure 2.45.

### **2.3.6 Effect of Cutting Condition**

Bayomi and Xie [75] indicated that the onset of shear localization in the Ti-6Al-4V alloy is dependent on the cutting speed and feed rate. Both these parameters cause temperature variations; therefore, the cooling approaches affect the chip characteristics and deformation behavior as well.

#### **2.3.6.1 Distance between Two Consecutive Shear Band**

Molinari [87] and Bayomi et al. [75] noted that the distance between two consecutive shear bands decreases when the cutting speed increases. But Mahcado and Wallbank [64] reported an increase in distance with cutting speed and also with feed. Bermingham et al. [85] compared distances for dry and cryogenic cutting. The cryogenic cutting process, in which the rake and flank faces were both cooled, is shown in Figure 2.44. They found that in cryogenic

machining, the distance was lower when the feed rate was high, but the distance was higher than the dry condition when feed rate was low.

### **2.3.6.2 Chip Thickness and Shear Angle**

Predicting the shear angle accurately is vitally important because most of the calculations in machining depend on it. Subramanian et al. [88] examined serrated chips from a hardened Fe-9.7%Ni-0.1%C alloy and showed that the shear angle increased with the cutting speed up to the microstructural softening point; after that point, it decreased in conjunction with the increase in the cutting speed. They related this change to the chip thickness value (Figure 2.46). This observation is further discussed in Section 4.2.5.5.

Bermingham et al. [85] showed that for Ti-6Al-4V, the chip thickness was lower in cryogenic conditions regardless of feed rate. They also observed that the shear angle was higher at low feed rates in dry and cryogenic conditions. During cryogenic machining, the shear angle was found to be lower at higher feed rates and higher at lower feed rates (Figure 2.47).

### **2.3.6.3 Comparison of Different Force Components**

Researchers measured the components of the forces in different types of cryogenic cooling approaches. Bermingham et al. [85] cooled the flank face of the tool and observed that no change occurred in the feed component of force but the cutting force was lower than the dry machining. Dhananchezian et al. [86] cooled the flank and the rake face along with the tool surface and observed that cryogenic machining required less force than wet machining when an emulsion of cutting fluid was used as a coolant. They noted that lower temperatures during cryogenic machining were responsible for lower values of both components of forces. They also found that the cutting and feed forces decreased with increased cutting velocity (Figure 2.48).

On the other hand, Sun et al. [84] used compressed air cryogenic cooling and found that the cutting and feed forces were higher at the beginning of the machining process but lower when it ended than in dry machining.

#### **2.3.6.4 Surface Roughness**

Subsurface after-machining of Ti-6Al-4V was found to deform along the direction of machining due to thermal and mechanical effects [60,89]. The depth of the deformed zone depends on cutting conditions. Velasquez et al. [60] reported that the depth of the deformed zone increased with cutting speed. The roughness of the machined surface also depends on the machining condition. The type of tool also plays an important role. Dhananchezian et al. [86] measured the surface roughness in wet (emulsion of cutting fluid) and cryogenic machining at different cutting speed using TiAlN coated tungsten carbide tool insert. They found that the cryogenic condition reduced surface roughness to a maximum of 35% over wet machining (figure 2.49) due to the low tool wear rate.

#### **2.3.6.5 Tool Wear**

High temperatures and high stress at the cutting edge, shorter tool chip contact length, the high chemical reactivity of titanium and the serrated chip formation process are responsible for shorter tool life, which is a major concern for manufacturing industries. Different types of wear occur during titanium alloy machining as shown in Figure 2.50.

Many researchers have studied tool wear in cryogenic conditions and compared it with dry machining [84-86,90,91]. Regardless of the liquid nitrogen cooling approach used, the cryogenic conditions reduce tool wear (Figure 2.51). Dhananchezian et al. [86] reported reduced tool wear rates at a maximum of 39% over wet machining (using an emulsion). It was mentioned

that the low temperatures and low adhesion are responsible for low tool wear rates when temperatures are 40–50% lower in cryogenic conditions measured using a non-contact, infrared thermometer.

Tool life can be expressed in terms of time or volume of material removal before cutting tools wear out or fracture. According to ISO3685 standards [92], the end of a tool's life occurs when the average flank wear exceeds 300 $\mu\text{m}$  or the maximum flank wear reaches 600 $\mu\text{m}$ , whichever occurs sooner. Bermingham et al. [85] studied the flank wear in dry and cryogenic conditions by dividing the flank face into two different portions, primary flank and nose, at different feed rates. They found that with increased feed rates, the tool life decreased but in all feed rates, the tool life at cryogenic conditions was higher (Table 2.4 and Figure 2.51).

## **2.4 Summary of Literature Survey**

In this chapter, the previous research on serrated chip formation of the Ti-6Al-4V alloy was investigated in cases involving high-speed machining. Serrated chips formed during low-speed machining of different materials, such as pure brass and AISI 1045, introduced some contradictions in terms of strain localization and crack initiation/propagation. A considerable amount of research focused on tool wear and the improvement of tool life, and cryogenic machining was introduced for this purpose. Tool wear during Ti-6Al-4V alloy machining does not only depend on diffusion but also on dissolution and adhesion. Understanding the effect of dissolution and adhesion as well as factors associated with them, such as temperature, contact length or area; require detailed knowledge of microstructure-based chip formation mechanisms and the characterization of dry and cryogenic conditions. The current work is clearly directed towards this area.

## TABLES

**Table 2.1** Classification of elements that form different types of titanium alloys [13].

<b>Alpha Stabilizer</b>	Al, O, N, C
<b>Beta Stabilizer</b>	<b>Beta Isomorphous-</b> V, Mo, Nb, Ta
	<b>Beta Eutectoid-</b> Fe, Mn, Cr, Ni, Cu, Si, H
<b>Neutral</b>	Zn, Sn

**Table 2.2** Important properties of different metals[15,93-97].

<b>Properties</b>	<b>Ti-6Al-4V</b>	<b>AISI-1045 Steel</b>	<b>Aluminum 1100</b>	<b>ETP Copper</b>
Yield Strength, MPa	880	505	103	76
Modulus of Elasticity, GPa	110	205	68.9	125
Density, g/cc	4.43	7.84	2.71	8.89
Thermal conductivity, W/m k	7.3	49.8	220	388

**Table 2.3** Yield strength and ultimate tensile strength variation with temperature of Ti-6Al-4V alloy [19].

Temperature ( $^{\circ}\text{C}$ )	Yield Strength (MPa)	Ultimate Tensile Strength (MPa)
25	1100	1550
300	950	1280
500	850	1120
700	700	900
900	550	700
1100	400	520

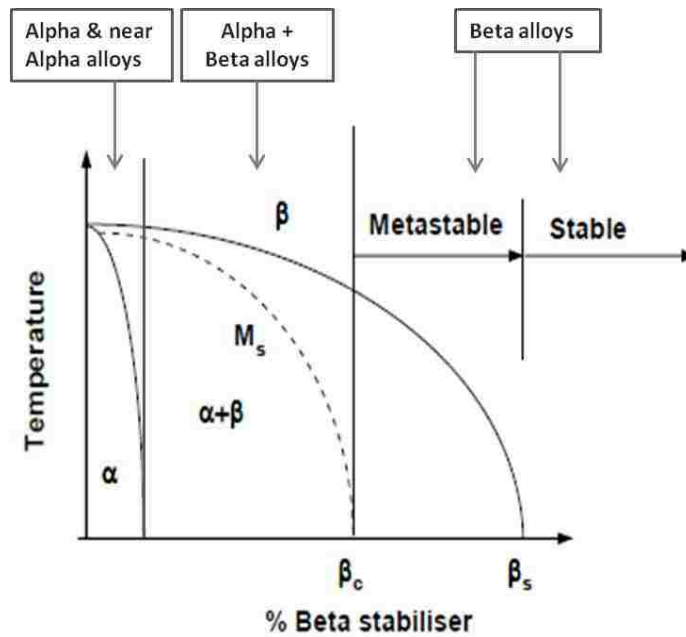
**Table 2.4** Tool life for each cutting condition and improvement with cryogenic coolant [85].

Condition	Tool Life <sup>a</sup> (s)				Improvement (%)
	Dry	Failure Location	Liquid Nitrogen	Failure Location	
f=0.36 mm/rev; a <sub>p</sub> =1.1	12	Nose	19	Nose	58
f=0.20 mm/rev; a <sub>p</sub> =2.0	51	Primary Flank	73	Nose	43
f=0.15 mm/rev; a <sub>p</sub> =2.7	75	Primary Flank	108	Nose	44

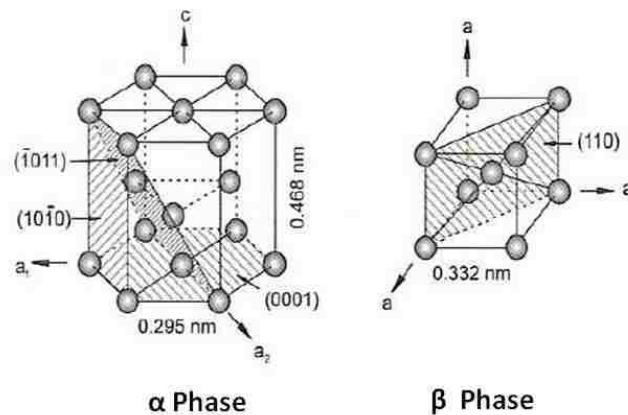
<sup>a</sup> Time in seconds until average wear reaches 300  $\mu\text{m}$ .



## FIGURES



**Figure 2.1** Phase diagram of titanium showing different types of titanium alloys based on the alloying elements [13].



**Figure 2.2** Hexagonal close packed structure and body centered cubic structure of  $\alpha$  and  $\beta$  phase respectively [13].

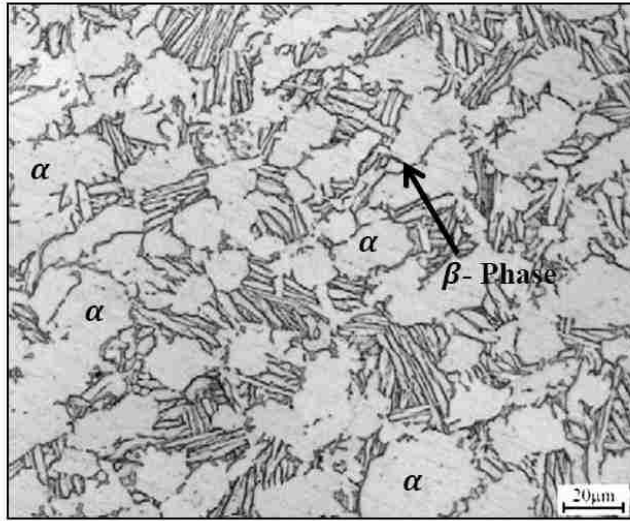


Figure 2.3 Optical image of Ti-6Al-4V [98].

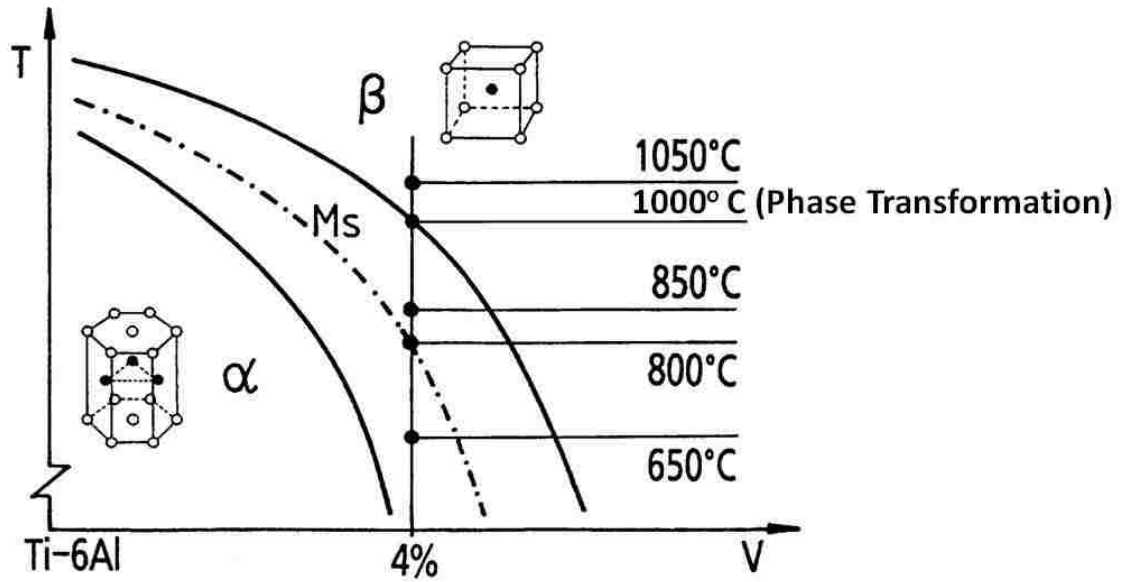
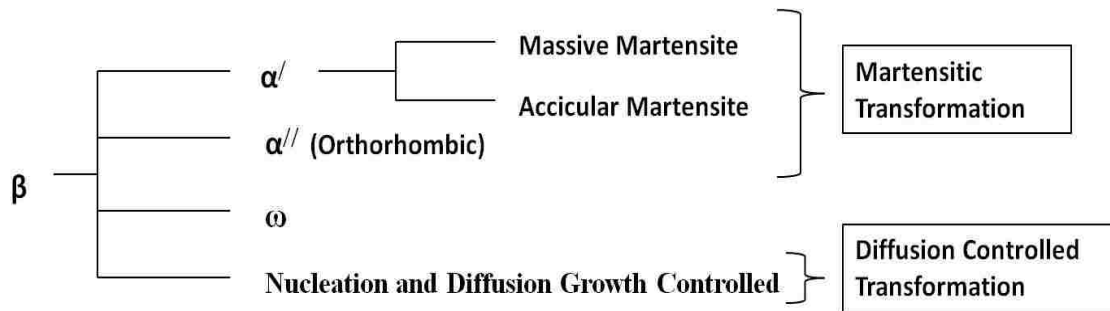
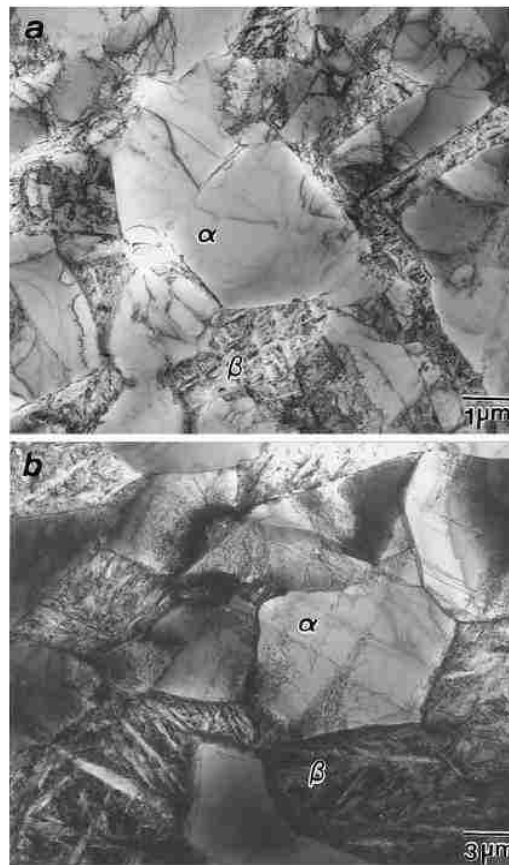


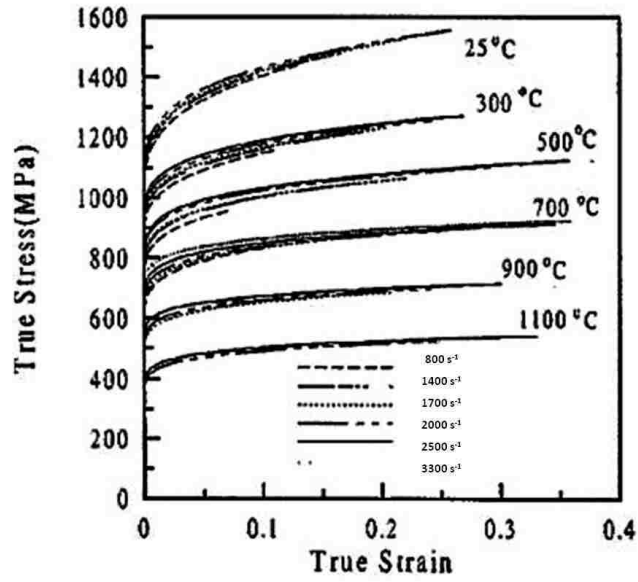
Figure 2.4 Phase diagram of Ti-6Al-4V [99].



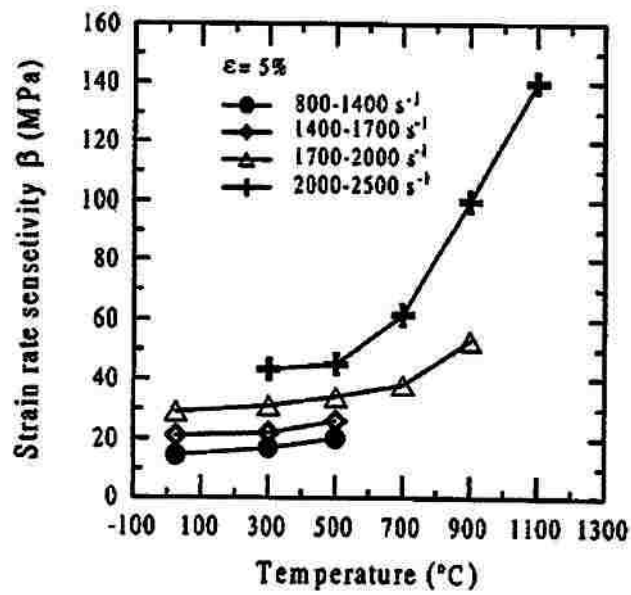
**Figure 2.5** Different types of phase transformations in Ti-6Al-4V where  $\omega$  phase requires very high rate of cooling, diffusion controlled process requires very slow cooling and martensitic transformation process requires intermediate rate of cooling and all these are dependent on the % of solute content as well.



**Figure 2.6** TEM bright-field images of: (a) fine (3  $\mu\text{m}$ ); and (b) coarse (11 $\mu\text{m}$ ) grained Ti-6Al-4V deformed at 600°C with a strain rate of  $10^{-3}\text{s}^{-1}$  ( $\epsilon=0.3$ ) [18].



**Figure 2.7** Typical true stress-strain curves of Ti-6Al-4V alloys deformed at different strain rates and temperatures [19].



**Figure 2.8** At a true strain of 0.05 variations of strain rate sensitivity as a function of temperature for deformation under different strain rate range [19].

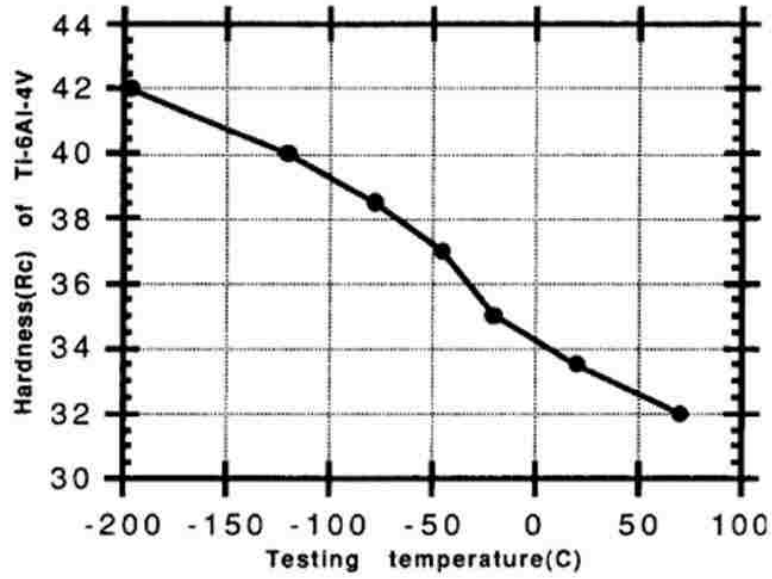


Figure 2.9 Hardness of annealed Ti-6Al-4V at various temperatures [9].

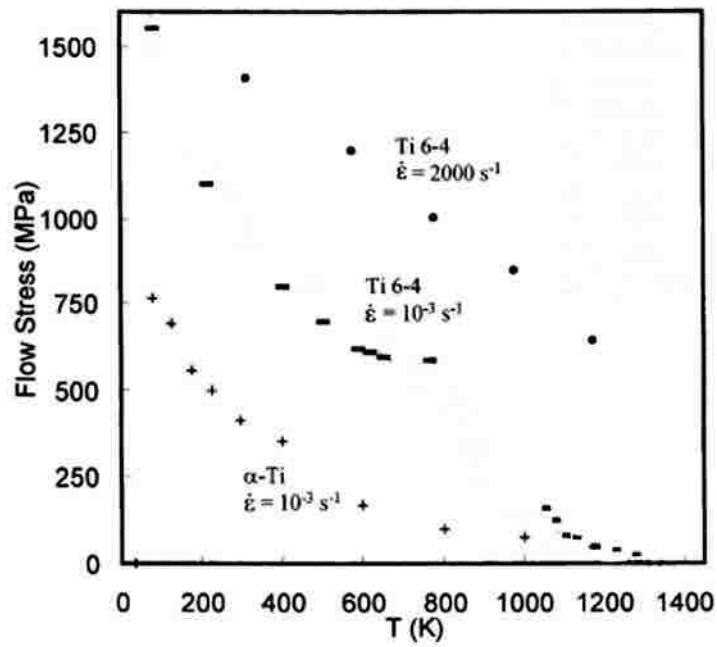
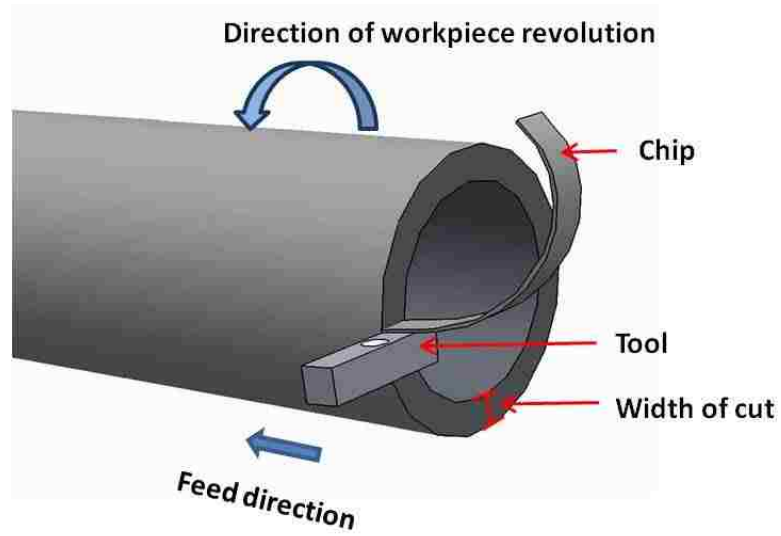
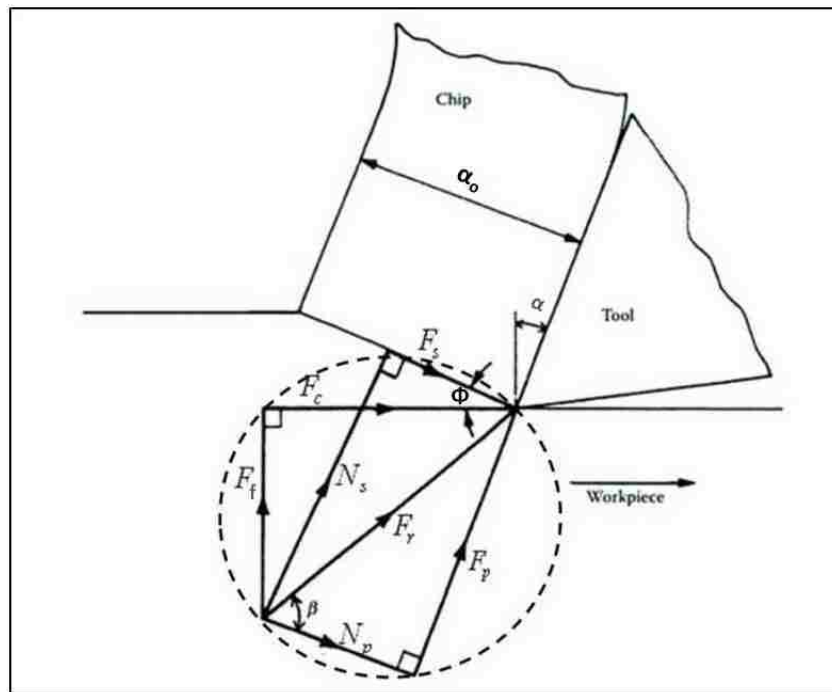


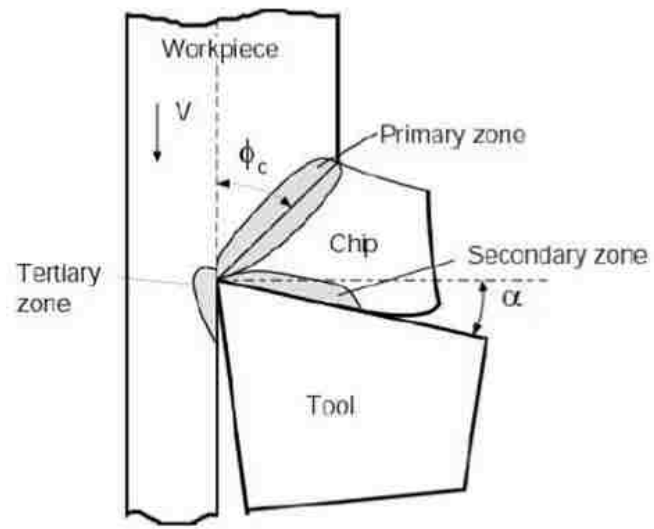
Figure 2.10 Temperature dependence of the yield stress of Ti-6Al-4V at low [100] and high [19] strain rates compared to  $\alpha$ -Ti [101]. At strain rate of  $10^{-3} \text{ s}^{-1}$  and at a temperature of 0K, the flow stress of Ti-6Al-4V is 1600MPa which reaches a plateau of 600MPa at around 600K. At higher strain rate there is no such plateau.



**Figure 2.11** Schematic diagram of orthogonal cutting.



**Figure 2.12** Force diagram for orthogonal cutting where  $F_c$  is cutting force,  $F_f$  is feed force,  $F_s$  is the shear force on the shear plane,  $N_s$  is the normal force on the shear plane,  $F_p$  is shear force on rake face and  $N_p$  is the normal force on the rake face [10].



**Figure 2.13** Deformation zones produced during orthogonal cutting [102].



(a) Continuous Chips

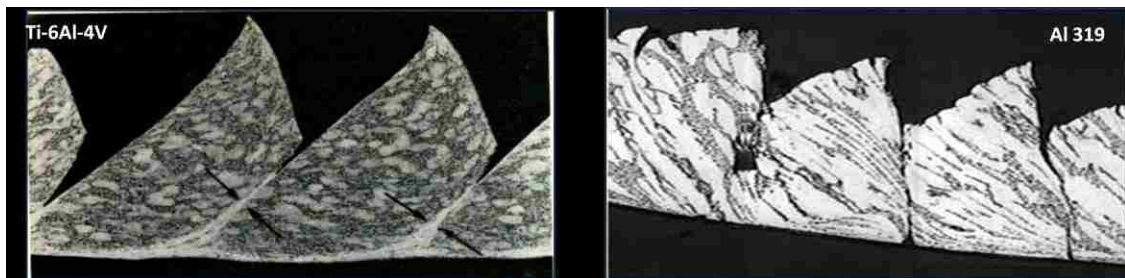
(b) Cyclic Chips

**Figure 2.14** Two main types of chips formed both for Ti 140A at different cutting conditions (a) Continuous chips of Ti 140 A, Cutting speed = 30.5m/min, Feed = 0.13mm/rev, (b) Cyclic chips of Ti 140 A, Cutting speed = 45.7m/min, Feed = 0.26mm/rev [7].



(a) Wavy Chips

(b) Segmental Chips

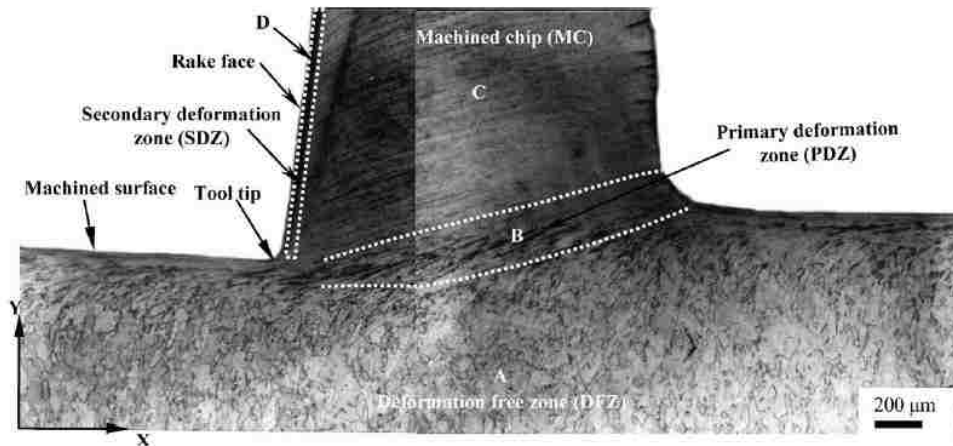


(a) Catastrophic Shear or Serrated Chips

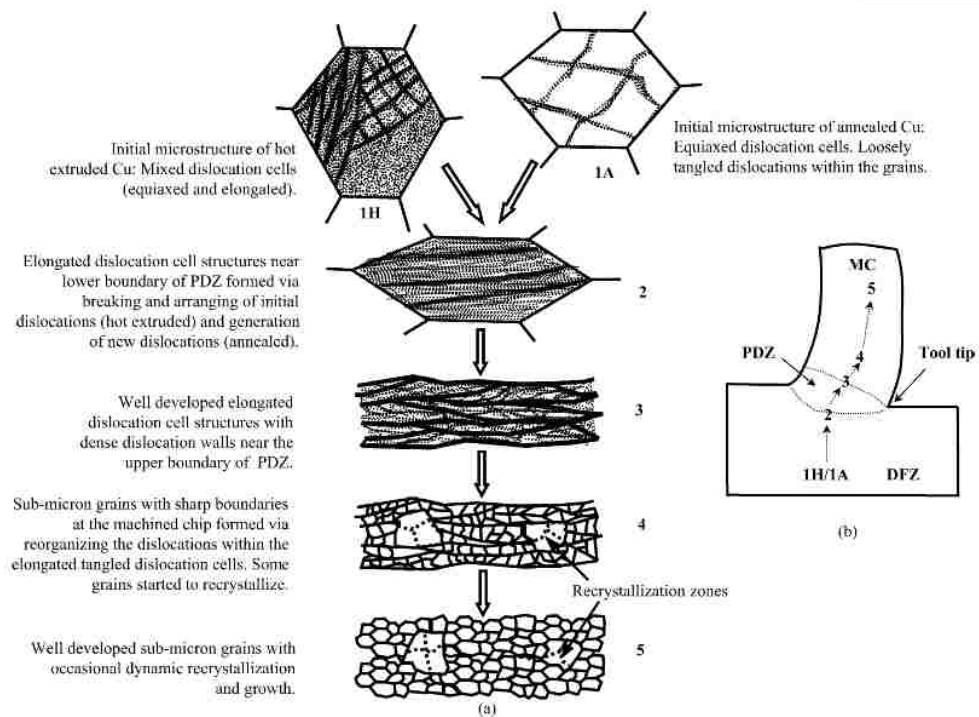
(b) Discontinuous Chips

**Figure 2.15** Different types of cyclic chips (a) Wavy chips [27] (b) Segmental chips [27] (c) Catastrophic shear or serrated chips [27] (d) Discontinuous chips [103].

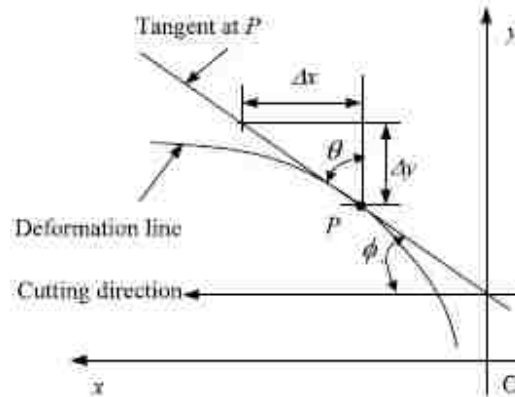
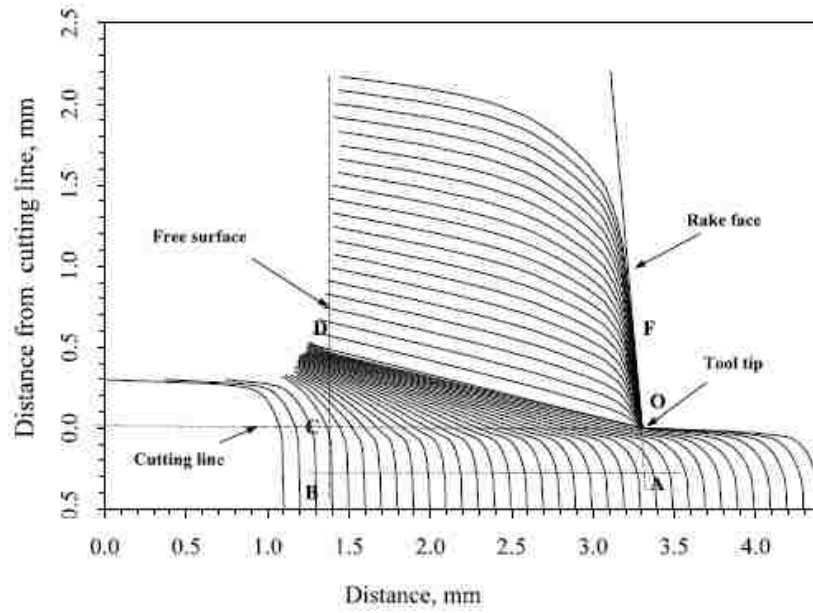




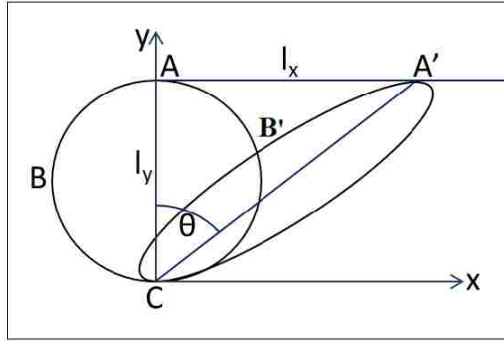
**Figure 2.16** Cross-sectional optical micrograph of the material (hot extruded Cu) ahead of the tool tip formed during orthogonal cutting [31].



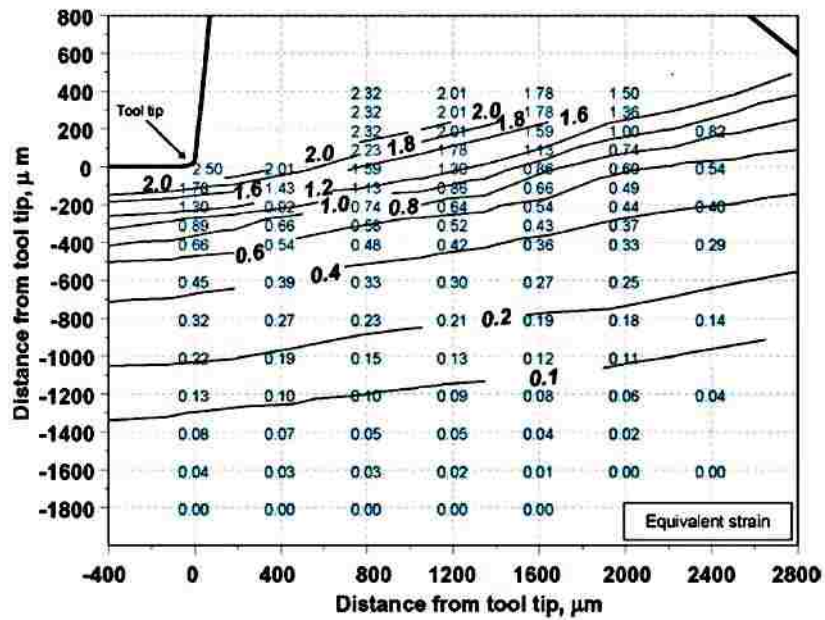
**Figure 2.17** (a) Schematic illustration of microstructural evolution and grain refinement induced by plastic deformation ahead of the tool tip and (b) the sequence of grain refinement events shown on the cross-section of the sample [31].



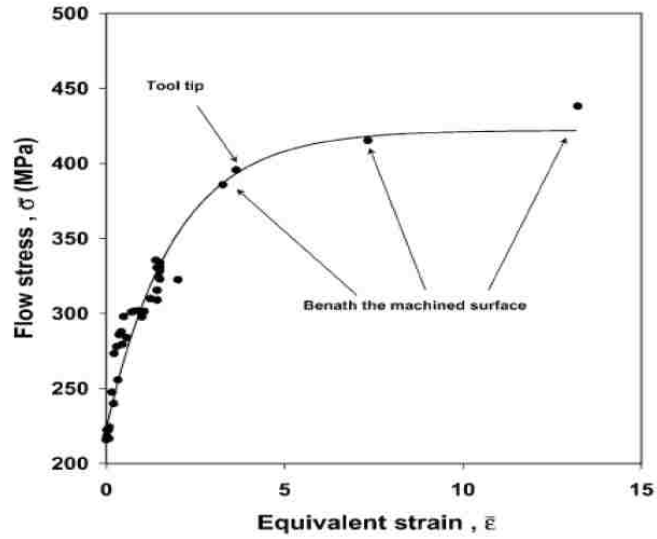
**Figure 2.18** (a) A computer generated image of the cross-section of the machined work piece with the chip still attached. The image was obtained by determining the location of each point on the deformation lines and these were plotted to actual scale shown on the diagram, (b) Schematic diagram showing the measurement of shear angles from the slopes of the deformation lines [30].



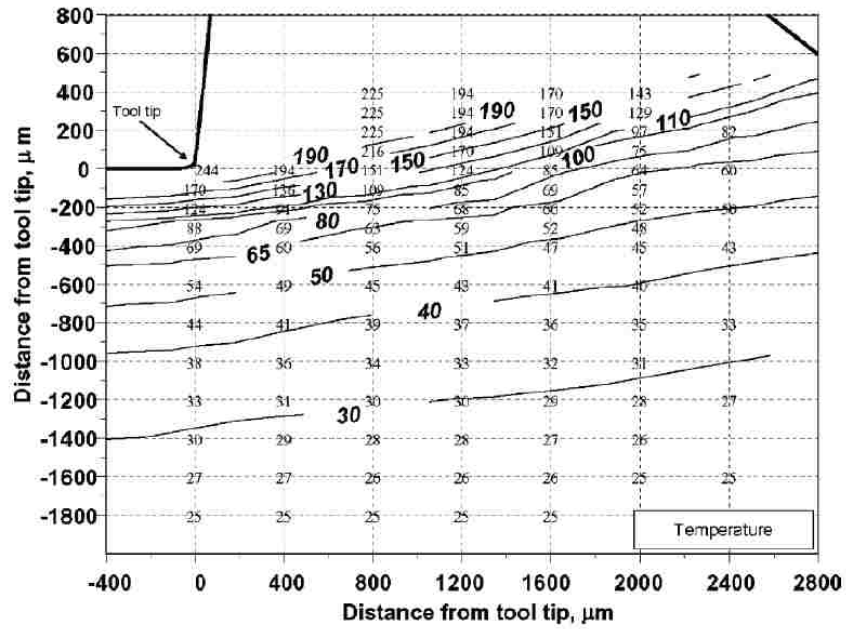
**Figure 2.19** Model for true shearing of a sphere[34]. Ideal spherical crystal ABC turns into A'B'C after shearing.  $l_x$  and  $l_y$  are the distances at the X and Y directions respectively and  $\theta$  is the deformation angle.



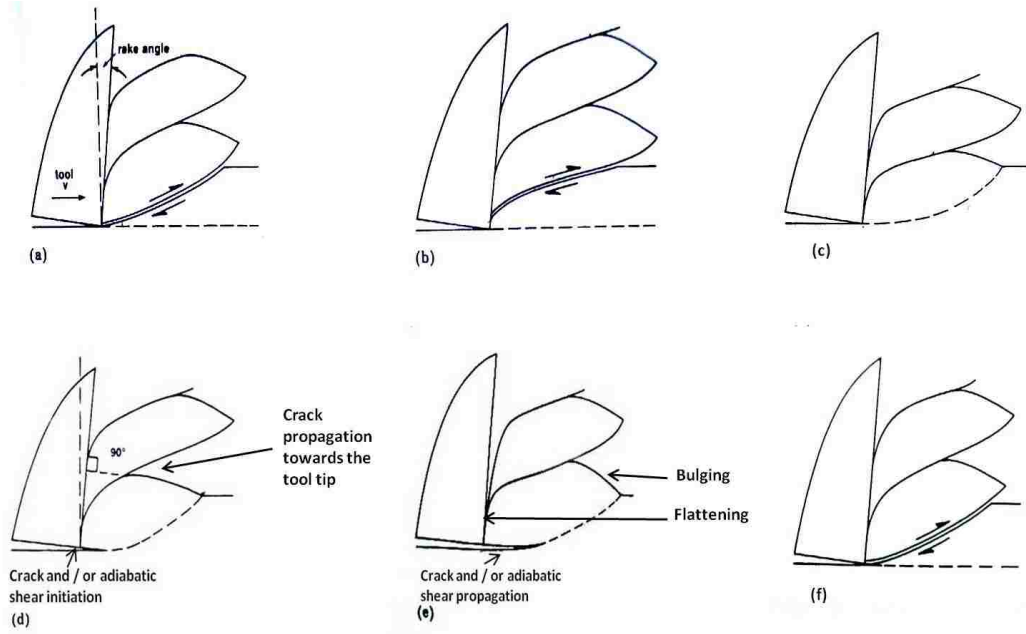
**Figure 2.20** Strain distribution diagram showing the values of equivalent shear strains,  $\bar{\epsilon}$ , in the material (Al 1100) ahead of the tool tip. Equivalent strains were estimated from the local shear angle values,  $\Phi$  using Eq. (2.13). The iso-strain contours are also shown [32].



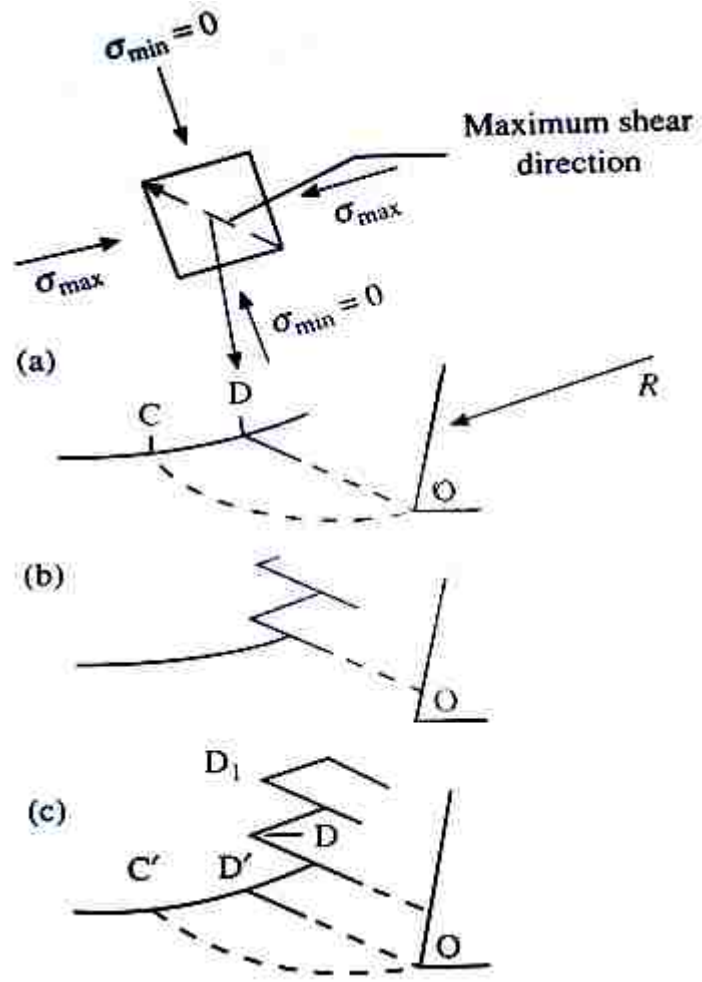
**Figure 2.21** The cumulative stress-strain curve of commercial purity copper subjected to orthogonal cutting [33].



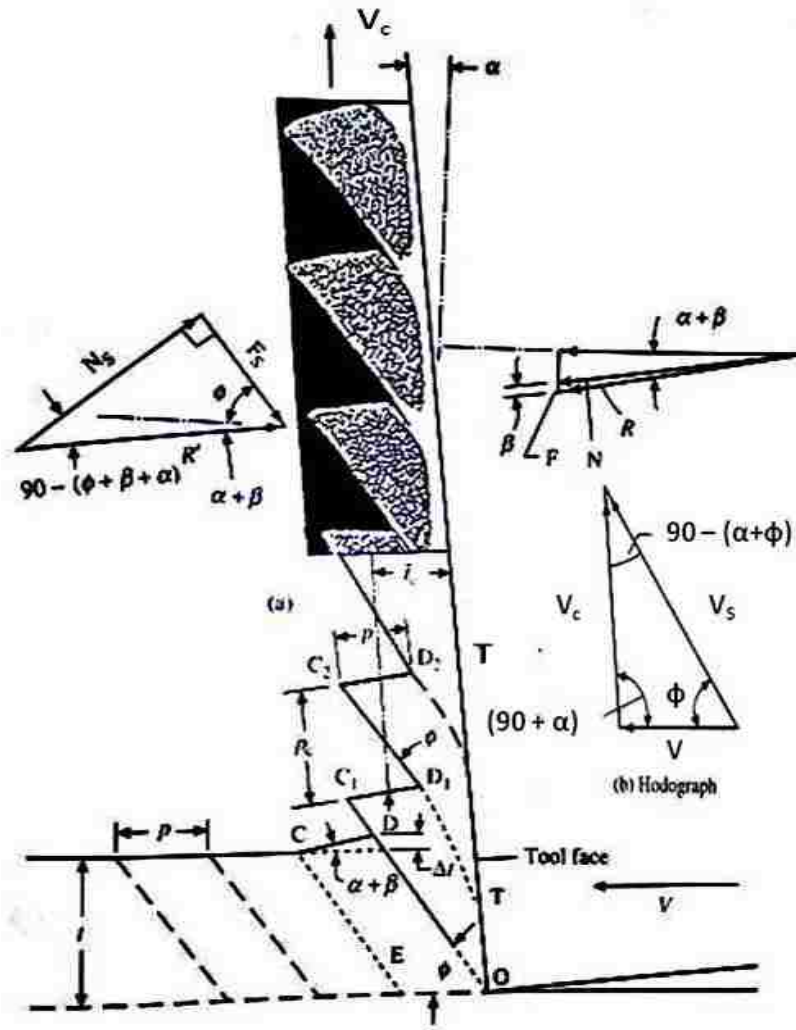
**Figure 2.22** Temperature distribution of the material ahead of the tool tip due to plastic deformation in 1100 Aluminum [32].



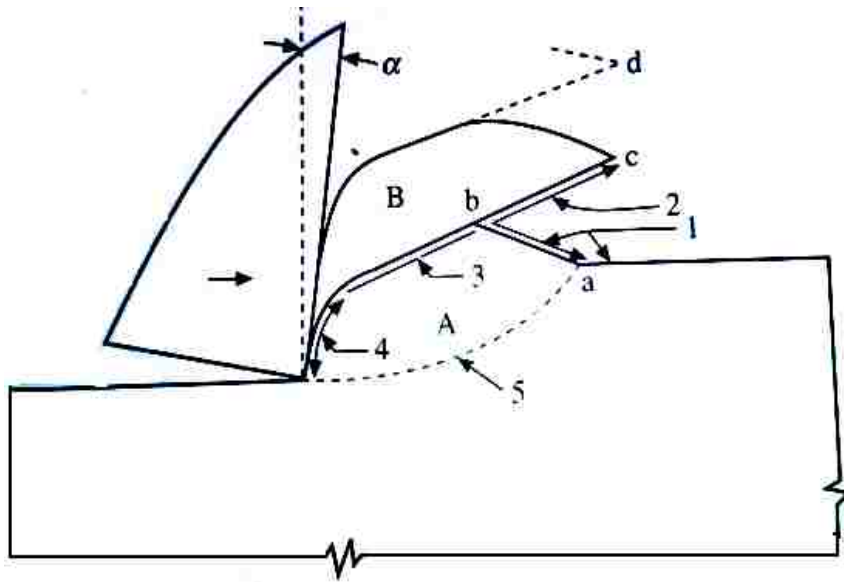
**Figure 2.23** Schematic diagram of a sequence of events, showing various stages involved in chip formation during machining titanium alloys [6].



**Figure 2.24** Mechanism of saw tooth chip formation by periodic crack formation process[54].

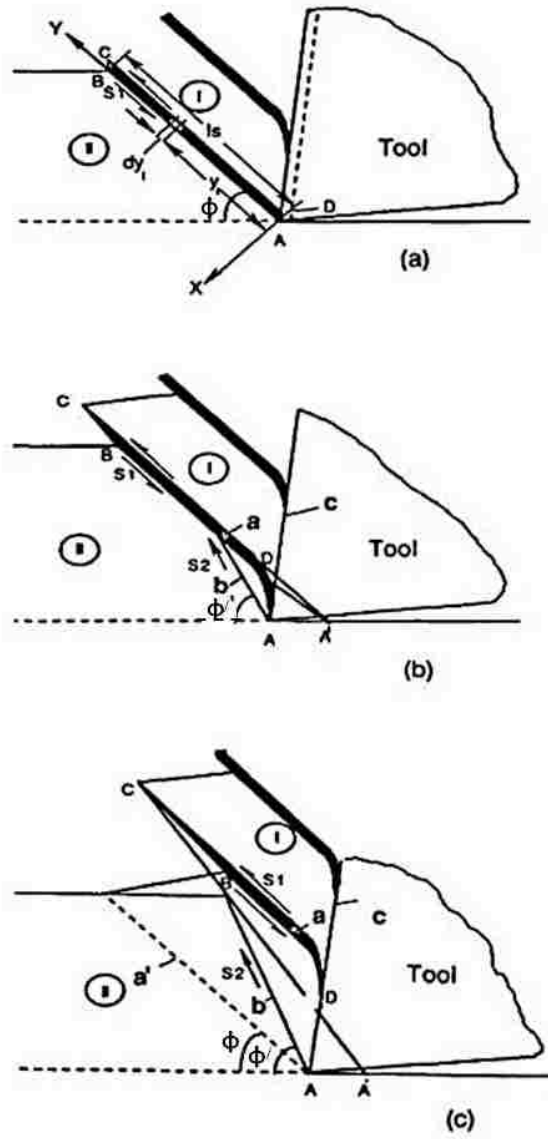


**Figure 2.25** (a) Free body diagram of chip, (b) Hodograph for gross cracked region of chip only [7].

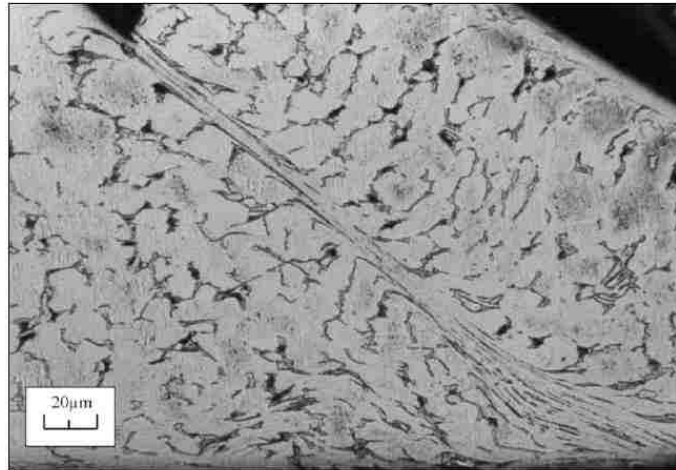


**Figure 2.26** Model used to explain adiabatic shear theory of saw tooth chip formation where A is the segment that is going to be formed and B is a well developed segment. 1 and 2 are two fractured surfaces and 3 shows contact area between A and B. 4 and 5 represent flattening and the path of strain localization respectively [62].

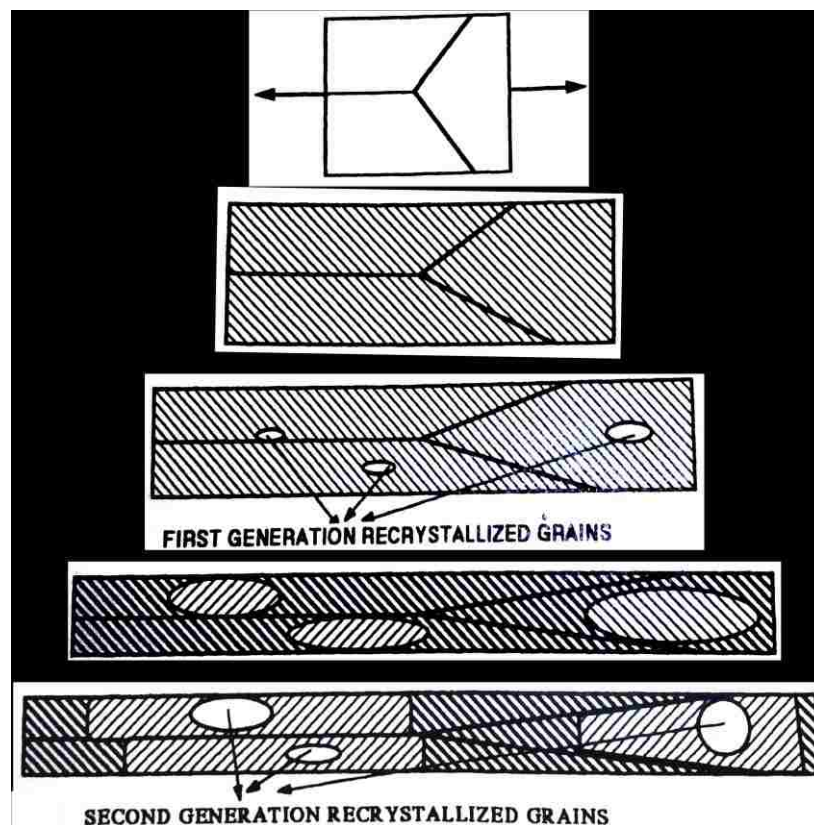




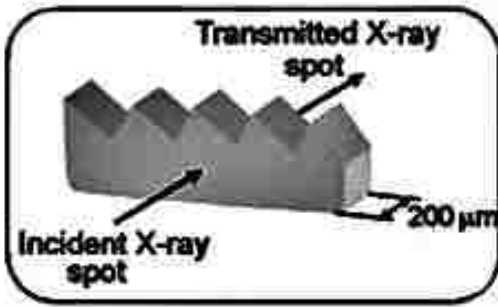
**Figure 2.27** Model for thermal analysis based on adiabatic shear theory where in (a) the strain localization path is initially straight, (b) shear force,  $S_2$  makes the path curve and (c) shear force,  $S_2$  acts on the material not along the strain localized region [63].



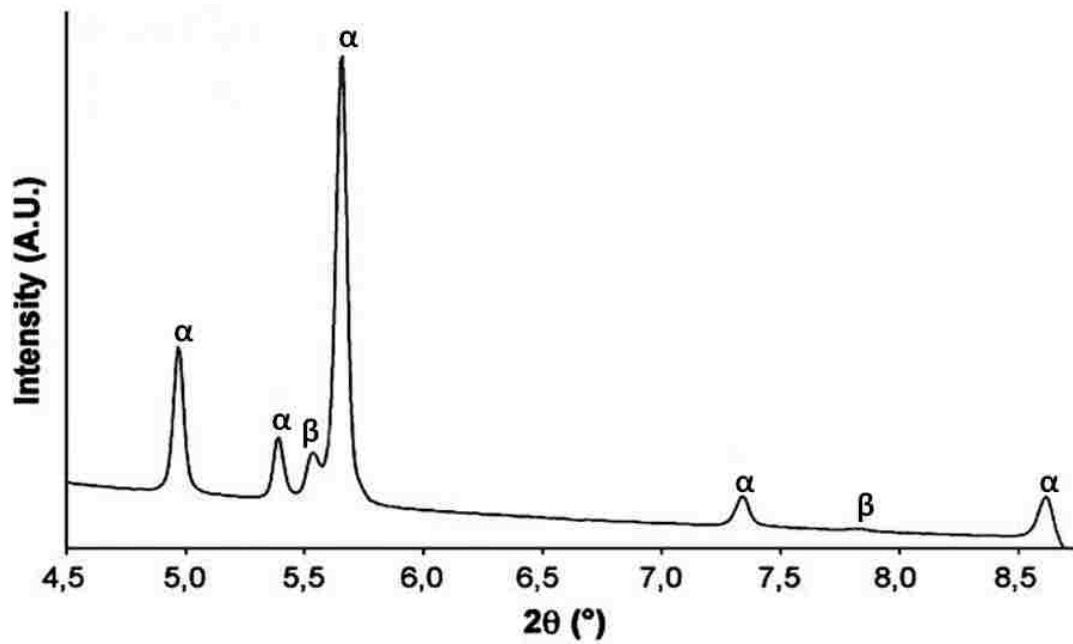
**Figure 2.28** Adiabatic transformed shear band in a chip of titanium alloy Ti-6Al-4V, obtained by orthogonal cutting at the velocity 13 m/s[87].



**Figure 2.29** Schematic illustration showing sequence of deformation-recrystallization steps in dynamic deformation [69].

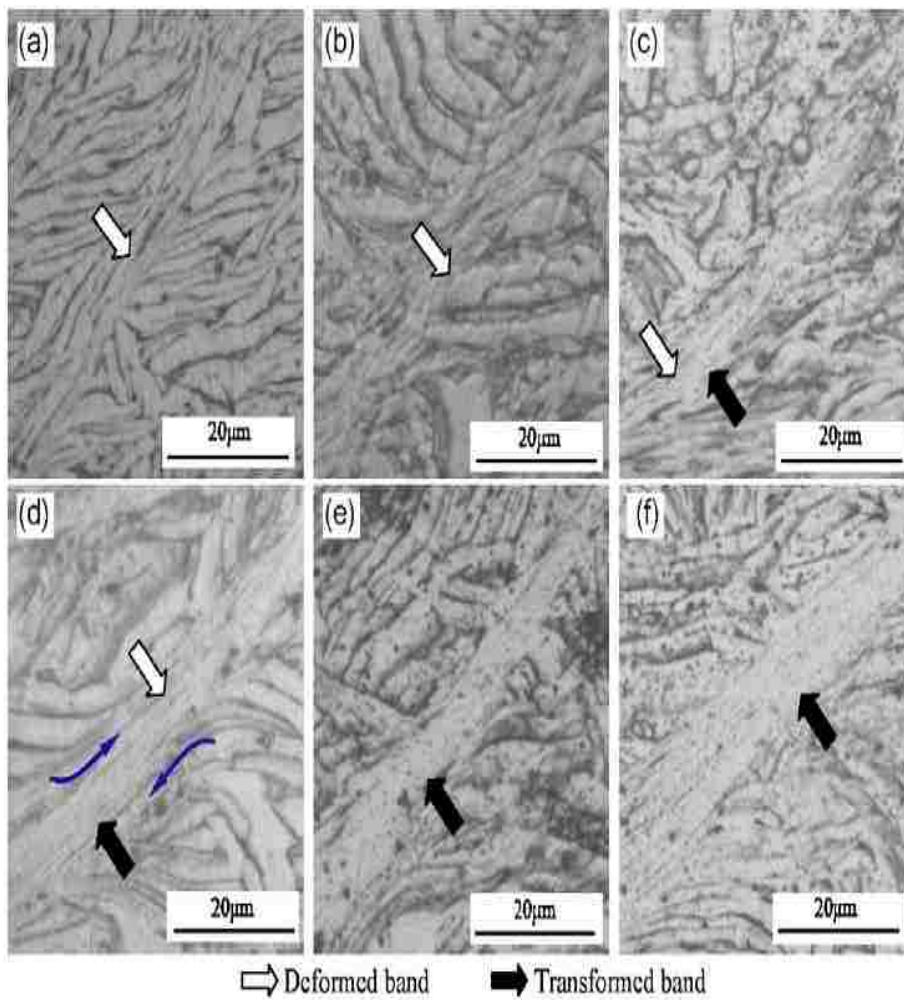


(a)

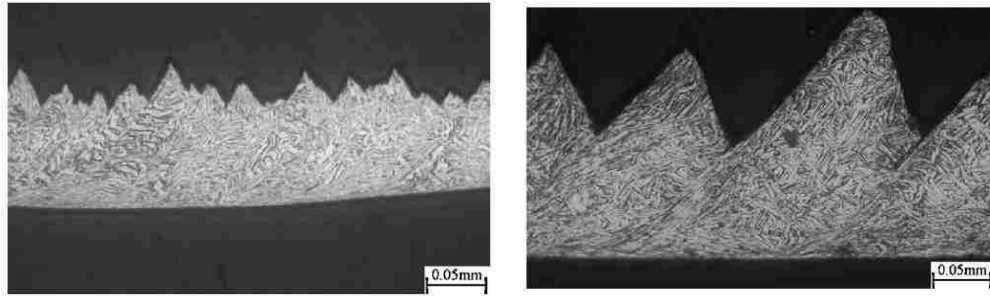


(b)

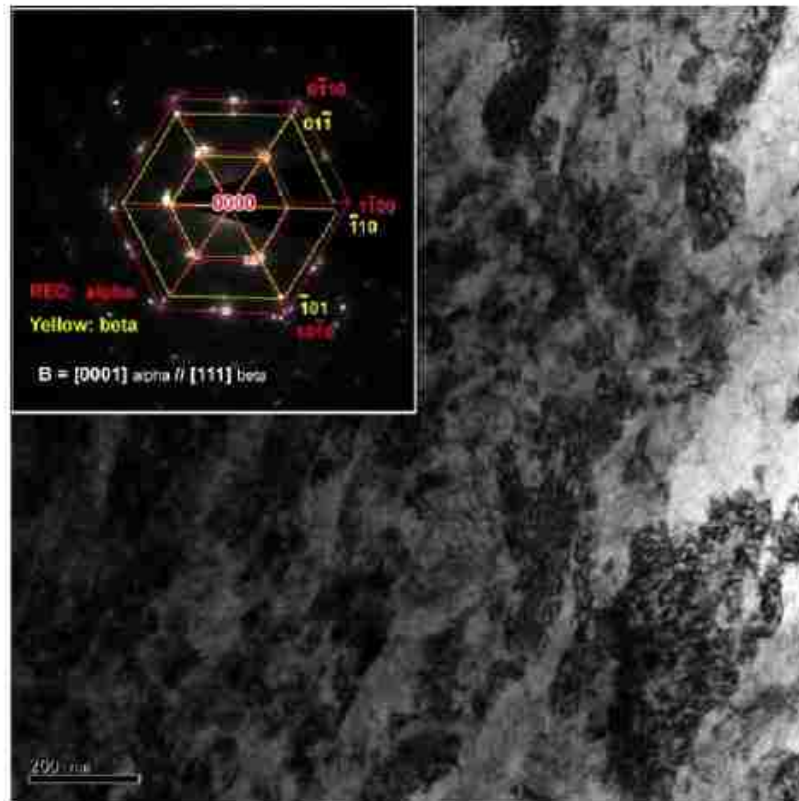
**Figure 2.30** (a) A Very thin transparent section was taken from the chip produced during machining of Ti-6Al-4V alloy at a cutting speed of 10m/s and (b) XRD analyses on the transparent section showed no phase transformation [60].



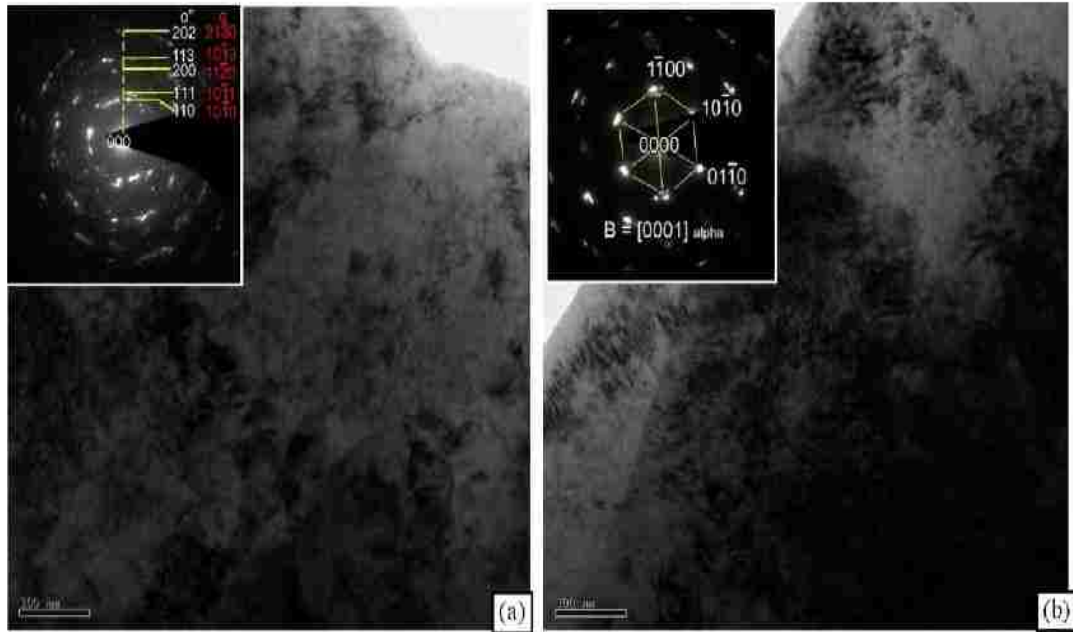
**Figure 2.31** Saw tooth chip formation in Ti-6Al-4V at a constant feed rate of 0.21 mm/rev at different cutting speed (a) 30.2 m/min, (b) 59.6 m/min, (c) 81.4 m/min, (d) 126.6 m/min, (e) 178.4 m/min and (f) 281.3 m/min [74].



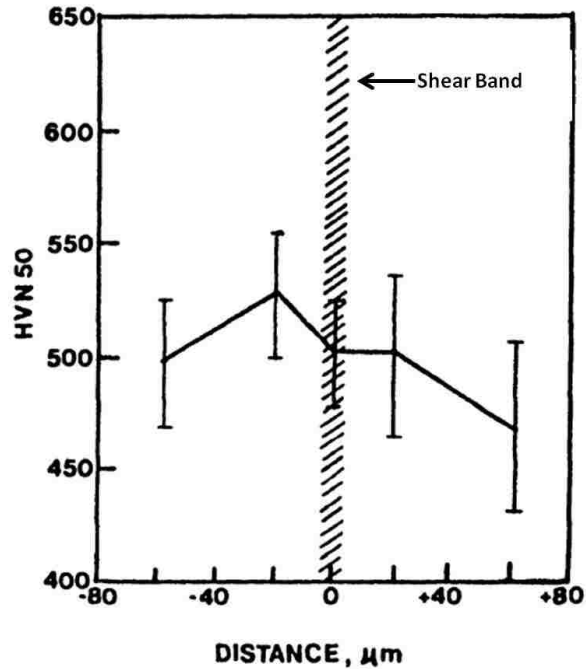
**Figure 2.32** At a constant feed rate of 0.21 mm/rev (a) Incipient separation of segments at a cutting speed of 30.2 m/min and (b) Complete separation of segments at a cutting speed of 59.6 m/min [74].



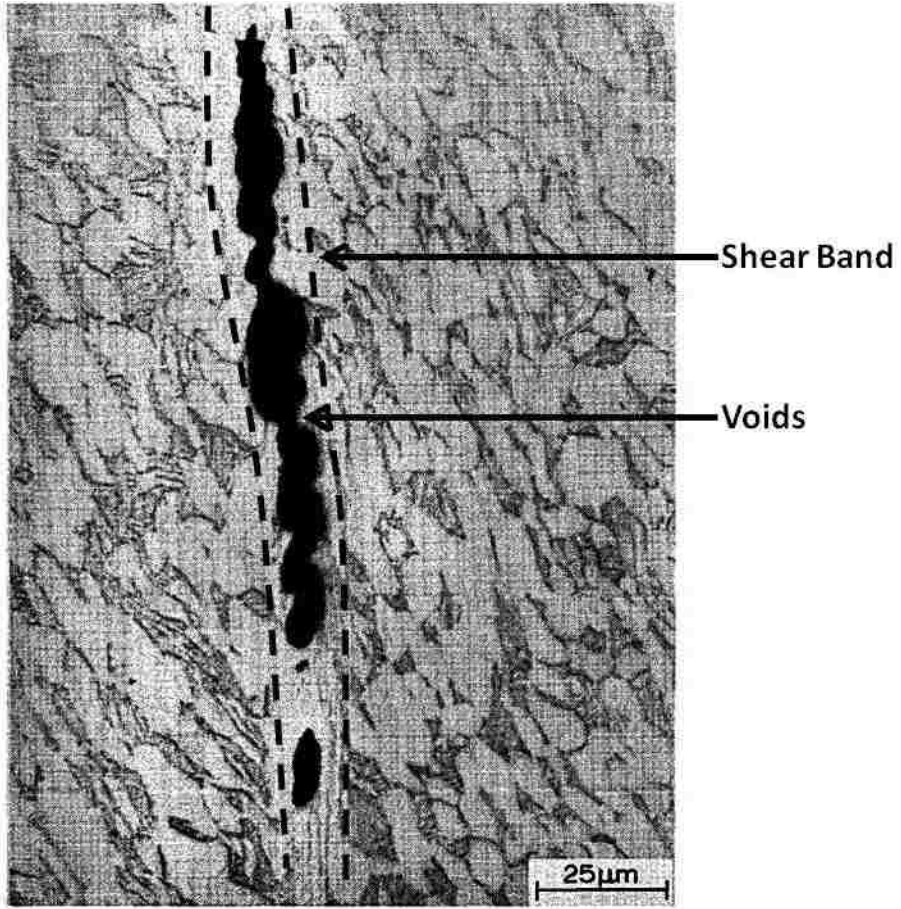
**Figure 2.33** TEM image of adiabatic shear band at a cutting speed of 59.6 m/min and feed rate 0.21mm/rev (Diffraction pattern was taken down  $[111]\beta$  and  $[0001]\alpha$ ) [74].



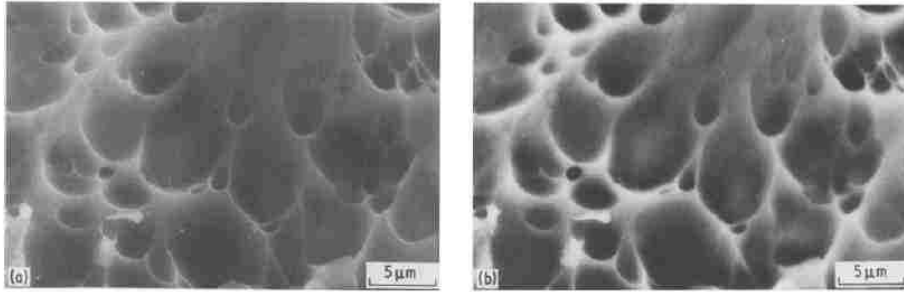
**Figure 2.34** TEM image of adiabatic shear band at cutting speed 126.6 m/min and feed rate 0.21mm/rev where (a) center of adiabatic shear band and (b) transitional region between matrix and center (Diffraction pattern was taken down  $[0001]_{\alpha}$ ) [74].



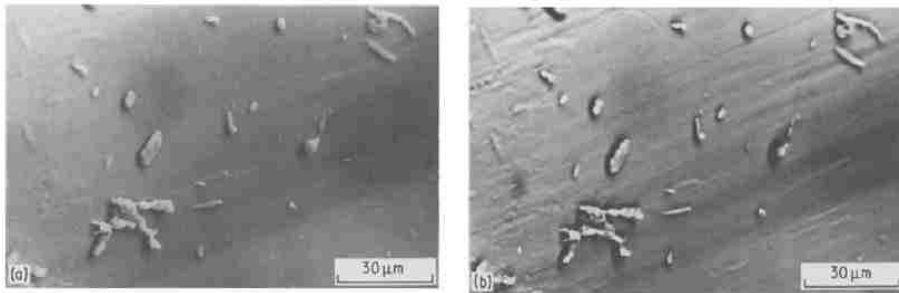
**Figure 2.35** Microhardness at different position including shear band of Ti-6Al-4V alloy [76].



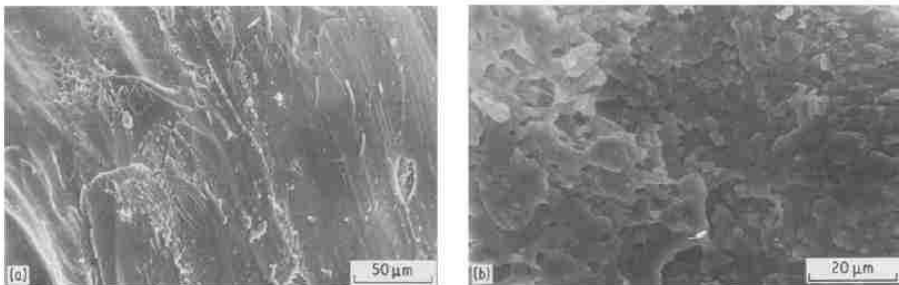
**Figure 2.36** Voids within well developed shear zone of Ti-6Al-4V alloy [78].



**Figure 2.37** Dimple shear band fracture surface (a) Secondary image (b) Backscattered image [79].

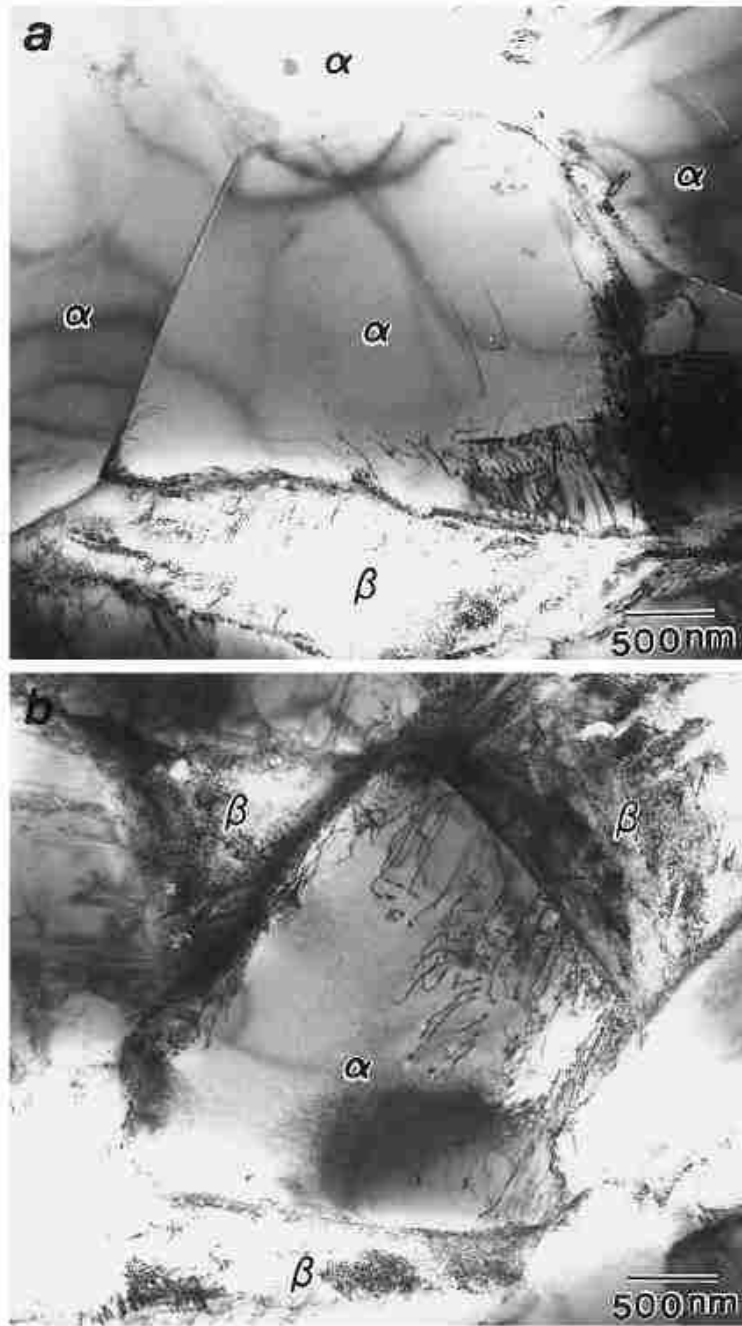


**Figure 2.38** Relatively smooth shear band fracture surface (a) Secondary image (b) Backscattered image [79].

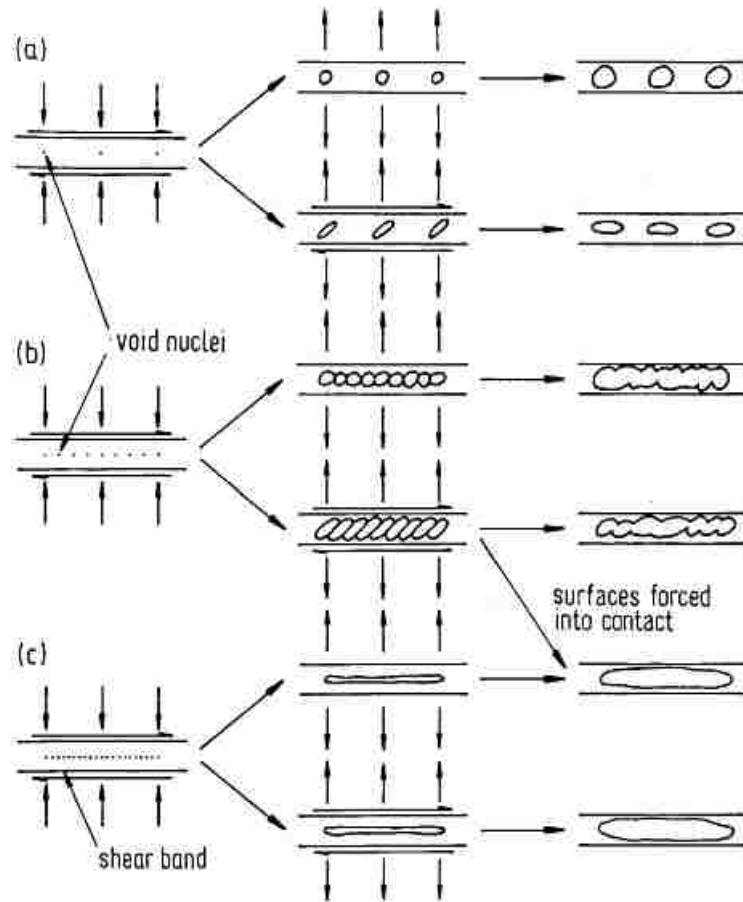


**Figure 2.39** Secondary image of shear band fracture surfaces partially covered with (a) Globular aggregate (b) Individual globules [79].





**Figure 2.40** Transmission electron micrographs of superplastically deformed specimens (3  $\mu\text{m}$ ) at 900°C: (a) an  $\alpha$  surrounded by  $\alpha$ ; and (b) an  $\alpha$  surrounded by  $\beta$  [18].



**Figure 2.41** Schematic illustration of evolution of void and fracture-surface morphologies in adiabatic shear bands; sequence a,b,c corresponds to increasing density of void nucleation sites[78].

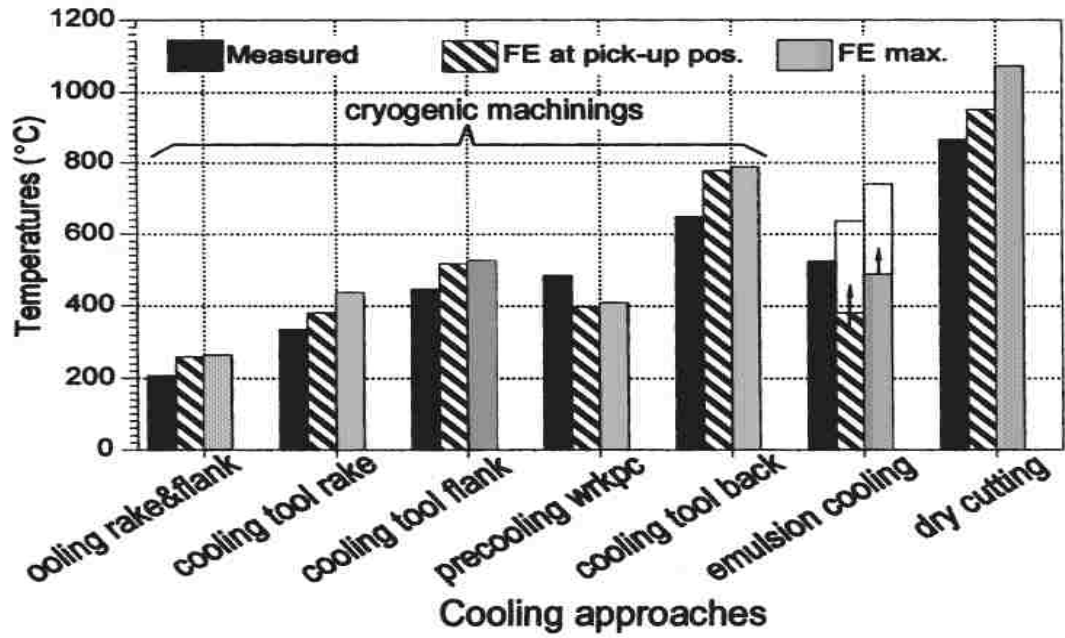
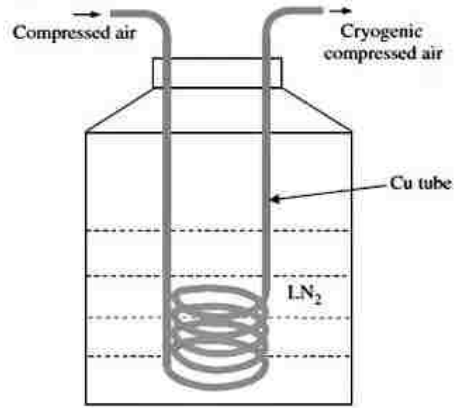
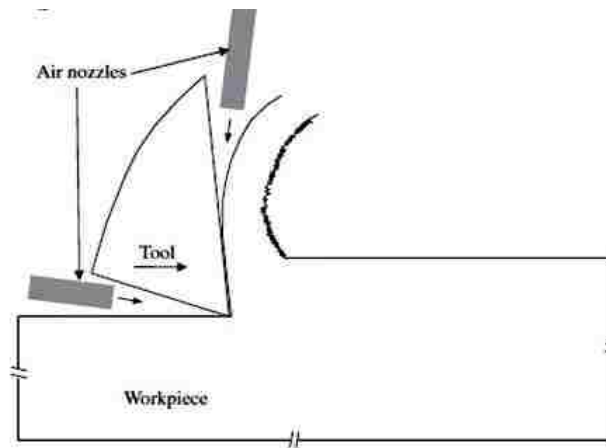


Figure 2.42 Measured and predicted tool temperature in different machining techniques [83].



(a)

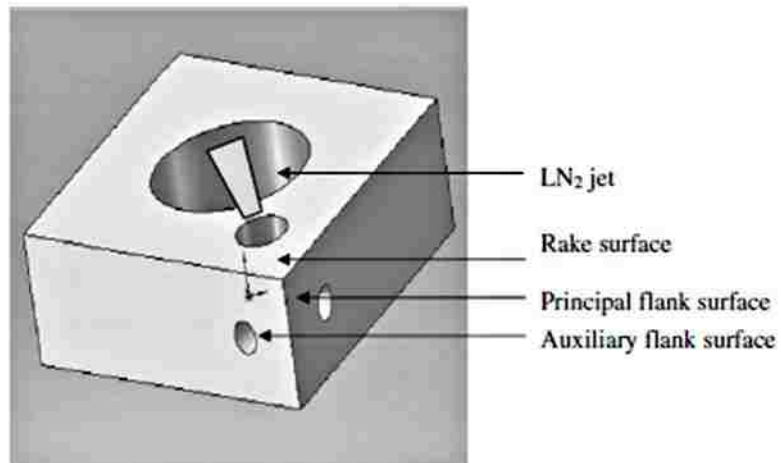


(b)

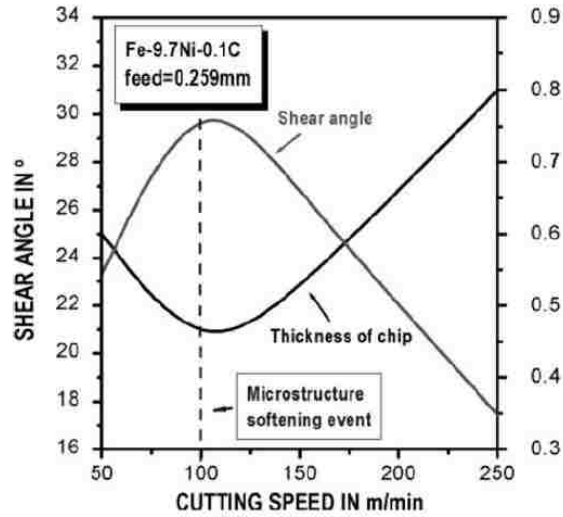
**Figure 2.43** Schematic illustration of (a) generation and (b) delivery of cryogenic compressed air to the cutting edge [84].



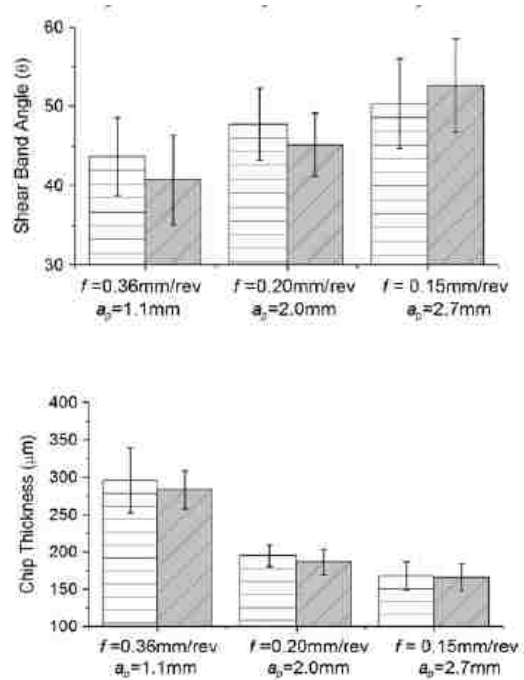
**Figure 2.44** Photograph of liquid nitrogen coolant delivery system showing modified tool holder nozzle for rake face cooling with an additional flank face cooling nozzle [85].



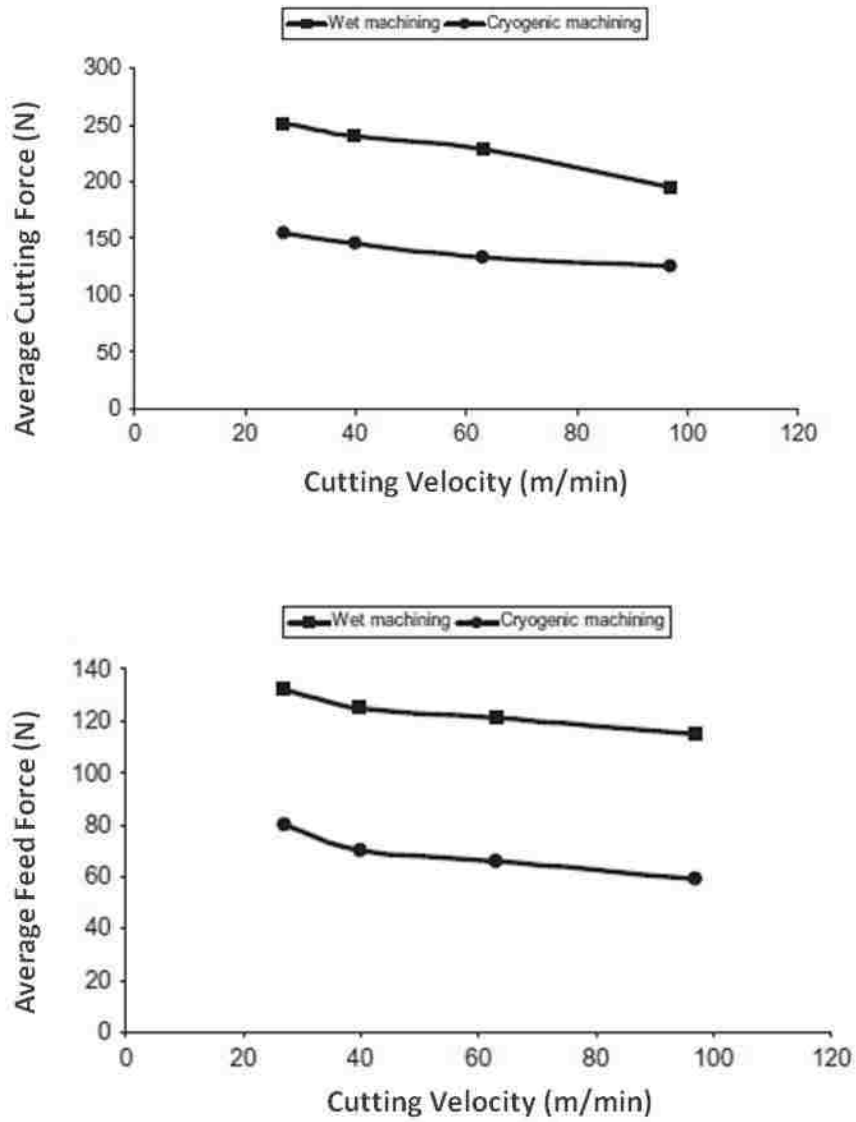
**Figure 2.45** Schematic representation of modified tool for cryogenic coolant delivery on rake and flank surfaces [86].



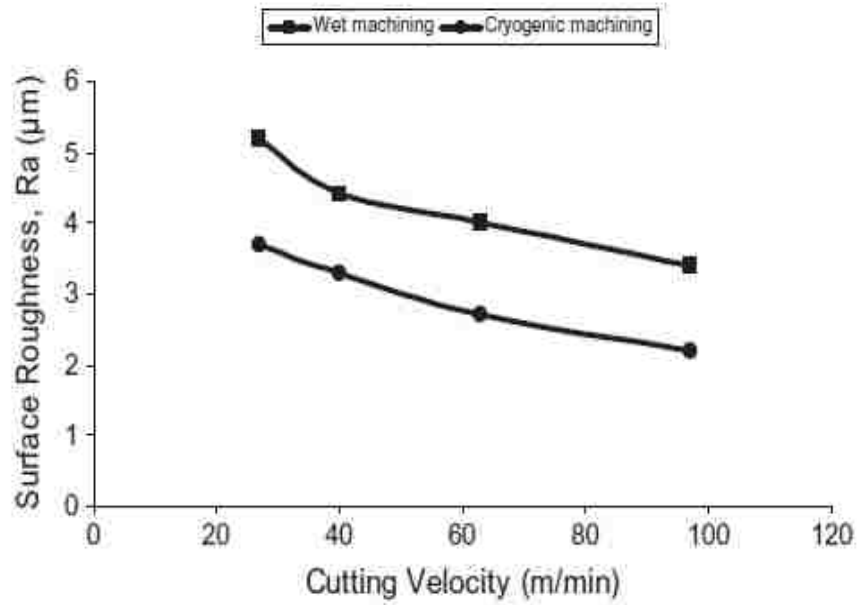
**Figure 2.46** The variation of measured thickness of flow chip and the calculated shear angle with cutting speed obtained in cutting hardened Fe-9.7%Ni-0.1%C alloy where serrated chips formed at a constant feed of 0.259 mm and a positive rake angle of  $\pm 5^\circ$  [88].



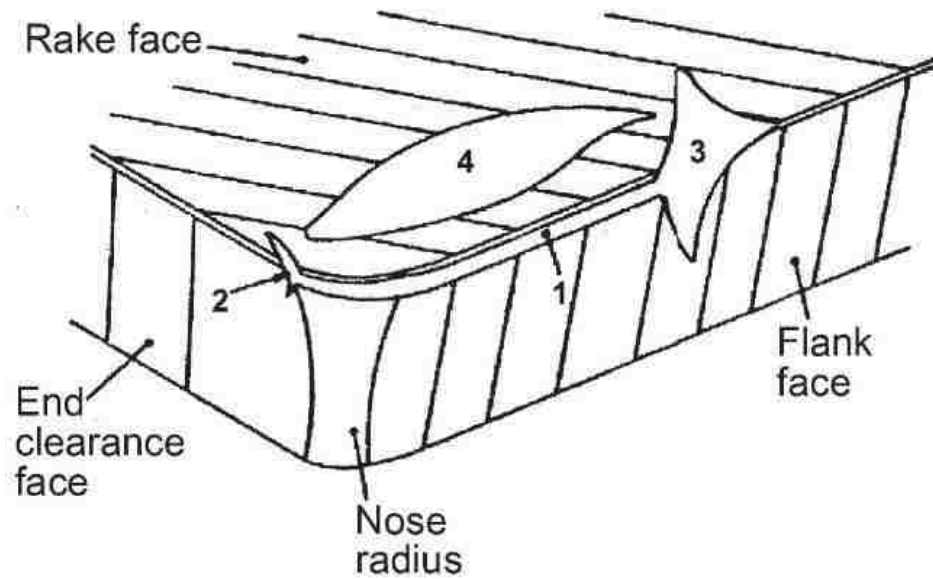
**Figure 2.47** Measurement of shear band angle and chip thickness in dry and cryogenic condition at different feed rates [85].



**Figure 2.48** Comparison of cutting and feed forces in wet and cryogenic machining [86].



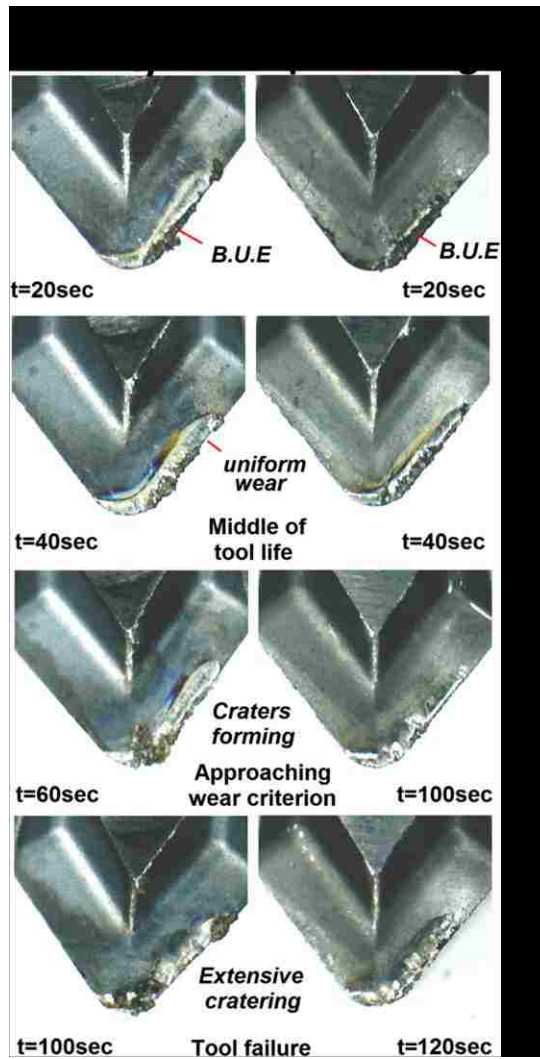
**Figure 2.49** Variation of surface roughness with cutting velocity in wet (using emulsion of cutting fluid) and cryogenic machining [86].



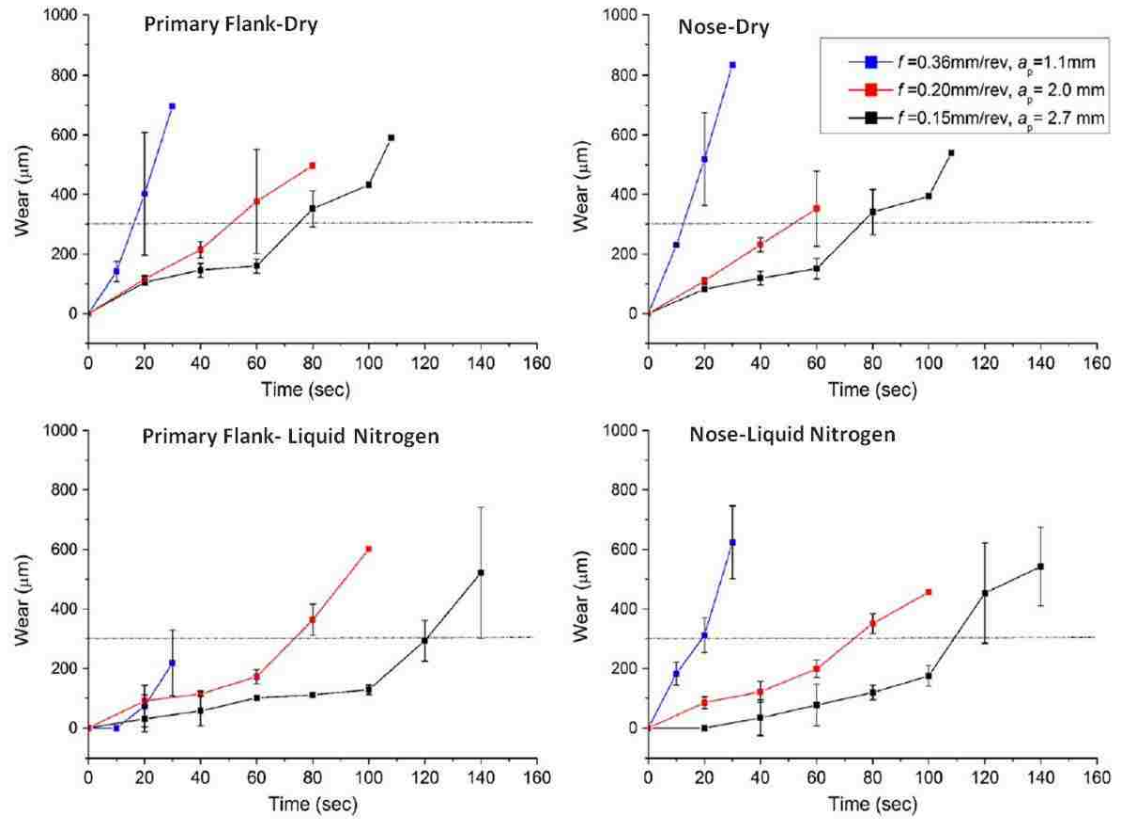
1 - Flank wear 2 - Nose wear 3 - Notch wear 4 - Crater wear

**Figure 2.50** Different types of tool wear [104].





**Figure 2.51** Rake wear during dry and cryogenic condition (cooling of tool flank face). Cutting speed-125m/min, Feed-0.15 mm/rev and width of cut-2.7mm [85].



**Figure 2.52** Average wear of the primary flank and nose during dry cutting and using cryogenic coolant [85].

## CHAPTER 3

### EXPERIMENTAL PROCEDURE

To observe the mechanisms of chip formation during machining process, an in-situ set-up was developed. Machining tests were performed at different feed rates at ambient and cryogenic conditions. Samples were examined by optical microscopes and SEM to understand the effect of the machining condition. Details of design of the set-ups used in these studies along the procedure of analyses would be discussed in this section.

#### 3.1 Workpiece Geometry

Ti-6Al-4V ( $\alpha$ - $\beta$ ) alloy, obtained in the form of extruded rods of diameter 25.45mm, were subjected to orthogonal cutting in this study. Composition of this material is shown in Table 3.1. For the tests, tubular samples with a wall thickness of 3mm were machined from the extruded rods. Microhardness of the alloy was  $380\pm 10$  HV which was measured using 50gm load.

**Table 3.1** Composition of Ti-6Al-4V used in this study [105].

Element	Al	V	Fe	O	C	N	Ti
Weight %	5.5-6.76	3.5-4.5	<0.25	<0.2	<0.08	<0.05	Balance

Microstructure of alloy is shown in Figure 3.1 indicating  $\alpha$  and  $\beta$  phase. The length and width of  $\beta$  phases were found to be  $4.86\pm 2.86$   $\mu\text{m}$  and  $1.03\pm 0.46$   $\mu\text{m}$  respectively. The  $\beta$  phases, distributed within the  $\alpha$ , were elongated along the extruded direction.

To compare continuous and serrated chip formation mechanisms, 6061 Aluminum alloy was machined. Dimensions of the 6061 Aluminum alloy extruded rods were same as Ti-6Al-4V alloy. Composition of 6061 Aluminum alloy is shown in Table 3.2.

**Table 3.1** Composition of 6061 Aluminum alloy [106].

Element	Mg	Si	Cu	Zn	Cr	Fe	Al
Weight %	1	0.6	0.3	0.3	0.2	0.7	Balance

### 3.2 In-Situ Machining

Details of design along with the components used to make the in-situ set-up are described in this section. Components of in-situ set-up are 1) Lathe, 2) Microscope, 3) Microscope Stand, 4) Milling Table and 5) Tool. Along with the set-up, the procedure of performing in-situ tests is described in this section as well.

#### 3.2.1 Schematic Design of In-Situ Set-Up

The goal of the in-situ machining was to observe chip formation processes during cutting at high magnifications (200X) using a microscope. Thus a scaled down version of a lathe was used. The directions of the movement of the workpiece and the tool of the in-situ set-up are shown schematically in Figure 3.2 (a). Also as the goal was to observe the region just ahead of the tool tip to the free surface under the microscope, the set-up was made in such a way that the whole region are on the same plane which is shown in Figure 3.2(b).

### 3.2.2 Components

The parts that are used for the in-situ set-up are described below with some their features.

#### Lathe

A small Sherline lathe (4500/4530) was used as shown in Figure 3.3 (a). The lathe has a steel bed of 381mm where the distance between the centers of the head and tail stock is 203mm and a cross slide of 70mm×152mm. A powerful 90V DC motor with a speed controller gives the freedom of controlling the speed from 70 to 2800 RPM without changing the belts. Adjustable laser engraved zero handwheels, made of Aluminum allow to have zero reading at any time without moving the leadscrew that makes dialing easier.

#### Microscope

Proscope HR2 handheld digital microscope (Figure 3.3 (b)) is used for the observations of the chips. The microscope has a 8.5mm long high resolution 2Mp color sensor. Depending on the lenses magnifications can be varied from 1× to 400×. The one that is being used for this set-up is a 200× lens. This microscope allows taking videos at different frames per second (2.5 fps – 30 fps) depending on the resolution (320 × 240pixels to 1600 × 1200 pixels). In this study 30fps at 320 × 240 pixels video mode was used to obtain the highest number of frames during machining. It was made sure that the cutting speed was very low so that clear images could be generated. Higher resolution images were also taken by performing intermittent machining. Lower feed rates (0.05mm/rev) and small width of cut (0.07mm) were applied so that smooth cut can be obtained with minimum vibration. Machining parameters like cutting speed, feed

rates and width of cut are very important to cover the whole region of interest and get clear images at 200x magnifications.

### **Microscope Stand**

A Luxo18730 microscope stand was used to fasten the microscope. This microscope stand has a unique feature of fine focusing in both horizontal and vertical directions. Because of a very heavy base, it allows to have good rigidity (Figure 3.3 (c)).

### **Milling Table**

To provide a stable base the lathe was mounted on top of milling table. The milling table has a longitudinal and a cross slide hand-wheel as shown in Figure 3.3 (d). Along with the fine focusing knobs of the microscope stand, these two wheels provide the freedom of moving and focusing in all the directions.

### **Tool**

Uncoated tungsten carbide (WC-Co) parting tools were used during in-situ machining. Length of the cutting edge of the parting tool was 0.07mm. A photograph of parting tool is shown in Figure 3.3 (e).

### **3.2.3 Assembly of In-Situ Set-Up**

An aluminum base was made for the milling table and the milling table was fixed on this base using screws. The lathe machine was clamped on top of the milling table with four t-nut screws. This whole assembly was then clamped on a bench top using seal clamps. The microscope was placed into the focus mount and fastened with a screw. The whole assembly is shown in Figure 3.4.

### **3.2.4 Procedure of In-Situ Machining**

The workpiece was placed in the 3 jaw chuck (Figure 3.3 (a)). After that the region of interest was focused under microscope to obtain clear images. As mentioned in Section 3.2.2, the cutting speed needed to be very low for good quality images. For this reason the chuck was rotated very slowly by hand. Also the cross slide hand wheel (Figure 3.3 (a)) was controlled manually to have the whole region of interest in focus.

### **3.3 High Speed Machining**

High speed machining was performed in a lathe at a high cutting speed, feed rates and width of cut. Details of the high speed machining setup are discussed below.

#### **3.3.1 Lathe for Orthogonal Cutting**

A Harrison M300 lathe (Figure 3.5) was used for high speed machining. This machine is a reliable center lathe which is very compact and simple to operate. The lathe is powered by a fan cooled 2.2 kw (3 HP) 3 phase, 1500 rpm motor with a foot operated and very powerful spindle-brake with electrical disengagement for interrupted cutting. The spindle speed can be chosen from 12 different speeds varied from 40 to 2500 rpm and the feed rates can be changed between 0.03mm and 1 mm per revolution.

#### **3.3.2 Machining Parameters**

In this study dry and cryogenic high speed machining tests were performed at a constant cutting speed of 540 rpm (43.2m/min) and at different feed rates ranging from very low to a very high values (0.1, 0.2, 0.25, 0.3 and 0.4 mm/rev). The width of cut was 3mm and it

was same for all the tests. Tests at each condition were performed twice. A constant rake angle of  $0^{\circ}$  and clearance angle of  $7^{\circ}$  was maintained for all tests.

### **3.3.3 Tool**

Uncoated tungsten carbide cutting (WC-Co) tools were used in the tests as shown in Figure 3.6. The length of long diagonal of the tool was 29.5mm. The tool had a hole of diameter 4.5mm in the middle that was used to fasten it in the tool holder. The length of the cutting edge was 15.6 mm.

### **3.4 Differences between the In-Situ and High Speed Set-Ups**

The differences between the in-situ and high speed machining tests are shown with the help of schematic in Figure 3.7. As presented in the figure the basic difference is in the feed direction but the direction of cutting is same. In case of in-situ tests the feed is directed towards the diameter of the extruded rods whereas in high speed machining it was along the periphery of the workpiece. The reason behind this is, as mentioned earlier, to have the chip, cutting tool and the region where the chip forms in the same plane so that the chips could be photographed while they are forming. The width of cut is equal to the wall thickness of the workpiece in high speed machining but for in-situ, it depends on the length of the cutting edge of the parting tool being used. Parting tools with smaller cutting edge helps to scale down the cutting process which was one of the design criteria.

### **3.5 Measurement System of Force Sensor**

Forces are exerted on the workpiece by the tool in two different directions namely in cutting and feed directions and from the measured value resultant and shear forces can be



calculated. A force sensor was developed by Pratibha [103] was used. Details of the force measurement will be discussed in this section.

### **3.5.1 Design**

A two axis force sensor used in this study that has a capability of measuring force values in cutting and feed directions. The idea was to develop a practical measurement system that could be installed easily in the lathe machine without changing the configuration of the lathe or the workpiece. The force sensor was attached with a tool holder mounting as shown in Figure 3.8(a). The tool holder mounting had a slot so that the mounting can be placed easily in the tool holder post of a lathe machine. Actual image of this tool holder mounting with force sensor is shown in Figure 3.8 (b).

### **3.5.2 Calibration**

The strain gauge produces an electrical signal depending on the strain applied on it. So to convert that signal to force, the sensor needed to be calibrated in both cutting and feed directions.

To calibrate the force sensor in the cutting direction, the system was mounted on a vice in such a way that the gravity force acted in the cutting direction. Cutting tool was replaced with an attachment for calibration. The attachment consisted of a screw to hold a hanger plate where the loads were hanged. The weights were attached gradually on the hanger plate and the corresponding voltage was measured via a data acquisition system (see Section 3.5.3). The total force applied on the screw was calculated using the following equation:

$$F_{sys} = M \times g + m \times g \quad (3.1)$$

where  $F_{sys}$  is the total force,  $g$  is the gravitational acceleration,  $M$  is the total applied weight and  $m$  is the weight of the hanger plate.

The maximum weight applied for calibration was 136.80 kg including the weight of hanger plate that was 0.70 kg. Voltage was measured during loading and also during unloading. The resulting graphs are shown in Figures 3.9 (a and b). An average voltage for a particular weight was calculated, then converted to force and plotted against the voltage values. The relationship between the applied force and the voltage was found linear as shown in Figure 3.9 (c) and the corresponding cutting force calibration equation can be described as:

$$F_c = -0.8076 \times V + 1678.8 \quad (3.2)$$

where  $F_c$  is the cutting force in N and  $V$  is the corresponding output voltage in units of millivolt (mV).

For the calibration in the feed direction the same procedure was followed exactly as for the calibration in the cutting direction except that while placing the system on the vice it was made sure that the gravity force acted in the direction of the feed. The plots used for the calibration in this direction are shown in Figures 3.10 (a-c) and the equation for the conversion of the output voltage to the feed force is as follows:

$$F_{cf} = 0.7926 \times V - 2376.6 \quad (3.3)$$

where  $F_f$  is the feed force in N and  $V$  is the corresponding output voltage in units of millivolt (mV).

### **3.5.3 Data Acquisition**

The data acquisition system comprised of a strain sensor, a wireless transmitter, an analog base station and a computer as shown in Figure 3.11.

As the tool came in contact with workpiece, the tool deflected due to strain depending on the applied load which produced an electrical signal. The electrical signal data was saved by the wireless transmitter (V-Link 2.4 GHz Wireless Voltage Node) during the machining period. Once the machining was completed, the signals data in the transmitter were transferred wirelessly to the receiver (MicroStrain Micro TxRx wireless base station W/ analog outputs) and then using an USB the data was sent to the computer. An 'Agile Link' program was then used to convert the signals to readable format.

### **3.6 Cryogenic Machining Approach**

During cryogenic machining tests the Ti-6Al-4V alloy workpiece was precooled using liquid nitrogen immediately before the machining process. The workpiece was immersed in a liquid nitrogen bath for 5 minutes. Calculated temperature of the workpiece after 5 minutes was  $-196^{\circ}\text{C}$  (see Appendix A). Then the workpiece was taken out of the bath and placed in the 3 jaw chuck of the lathe. Everything was set before taking the workpiece out of the bath so that machining could start as soon as it was placed in the chuck. It was made sure that the workpiece remain below the ambient temperature. At the start of the machining the calculated temperature was around  $-190^{\circ}\text{C}$  (see Appendix A). It can be seen in Figure 3.12 that even after running the test the whole workpiece was covered with ice. The same procedure was followed for in-situ cryogenic machining tests as well.

### 3.7 Sample Preparation and Metallographic Approach

In high speed machining operation, brakes were applied to stop the machine instantly in order to observe the microstructural changes that occurred during the cutting process. After stopping the machine, the tool holder post was moved away and a section was cut as shown in Figure 3.13 (b). From that section two different portions were taken for microstructural observations. One of the portions where the chip has just formed and attached with the bulk material that is yet to be machined and a portion from the chip that had formed already. Both of the sections are shown in Figure 3.13 (c).

The samples were then mounted using a mixture of mounting powder (Lecoset™ Cold-curing resin) and water at a ratio of 2:1. After that the samples were polished using grid papers starting from grid 180 followed by grinding 240, 320, 400, 600, 800 and 1200 grids. For mirror like surface polishing diamond suspensions were used and polished from 6 to 1 $\mu$ m.

Before etching all the samples were cleaned with water and ethanol. Kroll's reagent (92% H<sub>2</sub>O, 6% HNO<sub>3</sub> and 2% HF) was used as etchant and was applied for 20 seconds. Just after etching the etched surfaces were cleaned with cold water and ethanol.

Keyence VHX-600 digital microscope was used to observe the polished surfaces. Typical images taken with this microscope are shown in Figure 3.13 (d, e). Along with the optical microscope a scanning electron microscope, SEM (FEI Quanta FEG) was used.

Fracture surfaces of the chips were observed with SEM. The energy dispersive spectroscopy or EDS system of this SEM was used for quantitative analyses of compositions of diffused materials from the tools to the chips. The EDS was also used for analyzing the transferred material on the tool surfaces.

### **3.8 Surface Characterization**

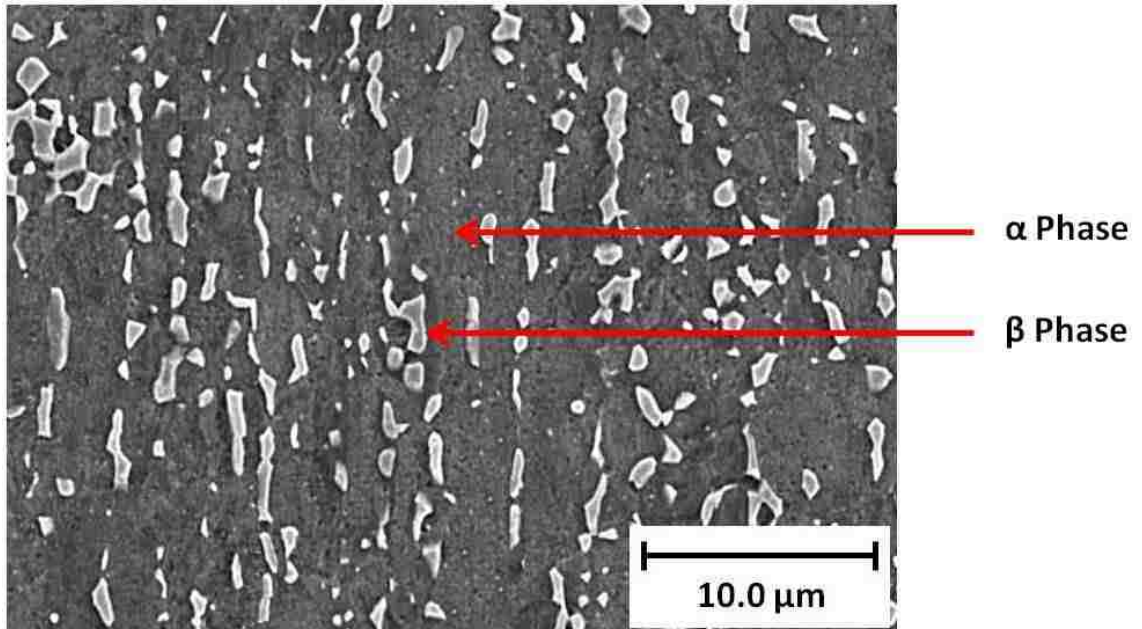
For the examination of machined surface quality, WYKO NT 1100 Optical Profiling System was used. The principle of optical interferometry is based on the superposition of separate light waves of similar frequency in such a way that the combined waves convey the information about the original state. The Wyko NT1100 provides high resolution, 3D surface measurement capability, from sub-nanometer roughness to millimeter-high. Advanced optics ensures sub-nanometer vertical resolution at all magnifications.

The Vertical Scanning Interferometry (VSI) mode was used in this study instead of the Phase Shifting Interferometry (PSI) mode due to the higher roughness of the machined surface. The basic interferometric principles are similar in both the techniques. However, in VSI mode, the white-light source is filtered with a neutral density filter, which preserves the short coherence length of the white light, and the system measures the degree of fringe modulation, or coherence, instead of the phase of the interference fringes. Under different cutting conditions, surface roughness values were expressed in terms of  $R_a$  and  $R_q$ .

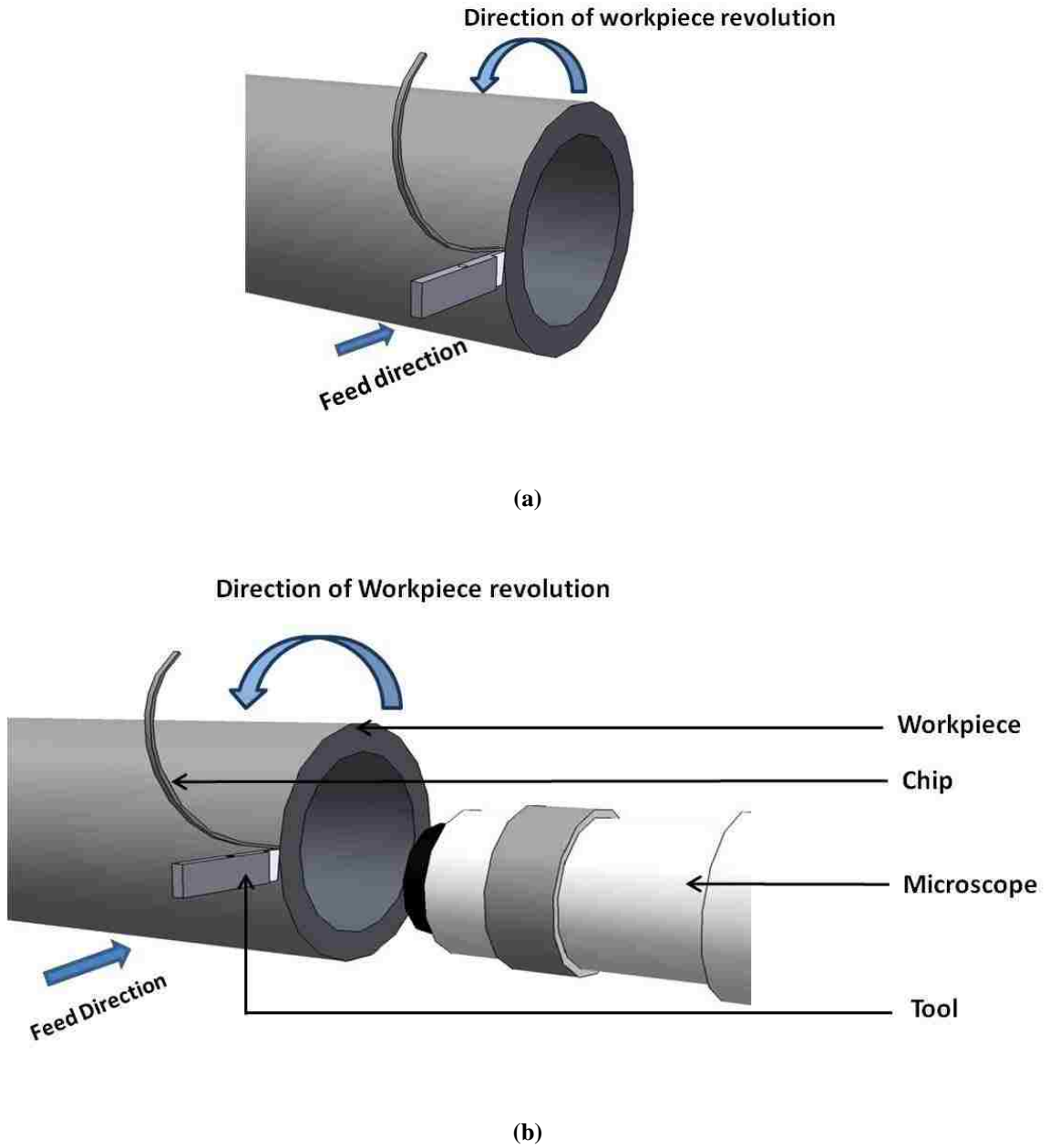
### **3.9 Microhardness Measurements**

Microhardness (Vickers Hardness, HV) at different positions of samples were measured using a Buehler Micromet II microhardness tester. In all the cases a load of 50 gram was applied for 12 seconds. Measurements on the impressions were performed using the Keyence optical microscope for higher accuracy.

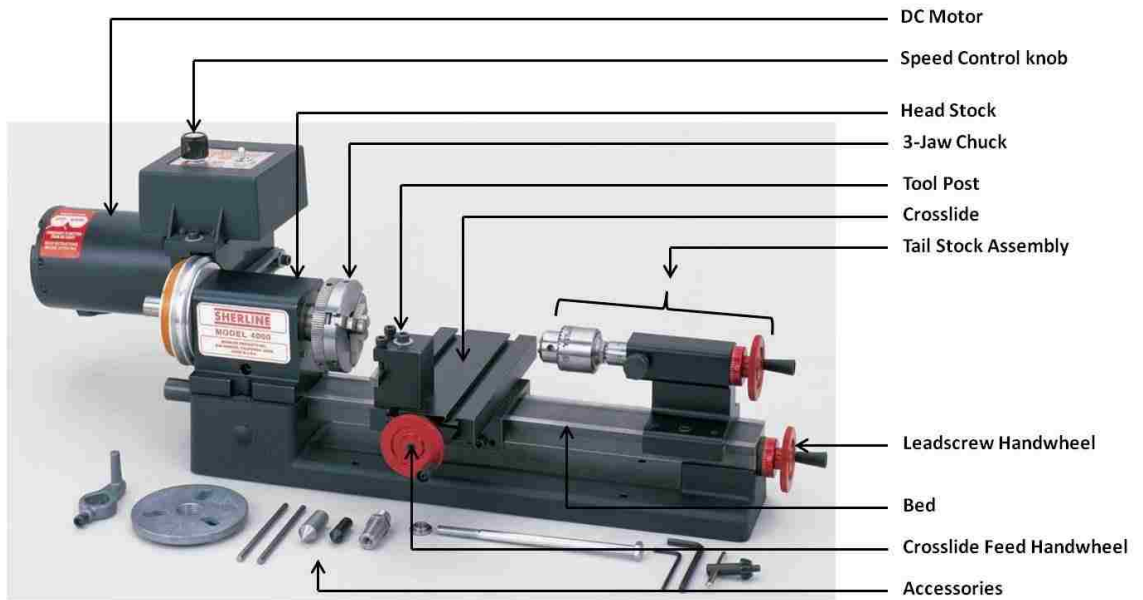
## FIGURES



**Figure 3.1** Microstructure of Ti-6Al-4V indicating  $\alpha$  and  $\beta$  phases.



**Figure 3.2** In-situ machining design showing the direction of workpiece revolution and feed where (a) shows the tool, workpiece and chip are on the same plane and (b) presents the overall schematic where this plane can be focused with a microscope.

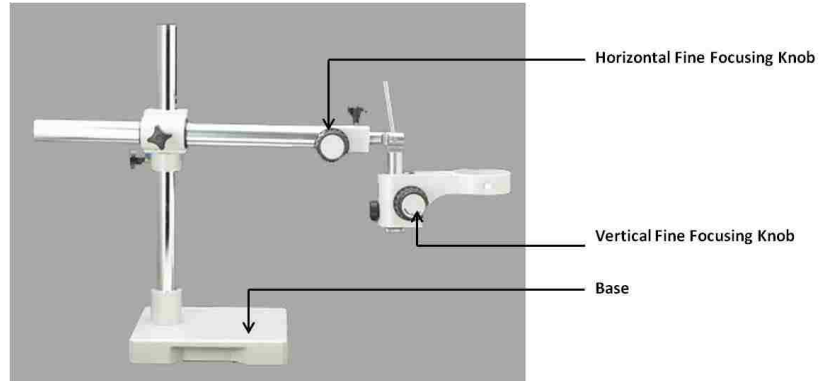


(a)

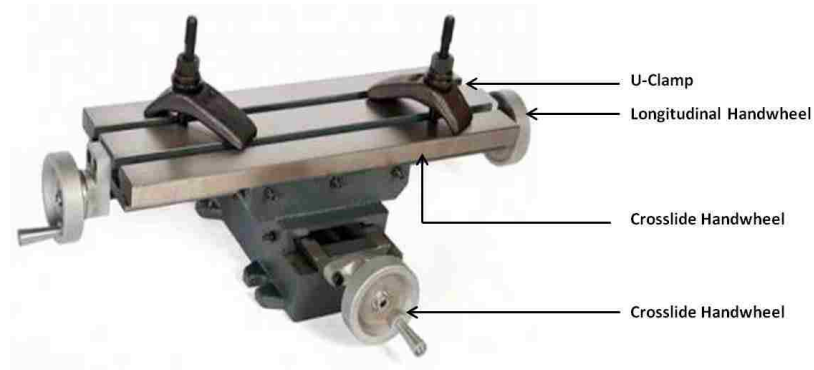


(b)

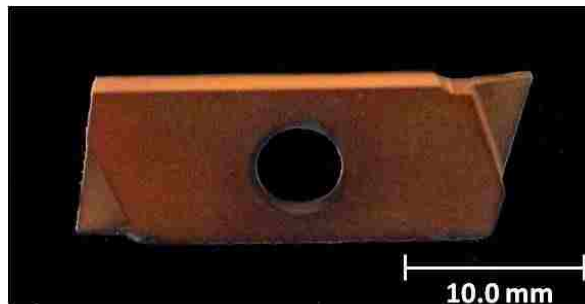




(c)

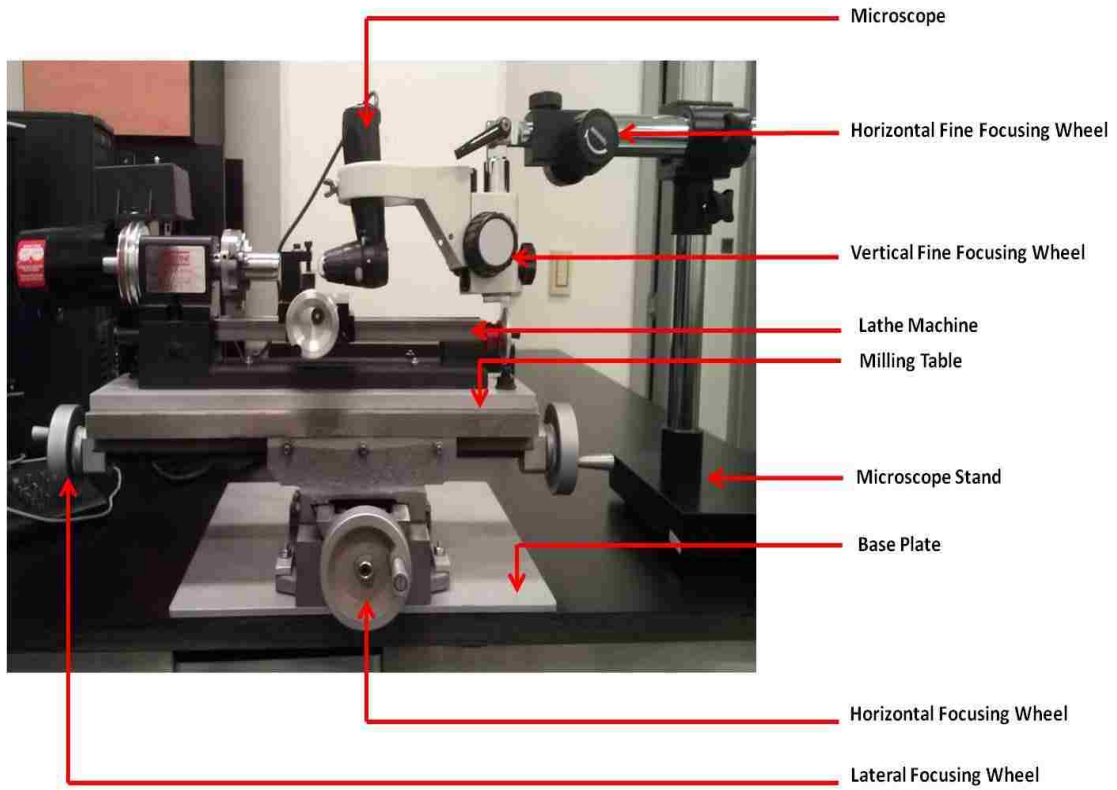


(d)

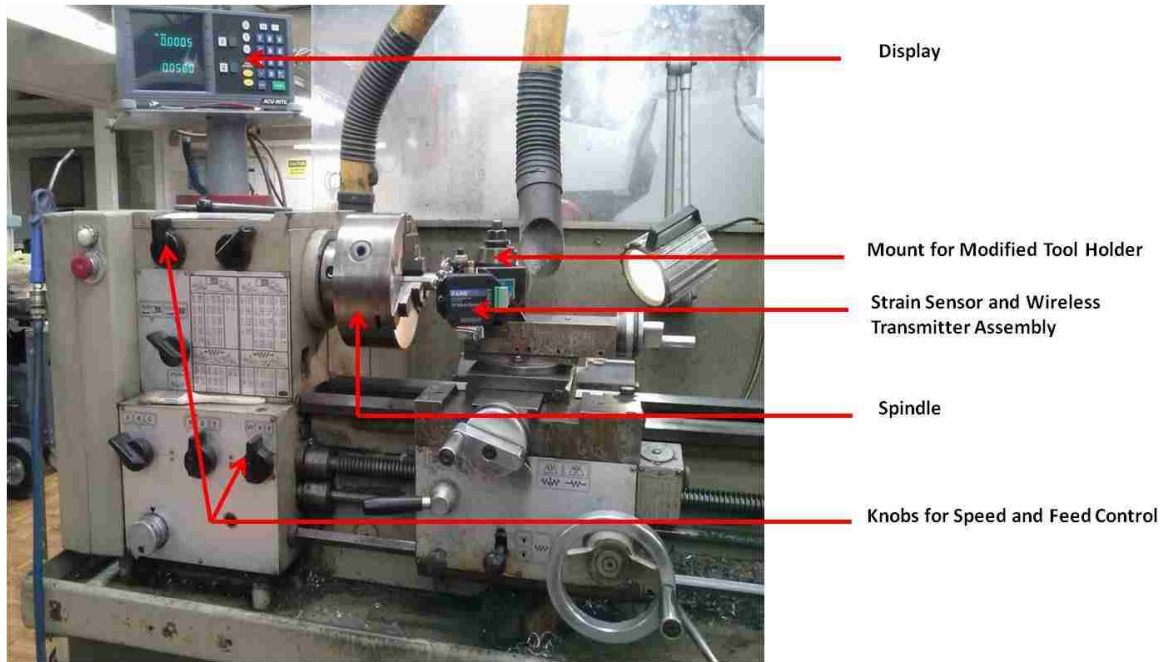


(e)

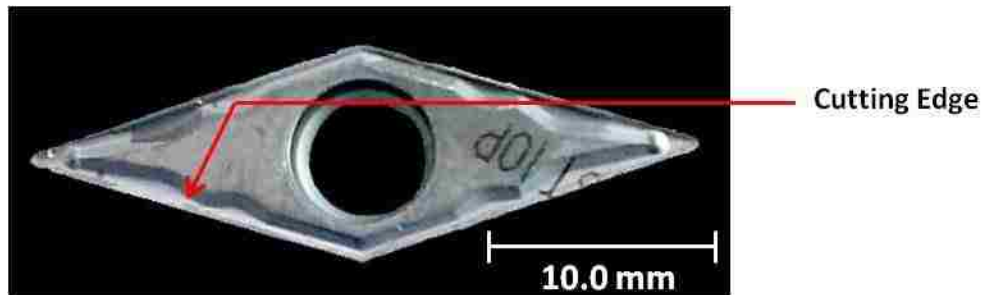
**Figure 3.3** Components of in-situ set-up (a) Sherline lathe (4500/4530) (b) Proscope HR2 handheld digital microscope (c) Luxo 18730 microscope (d) milling table and (e) Uncoated tungsten carbide parting tool.



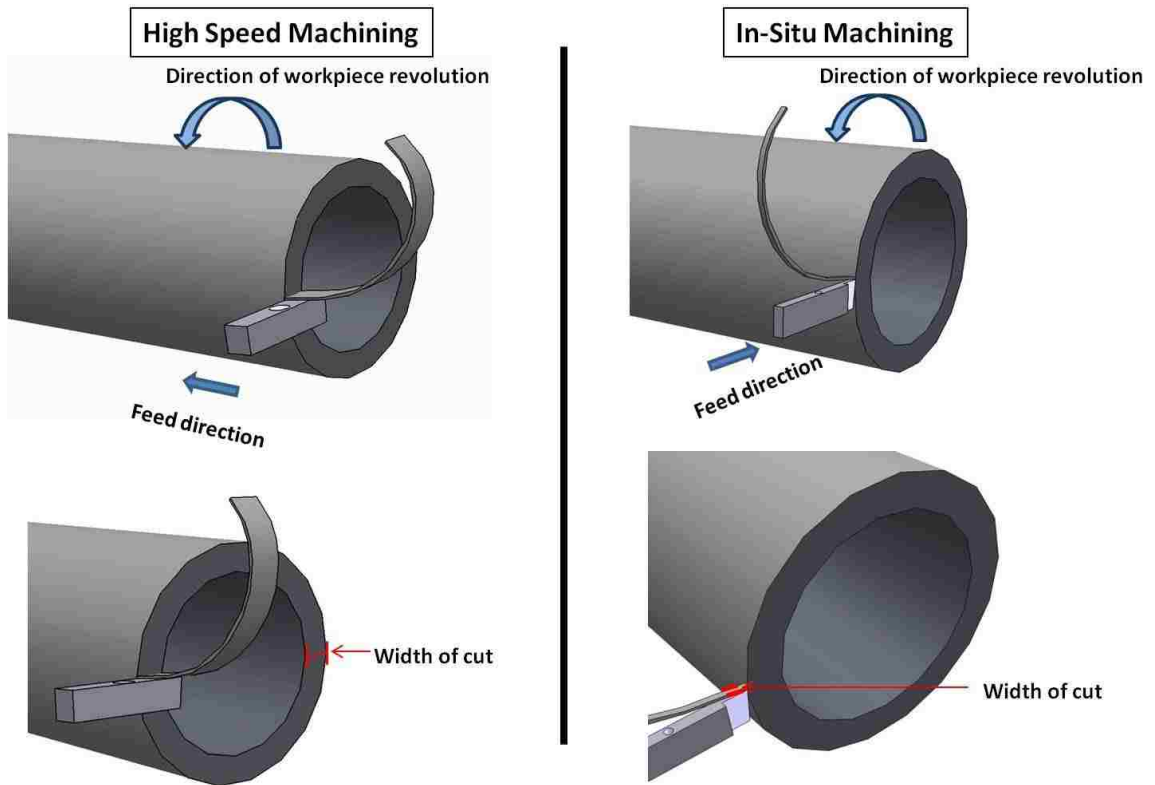
**Figure 3.4** In-situ set-up assembly and different parts.



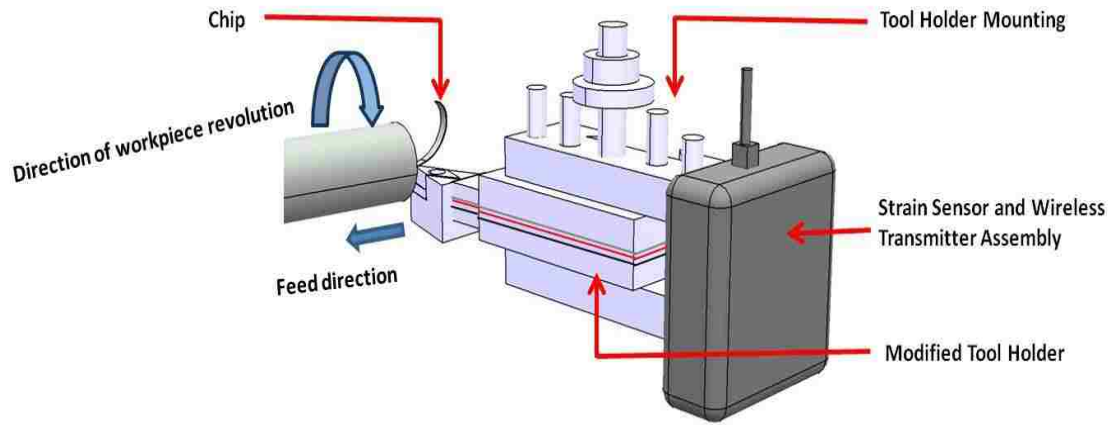
**Figure 3.5** Harrison M300 lathe for high speed machining.



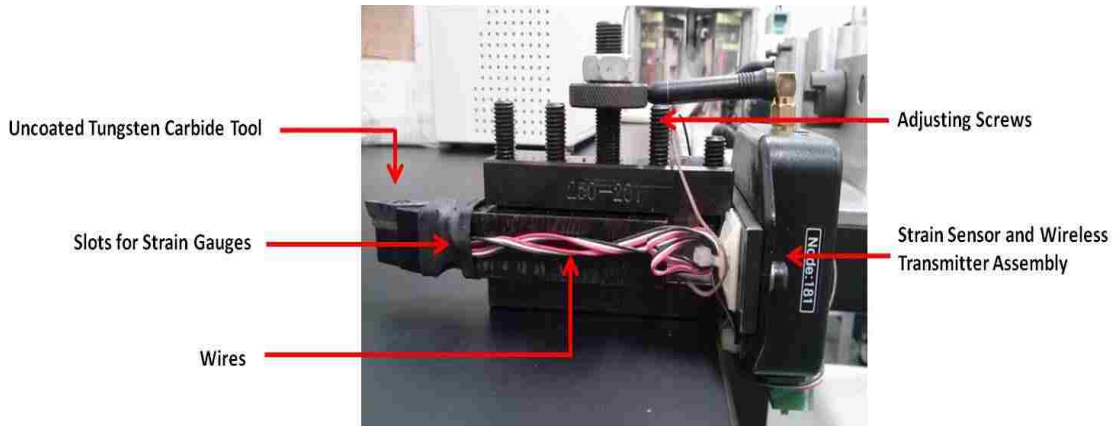
**Figure 3.6** Uncoated tungsten carbide tool.



**Figure 3.7** Schematic presentation of the difference between high speed and in-situ machining set-up.

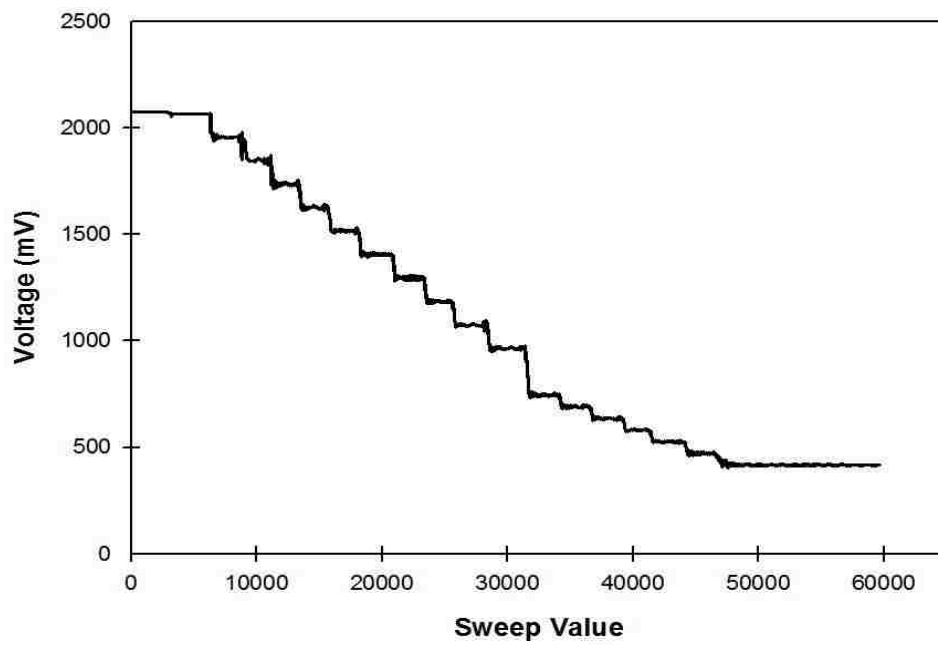


(a)

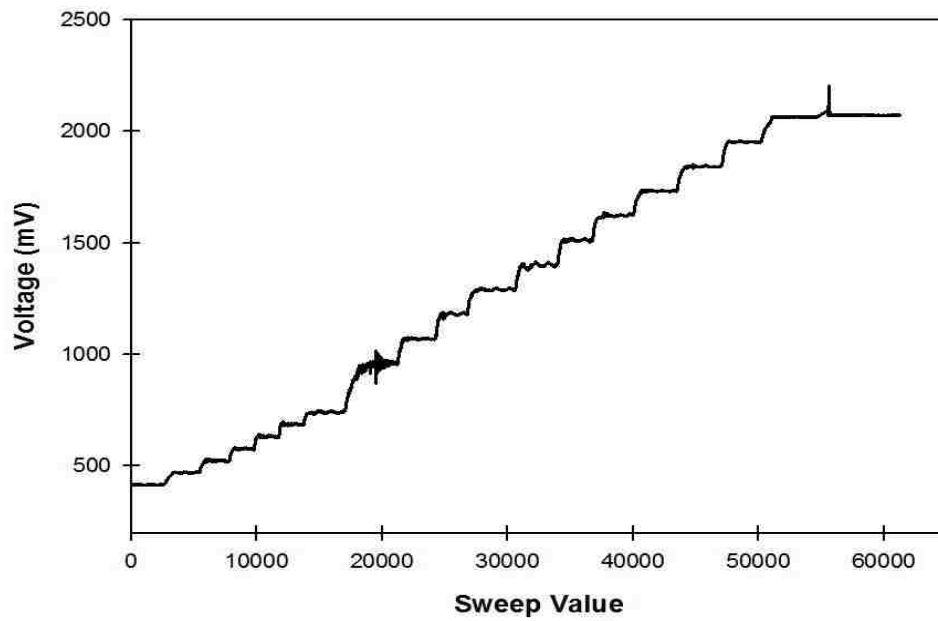


(b)

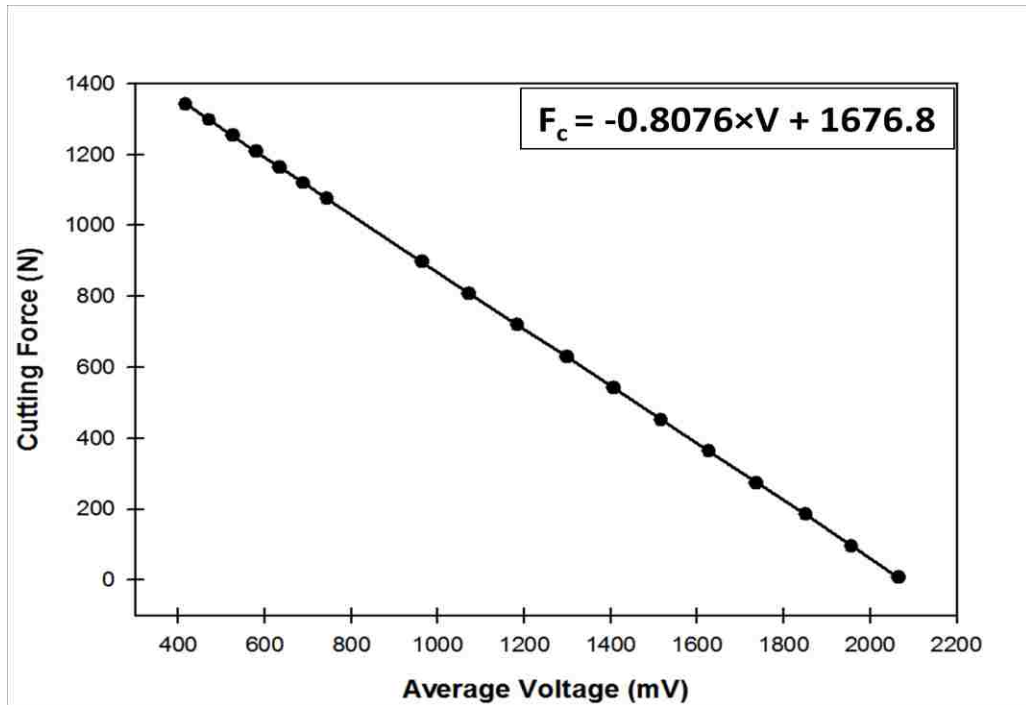
**Figure 3.8** (a) A schematic of the force sensor used to measure force during high speed machining and (b) actual image of the force sensor.



(a)

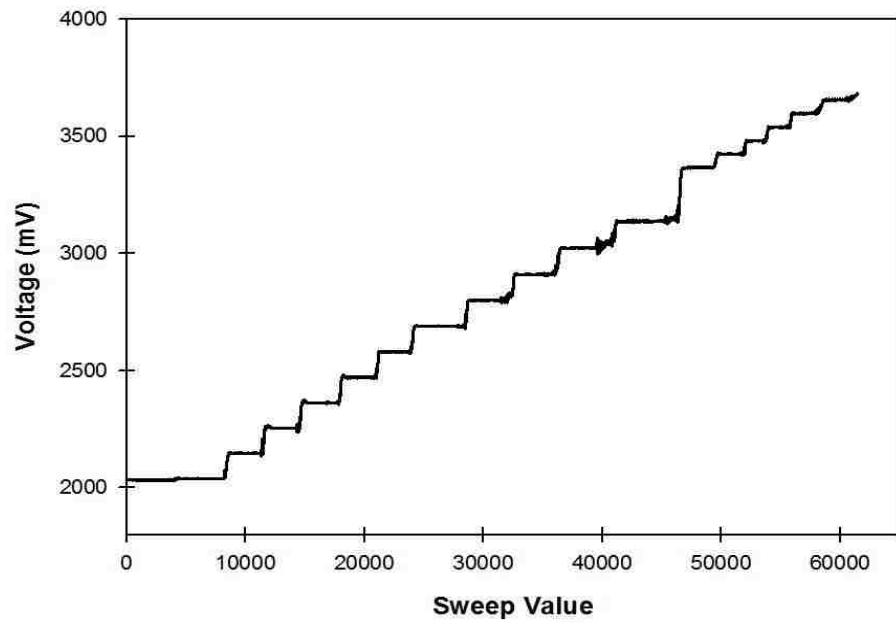


(b)

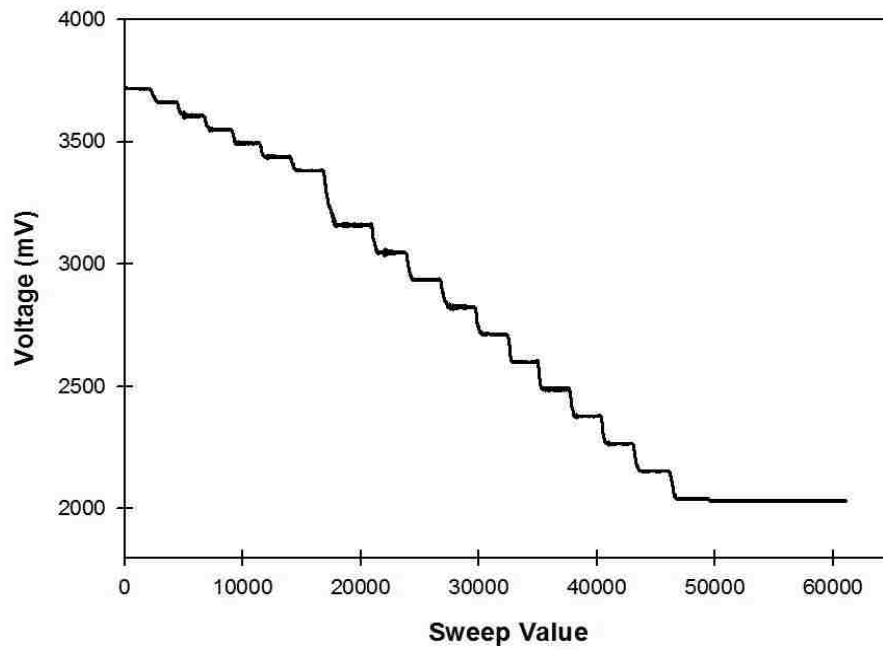


(c)

**Figure 3.9** Calibration of the force sensor in cutting direction where (a) shows the curve during loading, (b) during unloading and (c) final calibration graph for cutting force.

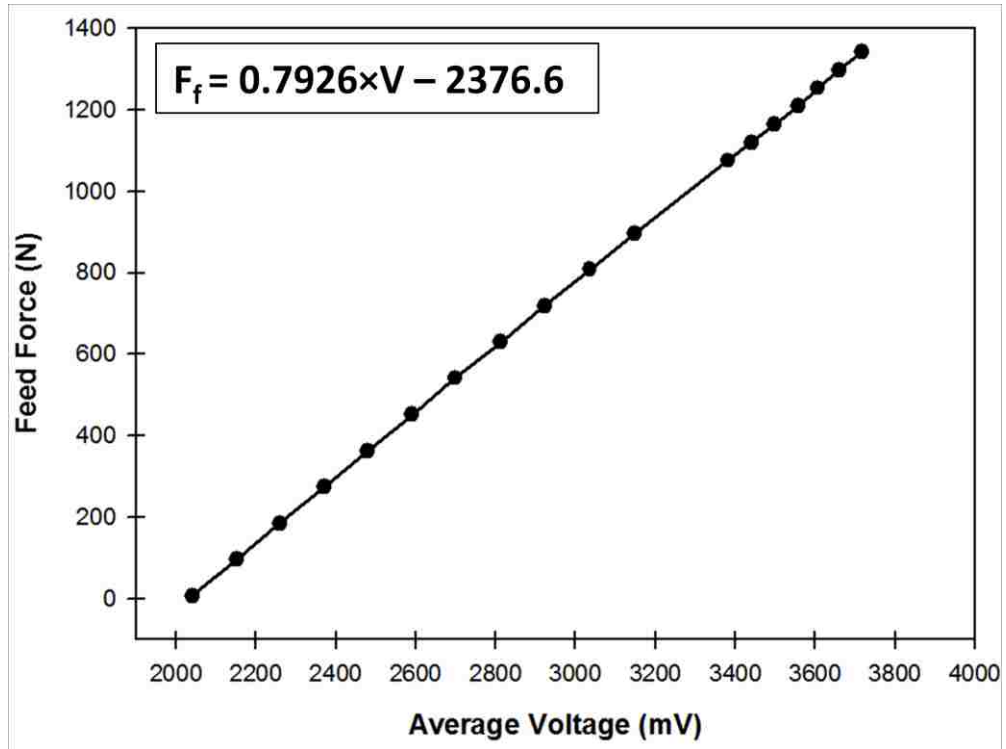


(a)



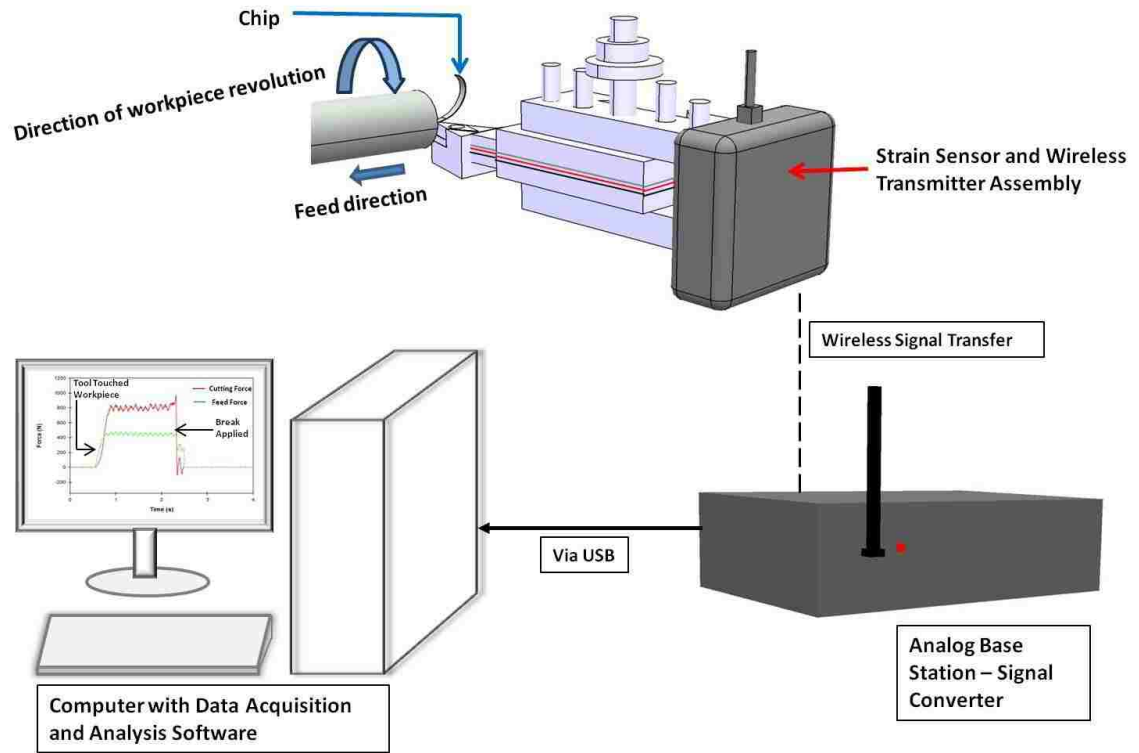
(b)



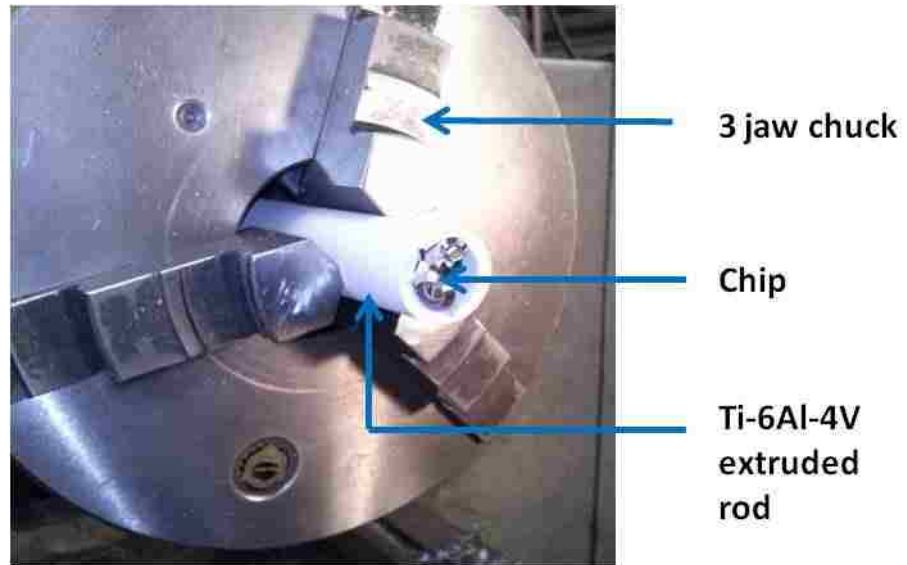


(c)

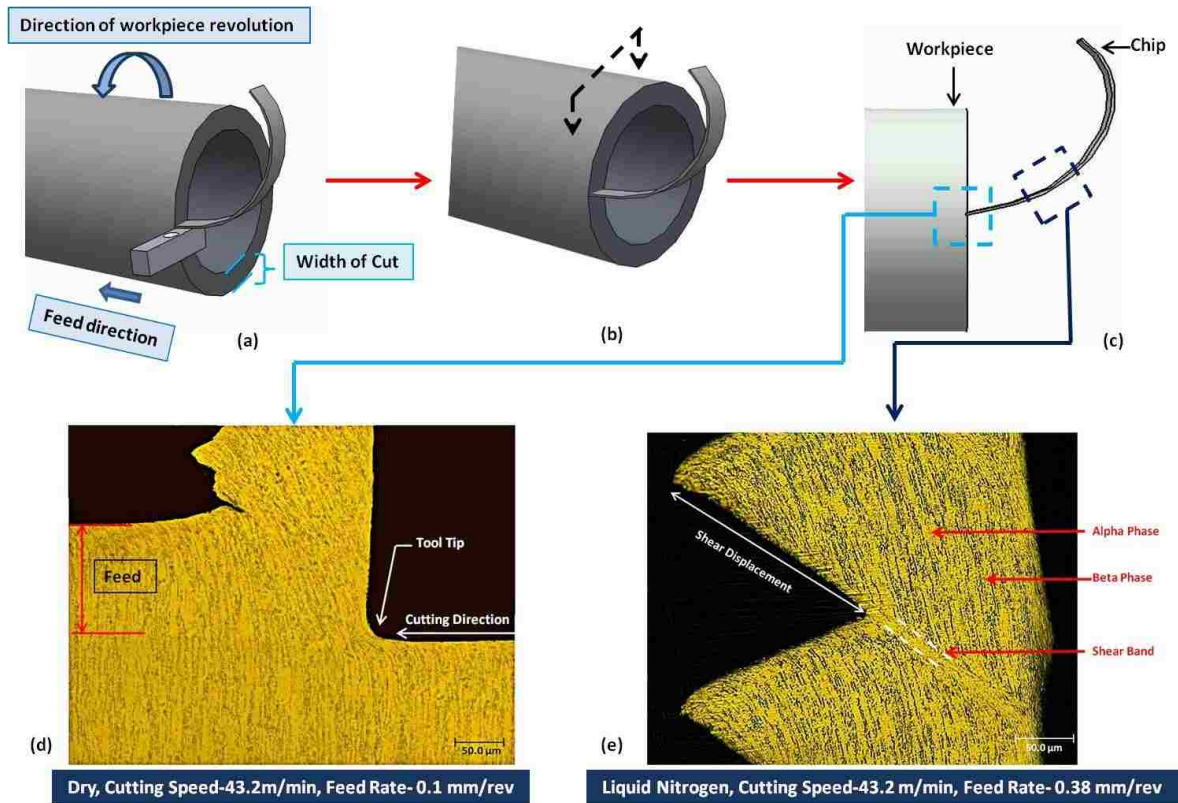
**Figure 3.10** Calibration of the force sensor in feed direction where (a) shows the curve during loading, (b) during unloading and (c) final calibration graph for feed force.



**Figure 3.11** Data acquisition system of the force sensor where the electrical signal obtained during machining is transferred wirelessly to the base station and then via USB transferred to convert it in a readable format.



**Figure 3.12** Workpiece covered with ice where no ice on chips formed after cryogenic machining.



**Figure 3.13** (a) Schematic presentation of workpiece and tool assembly of high speed machining where chip produced during interrupted cutting, (b) section that was cut to obtain the required samples, (c) location of the samples, (d) and (e) polished and etched samples taken from c.

## CHAPTER 4

### EXPERIMENTAL RESULTS

The effect of cryogenic machining on Ti-6Al-4V alloy was investigated considering the characteristics of the chips. To analyse the differences between dry and cryogenic machining the results were compared. Machined microstructures were the basis of all the quantitative analyses. Surface and subsurface characteristics of the machined surfaces and chips were also examined. Along with these studies details of chip formation process were analysed with the help of high magnification microstructures that can be obtained during machining by in-situ methods at slow cutting speed. All these results are presented in this section.

#### 4.1 In-Situ Machining

As mentioned in Section 2.3.2, there are contradictory views on the mechanism of serrated type of chip formation process [6], [7], which is a characteristic for Ti-6Al-4V alloy. In this section some important aspects of chip formation process are presented by providing microstructural evidences generated during in-situ machining methods.

##### 4.1.1 Average Cutting Speed and Feed Measurement for In-Situ Tests

During in-situ machining the chuck was rotated by hand to obtain low cutting speed (see Section 3.2.4). It was difficult to maintain a constant cutting speed throughout the in-situ machining tests. So for higher accuracy, the cutting speed was reported as average cutting speed for the in-situ machining tests in this study. The average cutting speed during in-situ machining tests were calculated from the total distance travelled by the tool along the

circumference of the workpiece and the total time required for the tool to travel that distance according to the general definition of speed:

$$\text{speed} = \frac{\text{Distance}}{\text{Time}} \quad (4.1)$$

Because of manual operation of cross slide hand wheel, there was a possibility that feed rates would vary during in-situ machining. To avoid this problem and ensure accuracy, instead of feed rate, feed was measured from the microstructure as shown in Figure 4.1 (a). The measured feed actually meant feed for a particular moment or feed for the chip that was about to form which could be taken as constant because one particular chip formation took very little time as will be discussed in Section 4.1.3.

#### **4.1.2 Microstructural Interpretation of Serrated Chip Formation**

Microstructures obtained during intermittent in-situ machining where the chuck was rotated for one or two seconds and then stopped to take pictures. After that the chuck was rotated again and thus the process continued. One of these pictures is shown in Figure 4.1 that showed several important features. As can be seen in Figure 4.1 (a), new fresh surface formed just below the tool tip, which indicated that the crack initiated from the tool tip. Also a close inspection of this microstructure revealed the path of strain localization which is pointed out in this figure. It was found that near the tool tip region the strain localization occurred in a curved path which then became straight. The machined surface was found wavy in nature.

Figure 4.1 (b) is the same microstructure as 4.1 (a) and is presented to indicate some other important characteristics of the chip which was about to form. A portion of the chip that was close to the tool was found to become flattened. Also the free surface of that very chip

started to bulge. Chips produced previously were found to touch each other though in some regions some cracks were observed between two consecutive chips. The feed value was measured from the micrograph as shown in Figure 4.1(a) which was 0.08mm for the chip that was about to form as shown in Figure 4.1(b). The knowledge obtained from this section will be used to describe schematically the serrated chip formation mechanisms in Section 5.1.

#### **4.1.3 Formation of Serrated Chips**

Sequential microstructures of the formation process of a particular serrated chip are shown in Figure 4.2. The feed value for the chip which was about to form was 0.07mm. These images were extracted from the video taken during in-situ machining process at an average cutting speed of 0.05m/min (video can be found in the CD included with the thesis, see Appendix B). In Figure 4.1, it was shown that strain localization occurred and also the crack initiated at the tool tip. This was the first step of serrated chip formation which is also shown in Figure 4.2 (a). As mentioned earlier, the videos were taken at a rate of 30 frames per second. Knowing the rate at which frames were acquired it was possible to calculate the elapsed time after which each of the microstructures of Figure 4.2 were taken was calculated. It was found that step 2 and step 3 of Figures 4.2 (b and c) took maximum time. Calculated time for completion of step -3 was 0.23 seconds whereas step 4 took only 0.03 seconds. This calculated time indicated that, after initiation in step 1, the crack propagated in a stable manner upto step 3. After that the stable crack propagation became unstable and formed a new chip B as shown in Figure 4.2 (d). The speed of crack propagation was calculated after measuring the crack length from the microstructure of Figure 4.2 (c). The length of the stable crack was 92 $\mu$ m whereas the unstable crack length was 46.85  $\mu$ m. The speed of stable crack propagation was 0.4mm/sec and

for unstable crack the speed was 1.56mm/sec. Maximum chip thickness of the new chip B (Figure 4.2 (d)) was 90.88 $\mu$ m (measured from microstructure).

It was also observed that during the stable crack propagation period the chip that was about to be formed became flattened gradually and bulged. As a result of this the crack between the chip that was being formed and the one before it became closed. It can be seen in Figure 4.2 (d) that the crack between chip A and B has closed. Also during the formation process of chip B, a fresh surface was formed as shown in Figure 4.2 (d). Irrespective of the size, every single serrated chip showed these features as they formed in the same way. All these important features mentioned in this section were applied in the proposed mechanism of serrated chip formation described in Section 5.1.

#### **4.1.4 Characteristics of Serrated Chip Formation during Cryogenic Machining**

Precooled Ti-6Al-4V samples were used for in-situ cryogenic observations (see Section 3.6). Serrated chip formation process in cryogenic condition was found to be microscopically similar to dry. But there was one basic difference that occurred during machining of precooled samples. Cracks between two consecutive chips were much more prominent and most of them did not close as shown in Figure 4.3. The knowledge of lesser tendency of crack closure during in-situ cryogenic machining was applied in Section 5.1 in developing serrated chip formation mechanisms.

#### **4.1.5 Difference between Serrated and Continuous Chips Formation Process**

To determine the differences between serrated chip and continuous chip formation mechanisms, 6061 aluminum alloy was machined in-situ at an average cutting speed of



0.02m/min. The sequential microstructures are shown in Figure 4.4 where the microstructure based measured feed was 0.1mm. As can be seen in Figure 4.4 (a), a large bright white plastically deformed region was formed and the size of this region increased gradually as the machining progressed. The length of this plastic zone along the cutting direction was measured from the micrograph shown in Figure 4.4 (c). The length was found to be 429.7  $\mu\text{m}$ . Finally a crack initiated and propagated (Figure 4.4 (d)) which separated the plastically deformed zone as a continuous chip from the rest of the workpiece. The large size of plastically deformed region during machining 6061 aluminum indicated that there was no strain localization but homogeneous deformation as expected from previous work [7].

## **4.2 High Speed Machining of Ti-6Al-4V (Dry and Cryogenic)**

High speed machining was performed at constant speed and from very low to very high feed rates under both ambient and cryogenic conditions. Important microstructural features along with quantitative analyses of microstructures and comparisons are presented in this section.

### **4.2.1 Microstructure of Material Ahead of Tool Tip**

The microstructure of the material ahead of the tool tip gives an idea about the deformation state during the machining process of Ti-6Al-4V. Machining at high speed sometimes does not simulate exactly the same deformation behaviour of the material ahead of the tool tip despite of stopping the process by applying quick stop break [33]. But in this study high speed machining was performed from very low to high feed rates in the same machine so comparing these results would still give a trend of their deformation behaviour and will be discussed in Section 5.3.

Throughout this study the feeds that were used for calculations were measured from the microstructure because microscopic measurements are more accurate than macroscopic values. It was found that the microstructure based measured feed rates were different than the applied ones. A summary of the applied feed rates and the ones measured from the microstructures for both dry and cryogenic conditions are shown in Table 4.1. During high speed machining the cutting speed was constant throughout the test and, like the cutting speed; the feed rates were also controlled by the machine. Although the feed measured from micrograph is the feed value at a particular moment during in-situ machining, in high speed machining this measured feed can be used as the actual feed rate because of the constancy of machining parameters throughout the test.

Typical microstructures of the material ahead of the tool tip machined under different conditions and at different feed rates are shown in Figure 4.5. Equivalent strain was measured at the tool tip region from the displacement of the  $\beta$  phase (see Sections 2.2.5.1 and 2.2.5.2). In dry condition, at 0.17mm/rev (Figure 4.5(a)) and 0.22mm/rev feed rates (Figure 4.5(b)) the equivalent strain values were 0.46 and 0.47 respectively. At 0.12mm/rev (Figure 4.5(c)) and 0.38mm/rev feed rates (Figure 4.5(d)) during the cryogenic condition, the equivalent strain values were 0.42 and 0.52, respectively.

In both conditions the equivalent strain values increased with the increase in feed rates. In case of dry machining the equivalent strain values increased from 0.44 to 0.51 whereas for cryogenic machining from 0.42 to 0.52 with feed rates. This observation was important to predict the deformation behaviour of the bulk material at different feed rates which is discussed in Section 5.5.

**Table 4.1** Applied feed rates and feed rates measured from microstructures.

<b>Applied Feed Rate (mm/rev)</b>	<b>Feed Rate from Microstructure in Dry machining (mm/rev)</b>	<b>Feed Rate from Microstructure in Cryogenic machining (mm/rev)</b>
0.10	0.09	0.12
0.20	0.17	0.18
0.25	0.22	0.24
0.30	0.26	0.26
0.40	0.32	0.38

#### **4.2.2 Chips Formed in Different Conditions**

Chips on which microstructural observations and calculations were performed in this study were taken from portions as described in Section 3.7 and shown in Figures 3.13 (c) and (e) to make sure that the chips were free from the effect applied break for quick stopping. It was observed that when the feed rate was ~ 0.1mm/rev, chips formed during dry and cryogenic conditions were identical in terms of the appearance of shear bands and cracks. In both these conditions the shear bands were not so prominent. Also there were no cracks in the chips as shown in Figures 4.6 (a) and (b).

During cryogenic machining at feed rates of 0.18mm/rev (Figure 4.6 (c)), 0.24mm/rev (Figure 4.6 (e)), 0.2mm/rev (Figure 4.6 (g)) and 0.38mm/rev (Figure 4.6 (i)), the shear bands

were prominent and there were cracks in the chips. Some of those cracks were wide and some were narrow. Around 70 to 80 chips were examined for each conditions and it was observed that there were no periodicity of those cracks. Also cracks vary in length without any particular trend.

At comparable feed rates of 0.17mm/rev (Figure 4.6 (c)), 0.22mm/rev (Figure 4.6 (f)), and 0.26mm/rev (Figure 4.6 (h)) in dry condition, the shear bands were prominent but the cracking tendency was different than for cryogenic machining. Almost 70-80 chips were examined and most of the chips did not have any cracks. Those which showed cracks, were very small in length compared to the cracks generated by cryogenic machining. Cracks, observed in chips produced during dry machining at feed rates of 0.32mm/rev, were similar to the cracks of cryogenic machining (Figure 4.6 (j)).

It could be concluded that serrated chips formed in all the machining conditions of this study but there were variations in cracking tendency which is summarized in Figure 4.7.

### **4.2.3 Adiabatic Shear Band and Crack Formation**

The difference in cracking tendency in different machining conditions as observed in Section 4.2.2, was further examined by performing SEM on the cross sections of the chips. The objective was to find out whether there was any relation between the type or location of cracks with shear bands.

Optical images of the cross section of serrated chips shown in Figure 4.6 revealed that irrespective of the cutting conditions or the cracking, there were two surfaces that were common which are indicated in Figure 4.8 (a). SEM images (Figures 4.8 (b) and (c)) of this common region shown in Figure 4.8 (a) showed they are within a region where the shape of the

$\beta$  phase changes extensively. There is a well defined boundary which is marked in red in Figures 4.8 (b) and (c). The change of shape of  $\beta$  phases within this region was due to severe shear type of deformation. The well defined boundary depicts that two region of Figure 4.8 (a) were well within the shear band and irrespective of cutting conditions, these two surfaces would always form within the shear band.

A wider cracked region was observed in chips produced during cryogenic machining at a feed rate of 0.38mm/rev as shown in Figure 4.9 (a). Low magnification (Figure 4.9 (b)) and high magnification (Figure 4.9 (a)) SEM images revealed the position of the crack tip which was found to be at the edge of the shear band. Another wide cracked chip, but produced during dry machining at a feed rate of 0.32mm/rev was examined as shown in Figure 4.10 (a). Backscattered SEM images of the cracked chip also showed the crack tip at the edge of the shear band.

Compared to the wider cracked chips, the narrow cracked chip (Figure 4.11(a)) was found to be well within the shear band as shown in the backscattered image of Figure 4.11(b). Another interesting feature was observed when analysing the chips formed during cryogenic machining at a feed rate of 0.38mm/rev. A wider crack as shown in Figure 4.12(a) was found to move out of the shear band. Secondary and backscattered SEM images as shown in Figures 4.12 (b) and (c) respectively confirmed that the propagation of the crack fractured the  $\beta$  phase.

In summary it can be concluded that irrespective of the cutting conditions, wider cracks had a tendency to move towards the edge of the shear bands whereas narrow cracks remained well within the shear bands. Further analyses were performed on the microstructures of the chips to quantify the severity (wide or narrow) of cracking and these are discussed in Section

5.2. Also the relation between cracking tendency and flow localization is discussed in Section 5.7.

#### **4.2.4 Fracture Surface Morphology**

Besides the cross section surface observations that have been already presented in the last two sections, another important consideration is the fracture surface of the serrated chip that indicates the type of fracture. For better visualization a low magnification SEM image indicating all the important regions is shown in Figure 4.13.

A low magnification SEM image of fracture surface is shown in Figure 4.14 (a) produced during machining of Ti-6Al-4V alloy in the dry condition at a feed rate of 0.32mm/rev and at a constant cutting speed of 43.2m/min. SEM image at higher magnification from a region indicated in Figure 4.14 (a) revealed dimples in the fracture surface as shown in Figure 4.14(b). At the same cutting condition, there were elongated dimples as well. These elongated dimples were separated by smooth regions as shown in Figure 4.15.

The fracture surface of serrated chips formed during cryogenic machining at a feed rate of 0.24mm/rev and at a constant cutting speed of 43.2m/min is shown in Figure 4.16 (a). SEM image at higher magnification (Figure 4.16(b)) revealed elongated dimples and these elongated dimples were separated by smooth regions similar to the fracture surface formed during dry machining (Figure 4.15).

These fracture surface morphologies depicted that serrated chip formation is a ductile fracture process that occurred due to slower propagation of crack. This observation corresponded to stable crack propagation, observed during in-situ machining as described in Section 4.1.3.

## 4.2.5 Quantitative Analyses of Chip Characteristics from Microstructure

Chip morphology and microstructure reflect all the unique characteristics of machining conditions. So, a systematic quantitative analysis was found to be useful for accurate characterization.

### 4.2.5.1 Chip Thickness Measurement

Serrated chips have a characteristic maximum and a minimum thickness. The method for measuring these two from the microstructure is described in Figure 4.17 where the lines representing maximum and minimum chip thickness are perpendicular to the rake surface. An average chip thickness was also calculated from these values according to-

$$\text{Average chip thickness} = \frac{\text{Maximum Chip Thickness} + \text{Minimum Chip Thickness}}{2} \quad (4.2)$$

In each case ~15-20 chips were analyzed and all these results are plotted for comparison as shown in Figure 4.18 (a), (b) and (c).

As seen in Figure 4.18, the chip thickness value increased with the feed rates. All these three types of chip thickness showed a higher value in the dry condition compared to the cryogenic condition at a comparable feed rate. The values of chip thickness will be further used to make the schematic model of chips and this will be discussed in Section 5.3.

### 4.2.5.2 Variation of Distance between Shear Bands

The distance between the two consecutive shear bands was measured for all testing conditions as shown in Figure 4.17. It was observed that the distance between the shear bands increased with the increase of the feed rates. In the cryogenic condition, the distance increased

from  $26.78 \pm 4.82 \mu\text{m}$  to  $164.33 \pm 12.66 \mu\text{m}$  whereas in the dry condition it increased from  $23.36 \pm 0.66 \mu\text{m}$  to  $197.45 \pm 10.71 \mu\text{m}$ .

An interesting observation was that between feed rates of 0.10mm/rev to 0.40 mm/rev the distance between shear bands was higher in the case of cryogenic machining. These results are summarized in Figure 4.19. Like the chip thickness values, these distances are used for the models of chips as well discussed in Section 5.3.

#### 4.2.5.3 Shear Displacement Variation

Shear displacement is the step produced during the formation of serrated chips. The procedure of measuring the shear displacement is shown in Figure 4.20. It was observed that the distance between the shear displacements increased with increasing of the feed rates. In the cryogenic condition, the displacement increased from  $12.23 \pm 1.75 \mu\text{m}$  to  $210.51 \pm 0.53 \mu\text{m}$  whereas in the dry condition it varied from  $15.04 \pm 3.62 \mu\text{m}$  to  $203.96 \pm 3.09 \mu\text{m}$ . Between 0.10mm/rev and 0.40 mm/rev feed rates these values were higher for the cryogenic condition as can be seen in Figure 4.21.

To understand the relation between shear displacement and chip thickness, normalized displacement was calculated according to:

$$\text{Normalized Displacement} = \frac{\text{Shear Displacement}}{\text{Maximum Chip Thickness}} \quad (4.3)$$

Normalized shear displacement values were found higher in cryogenic condition than dry machining that can be seen in Figure 4.22.



The shear displacement values are very critical, as they represent shear strain values in the shear bands. These unique characteristics of serrated chip will be further used for the schematic modelling of chips discussed in Section 5.3.

#### **4.2.5.4 Shear Band Width**

The width of the shear band varied from the free surface towards rake face as shown in Figure 4.23. So, an average value was taken after measuring it from different locations of shear bands. The method of measuring the shear band width is shown in Figure 4.20. A summary plot is shown in Figure 4.24. It was observed that in the cryogenic condition the width increased from  $2.84 \pm 0.77 \mu\text{m}$  to  $10.11 \pm 0.36 \mu\text{m}$  whereas in the dry condition it varied from  $1.85 \pm 0.33 \mu\text{m}$  to  $12.44 \pm 0.18 \mu\text{m}$ . These values are also used for the calculation of shear strain in shear bands (Section 4.2.8). The same trend of having higher values between 0.10mm/rev and 0.40mm/rev feed rates was observed in the case of cryogenic machining.

#### **4.2.5.5 Shear Angle Variation**

The shear angle is the direction of shear band formation and the method of measuring it from the microstructure can be seen in Figure 4.25 where the horizontal line is parallel to the cutting direction and the inclined line representing the shear angle is the direction of the shear band. A summarized plot of the measurements in all the machining conditions of this study is shown in Figure 4.26.

As can be seen in Figure 4.26, when cryogenic conditions were used, higher values of shear angles than the dry condition were observed. In the dry condition the angle was found to decrease with the increase of the feed rates whereas in the cryogenic condition the angle first increased to 0.20mm/rev feed rate to an angle of  $41.49^\circ$  and then decreased to  $38.53^\circ$ .

The shear force, the velocity in shear direction, the chip velocity etc required shear angle value for calculation. So, accurate measurement of the shear angle was very important. Throughout this study microstructure based measurements of shear angles were used. Thus it is important to validate the procedure of measuring shear angle that was used in this study. For this reason, the shear angle was calculated using theoretical equations as well and compared with the shear angle values for serrated chips reported in the literature.

Oxley and Welsh [3] proposed an equation for calculating the shear angle from the feed and chip thickness value according to the following formula:

$$\tan(\Phi) = \frac{f}{t_{\text{chip}}} \quad (4.4)$$

where  $\Phi$  is the shear angle,  $f$  is the feed and  $t_{\text{chip}}$  is the chip thickness. This equation was developed to analyze the shear angle of continuous chips. Ti-6Al-4V alloy produces serrated chips as shown in Figure 4.17 and these have a maximum and a minimum chip thickness value. So the average chip thickness was used in the calculation of the shear angle using Equation 4.4 and the summarized plot is shown in Figure 4.27. As can be seen, with the increase of feed rates the calculated shear angle values increased in both dry and cryogenic conditions. This is different from what we showed in Figure 4.26 where the shear angle was measured from microstructures. The discrepancy is due to the fact that, Equation 4.4 is valid for homogeneous deformation. Since serrated chips are associated with inhomogeneous deformations this formula should not be used to predict the shear angle. Also the result of Figure 4.26 where microstructure based measurements of shear angle is shown, matched with literature (Figure 2.46) which was also for serrated chips.

## **4.2.6 Force Measurements**

Cutting and feed forces were measured during high-speed machining which were used to calculate the resultant and shear forces. All these forces and their comparisons are presented in this section.

### **4.2.6.1 Measured Cutting and Feed Force**

For cutting force and feed force measurements, average force values were recorded in between the time when the workpiece came in contact with the tool and the brakes were applied. The duration of each of these tests was approximately 1.5 to 2.5 seconds. For all the conditions, cutting and feed forces were measured and the resulting values are shown in Figures 4.28 (a) and (b).

Both the cutting and the feed forces were found to increase with the feed rates. There were no significant differences in cutting forces between the dry and cryogenic conditions. But the feed forces were around ~10% higher for cryogenic machining between 0.1mm/rev and 0.30mm/rev feed rates and then they were almost the same.

As characteristics features of chips were taken as the basis for different types of analyses, shear forces were calculated for better understanding of the effect of cutting conditions. Resultant forces were calculated as well to find out whether there was any significant effect of dry or cryogenic condition on this particular force.

### **4.2.6.2 Comparison of Forces**

The directions of the different forces are shown in Figure 4.29. The resultant forces,  $F_r$  were calculated using the following equation [1]:

$$F_r = \sqrt{F_c^2 + F_f^2} \quad (4.5)$$

where  $F_c$  and  $F_f$  are the cutting and feed forces respectively.

Shear forces for each condition were calculated using the following equation [1]:

$$F_s = F_c \times \cos(\Phi) - F_f \times \sin(\Phi) \quad (4.6)$$

where  $F_s$ , is the shear force and  $\Phi$  is the shear angle measured from microstructure.

These four forces are displayed in Figure 4.30 (a-j) in both dry and cryogenic machining and for comparable feed rates. It was observed that cutting forces were always higher than the feed forces,  $F_c > F_f$ . In all the cutting conditions,  $F_r$  was higher than any other forces which could be easily understood from Equation 4.5.

At around 0.10mm/rev feed rate,  $F_s$  was lower than the  $F_f$  in both dry and cryogenic conditions, which can be seen in Figure 4.30 (a and b). With the increase of the feed rate,  $F_s$  was found to increase and eventually became higher than  $F_f$  value in both conditions. But the interesting part was, at a feed rate of 0.17mm/rev, the  $F_s$  was found to be very close to  $F_f$  in dry condition and at 0.22mm/rev  $F_s > F_f$  whereas for cryogenic condition and at comparable feed rates,  $F_s$  was still lower than the  $F_f$  (Figure 4.30 (c-f)). At very high feed rates the difference between  $F_s$  and  $F_f$  was found to be a lot higher in the dry than in the cryogenic condition.

The calculated  $F_s$  is the apparent  $F_s$  in shear bands because the angles which were used represented the angles of shear bands as discussed in Section 4.2.5.5. The higher tendency of increase of the  $F_s$  at comparable feed rates during dry machining is evidence that there are differences in terms of localization between dry and cryogenic machining, since localization is also associated with shear band.

### 4.2.6.3 Variation of Resultant and Shear Force

A summary plot was made to list the overall effect of feed rates and cutting conditions on  $F_r$  and  $F_s$  which is shown in Figure 4.31 (a) and (b). As can be seen from the Figure 4.31 (a),  $F_r$  increased with feed rates. Figure 4.31 (b) shows that  $F_s$  also increased with feed rates. Another interesting point was that  $F_s$  value was higher in the dry condition. It can be said that, in the dry condition  $F_s$  had a greater rate of increase (see Section 4.2.6.2) compared to cryogenic machining and at a comparable feed rate.

### 4.2.7 Apparent Shear Stress in Shear Band

Shear stress was calculated from the following equation [10]:

$$\tau = \frac{F_s}{A_s} = \frac{F_c \times \cos(\Phi) - F_f \times \sin(\Phi)}{\frac{w \times f}{\sin(\Phi)}} \quad (4.7)$$

where  $\tau$  is the shear stress in the shear band,  $A_s$  is the area of the shear plane (Figure 4.32),  $w$  is the width of cut and  $f$  is the feed. The shear stress calculated using Equation 4.7 can be termed as the apparent shear stress in the shear band consistent with the apparent shear force in the shear band as discussed in Section 4.2.6.2.

Figure 4.33 shows the variation of the apparent shear stress in the shear band ( $\tau$ ) with the feed rate in both dry and cryogenic conditions. To find out the trend a first order linear regression analysis was performed. It was observed that  $\tau$  was higher in the dry condition and it showed an increase with the feed rates as well.

The increase in  $\tau$  with feed rate was due to the fact that additional material was cut as the feed rate was increased. The apparent normalized shear stress in the shear band was

calculated by normalizing  $F_c$  and  $F_f$  with respect to feed and it was observed that the apparent normalized shear stress in the shear band decreased with the increase of feed rate as shown in Figure 4.34. This meant that the strength of the material in the shear band decreased with the increased value of feed rates. The softening of the material within the shear band along with the higher value of  $\tau$  during dry machining will be further discussed in Section 5.5.

#### 4.2.8 Variation of Shear Strain in Shear Band

The value of shear strain in the shear band is very important in order to understand the extent of shear localization. Shear strain in the shear band was calculated using the following equation:

$$\gamma = \frac{\text{Shear Displacement}}{\text{Shear Band Width}} \quad (4.8)$$

where  $\gamma$  is the shear strain in the shear band. Both the shear displacement and the shear band width were measured from the microstructure as described in Section 4.2.5.3 and 4.2.5.4, respectively.

Variation of shear strains in shear bands for all the cutting conditions and parameters are summarized in Figure 4.35. A first order linear regression was performed to find out the trend. It was observed that in both dry and cryogenic conditions the shear strain in the shear band increased with the feed rate because the removal of extra material causes the chip thickness to increase. In cryogenic machining and at low to medium feed rates the shear strain in the shear band was lower. At higher feed rates this trend changed. This will be explained later in Section 5.7.

#### 4.2.9 Velocity Calculations

Machining involves high strain rates and strain rate calculations require the velocity in specific directions. The apparent velocity in the shear band was calculated from the following equation [7]:

$$V_s = \frac{V}{\cos(\Phi)} \quad (4.9)$$

where  $V_s$  is the apparent velocity in the shear band and  $V$  is the cutting speed which is constant in this study.

The velocity of the chip was also calculated using the following equation [7]:

$$V_{\text{chip}} = V \times \tan(\Phi) \quad (4.10)$$

where  $V_{\text{chip}}$  is the velocity of chip.

Results of calculated velocities are shown in Figure 4.36 (a and b). Both of the velocities increase with increasing feed rate. Also in the cryogenic condition the velocities were found to be higher.

#### 4.2.10 Variation of Strain Rate

Localization depends on the strain rate and for this reason effort has been made to calculate this. The applied strain rate and the strain rate in the shear plane are different. Detailed methods of calculating these two strain rates are discussed here.

#### 4.2.10.1 Calculation of Bulk Strain Rate

Bulk strain rate is actually the applied strain rate. An equation was developed for calculating the bulk strain rate from the machining parameters as follows:

$$\text{Bulk Strain Rate} = \frac{V \times f}{w} \quad (4.11)$$

where  $V$  is the cutting speed in rev/min,  $f$  is the feed rate in mm/rev and  $w$  is the width of cut in mm. Variation of bulk strain rate is shown in Figure 4.37. In this study the cutting speed and width of cut were constants for this reason it changed linearly with the feed rates.

#### 4.2.10.2 Measurement of Strain Rate in Shear Plane

Strain rate in the shear plane actually depicts the strain rate in the shear band which was calculated using the following equation [10]:

$$\text{Strain Rate in Shear Plane} = \frac{V_s}{w_{SB}} = \frac{V}{\cos(\Phi)} \quad (4.12)$$

where  $V_s$  is the velocity in the shear band as shown in Section 4.2.9 and  $w_{sb}$  is the width of the shear band measured from the microstructure as described in Section 4.2.5.4. Figure 4.38 shows the variation of strain rate in the shear plane with the feed rate in both dry and cryogenic conditions. It was observed that the shear strain rate decreases with the feed rate which was just opposite of bulk strain rate as discussed in the last section. The reasons for the opposite effect of these two will be discussed in Section 5.6.

#### 4.2.11 Subsurface Deformation State

Machining affects the final product in various ways and one way of understanding the effect is to measure the depth of the deformed zone below the machined surface. Figure 4.39



(a) and (b) show the way of measuring the depth of the deformed zone. The depth of deformed zone was found to increase with feed rates as shown in figure 4.40.

In cryogenic machining, the depth of the deformed zone increased from  $35.00 \pm 4.20 \mu\text{m}$  to  $68.97 \pm 0.91 \mu\text{m}$  whereas in the dry condition it increased from  $29.57 \pm 4.20 \mu\text{m}$  to  $59.75 \pm 4.15 \mu\text{m}$ . In case of low to medium feed rates the depth of deformed zone was found slightly higher in the cryogenic condition than in the dry.

#### **4.2.12 Machined Surface Characteristics**

Machined surface characteristics such as the surface roughness of the finished product are an important way to judge the quality of machining. Wyko images, taken for all machining conditions are shown in Figure 4.41. Summarized plots of average surface roughness,  $R_a$  and average root mean squared surface roughness,  $R_q$  are shown in Figures 4.42 (a) and (b).

In cryogenic machining, the average surface roughness increased from  $0.26 \pm 0.04 \mu\text{m}$  to  $1.25 \pm 0.14 \mu\text{m}$  and the average root mean squared surface roughness from  $0.33 \pm 0.05 \mu\text{m}$  to  $1.6 \pm 0.14 \mu\text{m}$  whereas in the dry condition the average surface roughness increased from  $0.26 \pm 0.01 \mu\text{m}$  to  $0.97 \pm 0.22 \mu\text{m}$  and the average root mean squared surface roughness from  $0.38 \pm 0.06 \mu\text{m}$  to  $1.16 \pm 0.28 \mu\text{m}$ . In case of low to medium feed rates cryogenic machining produced slightly rougher surface than dry cutting.

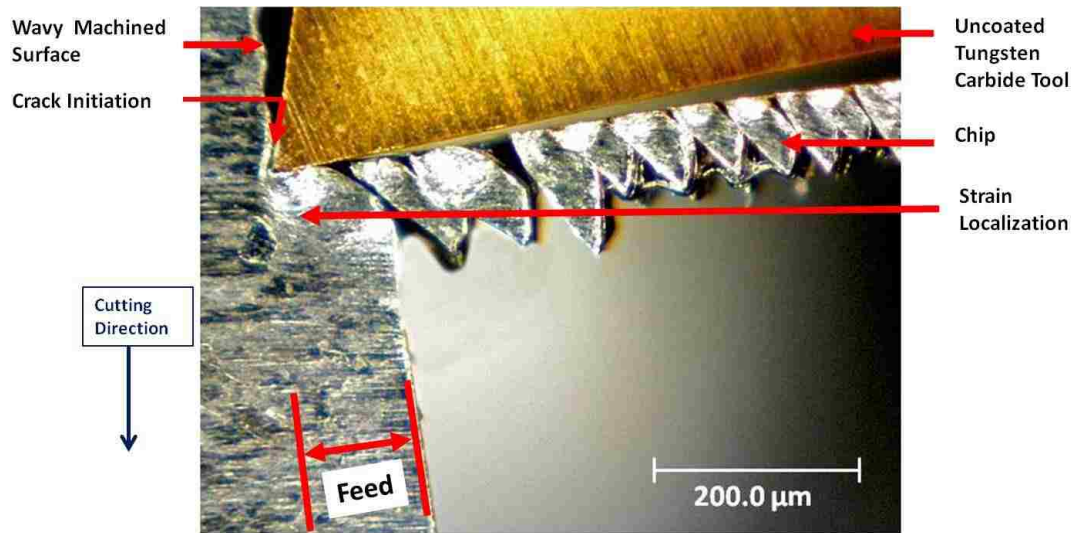
#### **4.2.13 Tool Wear and Adhesion**

As mentioned earlier, uncoated tungsten carbide tools were used in this study. After machining, it was observed that the cutting tool was damaged and the rake face of the tool showed crater wear. Figure 4.43 (a) shows the crater wear and the damaged cutting edge. EDS

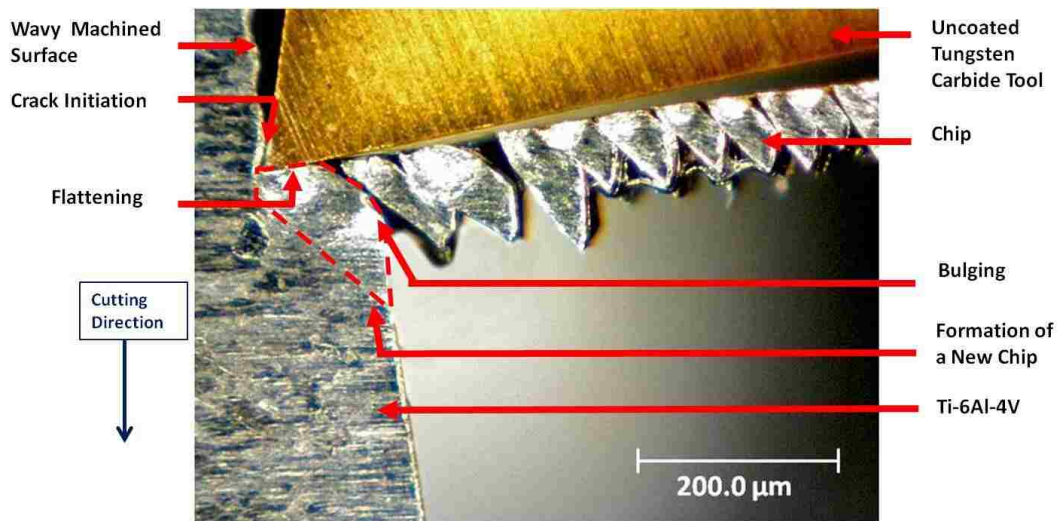
analysis (Figure 4.43 (b)) on the region of crater wear showed the presence of a high percentage of tungsten and carbon. Also a small percentage of titanium was present on the same region because of adhesion.

High amount of adhesion was observed at a distance place from the cutting edge in both dry and cryogenic conditions as shown in Figure 4.44 (a) and 4.45 (a) and this was confirmed by EDS analyses as shown in Figure 4.44 (b) and 4.45 (b). The effects of cryogenic machining in terms of tool wear and adhesion will be further discussed in Section 5.4.

## FIGURES



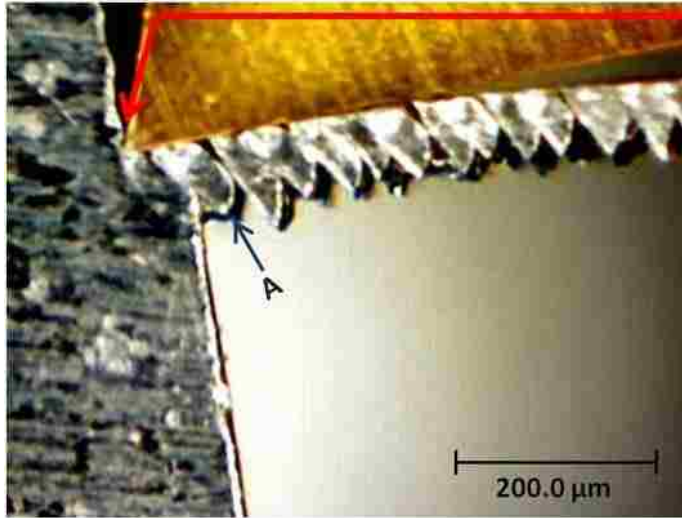
(a)



(b)

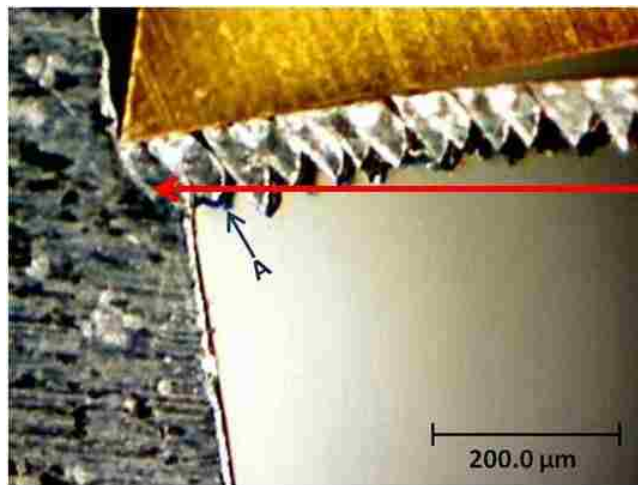
**Figure 4.1** Microstructure obtained during in-situ machining where (a) shows the path of strain localization and in (b) (in that same microstructure) some important features of the chips that was going to be formed are pointed out.

Direction of Cutting



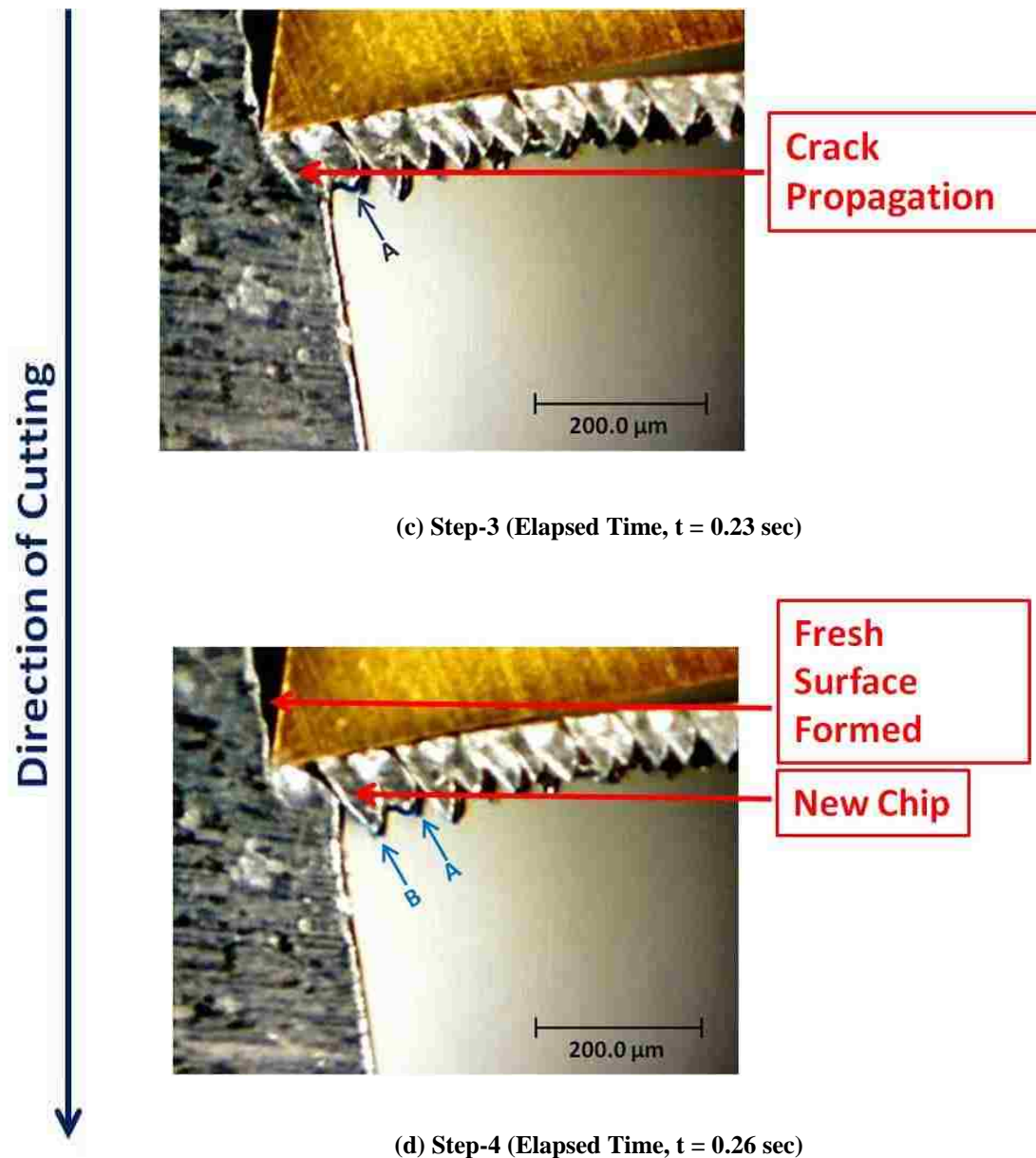
Crack  
Initiation

(a) Step-1 (Elapsed Time,  $t = 0$  sec)

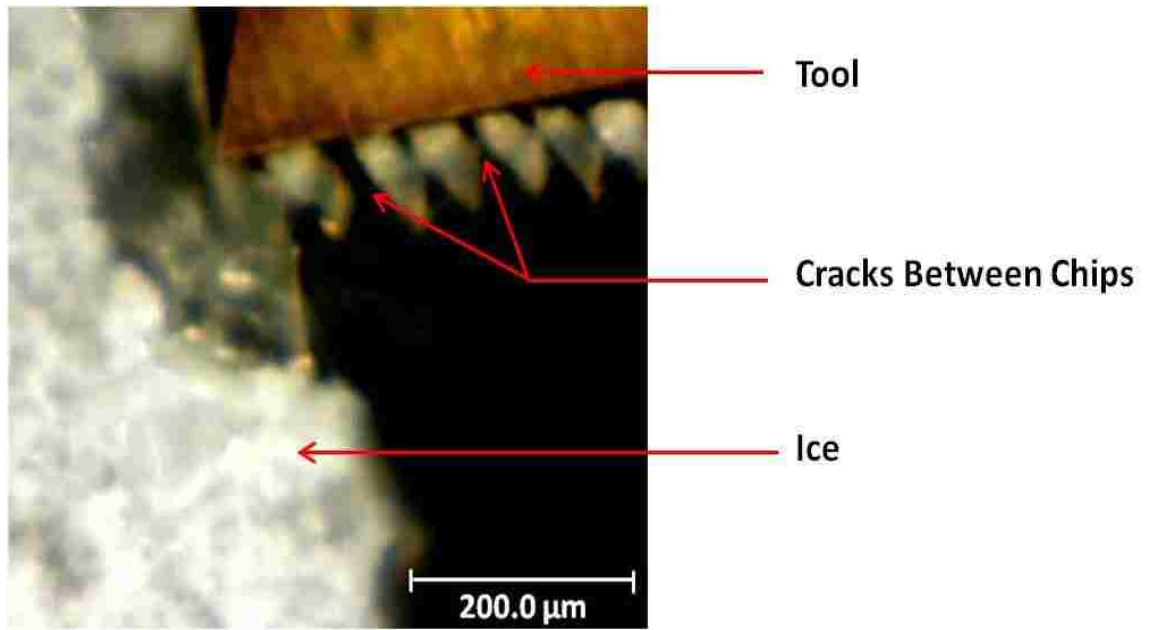


Crack  
Propagation

(b) Step-2 (Elapsed Time,  $t = 0.10$  sec)

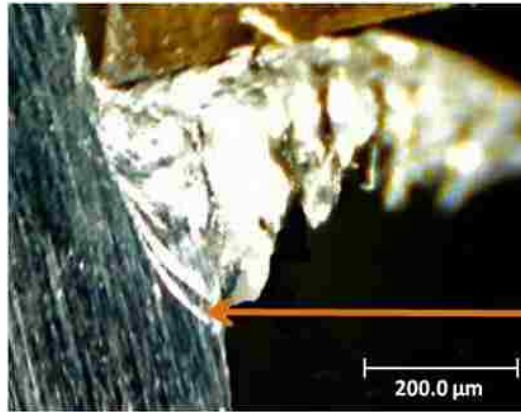


**Figure 4.2** Sequential microstructural observation of formation of a particular serrated chip during in-situ machining of Ti-6Al-4V where (a) reveals that the crack initiated at the tool tip, then (b) and (c) present the steps of stable propagation of the crack which was within the strain localized region formed in step 1 and finally in (d) the new chip B had formed by unstable crack propagation ( Average cutting speed- 0.06m/min, Feed- 0.07mm and width of cut 0.07mm).



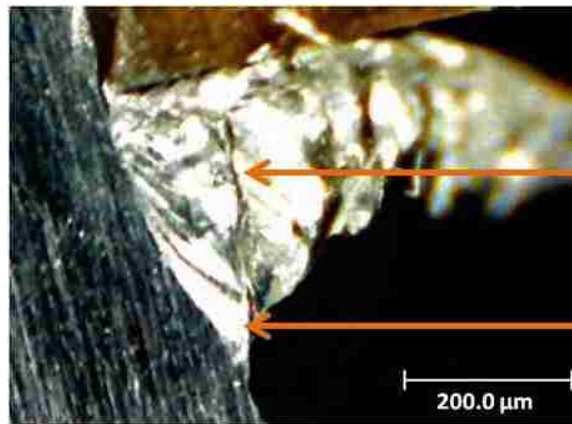
**Figure 4.3** Microstructure obtained during cryogenic machining of Ti-6Al-4V (Average cutting speed- 0.06m/min, Feed- 0.05mm and width of cut 0.07mm).

Direction of Cutting



Movement of plastic zone

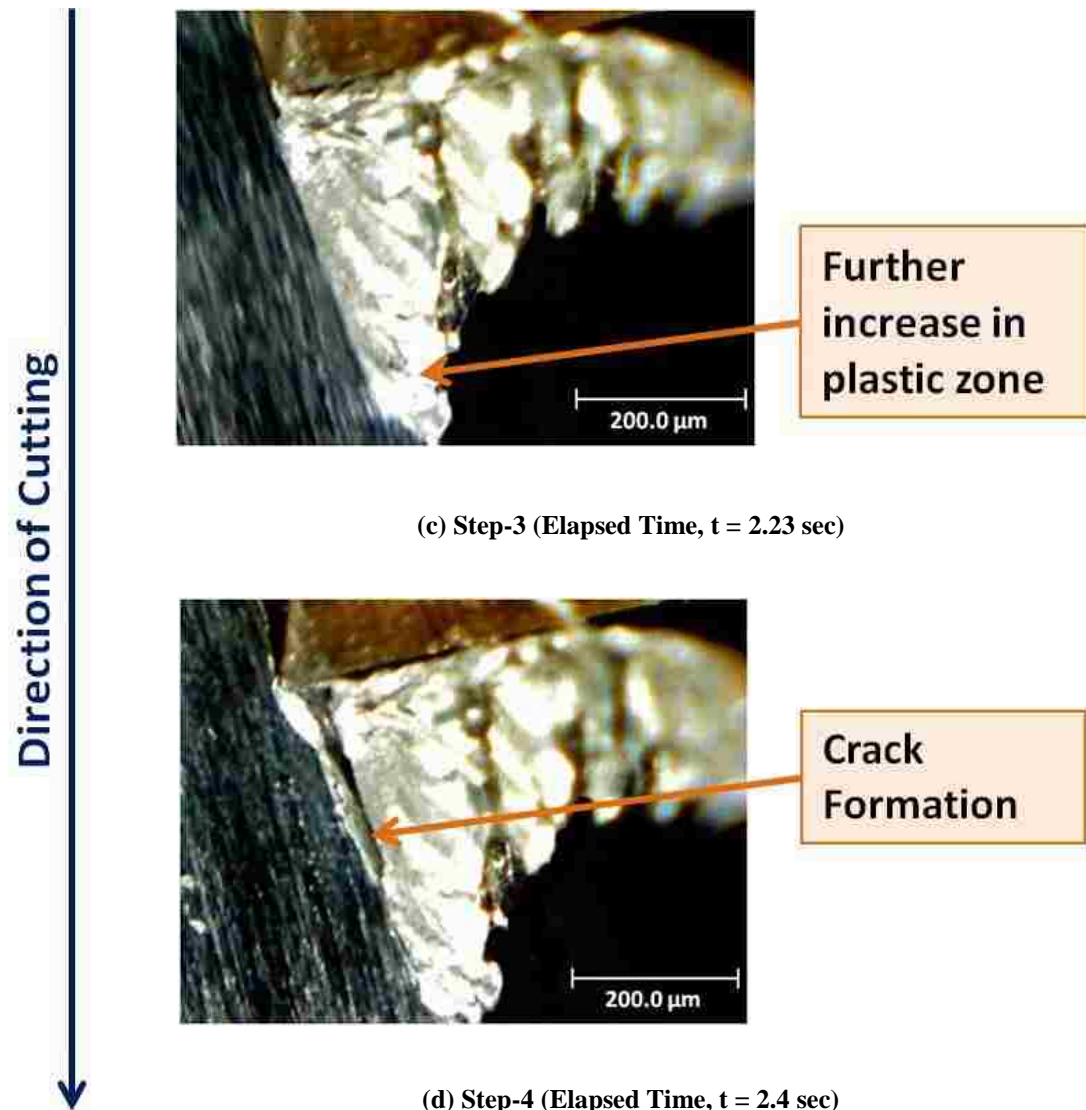
(a) Step-1 (Elapsed Time,  $t = 0$  sec)



Crack

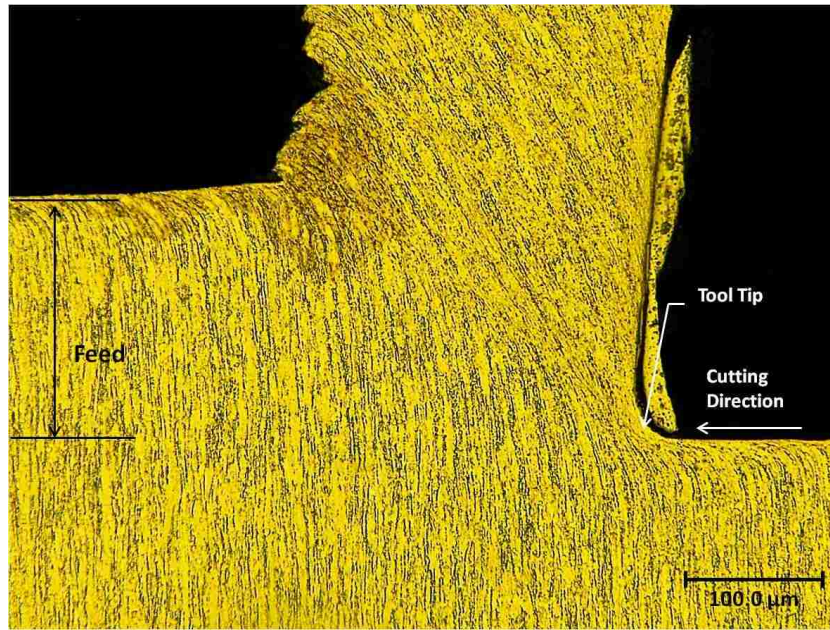
Increase in plastic zone

(b) Step-2 (Elapsed Time,  $t = 0.86$  sec)

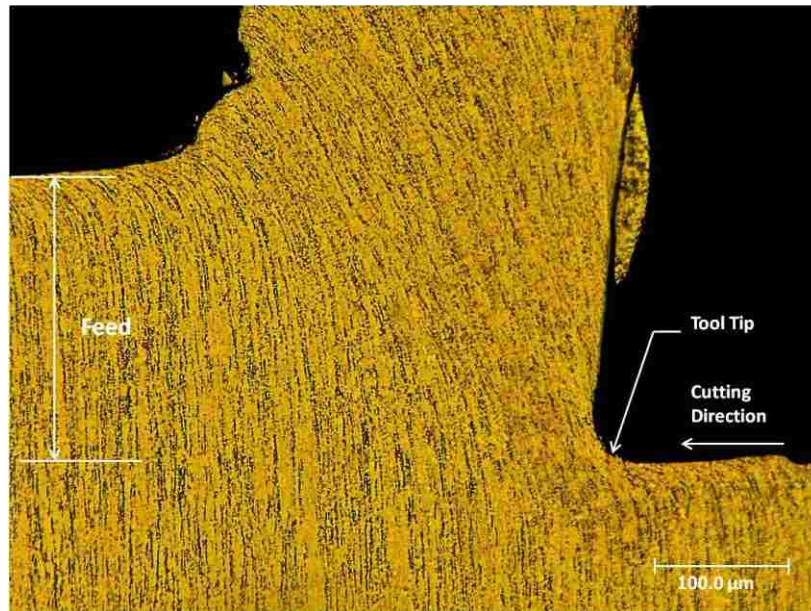


**Figure 4.4** Sequential microstructural observation of formation of a continuous chip during in-situ machining of 6061 Aluminum where (a) reveals that a plastic zone formed and it moved forward, (b) and (c) shows that the size of that plastic zone increased and kept moving forward and in (d) the whole plastically deformed portion got separated (Average cutting speed- 0.02m/min, Feed- 0.1mm and width of cut 0.07mm).

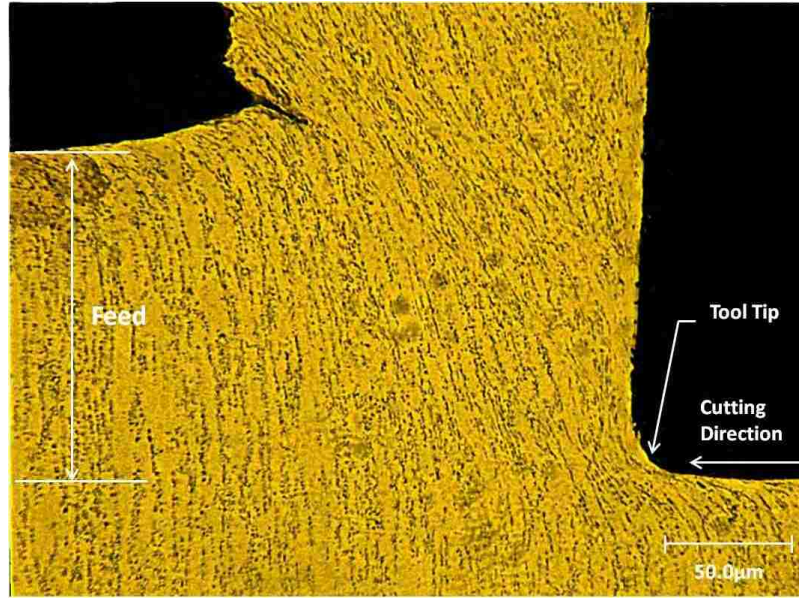




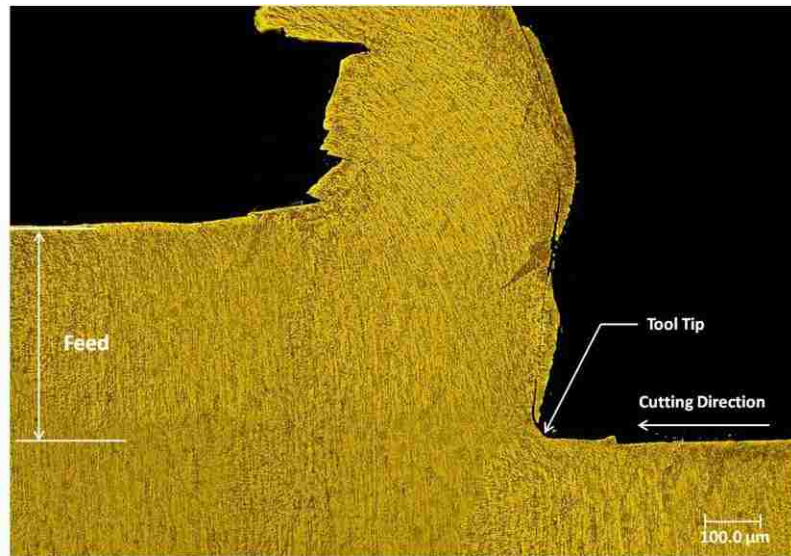
(a)



(b)

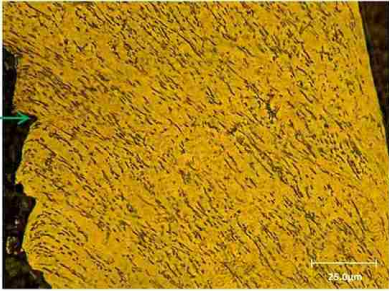

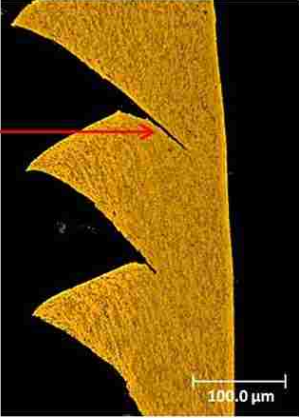
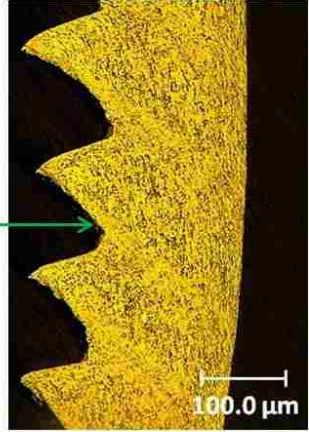
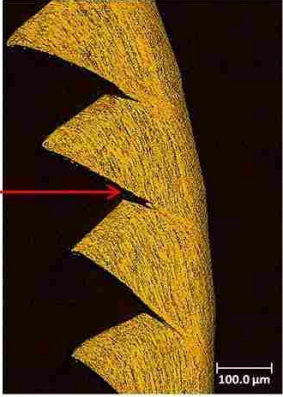
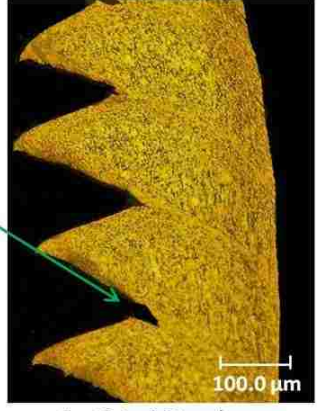


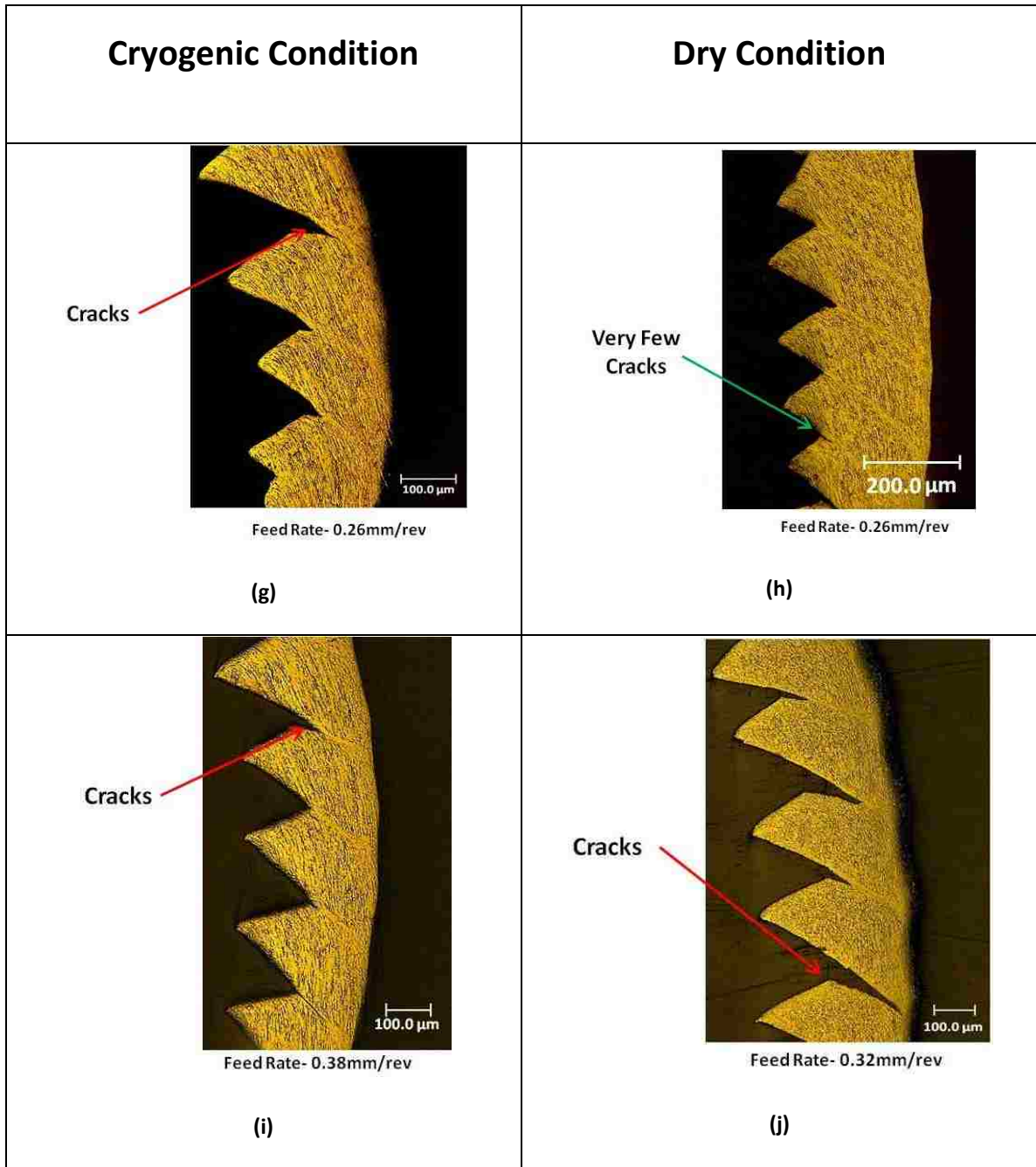
(c)



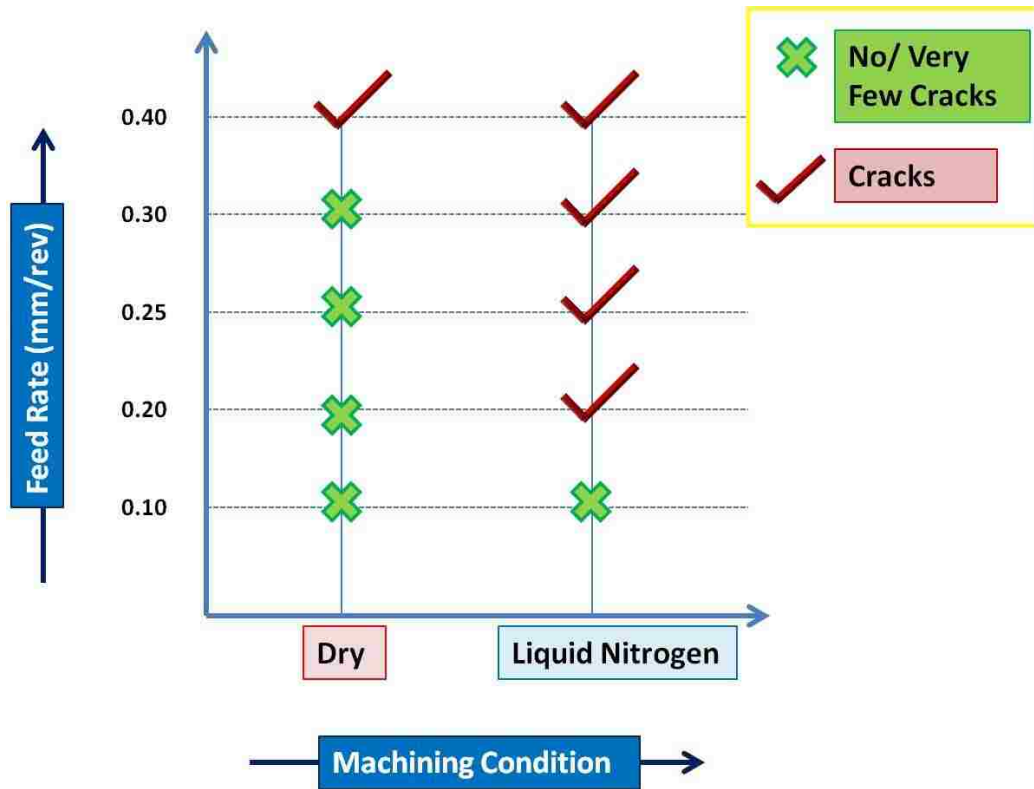
(d)

**Figure 4.5** Cross sectional optical image of material ahead of tool tip of Ti-6Al-4V alloy subjected to orthogonal cutting at a cutting speed of 43.2m/min where (a) in dry condition and at feed rates of 0.17mm/rev, (b) in dry condition and at feed rates of 0.22mm/rev (c) in cryogenic condition and at feed rates of 0.12mm/rev and (d) in cryogenic condition and at feed rates of 0.38 mm/rev.

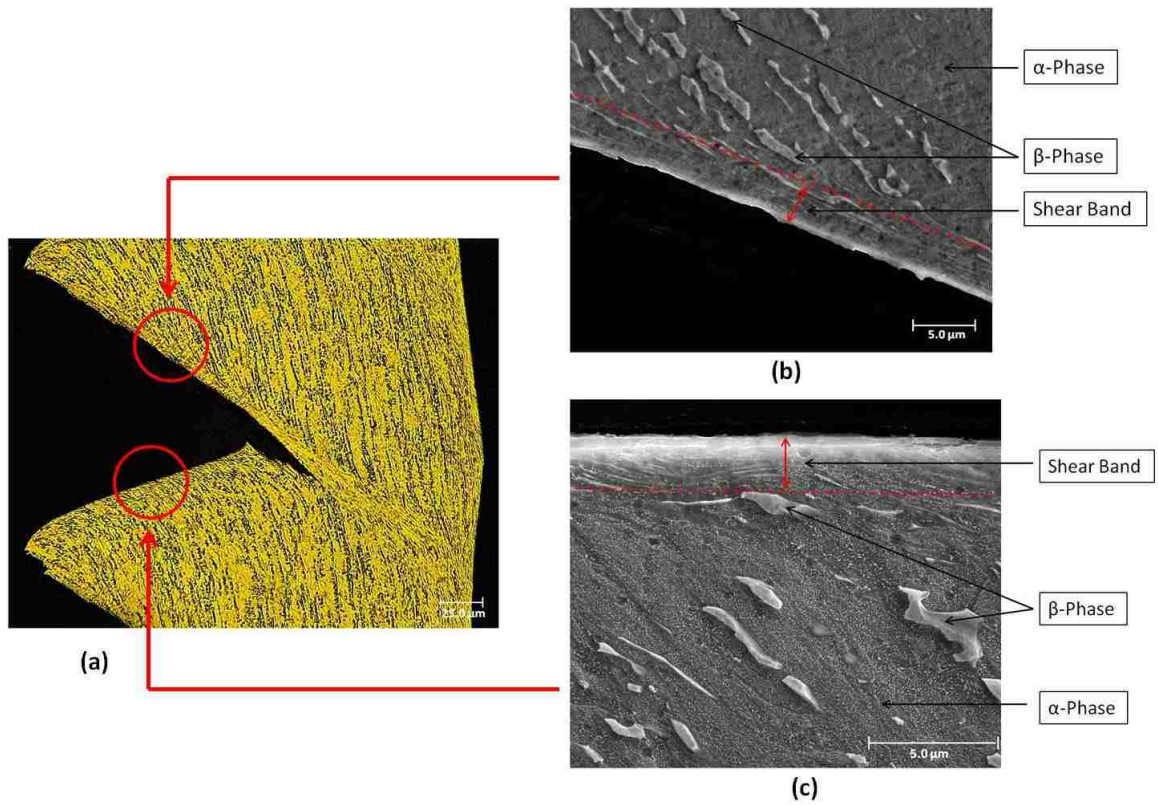
Cryogenic Condition	Dry Condition
<p data-bbox="324 436 389 487">No Cracks</p>  <p data-bbox="560 642 716 663">Feed Rate- 0.12 mm/rev</p> <p data-bbox="548 705 581 739">(a)</p>	<p data-bbox="941 424 1006 474">No Cracks</p>  <p data-bbox="1144 646 1291 667">Feed Rate- 0.09 mm/rev</p> <p data-bbox="1136 705 1169 739">(b)</p>
<p data-bbox="373 894 454 924">Cracks</p>  <p data-bbox="532 1197 738 1218">Feed Rate- 0.18mm/rev</p> <p data-bbox="548 1264 581 1297">(c)</p>	<p data-bbox="958 966 1039 1016">No Cracks</p>  <p data-bbox="1112 1201 1318 1222">Feed Rate- 0.17mm/rev</p> <p data-bbox="1136 1268 1169 1302">(d)</p>
<p data-bbox="373 1524 454 1554">Cracks</p>  <p data-bbox="532 1743 714 1764">Feed Rate- 0.24mm/rev</p> <p data-bbox="548 1801 581 1835">(e)</p>	<p data-bbox="933 1516 1047 1566">Very Few Cracks</p>  <p data-bbox="1120 1747 1312 1768">Feed Rate- 0.22mm/rev</p> <p data-bbox="1136 1806 1169 1839">(f)</p>



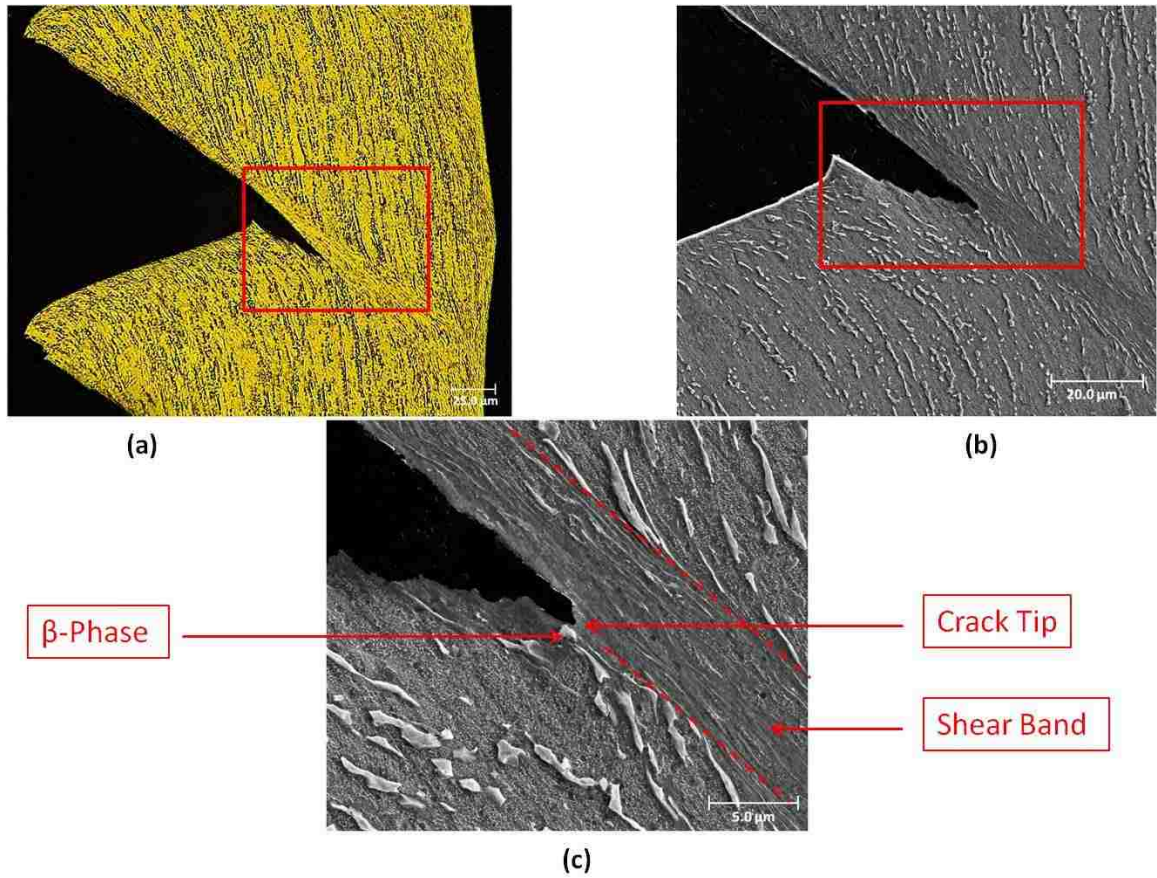
**Figure 4.6** Serrated chips formed during machining of Ti-6Al-4V alloy at a cutting speed of 43.2m/min and at feed rates of (a) 0.12 mm/rev, (c) 0.18 mm/rev, (e) 0.24 mm/rev, (g) 0.26 mm/rev and (i) 0.38 mm/rev in cryogenic conditions and (b) 0.09 mm/rev, (d) 0.17 mm/rev, (f) 0.22 mm/rev, (h) 0.26 mm/rev and (j) 0.32 mm/rev in dry conditions where their differences in terms of cracking tendency is shown.



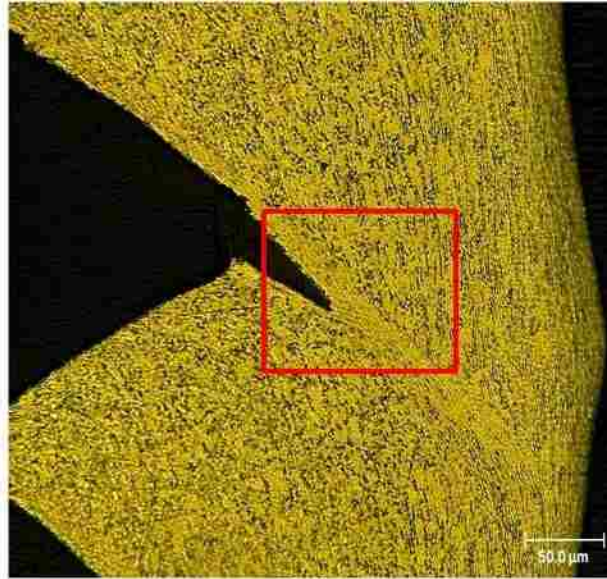
**Figure 4.7** Summary of cracking tendency of serrated chips formed during machining of Ti-6Al-4V alloy in dry and cryogenic condition, at a cutting speed of 43.2m/min and at comparable feed rates.



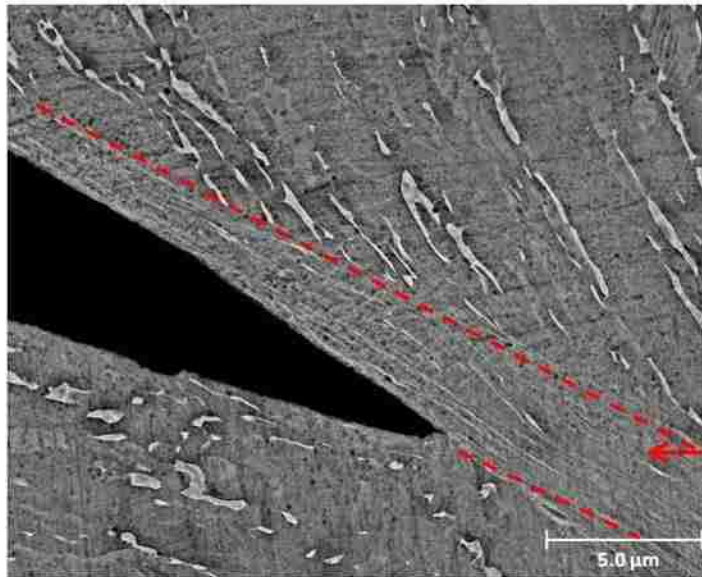
**Figure 4.8** Optical image showing (a) surfaces of serrated chip, formed during Ti-6Al-4V alloy machining in the cryogenic condition at a cutting speed of 43.2m/min and at a feed rates of 0.38mm/rev where (b) and (c) are the SEM images of the corresponding regions shown with circles indicating that the surfaces are well within the shear band.



**Figure 4.9** (a) Optical image of wider cracked surface of serrated chip formed during Ti-6Al-4V alloy machining in the cryogenic condition, at a cutting speed of 43.2m/min and at a feed rates of 0.38mm/rev (b) low magnification SEM images and (c) high magnification SEM images of the wider cracked region indicating that the crack tip shifted towards the edge of the shear band.



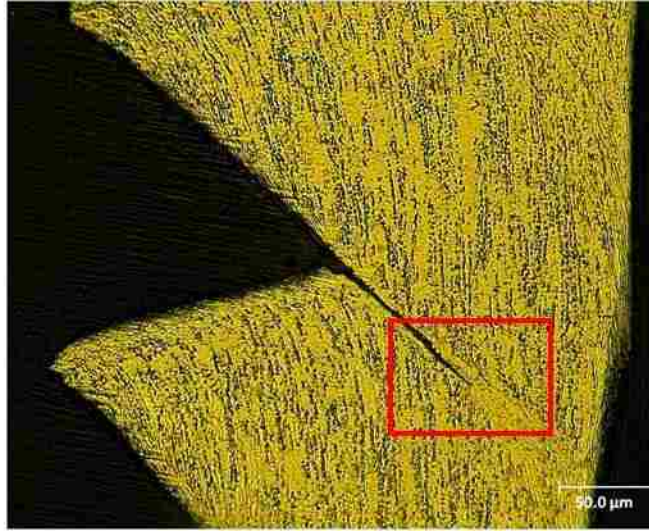
(a)



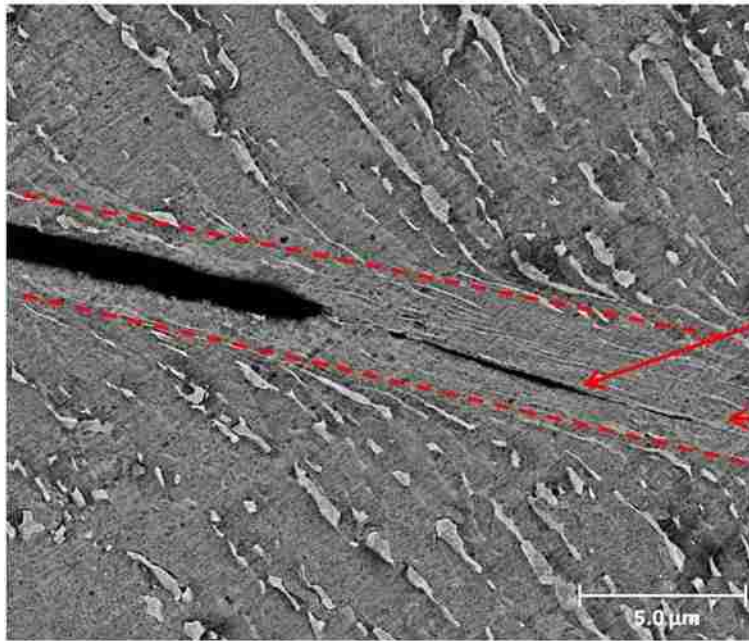
(b)

**Figure 4.10** (a) Optical image of wider cracked surface of serrated chip formed during Ti-6Al-4V alloy machining in dry condition, at a cutting speed of 43.2m/min and at a feed rates of 0.32mm/rev (b) backscattered SEM image of the wider cracked region indicating that the crack tip shifted towards the edge of shear band.





(a)

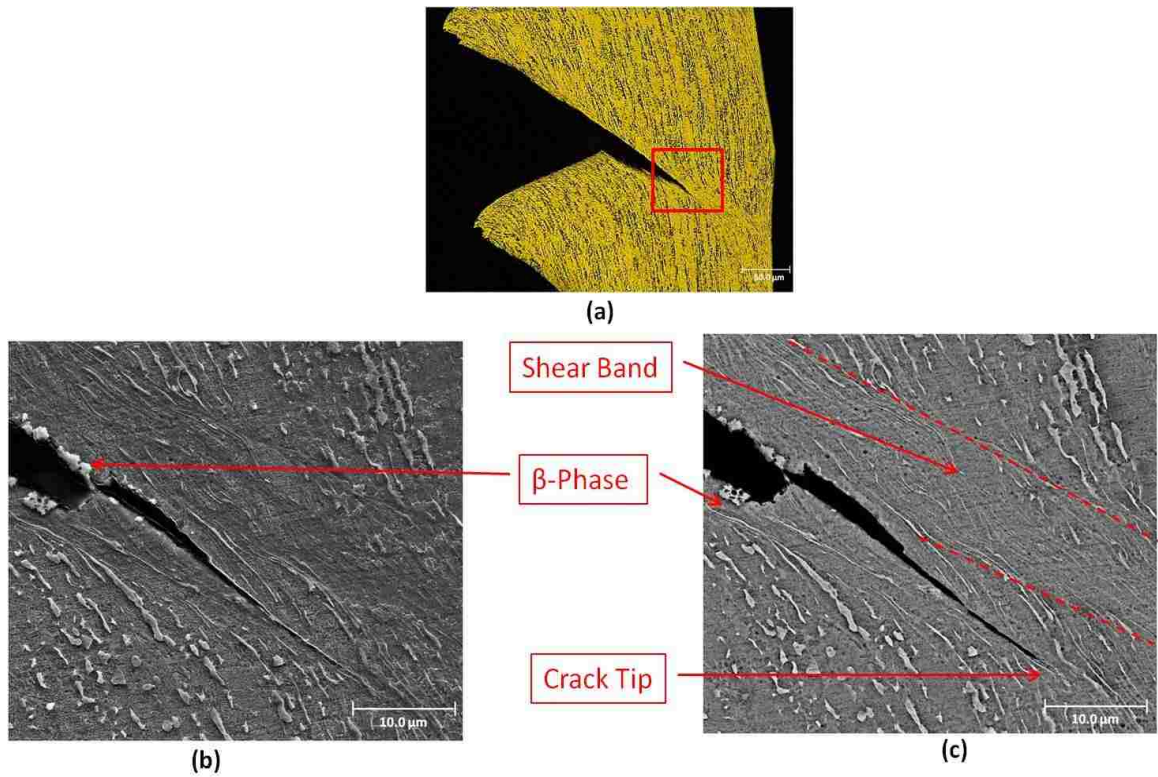


Crack

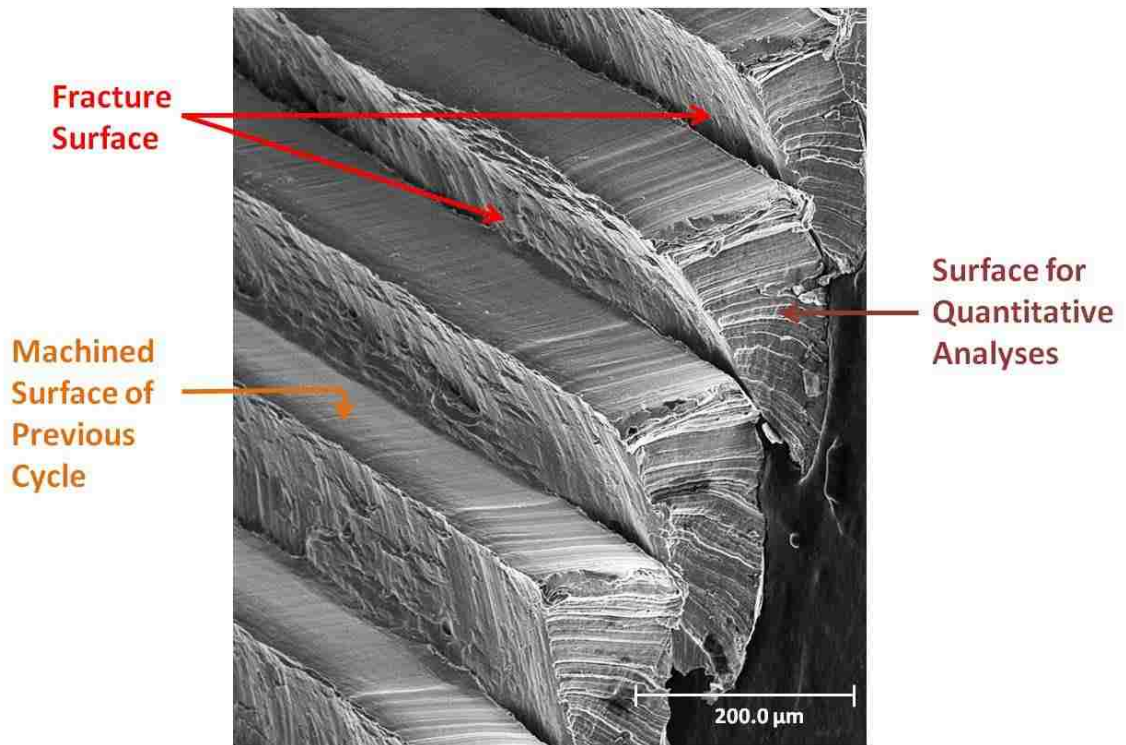
Shear Band

(b)

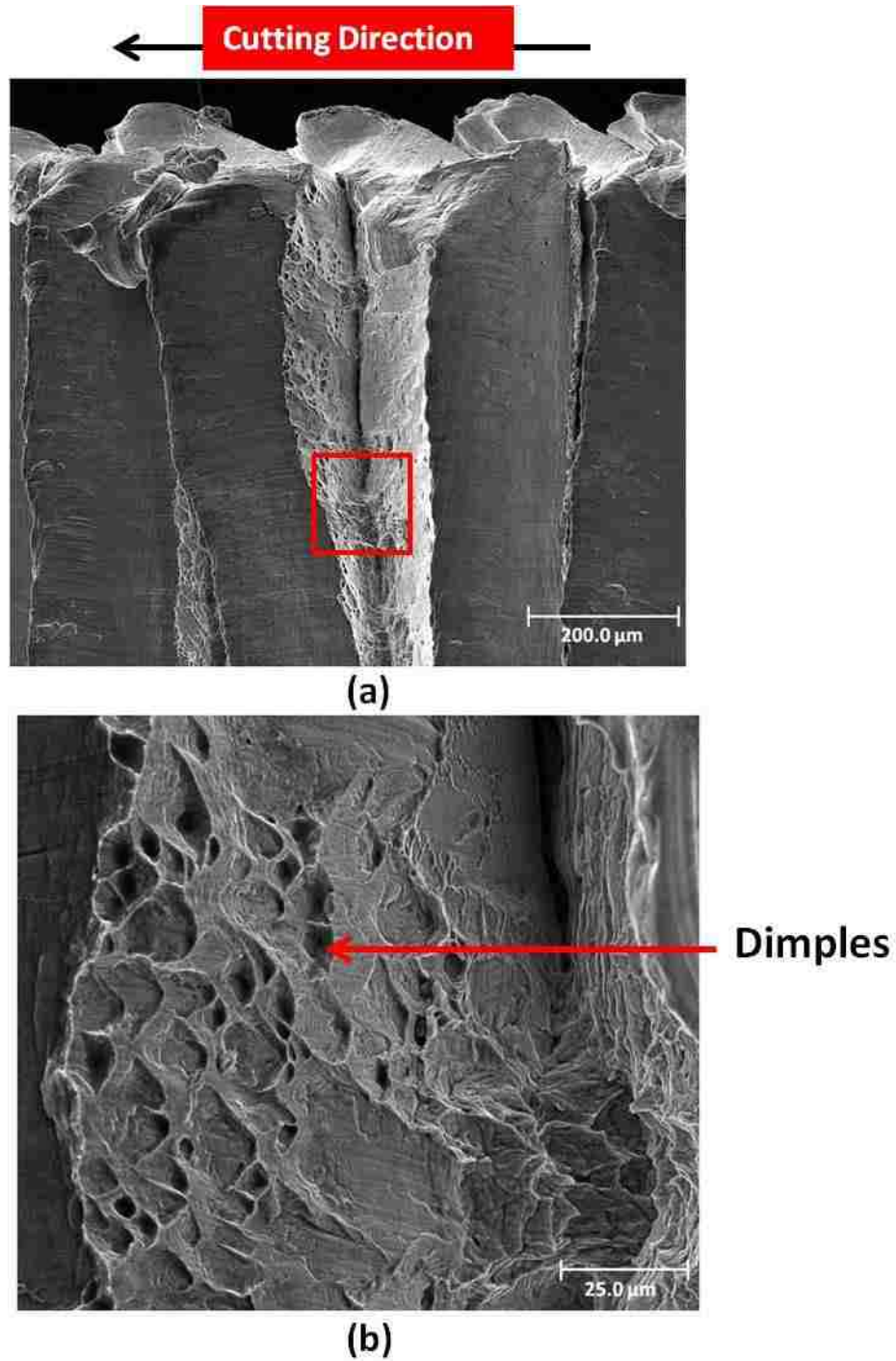
**Figure 4.11** (a) Optical image of narrow cracked surface of serrated chip formed during Ti-6Al-4V alloy machining in cryogenic condition, at a cutting speed of 43.2m/min and at a feed rates of 0.38mm/rev (b) backscattered SEM image of the narrow cracked region indicating that the cracked surface is well within the shear band.



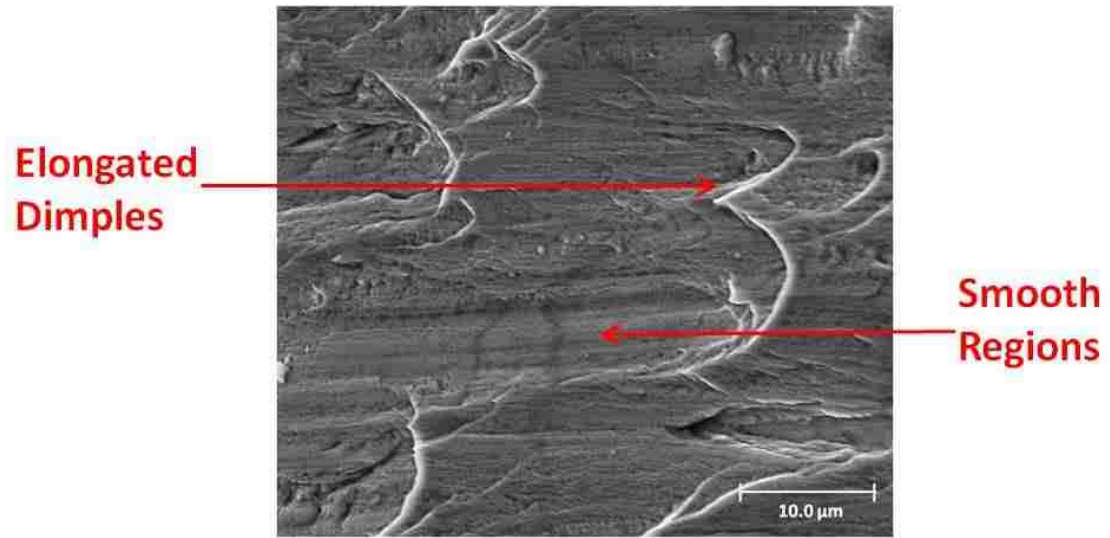
**Figure 4.12** (a) Optical image of wider cracked surface of serrated chip formed during Ti-6Al-4V alloy machining in cryogenic condition, at a cutting speed of 43.2m/min and at a feed rate of 0.38mm/rev where (b) secondary and (c) backscattered SEM images of the corresponding region showing that the cracked surface moved out of the shear band and fractured beta particle.



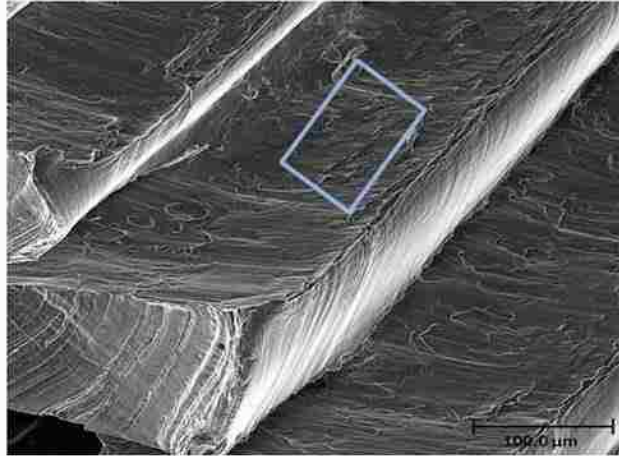
**Figure 4.13** Different regions of interest indicated in the SEM image of serrated chips formed during Ti-6Al-4V alloy machining in cryogenic condition, at a cutting speed of 43.2m/min and at a feed rate of 0.24mm/rev.



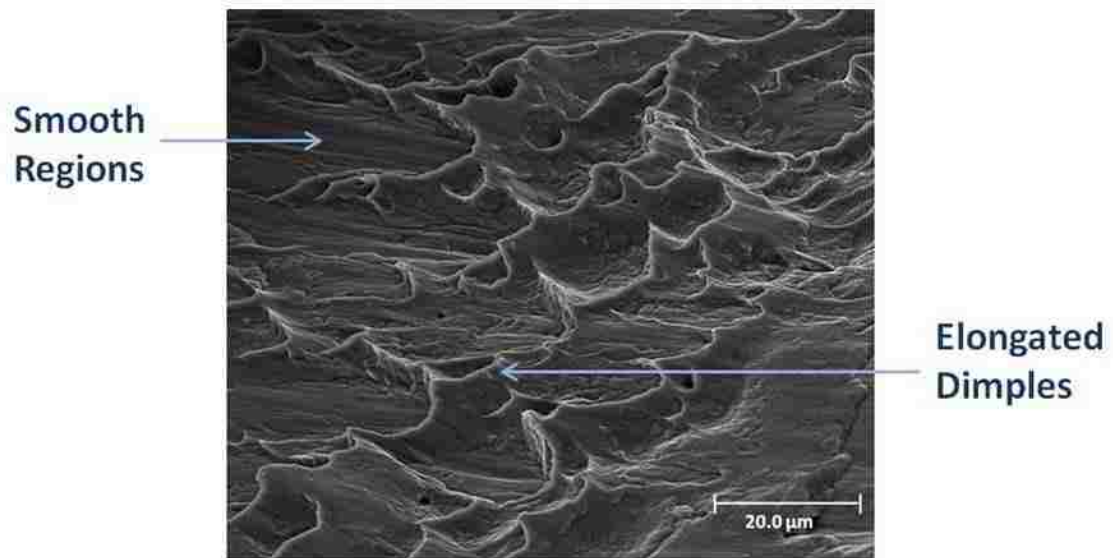
**Figure 4.14** (a) SEM image of a serrated chip of Ti-6Al-4V alloy machined in the dry condition, at a cutting speed of 43.2m/min and at a feed rate of 0.32mm/rev showing the region of fracture surface from which higher magnification image was taken and (b) High magnification SEM image showing a dimple type fractured surface.



**Figure 4.15** SEM image showing elongated dimples as well as comparatively smooth regions in the fracture surface of Ti-6Al-4V alloy machined in dry condition, at a cutting speed of 43.2m/min and at a feed rate of 0.32mm/rev.

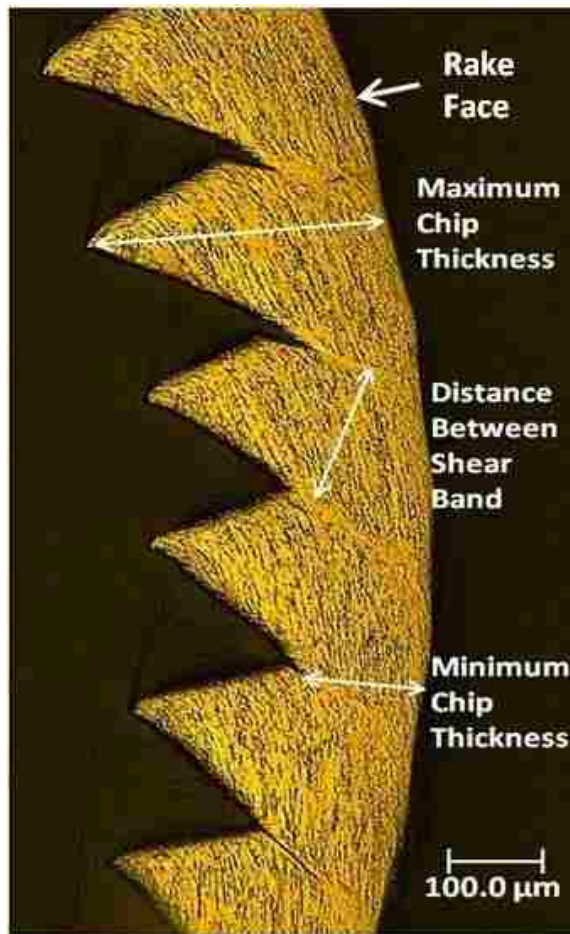


(a)

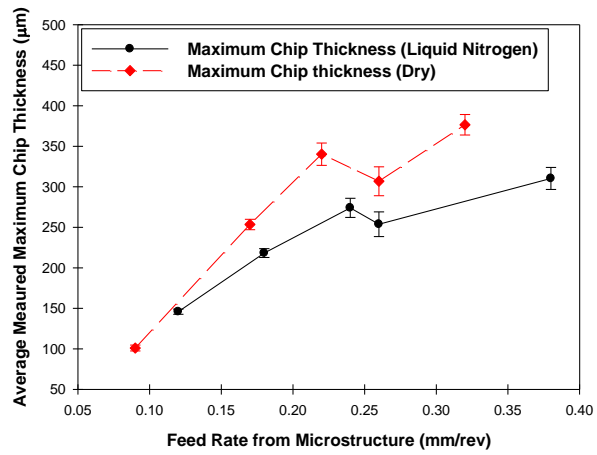


(b)

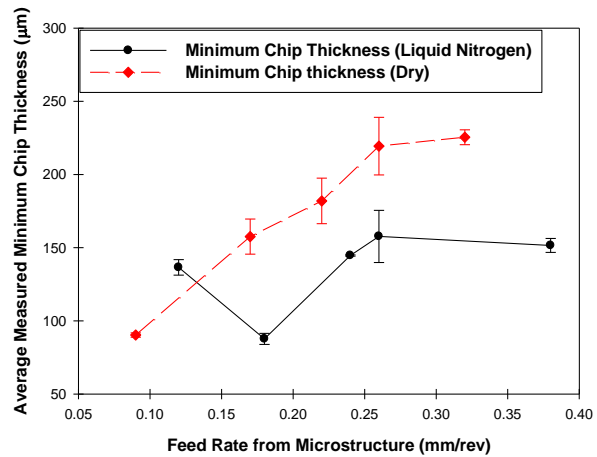
**Figure 4.16** (a) SEM image of serrated chip of Ti-6Al-4V alloy machined in the cryogenic condition, at a cutting speed of 43.2m/min and at a feed rate of 0.24mm/rev showing the region of fracture surface from which higher magnification image was taken and (b) High magnification SEM image showing elongated dimples as well as comparatively smooth regions within the fractured surface of Ti-6Al-4V alloy.



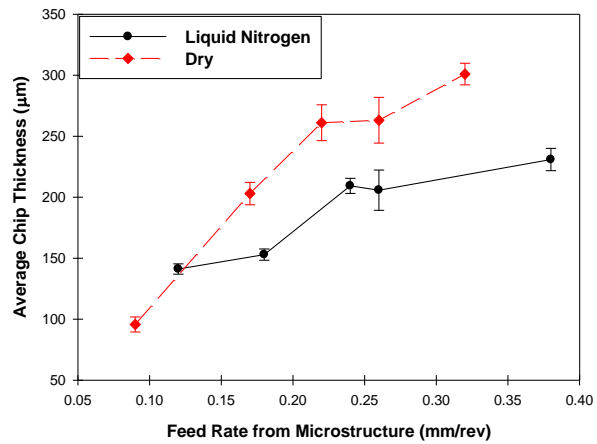
**Figure 4.17** Optical image of serrated chips obtained during machining in cryogenic condition at a cutting speed of 43.2m/min and at a feed rate of 0.38mm/rev indicating the procedure for measuring maximum, minimum chip thickness and distance between shear bands. Maximum and minimum chip thickness lines are perpendicular to the rake face whereas the line representing the distance between the shear band is also perpendicular to the shear bands.



(a)



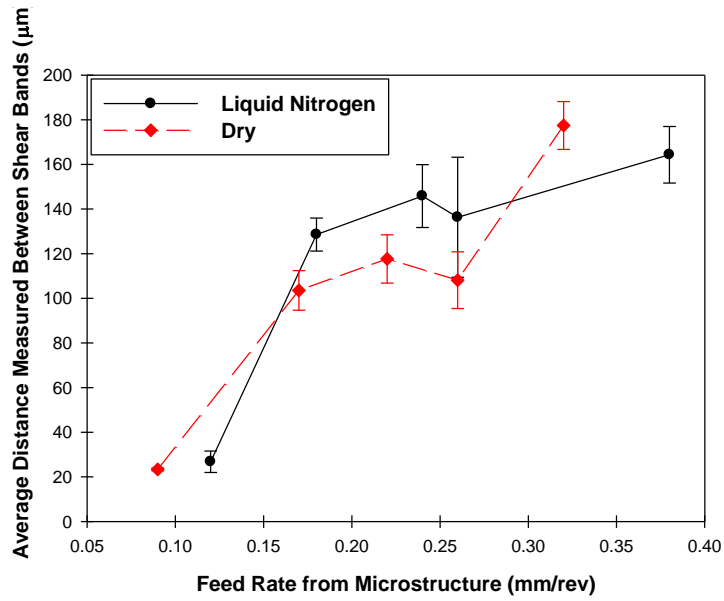
(b)



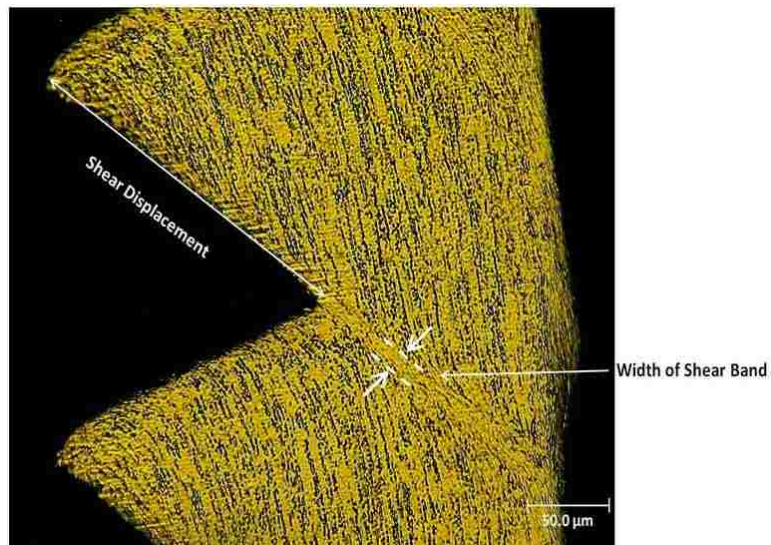
(c)

**Figure 4.18** Variation of chip thickness with feed rates (measured from microstructures) at a cutting speed of 43.2m/min in dry and cryogenic conditions where (a) shows maximum chip thickness, (b) shows minimum chip thickness and (c) shows average chip thickness.

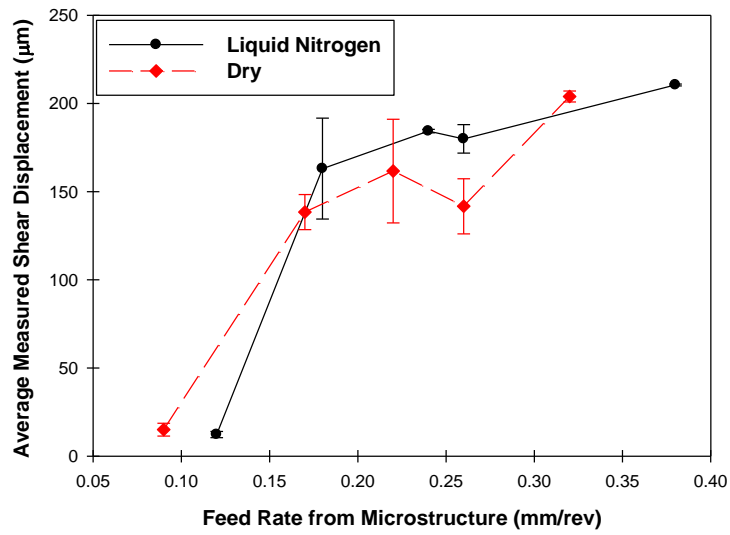




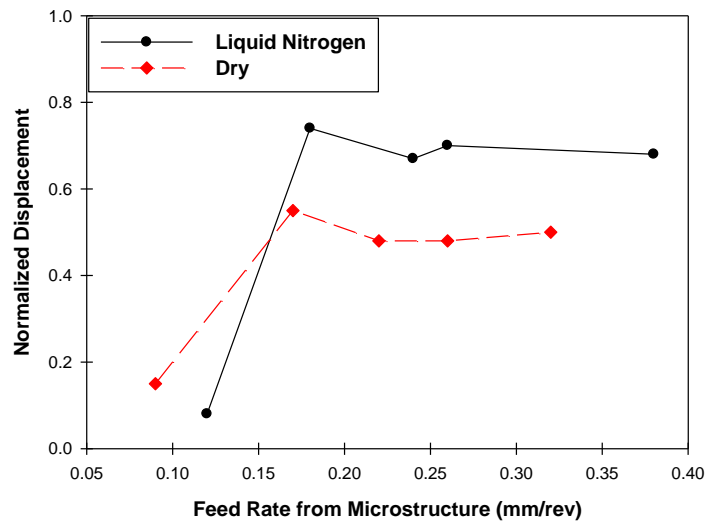
**Figure 4.19** Variation of the average distance between two consecutive shear bands with feed rates (measured from microstructures) at a cutting speed of 43.2m/min in dry and cryogenic conditions.



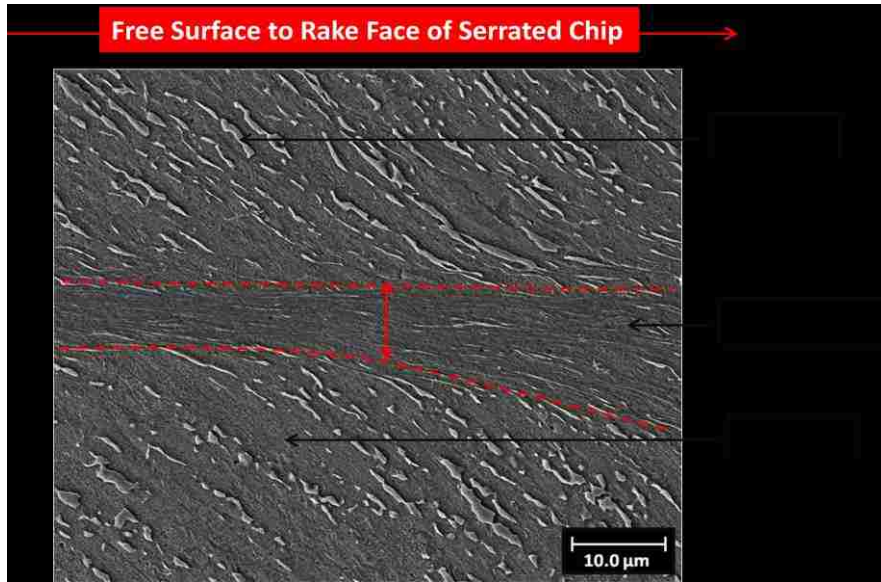
**Figure 4.20** Optical image of serrated chips obtained during machining in cryogenic condition at a cutting speed of 43.2m/min and at a feed rate of 0.38mm/rev indicating the procedure of measuring shear displacement and width of shear bands.



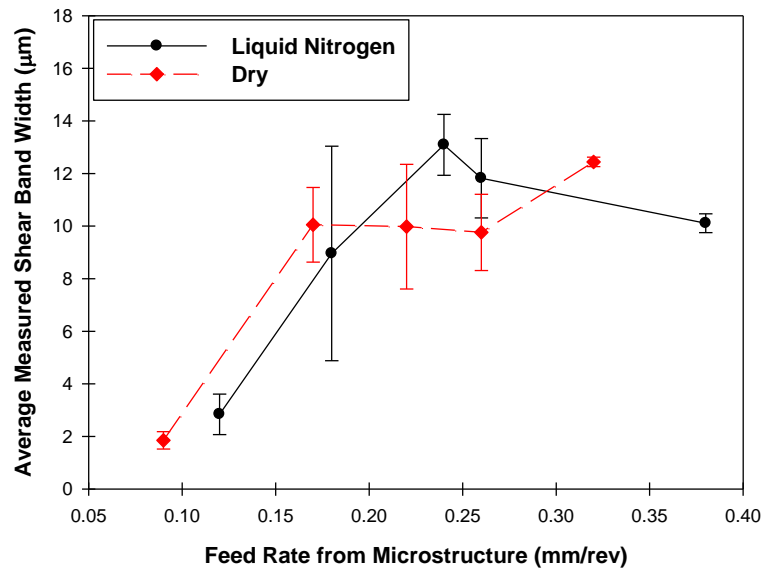
**Figure 4.21** Variation of average shear displacement with feed rates (measured from microstructures) at a cutting speed of 43.2m/min in dry and cryogenic conditions.



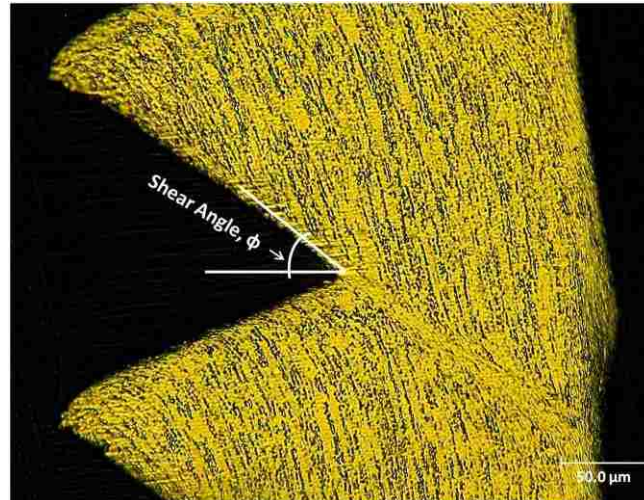
**Figure 4.22** Variation of normalized displacement with feed rates (measured from microstructures) at a cutting speed of 43.2m/min in dry and cryogenic conditions.



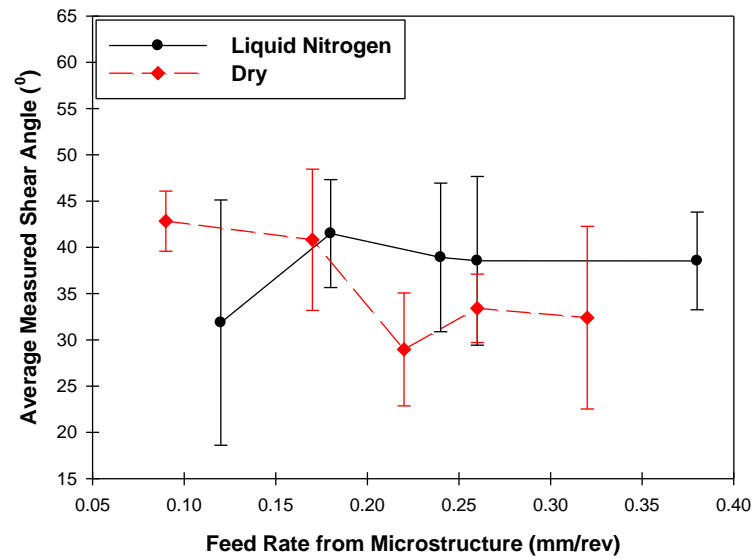
**Figure 4.23** SEM image of serrated chips obtained during machining in cryogenic condition at a cutting speed of 43.2m/min and at a feed rate of 0.38mm/rev showing the variation of shear band width from free surface towards the rake face of the chip.



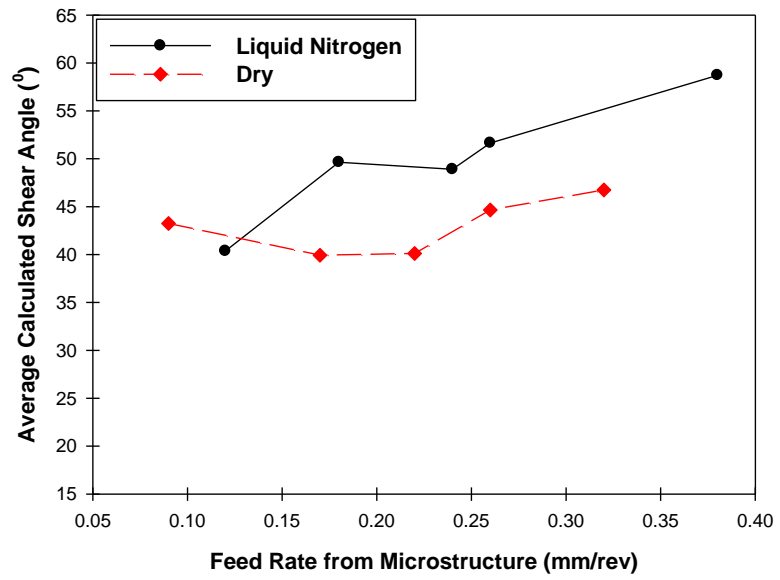
**Figure 4.24** Variation of average shear band width with feed rates (measured from microstructures) at a cutting speed of 43.2m/min in dry and cryogenic conditions.



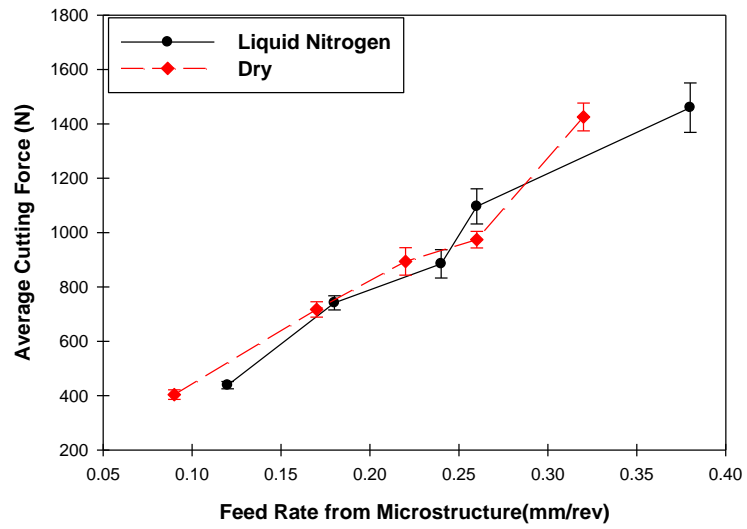
**Figure 4.25** Optical image of serrated chips obtained during machining in cryogenic condition at a cutting speed of 43.2m/min and at a feed rate of 0.38mm/rev indicating the method of measuring the shear angle.



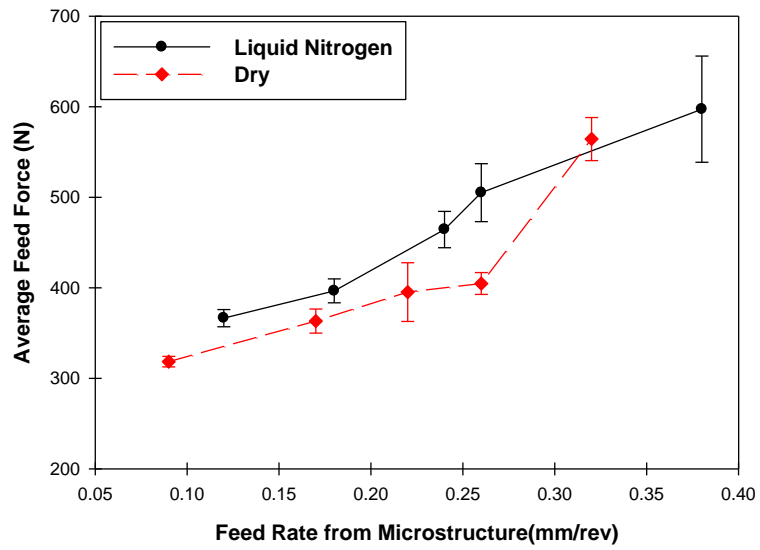
**Figure 4.26** Variation of the average shear angle with feed rates (measured from microstructures) at a cutting speed of 43.2m/min in dry and cryogenic conditions.



**Figure 4.27** Variation of average shear angle calculated from Equation (4.4) with feed rate at a cutting speed of 43.2m/min in dry and cryogenic conditions.

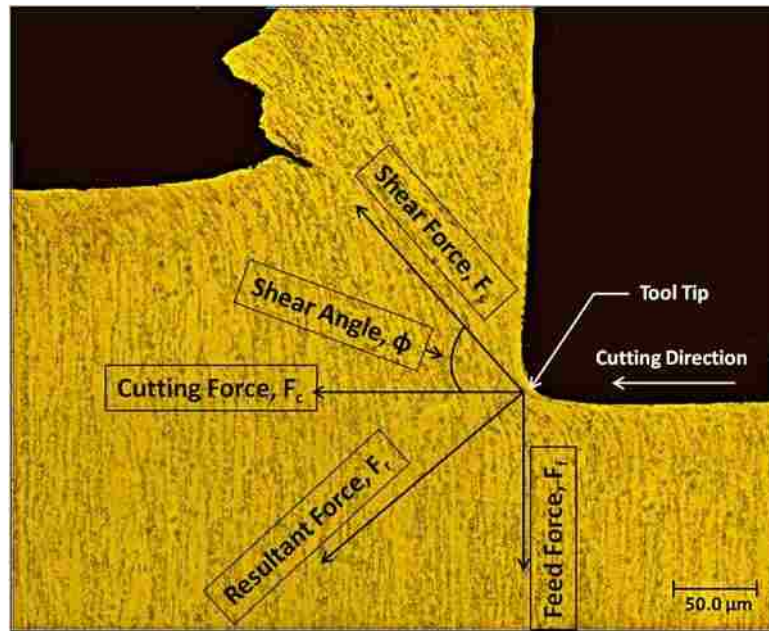


(a)

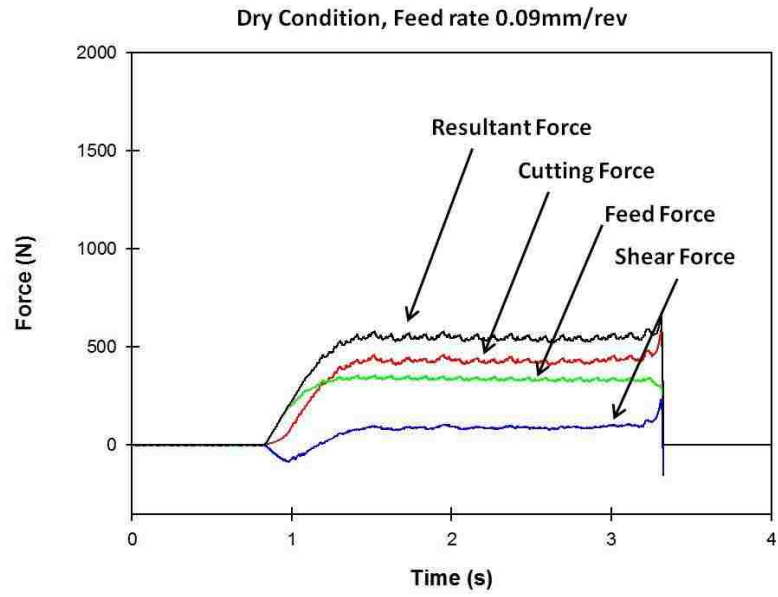


(b)

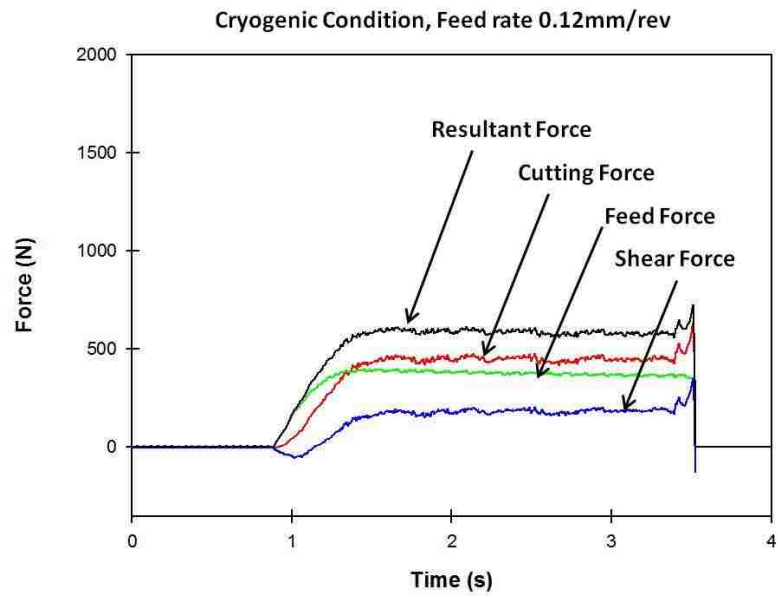
**Figure 4.28** Variation of (a) average cutting force and (b) average feed force with feed rates at a cutting speed of 43.2m/min in dry and cryogenic conditions.



**Figure 4.29** Direction of the different forces that act on the material during orthogonal cutting.

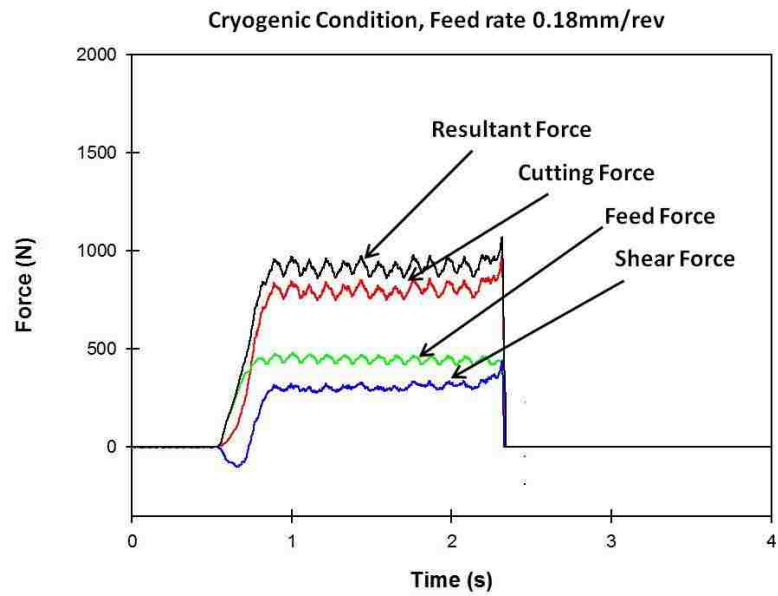
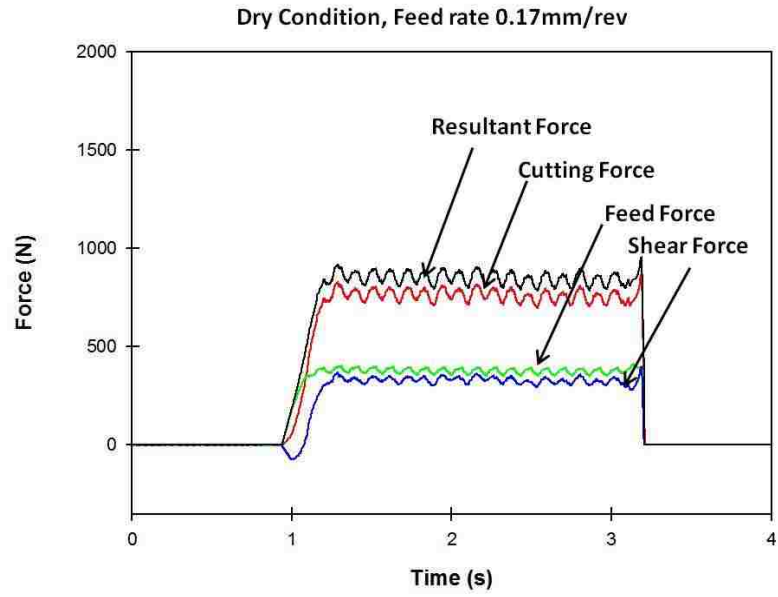


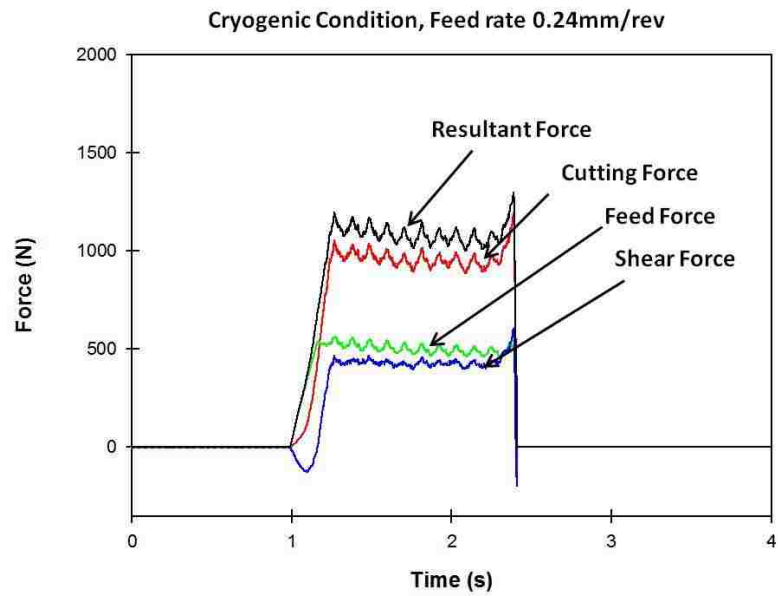
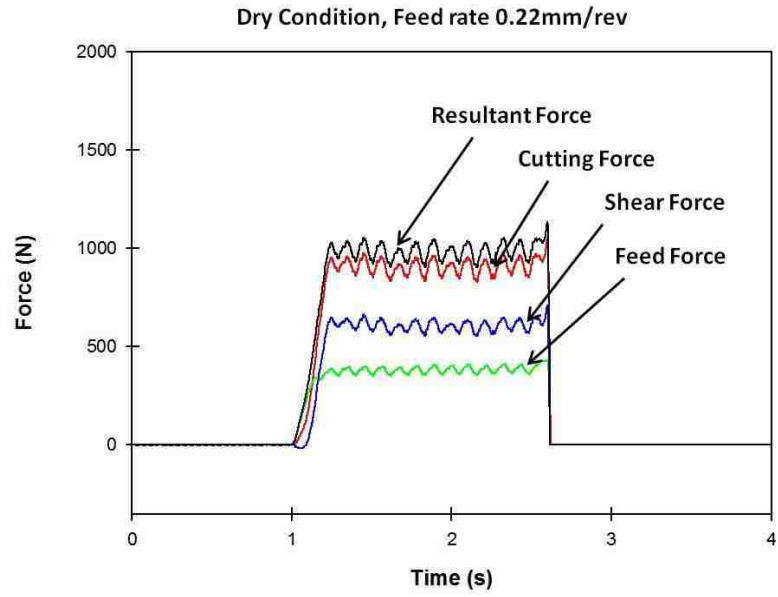
(a)

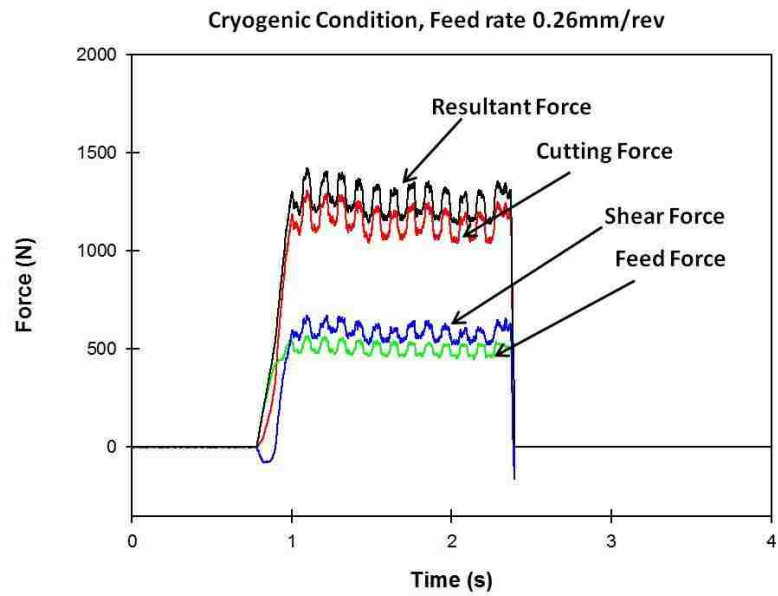
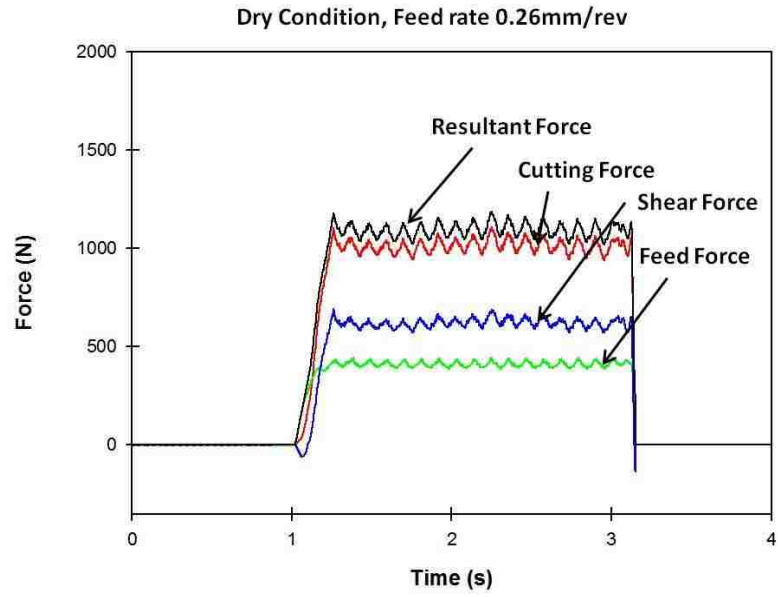


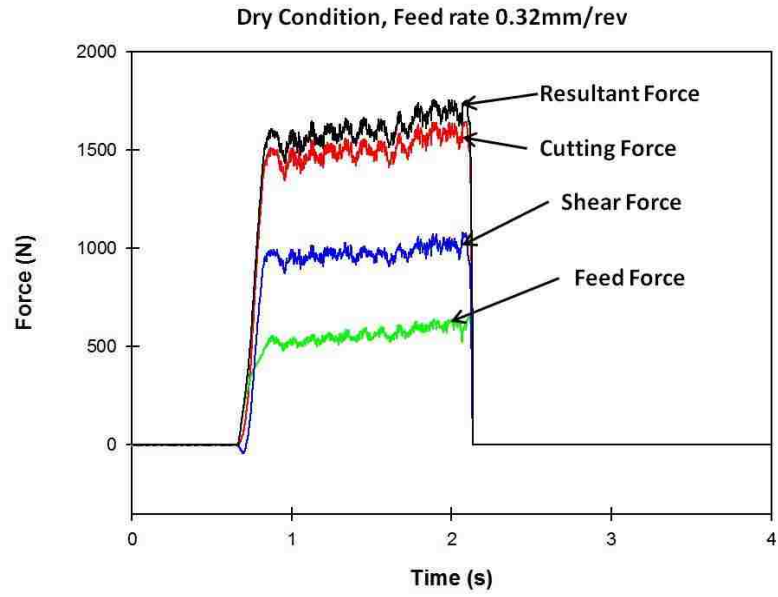
(b)



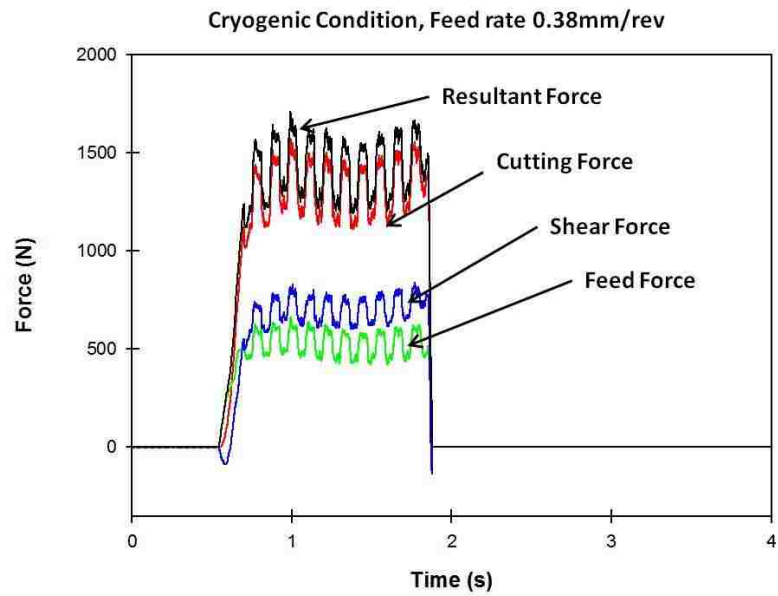






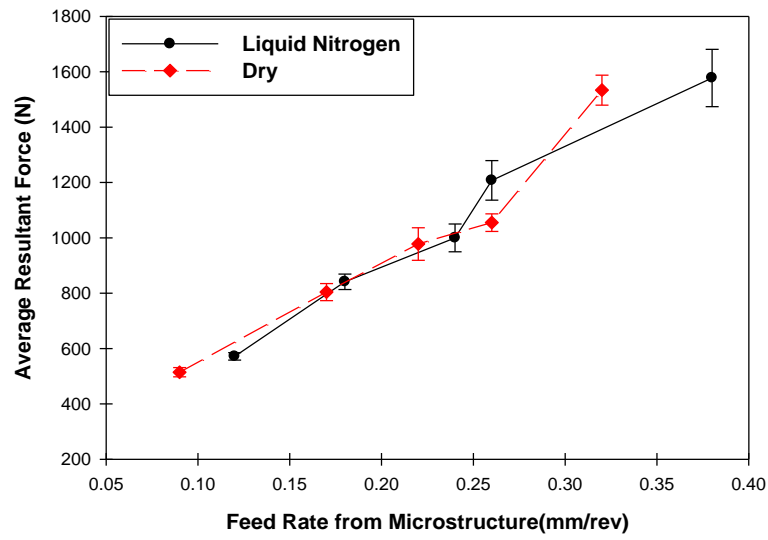


(i)

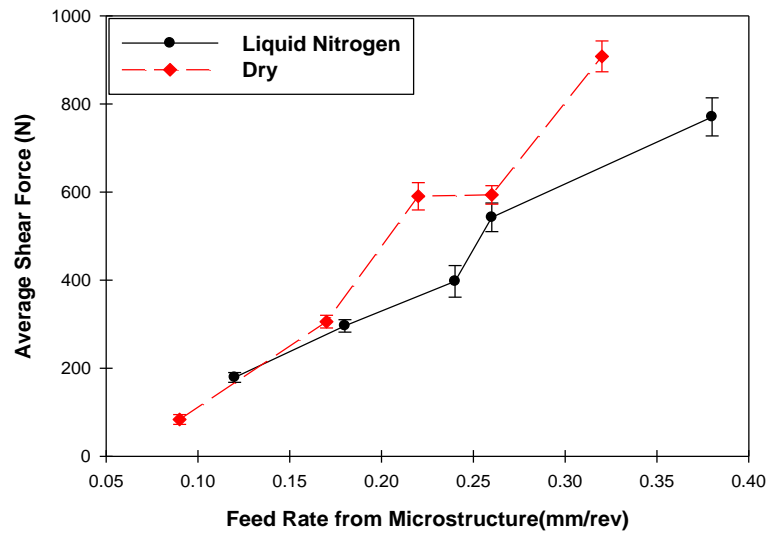


(j)

**Figure 4.30** Comparison of different type of forces of dry and cryogenic conditions at cutting speed of 43.2m/min and at various feed rates.



(a)



(b)

**Figure 4.31** Variation of (a) average resultant force and (b) average shear force with the feed rate at a cutting speed of 43.2m/min in dry and cryogenic conditions.

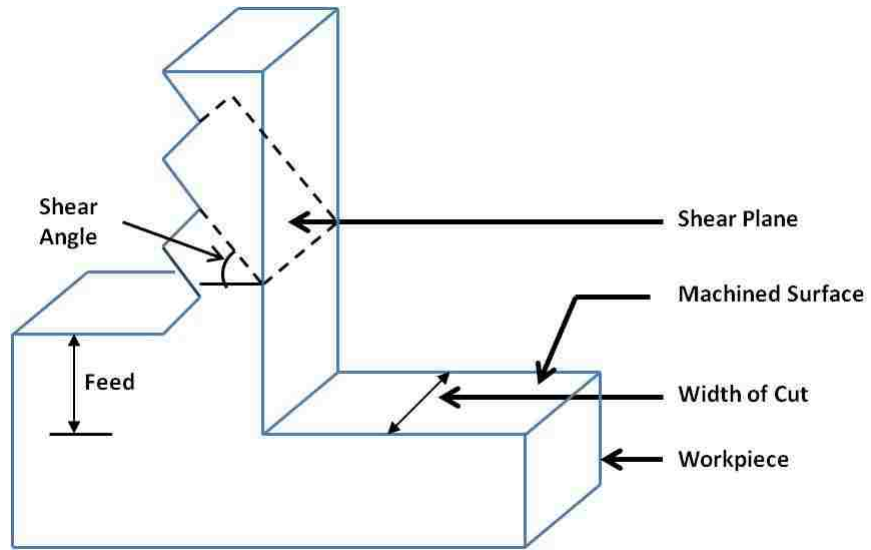


Figure 4.32 Schematic diagram to demonstrate shear plane.

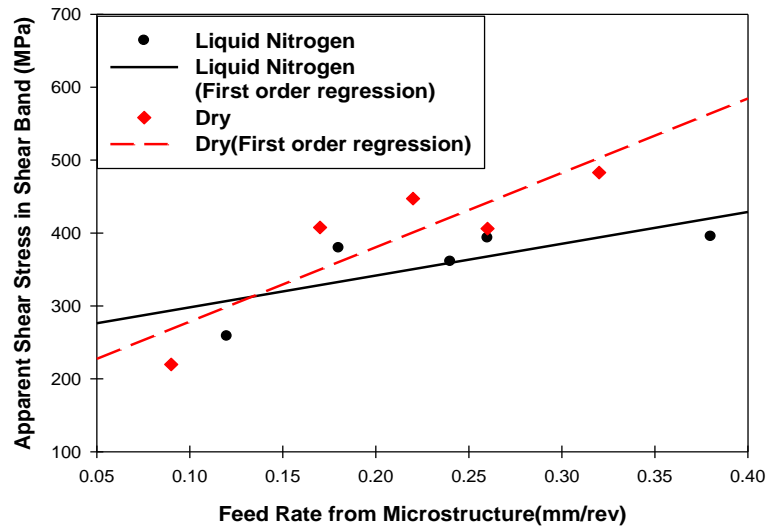
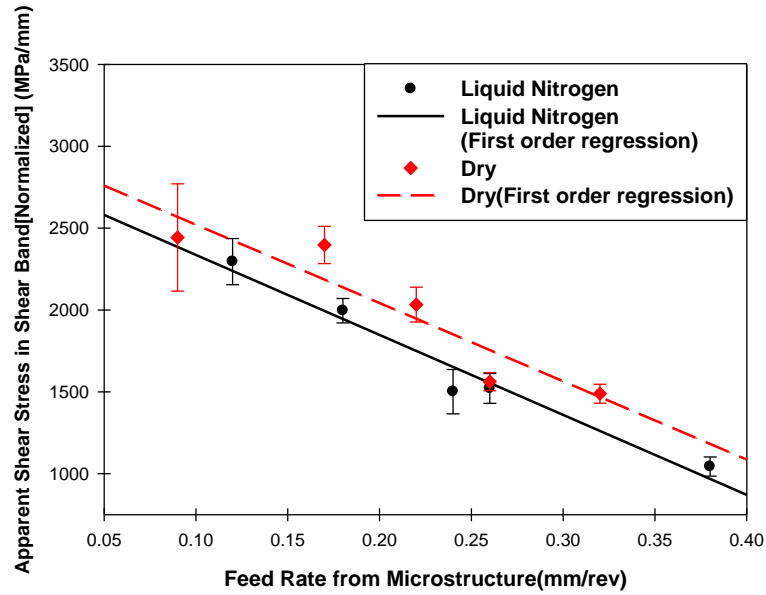
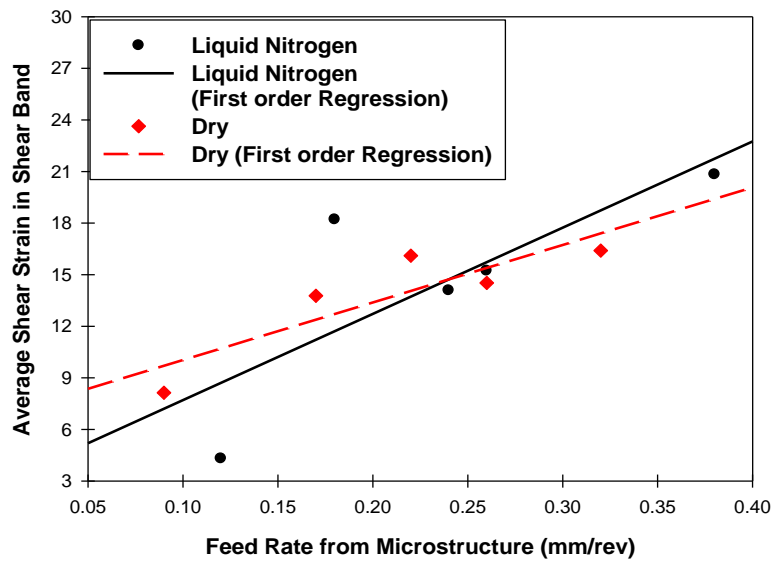


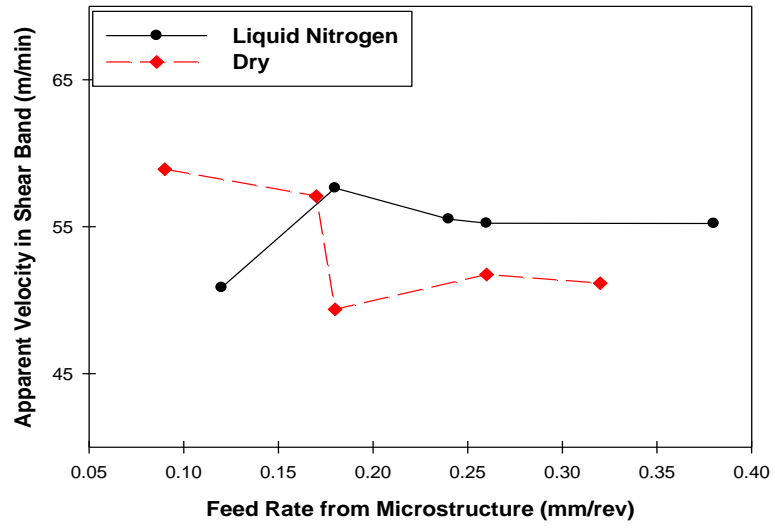
Figure 4.33 Variation of the apparent shear stress in shear band with the feed rate at a cutting speed of 43.2m/min in dry and cryogenic conditions.



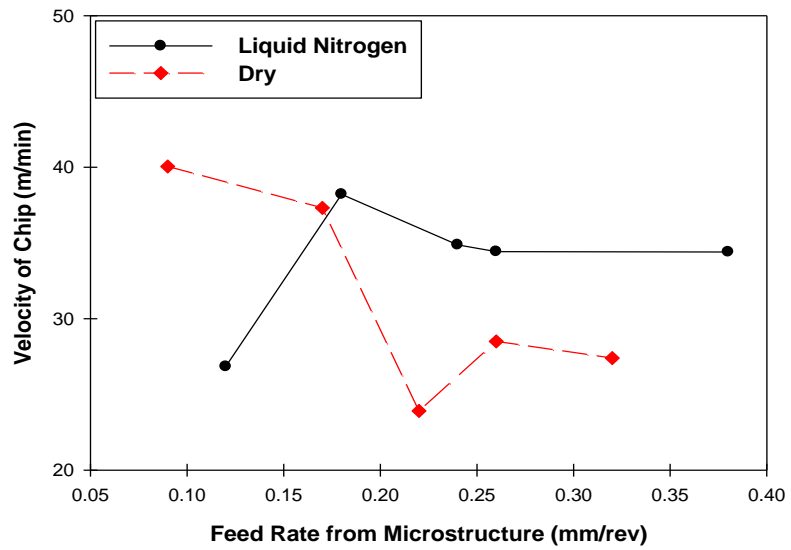
**Figure 4.34** Variation of apparent normalized shear stress in the shear band [normalized with respect to feed] with the feed rate at a cutting speed of 43.2m/min in dry and cryogenic conditions.



**Figure 4.35** Variation of the average shear strain in the shear band with the feed rate at a cutting speed of 43.2m/min in dry and cryogenic conditions.



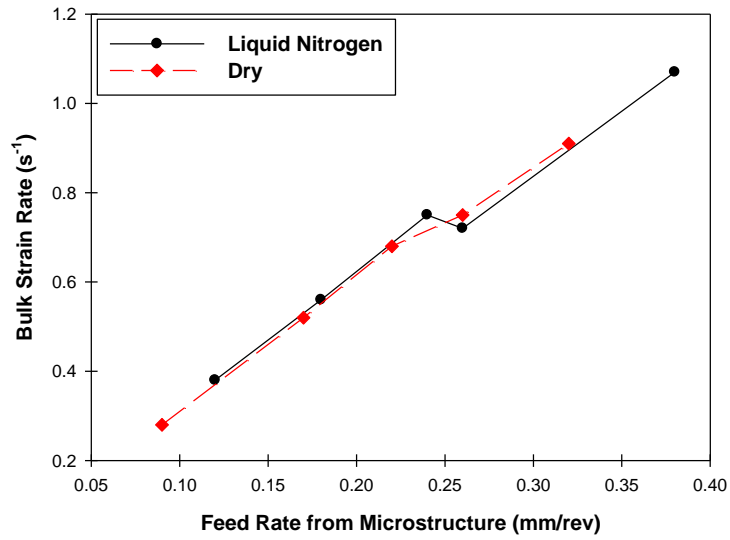
(a)



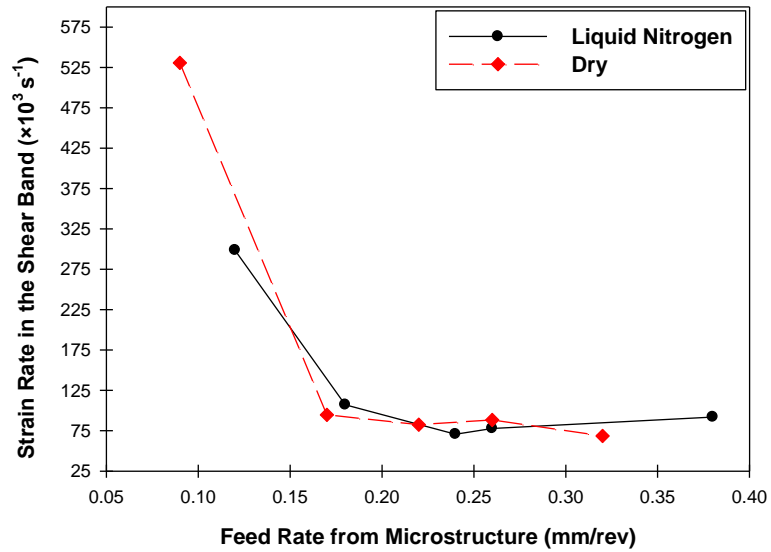
(b)

**Figure 4.36** Variation of (a) apparent velocity in the shear band and (b) velocity of chip with the feed rate at a cutting speed of 43.2m/min in dry and cryogenic conditions.

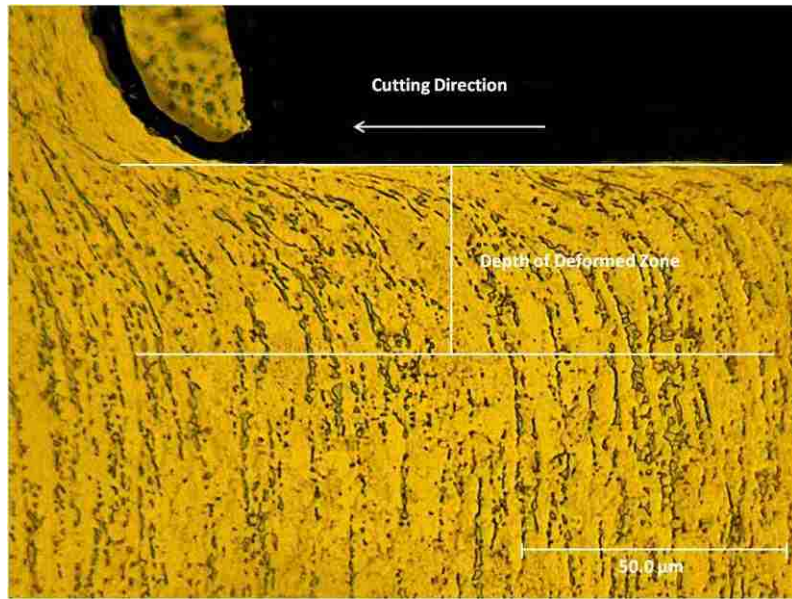




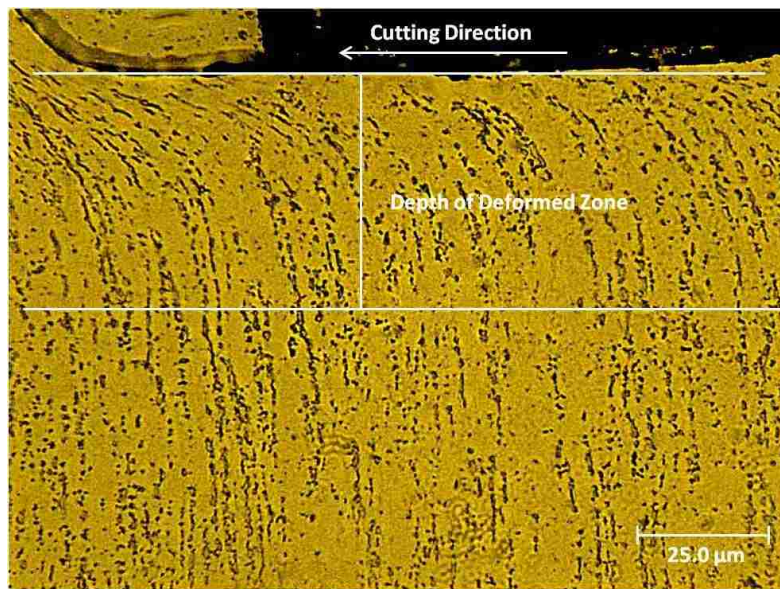
**Figure 4.37** Variation of the bulk strain rate with the feed rate at a cutting speed of 43.2m/min in dry and cryogenic conditions.



**Figure 4.38** Variation of (a) the average resultant force and (b) the average shear force with the feed rate at a cutting speed of 43.2m/min in dry and cryogenic conditions.

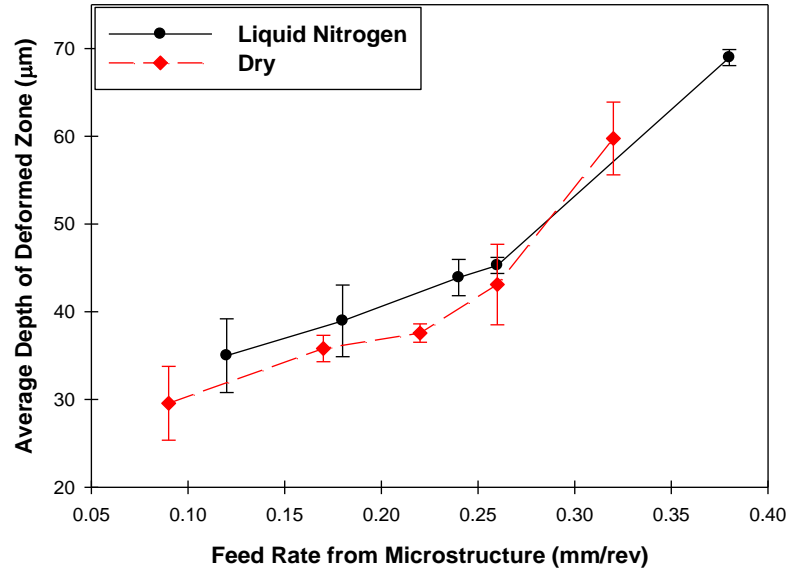


(a)



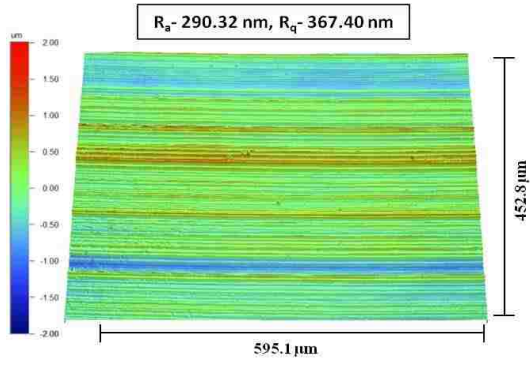
(b)

**Figure 4.39** Optical image of subsurface deformation at a cutting speed of 43.2m/min where (a) in the dry condition and at a feed rate of 0.17mm/rev and (b) in the cryogenic condition and at a feed rate of 0.26mm/rev.



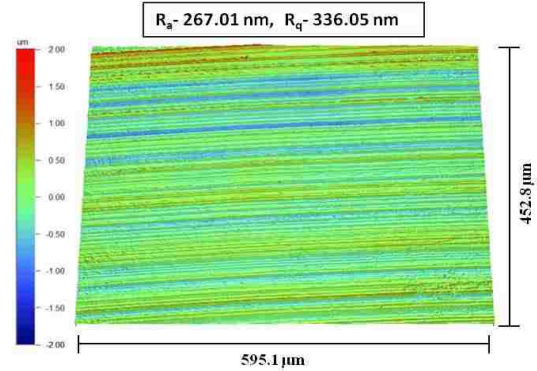
**Figure 4.40** Variation of average depth of deformed zone (measured from microstructure) with the feed rate at a cutting speed of 43.2m/min in dry and cryogenic conditions.

## Cryogenic Condition

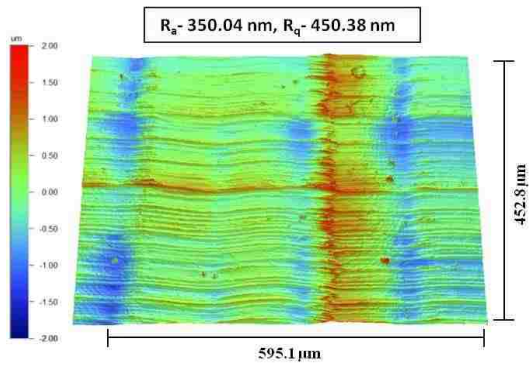


Feed Rate- 0.12 mm/rev

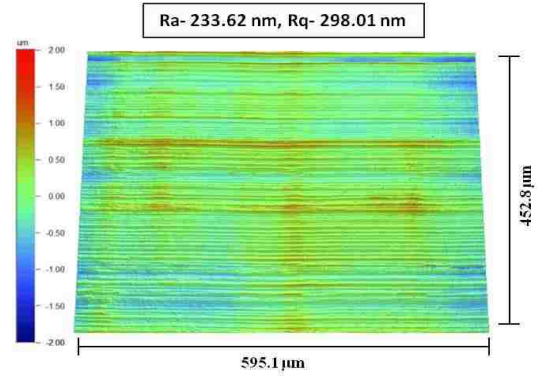
## Dry Condition



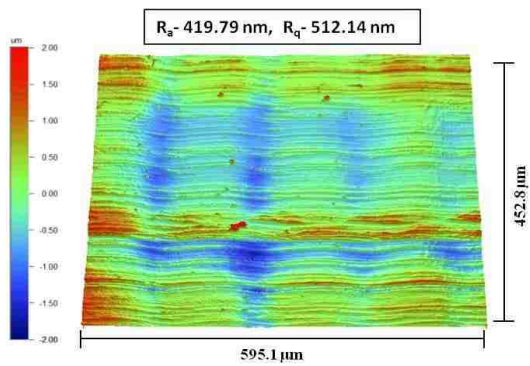
Feed Rate- 0.09 mm/rev



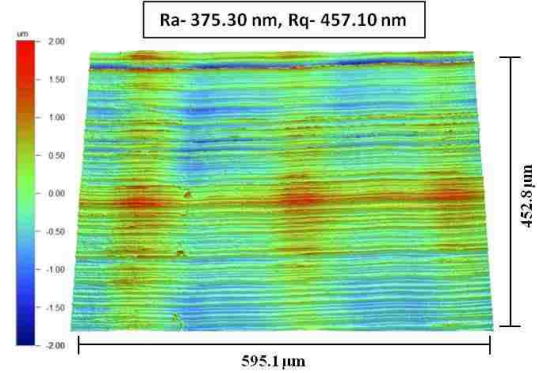
Feed Rate- 0.18 mm/rev



Feed Rate- 0.17 mm/rev

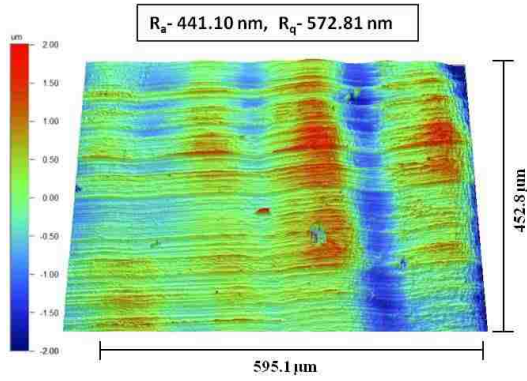


Feed Rate- 0.24 mm/rev



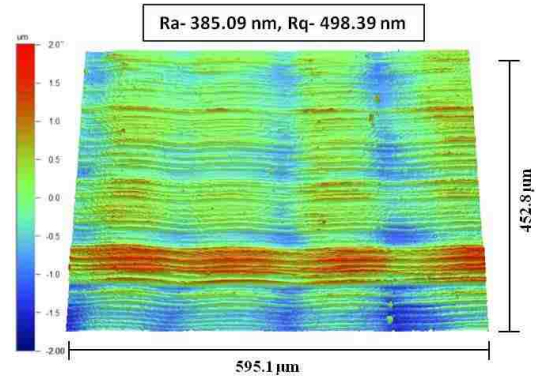
Feed Rate- 0.22 mm/rev

## Cryogenic Condition

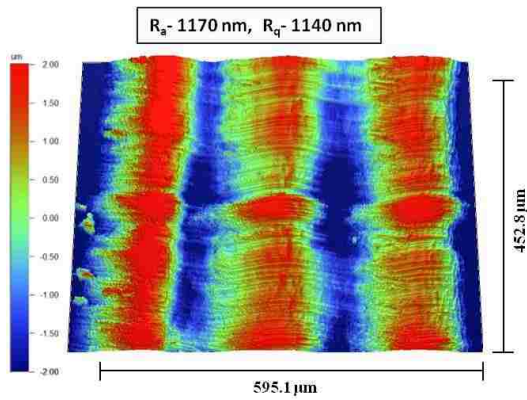


Feed Rate- 0.26mm/rev

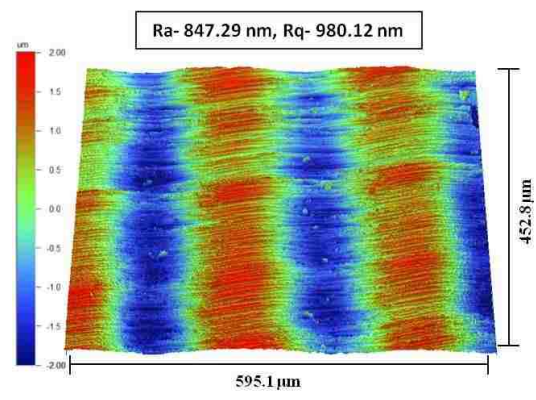
## Dry Condition



Feed Rate- 0.26mm/rev

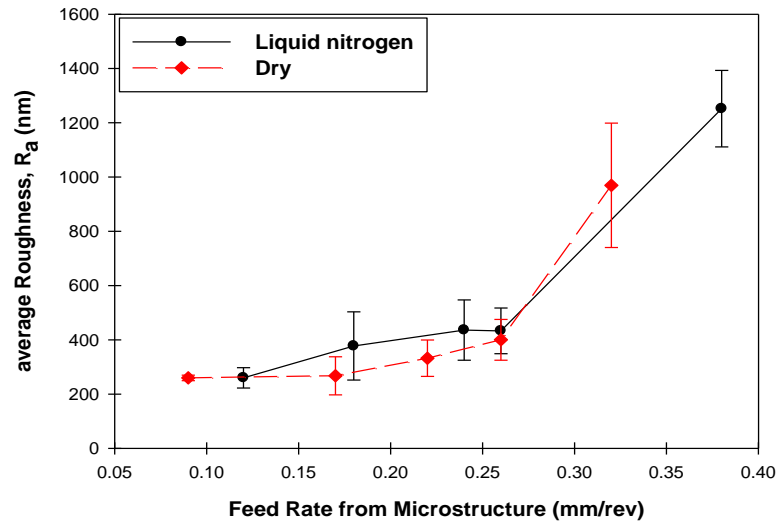


Feed Rate- 0.38 mm/rev

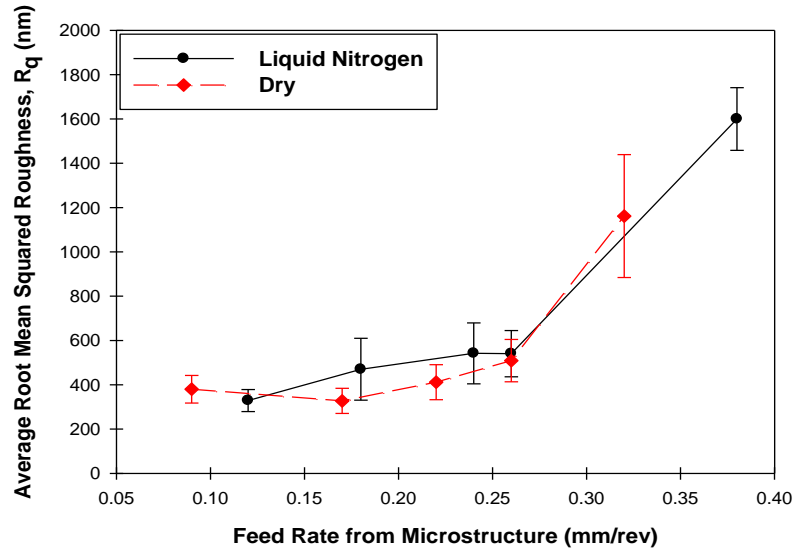


Feed Rate- 0.32 mm/rev

**Figure 4.41** Variation of machined surface roughness,  $R_a$  and root mean squared roughness,  $R_q$  at comparable feed rates in dry and cryogenic conditions machined at a cutting speed of 43.2m/min.

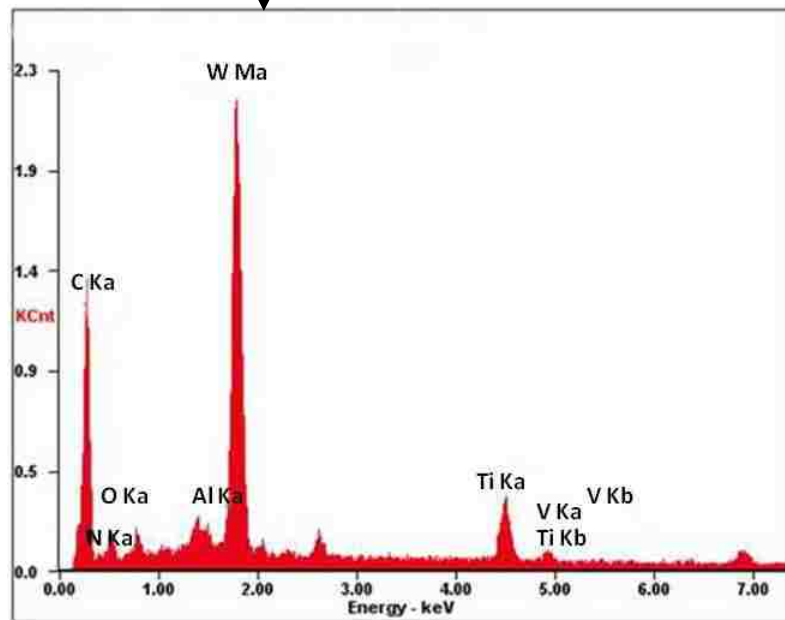
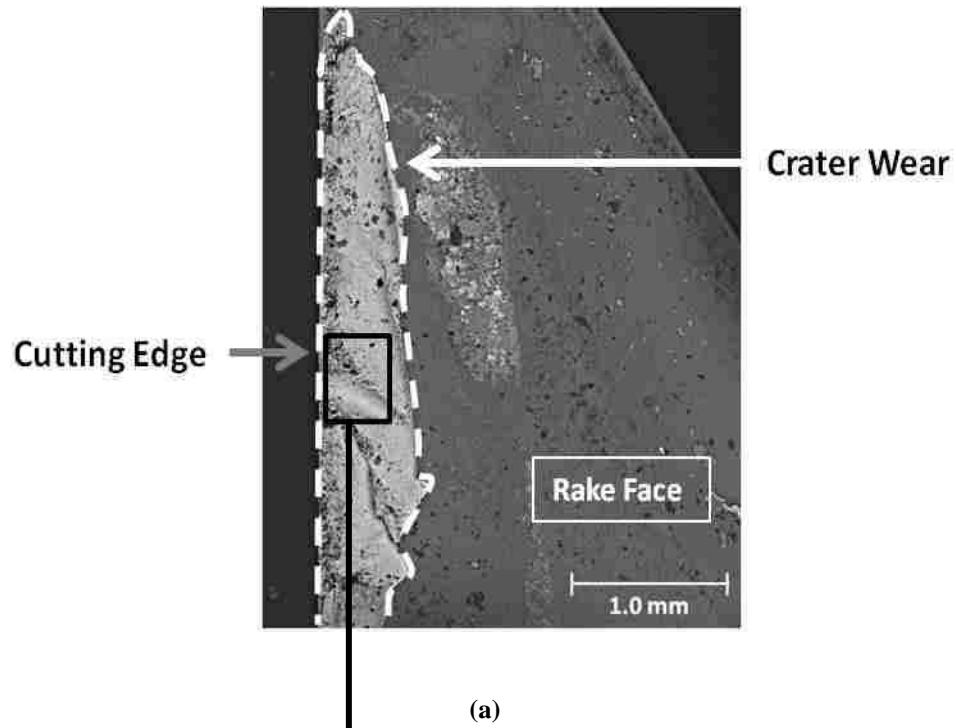


(a)

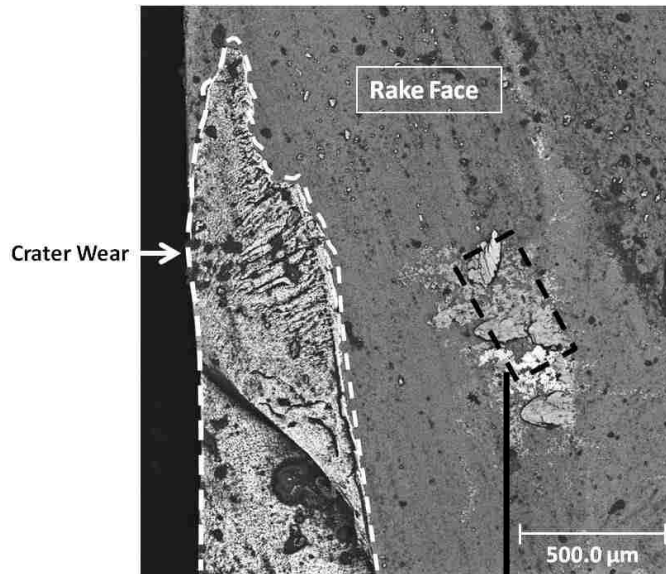


(b)

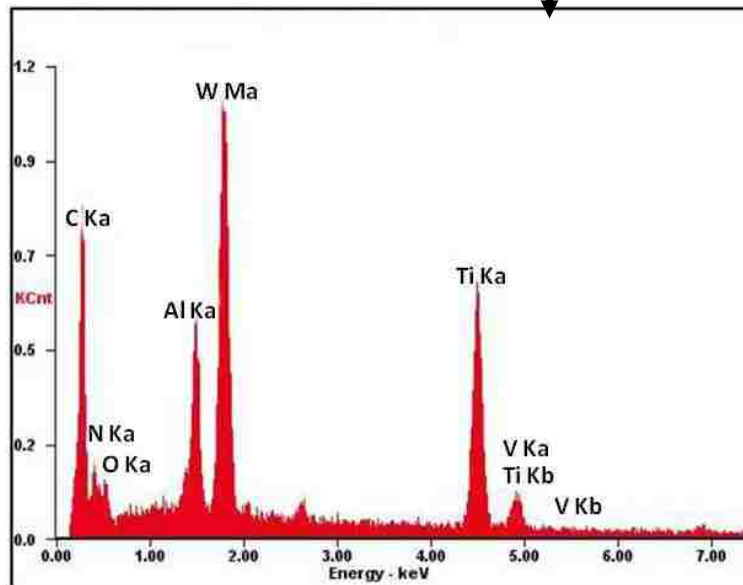
**Figure 4.42** Variation of (a) average surface roughness,  $R_a$  and (b) average root mean squared roughness,  $R_q$  with feed rates at a cutting speed of 43.2m/min in dry and cryogenic conditions.



**Figure 4.43** Uncoated tungsten carbide tool after cryogenic machining at a cutting speed of 43.2 m/min and at feed rate of 0.26 mm/rev where (a) shows damaged cutting edge due to crater wear and (b) shows the EDS analysis that reveals a high percentage of tungsten and carbon with some titanium due to adhesion.



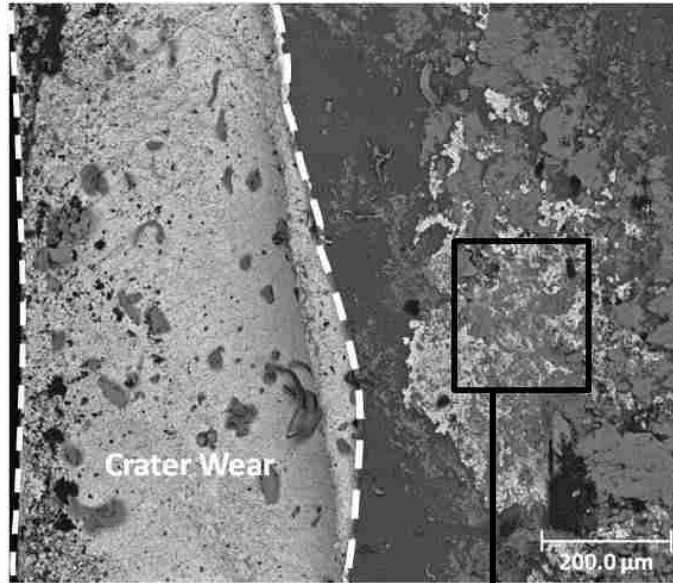
(a)



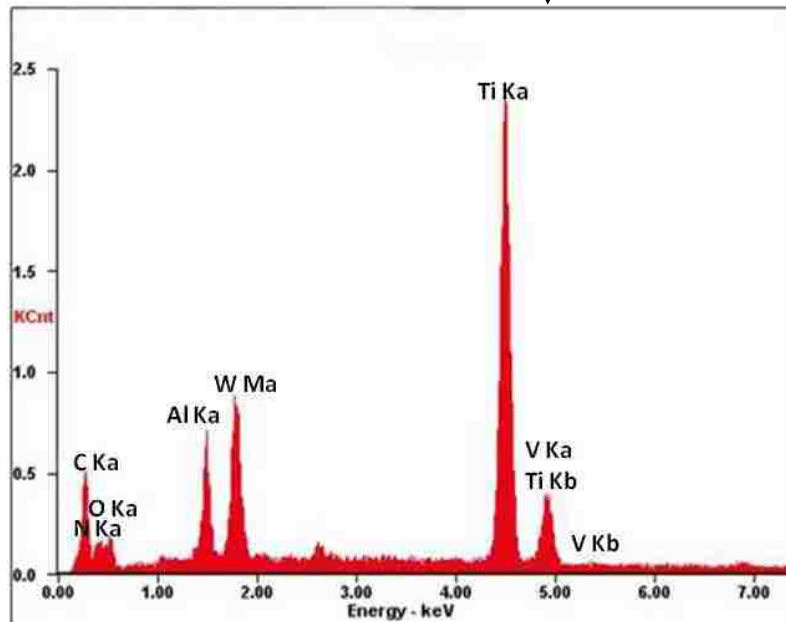
(b)

**Figure 4.44** Uncoated tungsten carbide tool after dry machining at a cutting speed of 43.2 m/min and at a feed rate of 0.17 mm/rev where (a) shows crater wear and (b) shows the EDS analysis that reveals adhesion of titanium.





(a)



(b)

**Figure 4.45** Uncoated tungsten carbide tool after cryogenic machining at a cutting speed of 43.2 m/min and at feed rate of 0.26 mm/rev where (a) shows crater wear and (b) shows the EDS analysis that reveals adhesion of titanium.

# CHAPTER 5

## DISCUSSION

This section focuses on establishing correlations between the microstructural observations and the quantitative analyses of chip characteristics described in Chapter 4. A serrated chip formation mechanism is also developed from in-situ microstructural observations. Empirical models of chips based on microstructures obtained from high speed machining are also presented. With the help of serrated chip formation mechanisms and empirical models of serrated chips, the significance of cryogenic machining is discussed.

### 5.1 Serrated Chip Formation Mechanism

A serrated chip formation mechanism is developed on the basis of microstructural observations shown in Sections 4.1.2 and 4.1.3. Accordingly the mechanism leading to chip formation occurred in four steps. The important features of these steps are shown in Figures 5.1 (a-d).

The first step of serrated chip formation is the strain localization in the chip. The strain becomes localized along a straight path but close to the tool tip it forms a curved surface. A complete serrated chip is shown in Figure 5.1(a) that formed in the previous cycle, which created a rough machined surface. Also a crack generated between the chip segment and the one that is about to form. The curved strain localization path close to the tool tip in the chip that is about to form has a similar pattern to the rough surface produced in the previous cycle.

The second step (Figure 5.1 (b)) is termed the crack initiation step and shows that a crack initiates at the tool tip and a fresh surface is generated. Also, a portion of the chip being formed is flattened by the rake face of the tool. For this reason, the rear portion of the crack, near the tool tip, (between the chip being formed and the one before it) becomes slightly closed.

After the crack initiation, it propagates in a stable manner, which constitutes the third step (Figure 5.1 (c)). This is the stable crack propagation step. Crack propagation follows the path of strain localization (shear band). During this process the flattening of the chip being formed continues. Also, the free surface of the chip starts to bulge due to the advancement of the tool. Gradual flattening and bulging further closes the crack between the chip being formed and the one before it.

When the stable crack advances sufficiently near to the free surface, it propagates in an unstable manner and forms a new chip. The transition from stable to unstable crack was discussed in terms of crack length, time and crack propagation speed in Section 4.1.3. The entire process starts again as strain becomes localized for the next cycle. During this whole process a new rough surface is generated as shown in Figure 5.1 (d). Another important aspect presented in this figure is the fact that the crack between two chips which had seized (complete closure) in the previous step started to open again. In fact the closure of the crack between two consecutive chip segments is predicted to depend on the pressure and temperature. The effect of temperature and pressure can be better understood from the microstructures of serrated chips formed during in-situ cryogenic machining and high speed machining which is discussed in Section 5.2.

To present the gradual movement of the tool, a summary figure that depicts all the steps discussed above is shown in Figure 5.2. Also an axis showing the sliding direction is included for a better understanding of the position of the tool and the sliding of chips. As can be seen, the tool mainly moves in the cutting direction along with a slight movement in the direction of feed. But the tool never touches the bottom surface that is being produced. During this movement of the tool, chip A shown in Figure 5.2, slides along the rake face. Sliding mainly occurs in the second, third and fourth steps.

## **5.2 Difference in Serrated Chip Characteristics during Slow and High Speed Machining**

Microstructures obtained during in-situ dry machining showed crack closure and re-opening between two consecutive chips at the rear part near the tool tip which are also presented in the proposed serrated chip formation mechanisms (see Section 5.1). As described in Section 5.1, the crack in the chips initiates and propagates along the strain localization path which is the location of the shear band. During in-situ cryogenic machining it was observed that the cracks between two consecutive chips were much more prominent and most of those cracks did not seize (Figure 4.3). The feature of prominent crack in the chips formed during in-situ cryogenic machining is shown schematically in Figure 5.3 (b) and for comparison, chips formed during in-situ dry machining is also presented in Figure 5.3 (a). So it can be predicted that the temperature within the shear band would be critical for crack closure and if the temperature is not sufficiently high then the cracks would not seize.

Microstructures of serrated chips formed at different feed rates during high speed dry and cryogenic machining were shown in Figure 4.6. In all the conditions, it was observed that

there were no cracks between two consecutive chips at the rear part which is the region close to rake face. So it can be concluded that during high speed machining the temperature within the shear band was sufficiently high, so cracks near the rake face were able to seize.

Crack seizure between two consecutive chips seems to be a welding process and in welding, force is another important factor beside temperature. Figure 5.4 shows the distribution of forces along different faces of the tool. The feed force and the direction of the chips sliding is along the direction of the rake face. The feed force was found to increase with feed rates during high speed machining as shown in Figure 4.28 (b). So it can be concluded that during high speed machining the tendency of crack seizure near the rake face would increase with the feed rate.

During high speed machining, at comparable feed rates of 0.20mm/rev to 0.30 mm/rev, a variation in cracking tendency at the free surface of the serrated chips was observed as shown in Figures 4.6 and 4.7. Along with the difference in cracking tendency of the chips, there are variations in terms of severity of cracks as well. As shown in Figures 4.6 and 4.9-4.12, some cracks were wide, some were narrow and some went outside the shear band whereas others either remained well inside the shear band or moved along the edge of the shear band. For a better understanding of the severity of cracking, different types of cracks in chips, which were formed under certain machining conditions are analyzed in terms of shear strain in the shear band and strain rate in the shear plane. As there are variations in cracks, the calculation of shear displacement becomes complicated. So to generalize this, the procedure which is used for these cracked chips is shown in Figure 5.5. As can be seen, a line (white dashed line) was drawn along the edge of the bottom portion of the fractured surface. The shear displacement was then measured from the edge of the top fractured surface up to the dashed line.

Figures 5.6 (a) and 5.7 (a) show different types of cracks those were produced at a certain feed rate during cryogenic and dry machining respectively. The corresponding value of shear strain in the shear band and strain rate in the shear plane is also shown in Figures 5.6 (b) and 5.7 (b). It is concluded that, narrow cracks have higher shear strain in shear band compared to wide cracks. It is also found that the cracks that go deep inside towards the rake face developed at high strain rate in shear plane. A combination of high shear strain in shear band and strain rate in shear plane is observed in cases where the cracks are not only narrow but go deep inside the chips.

In summary it can be said that the crack seizure at the rake face between two consecutive chips during slow or high speed machining is dependent on the pressure and temperature. The type of crack at the free surface is dependent on shear strain and the shear strain rate.

### **5.3 Schematic Models of Chips Based on Microstructural Quantitative Analyses**

At a cutting speed of 43.2m/min, chips formed during cryogenic machining at feed rates from 0.15mm/rev to 0.30mm/rev and showed significant differences in terms of cracking tendency and shear strain in shear band compared to dry cutting. For a better understanding of the significance of cryogenic machining (Section 5.4) empirical models of chips of both dry and cryogenic condition were developed based on the values measured from the microstructure which were shown in Figures 4.18, 4.19, 4.21, and 4.24.

These schematic models (Figure 5.8) represent the chips of dry and cryogenic machining at feed rates between 0.10mm/rev to 0.30mm/rev. Within this range, chips produced during

cryogenic conditions have higher shear displacement, higher distance between two consecutive shear bands and higher shear angle with lower maximum and minimum chip thickness than dry conditions. From these schematics, it can be clearly seen that for the same amount of material removal the number of shear bands would be lower in the cryogenic condition. Some other important aspects of these schematics will be used in Section 5.4.

## 5.4 Tool Wear, Diffusion and Adhesion

Machining of Ti-6Al-4V alloy shows high reactivity and involves high temperature at the tool/chip interface as mentioned in Section 2.3.6.5. Hartung et al. [47] examined two potential tool materials namely poly-crystalline diamond (PCD) and tungsten carbide and from their calculations and observations they concluded that there are no potential tool materials which have sufficient chemical stability with respect to Titanium. N.P.Suh [46] mentioned solution wear and diffusion wear during machining and both of these are related to chemical stability. The rate of dissolution,  $\dot{c}$  can be calculated from [46]-

$$\dot{c} = \frac{\partial c}{\partial t} = \alpha (c_s - c)v\beta \exp\left(-\frac{\Delta G}{kT}\right) \quad (5.1)$$

where  $\alpha$  is a proportionality constant,  $c$  is the concentration of the dissolved material,  $c_s$  is the maximum solubility,  $v$  is the frequency of atomic oscillation,  $\beta$  is the number of atoms leaving and joining the solution,  $\Delta G$  is the activation energy for dissolution,  $k$  is Boltzmann's constant and  $T$  is the absolute temperature at the interface. From Equation 5.1 it can be concluded that lower temperatures at the tool/chip interface would lower the rate of dissolution.

After analysing the tool (poly-crystalline diamond (PCD) and tungsten carbide) subjected to machining of Ti-6Al-4V Hartung et al. [47] proposed a model based on diffusion wear. They

showed that the tool material reacts with Ti-6Al-4V and forms a stable reaction layer (Figure 5.9). This stable layer could be protective as the rate of diffusion would be lower due to a lower concentration gradient at the tool/chip interface. But in case of sliding which would remove that stable layer, a fresh tool surface would come into contact with the chip and then diffusion would commence again. Due to diffusion of material from the tool to the chip, the tool would become weak and ultimately failure would result [46]. Thus it can be said that the sliding distance needs to be minimized and with lower temperatures need to be maintained in order to reduce tool wear.

It was observed from the serrated chip formation mechanisms (Figure 5.2) that, the chip that is going to be formed (chip B) gradually flattens during stable crack initiation and propagation step. In Sections 4.1.3 and 5.1, it was mentioned that stable crack initiation/propagation is the slowest step where the chip stays in close contact with the tool. So a smaller contact time along with lower temperature would be advantageous to achieve a lower amount of material diffusion from the tool to the workpiece. It was shown in Figure 4.36 (b) that the velocity of the chip was greater in the cryogenic conditions which depicts low tool/chip contact time. EDS analysis on the rake face of chip in dry condition (Figure 5.10 (b)) and at a feed rate of 0.22mm/rev shows 8.5% Carbon whereas even at higher feed rates (0.24mm/rev) the percentage of Carbon is lower (4.5%) in the cryogenic condition (Figure 5.11 (b)). So it can be concluded that at comparable feed rates lower tool/chip contact time and lower temperature during cryogenic machining reduces material diffusion from the tool to the chip.

It can be seen from Figure 5.2 that once chip B forms, chip A slides along the rake face. During the formation of chip B, sliding of chip A is very limited. The stable layer, due to diffusion of material during the formation of chip B, would be removed from the cutting edge as the next



chip forms and chip B slides. This layer would then adhere to the rake face of the tool. For this reason higher amount of adhesion were observed at a distance from the cutting edge (Figures 4.43 and 4.44). From the observations of serrated chip formation mechanisms it can be concluded that the number of chips are proportional to sliding distance. If the number of chips can be decreased then the removal of the reaction layer from the cutting edge would be lower which would improve tool life.

As can be seen from empirical models (Figure 5.8), chips formed during cryogenic machining at a cutting speed of 43.2m/min and at feed rates between 0.15mm/rev to 0.30mm/rev are characterized by a greater distance between two consecutive shear bands which translates to greater tool/chip contact length. In this feed rate range during cryogenic machining the contact length increases by ~ 25%. This higher contact length during cryogenic machining indicates that the number of chips would be lower for a certain amount of removed material. So it can be said that at a cutting speed of 43.2m/min and within a feed rate range of 0.15mm/rev to 0.30mm/rev, machining in cryogenic conditions would increase tool life.

Another important aspect of the increased tool chip contact length is the decrease in pressure on the cutting edge of the tool. It was shown in Figure 4.28(a) that the cutting force was the same in both dry and cryogenic machining. Also in this study the width of cut was constant which was 3mm. So ~ 25% increase in contact length increases the contact area by ~ 25% which eventually leads to a decrease in pressure on the cutting edge of the tool by ~ 25% during cryogenic machining at a cutting speed of 43.2m/min and within a feed rate range of 0.15mm/rev to 0.30mm/rev and this also helps to increase the tool life.

## 5.5 Strain Rate, Shear Band Temperature and Flow Localization

The bulk strain rate and strain rate in the shear plane were calculated using Equations 4.11 and 4.12 respectively. The strain rate in the shear plane is plotted against the bulk strain rate as shown Figure 5.12. As can be seen from Figure 5.12, with the increase of the bulk strain rate, the strain rate in the shear plane during cutting decreased. It was shown in Figure 4.37 that the bulk strain rate increases with the feed rates. So it can be concluded that the greater the feed rate the greater time is required for localization in the shear band. The same trend of delay in localization was mentioned by Fressengeas [107].

Machining is associated with high strain rate and high temperature. The opposing effects of strain hardening and thermal softening produced by strain rate and temperature, respectively create an instability during machining Ti-6Al-4V alloy as mentioned earlier. In this study, the temperature within the shear band is calculated using equation 2.29.

$$T_{sz} = \frac{\tau \gamma}{J \rho C} \left[ \frac{1}{1 + 1.328 \sqrt{\frac{K \gamma}{V f}}} \right] + T_{amb} \quad (2.29)$$

The variation of temperature in the shear band with the feed rate is shown in Figure 5.13. It is observed that higher feed rates generate higher temperature in shear bands and at comparable feed rates dry conditions have higher temperature in the shear band than in cryogenic conditions.

It was observed that the apparent shear stress in the shear band increases with the feed rate (Figure 4.33). From the calculation of delay in localization and higher temperature in the shear band at higher feed rates, it can be predicted that extra effort is required for localization

to occur. It may be for this reason that higher apparent shear stresses were observed at higher feed rates. Higher temperatures within shear bands at comparable feed rates in dry conditions (Figure 5.13) also support the prediction because the apparent shear stress in shear band was higher in dry condition figure 4.33. This prediction can be further authenticated if the instability (see section 2.3.3.1) is found to be different for dry and cryogenic condition within a feed rate range of 0.15mm/rev to 0.30mm/rev. Because there were significant differences observed in terms of increase in apparent shear force in the shear band as mentioned in Section 4.2.6.2.

## 5.6 Specific Cutting Energy and Bulk Deformation

It is important to understand the overall deformation behaviour and associated energy for the calculation of instability criteria (see Section 2.3.3.1). The specific cutting energy can be calculated by using the following equation proposed by Boothroud and Knight [108]:

$$U = \frac{\text{Energy Consumption Rate}}{\text{Material Removal Rate}} = \frac{V \times F_c}{V \times f \times w} \quad (5.2)$$

where  $U$  is the specific cutting energy (rate of energy consumed per amount of removed material),  $V$  is the cutting speed,  $F_c$  is the cutting force,  $f$  is the feed and  $w$  is the width of cut. Calculated values are plotted against feed rates for both dry and cryogenic conditions (Figure 5.14) where it can be observed that with the increase of the feed rate the specific cutting energy is decreasing.

As material is removed in the form of chips during machining, the energy expenditure for this process includes deformation in shear band, secondary deformation zone and also in the bulk region. So the total energy can be divided as-

$$U_{\text{total}} = U_{\text{SB}} + U_{\text{Bulk}} + U_{\text{SDZ}} \quad (5.3)$$

where  $U_{\text{total}}$  is the total spent energy,  $U_{\text{SB}}$  is the energy spent in shear band,  $U_{\text{Bulk}}$  is the energy spent in the bulk region and  $U_{\text{SDZ}}$  is the energy spent in the secondary deformation zone. The shear band, secondary deformation zone and the bulk region are shown in Figure 5.15.

It has already been shown that temperature in the shear band increases with the feed rate (Figure 5.13). As temperature is associated with deformation, the total energy consumed in the shear band would increase with the feed rate. Indentation in material ahead of the tool tip shows (Figure 5.16 (a) and (b)) a lower hardness at the tool tip region but no significant variation in the bulk. Also equivalent strain at the tool tip was found to increase with feed rate as mentioned in Section 4.2.1. Tool tip is located within the secondary deformation zone. So it can be concluded that the total energy consumed in the secondary deformation zone will increase with the feed rate. Some of the chips obtained during machining at higher feed rates show almost no deformation in the bulk region, as shown in Figure 5.17. Lower bulk deformation during dry and cryogenic machining was reported in the literature [84] as well. From the calculations and microstructural observations it can be concluded that with the increase of the feed rate, the temperature rise in the bulk region would be lower due to lower deformation in the bulk region.

To compare the energy efficiency of dry and cryogenic machining, the volume of a single chip and a shear band is calculated by considering the cross section of the chip as a trapezoid and the shear band as a rectangle (Figure 5.8). Moreover the volume percentage of the shear band in a single chip is plotted against the feed rates as shown in Figure 5.18. It is found that between low (0.1mm/rev) to medium (0.30mm/rev) feed rates, the volume percentage of the shear band are greater in the cryogenic condition. This actually represents the percentage of specific cutting energy spent in the shear band as this energy is calculated based on per amount

of material removed. So, it can be concluded that at 43.2 m/min cutting speed, in between low (0.1mm/rev) to medium (0.30mm/rev) feed rates cryogenic machining is energy efficient.

## 5.7 Shear Strain in Shear Band and Instability Criteria

A deformation process that involves high temperature at a constant strain rate requires high total strain to initiate catastrophic flow [109]. It was shown in Figure 4.35, that the shear strain in the shear band was lower at low to medium feed rates in the cryogenic condition. This would mean that within this feed rate range localization is easier in cryogenic machining. As strain localization is a plastic instability, an instability criterion should be used to validate this statement.

The instability criterion was shown in Equation 2.24.

$$0 \leq \frac{\frac{\partial \tau}{\partial \gamma}}{-\frac{\partial \tau}{\partial \theta} \frac{d\theta}{d\gamma}} \leq 1 \quad (2.24)$$

As can be seen, Equation 2.24 involves the bulk temperature above the ambient temperature. In Section 5.6, it was discussed that with the increase of feed rates, the temperature rise in the bulk region decreases.

An equation is developed in this study for calculating instability which is shown below:

$$0 \leq \frac{\frac{\partial \tau}{\partial \gamma}}{\frac{\partial \tau}{\partial T_{SZ}} \frac{\partial T_{SZ}}{\partial \gamma}} \leq 1 \quad (5.3)$$

where  $\tau$  is the shear stress in shear band,  $\gamma$  is the shear strain in shear band and  $T_{SZ}$  is the temperature in shear band. In this equation the shear band temperature is used instead of the bulk temperature. As shown in Figure 5.13 the temperature in the shear band increases with

feed rates. From Figure 5.13 and the discussion of Section 5.6, it can be said that with the increase in feed rate, the temperature in the shear band increases and the temperature in the bulk material decreases. As these two temperatures have opposite trends so their effect on the shear stress would be opposite as well. For this reason, a positive slope of  $\frac{\partial \tau}{\partial T_{SZ}}$  is used in the developed equation instead of  $(-\frac{\partial \tau}{\partial \theta})$  of Equation 2.24.

From the values of the apparent shear stress, the shear strain and the temperature in shear band, Figures 5.19 (a), (b) and (c) are plotted for all the feed rates in both dry and cryogenic conditions,. A second order linear regression was used to make sure that  $R^2$  values are close to unity. For each feed rate of each condition, two very close values were taken from each curve of Figure 5.19 (a), (b) and (c) and slopes were calculated. The values of the slopes for dry and cryogenic conditions at different feed rates are shown in Tables 5.1 and 5.2, respectively.

**Table 5.1** Values of slopes ( $\frac{\partial \tau}{\partial Y}$ ,  $\frac{\partial \tau}{\partial T_{SZ}}$  and  $\frac{\partial T_{SZ}}{\partial Y}$ ) for dry machining at different feed rates.

Feed Rate from Microstructure (mm/rev)	$\frac{\partial \tau}{\partial Y}$	$\frac{\partial \tau}{\partial T_{SZ}}$	$\frac{\partial T_{SZ}}{\partial Y}$
0.09	30.88	0.21	120.70
0.17	29.09	0.15	231.08
0.22	29.09	0.13	235.49
0.26	26.92	0.11	255.05
0.32	25.10	0.08	283.80

**Table 5.2** Values of slopes ( $\frac{\partial\tau}{\partial Y}$ ,  $\frac{\partial\tau}{\partial T_{SZ}}$  and  $\frac{\partial T_{SZ}}{\partial Y}$ ) for cryogenic machining at different feed rates.

Feed Rate from Microstructure (mm/rev)	$\frac{\partial\tau}{\partial Y}$	$\frac{\partial\tau}{\partial T_{SZ}}$	$\frac{\partial T_{SZ}}{\partial Y}$
0.12	15.92	0.16	94.44
0.18	6.39	0.07	108.75
0.24	5.56	0.07	111.76
0.26	2.43	0.04	113.16
0.38	0.53	0.004	121.86

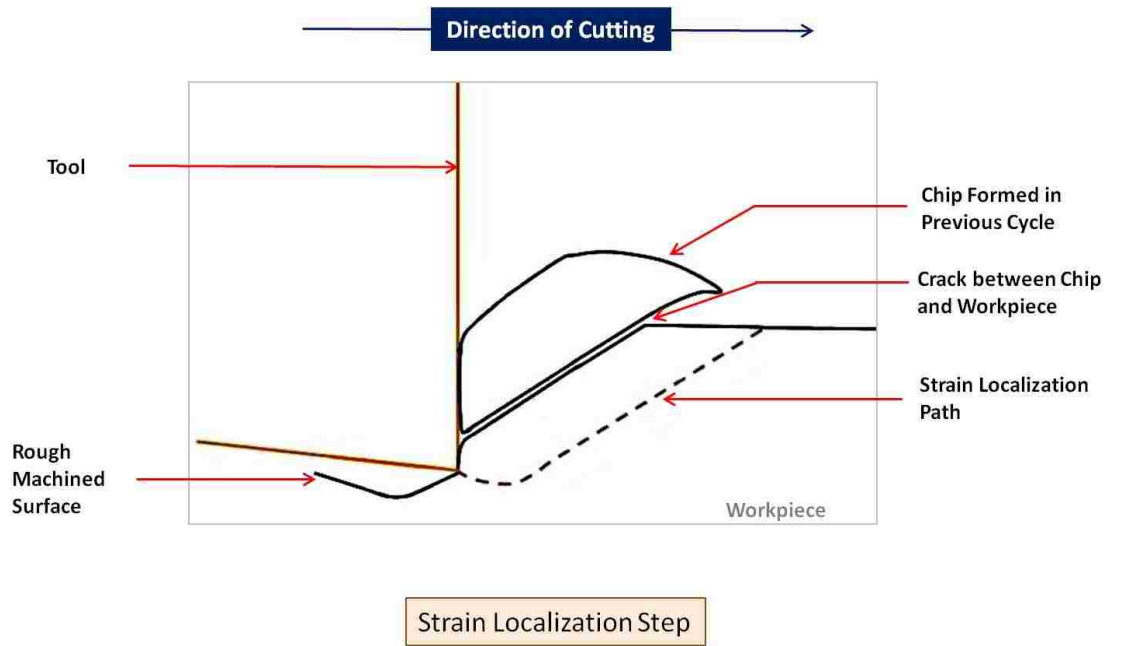
The values of the slopes were then inserted into  $\frac{\frac{\partial\tau}{\partial Y}}{\frac{\partial\tau}{\partial T_{SZ}} \frac{\partial T_{SZ}}{\partial Y}}$  (see Equation 5.3) to calculate the values of instability (a dimensionless parameter) for both dry and cryogenic conditions at different feed rates. The calculated values were then plotted against the feed rate to find out their trend (Figure 5.20).

It can be seen from Figure 5.20 that at feed rates of ~0.1mm/rev, the value of instability for dry and cryogenic condition is greater than 1 where serrated chips formed but the shear bands were not prominent as mentioned in Section 4.2.3 and shown in Figure 4.6. Also at feed rates above 0.30 mm/rev, higher value of instability is observed in dry and cryogenic condition (Figure 5.20) but the values are very close to unity. The microstructures of the chips at these feed rates in both the conditions were identical in terms of the appearance of shear bands and cracking tendency (Figure 4.6).

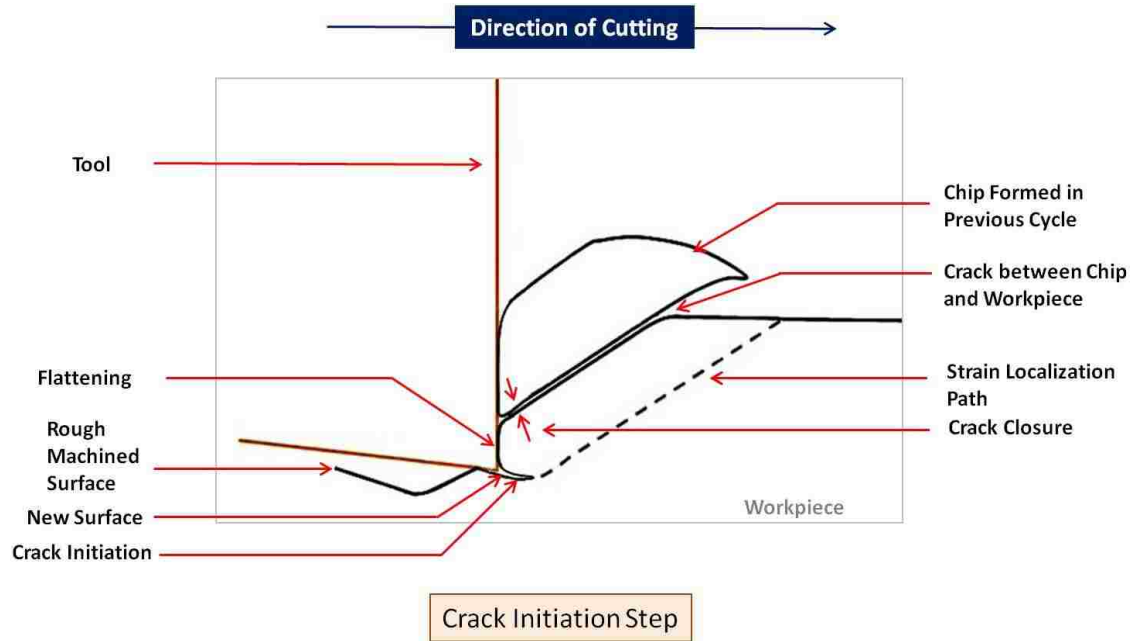
At feed rates from  $\sim 0.15\text{mm/rev}$  to  $\sim 0.30\text{mm/rev}$ , the instability values are found to increase for the dry condition but it shows a decreasing trend in the cryogenic condition. Within the same feed rate range a significant difference was observed in the microstructures of the chips in terms of cracking tendency which was shown in Figures 4.6 and 4.7 and discussed in Section 4.2.3. Also the results of quantitative analyses based on microstructures of chips showed variations in shear distance between shear bands, shear displacement and shear band width within the same feed rate range as discussed in Sections 4.2.5.2, 4.2.5.3 and 4.2.5.4. A lower value of shear strain in the shear band (see Section 4.2.8) was also observed in this feed rate range during cryogenic machining. As mentioned earlier in this section that lower value of total shear strain depicts easier localization in shear band, so it can be concluded that the decreasing trend in instability for cryogenic machining (Figure 5.20) depicts easier localization or easier catastrophic shear that leads to higher cracking tendency. The apparent shear force in the shear band showed a greater tendency of increase in value in dry machining within the same feed rate range as discussed in Section 4.2.6.2 and it was predicted in section 5.5 that the requirement for this increased effort might be due to the difficulty in localization. The instability calculation justifies this argument as well.



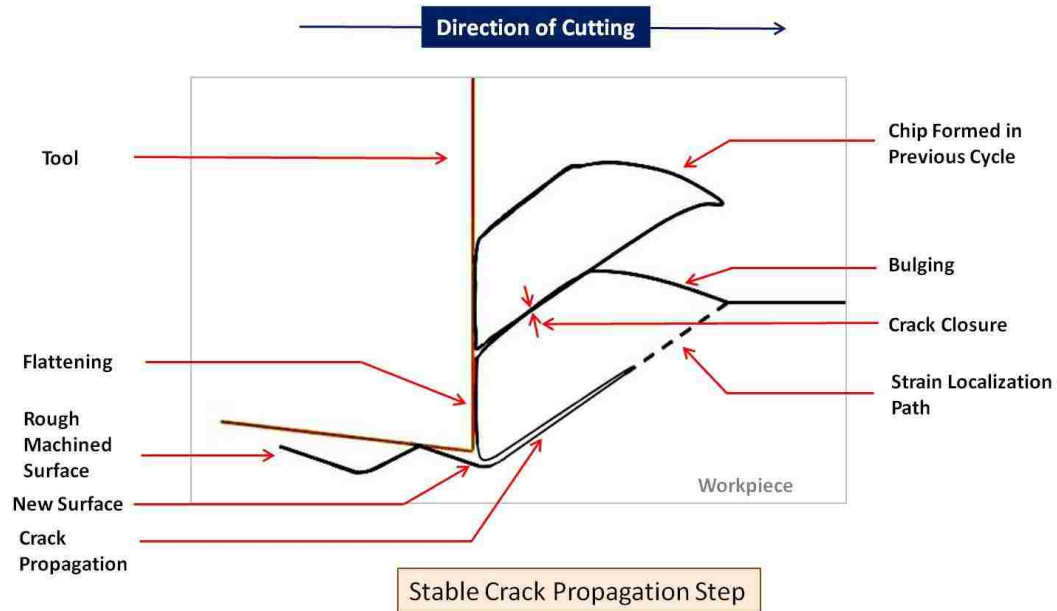
# FIGURES



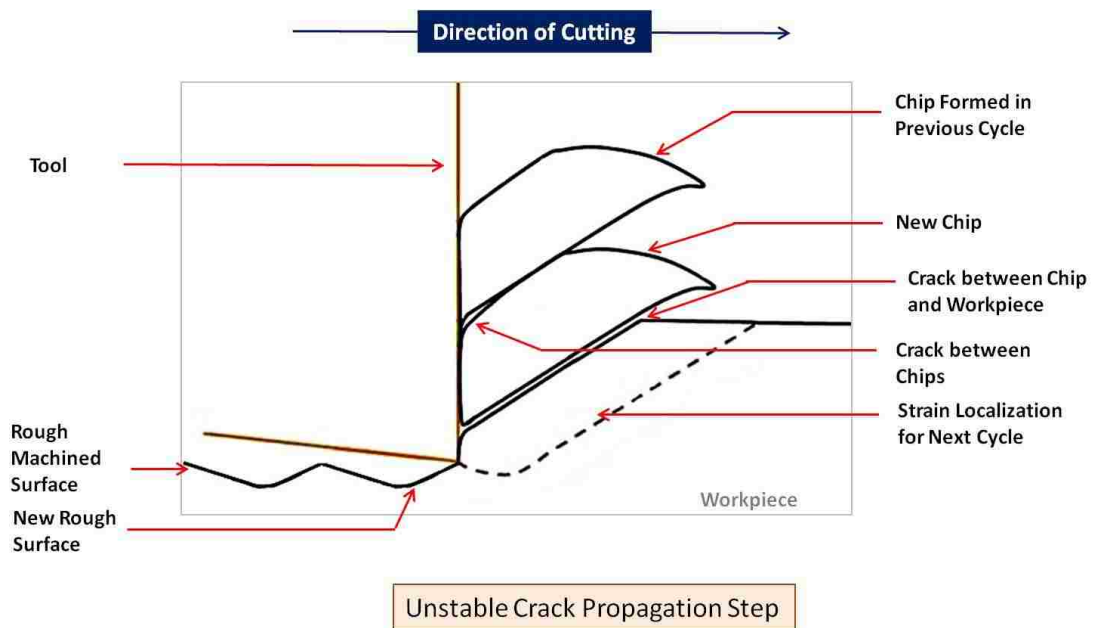
(a)



(b)

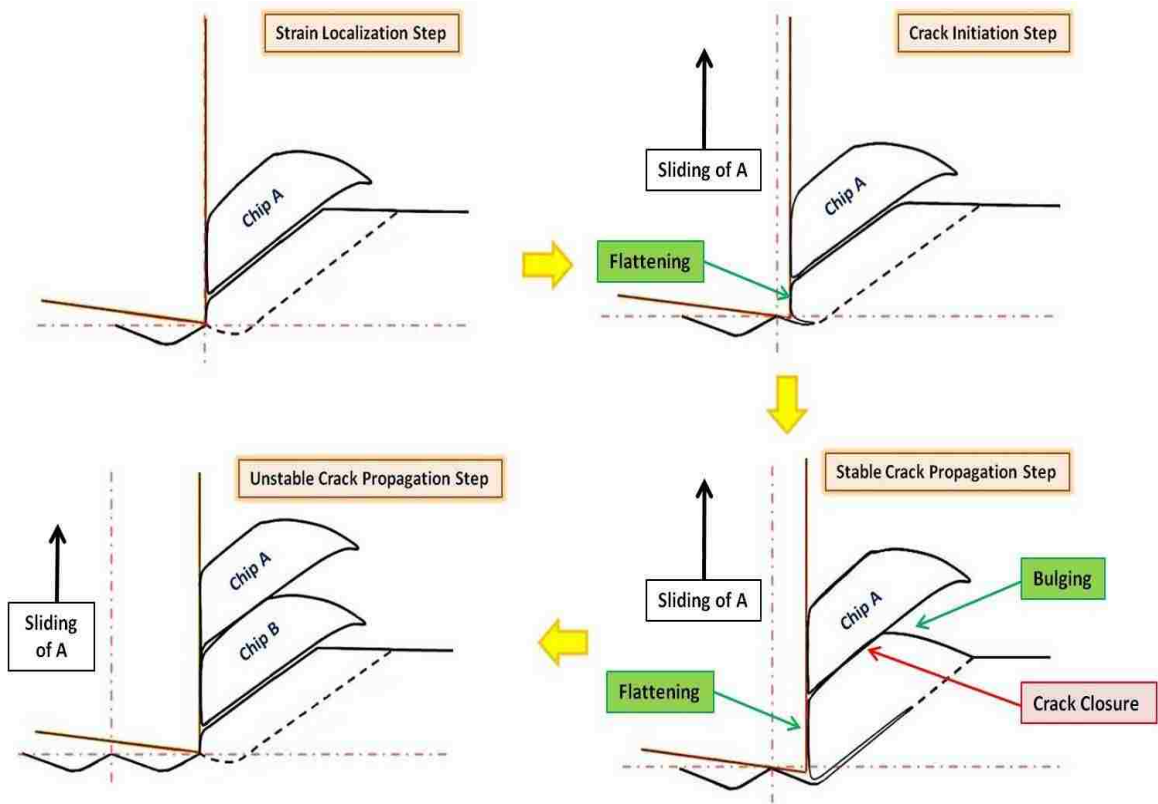


(c)

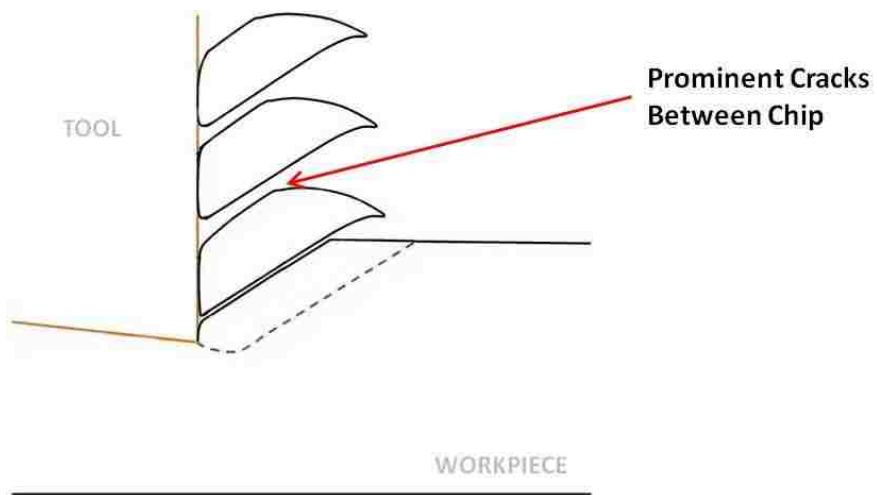
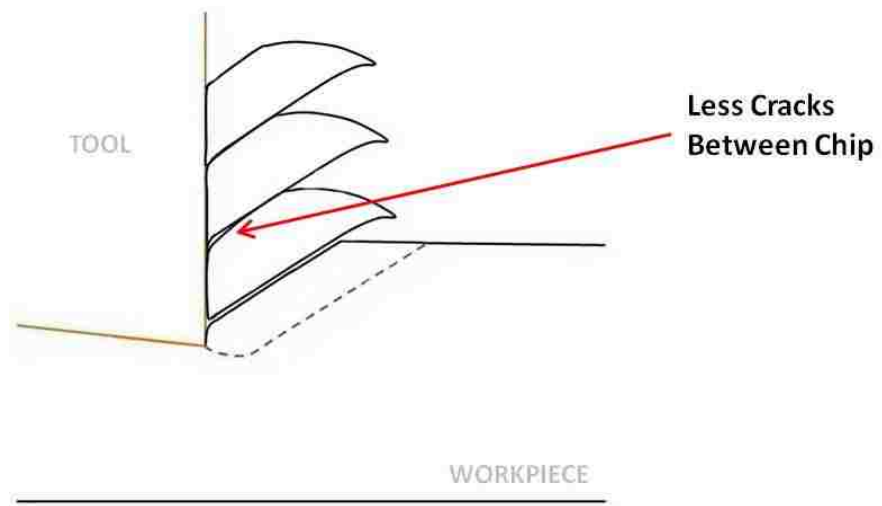


(d)

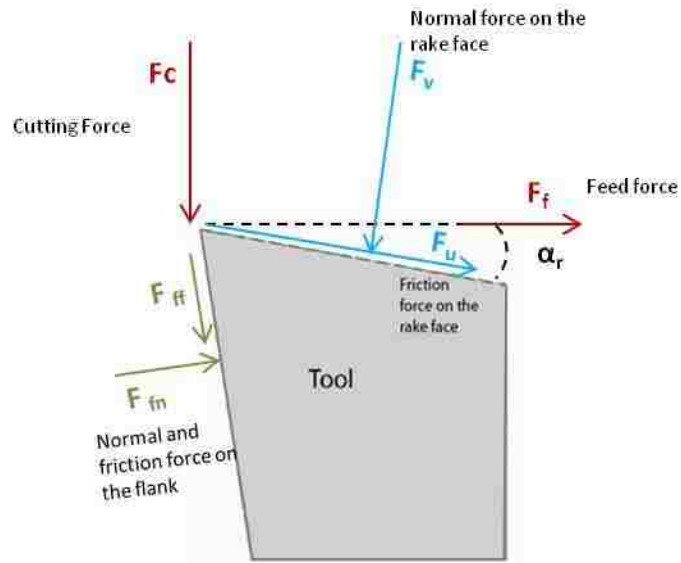
**Figure 5.1** Stepwise features of serrated chip formation mechanism developed on the basis of microstructural evidences where (a) the first step is strain localization, (b) the second step shows crack initiation, (c) the third step showing stable crack propagation and (d) the final step is unstable crack propagation.



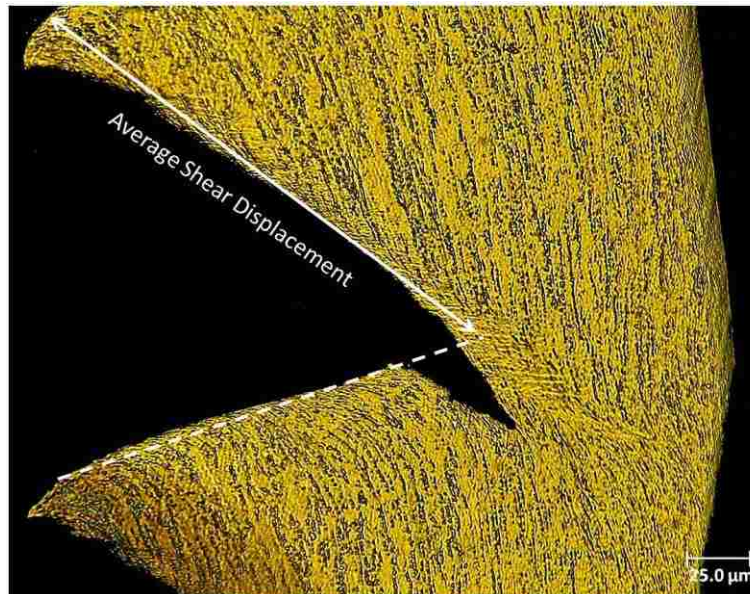
**Figure 5.2** Summary of the serrated chip formation mechanism developed through microstructural analyses that includes the gradual movement of the tool, strain localization, crack initiation/propagation, crack closure between two consecutive chips and generation of machined surface.



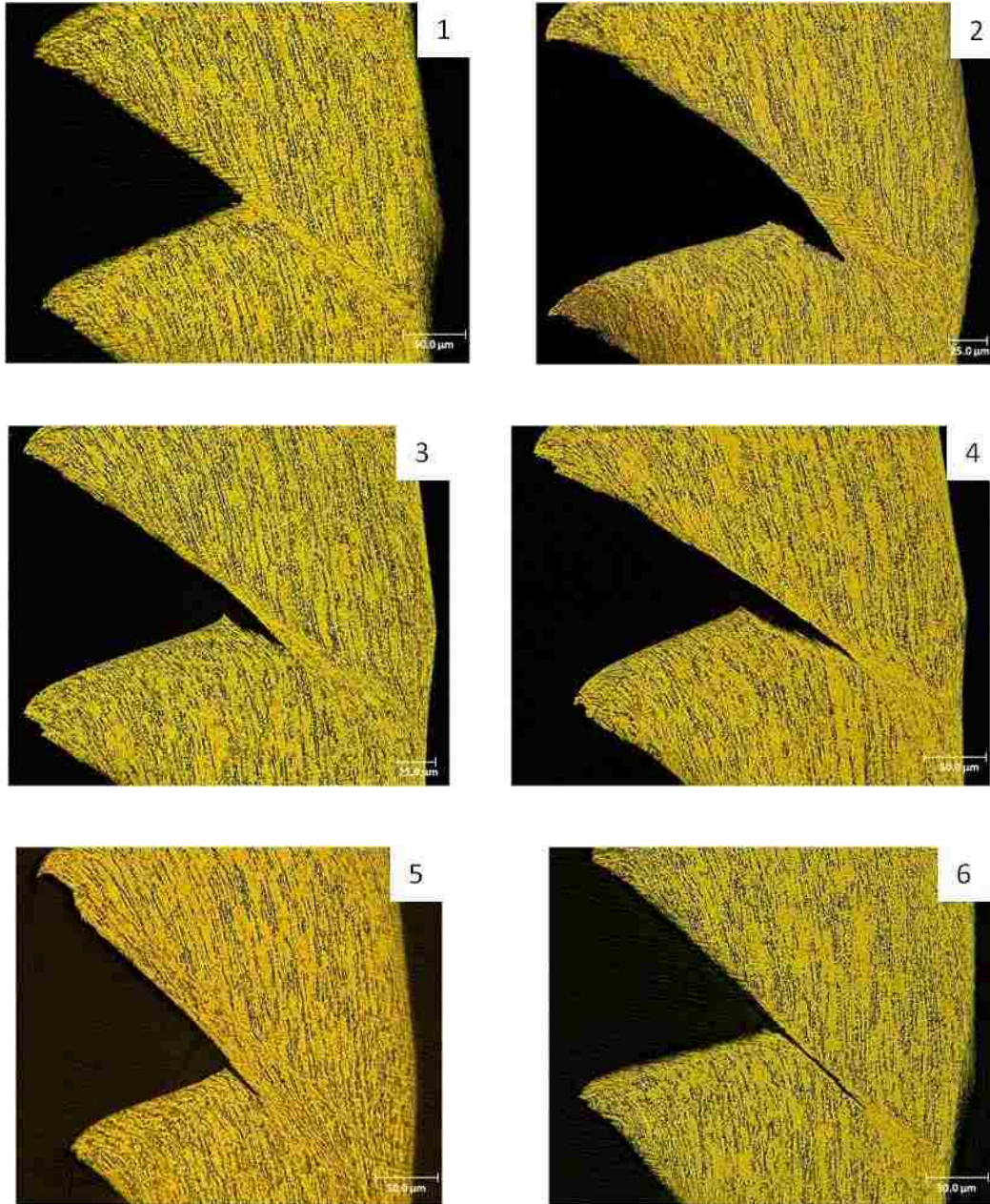
**Figure 5.3** Characteristics of serrated chips formed during in-situ (a) dry and (b) cryogenic machining.



**Figure 5.4** Distribution of forces along different faces of tool when the rake angle is  $\alpha_r$  [102].



**Figure 5.5** Optical image of serrated chip obtained during cryogenic machining at a cutting speed of 43.2m/min and at a feed rate of 0.38mm/rev indicating the procedure of measuring shear displacement in which crack formed.

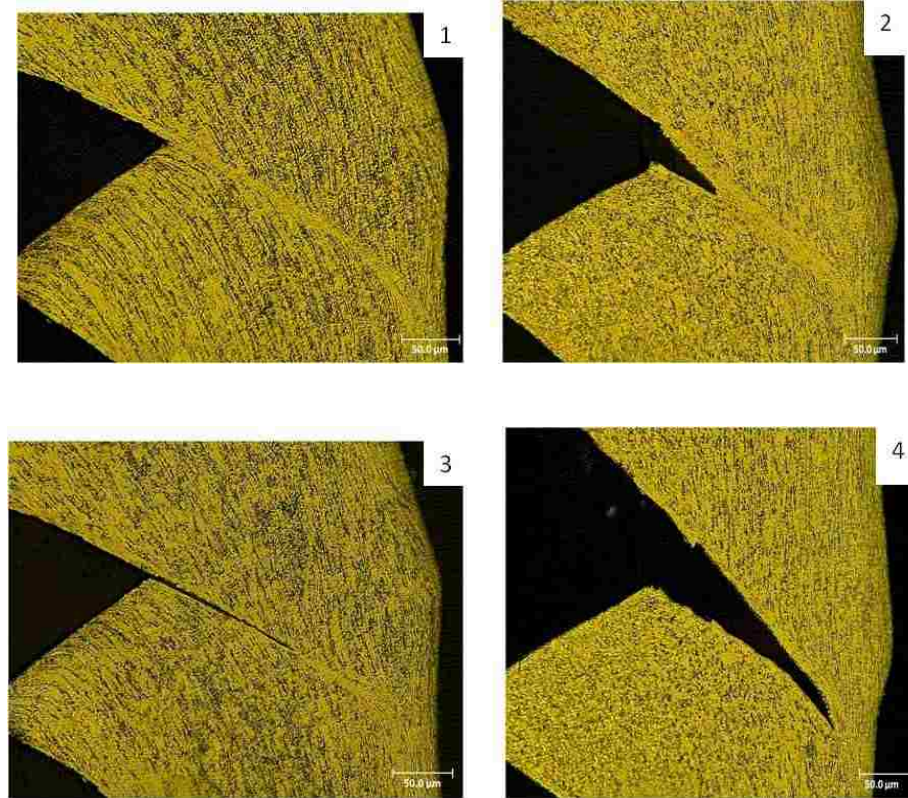


(a)

<b>Image No.</b>	<b>Shear Displacement (μm)</b>	<b>Width of Shear Band (μm)</b>	<b>Shear Strain</b>	<b>Shear Angle (°)</b>	<b>Strain Rate in Shear Direction (× 10<sup>3</sup> s<sup>-1</sup>)</b>
1	207.48	8.79	23.60	37.005	102.58
2	215.59	10.26	21.01	32.275	83.00
3	142.78	6.5	21.97	37.779	140.15
<b>4</b>	<b>227.53</b>	<b>6.07</b>	<b>37.48</b>	<b>32.735</b>	<b>141.02</b>
<b>5</b>	<b>225.18</b>	<b>7.1</b>	<b>31.72</b>	<b>46.165</b>	<b>146.43</b>
<b>6</b>	<b>212.30</b>	<b>5.9</b>	<b>35.98</b>	<b>43.649</b>	<b>168.64</b>

(b)

**Figure 5.6** (a) Optical images of different types of serrated chips formed during cryogenic machining at a cutting speed of 43.2m/min and at a feed rate of 0.38mm/rev and (b) shows corresponding shear strain in shear band and strain rate in shear plane.



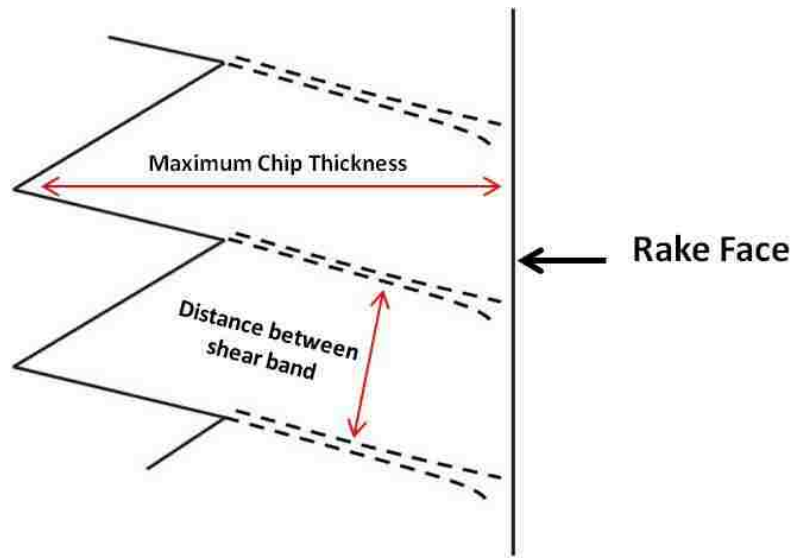
(a)

Image No.	Shear Displacement (μm)	Width of Shear Band (μm)	Shear Strain	Shear Angle (°)	Strain Rate in Shear Direction ( $\times 10^3 \text{ s}^{-1}$ )
1	199.21	6.83	29.16	38.02	133.82
2	235.54	8.52	27.65	32.57	100.33
<b>3</b>	<b>209.61</b>	<b>5.51</b>	<b>38.04</b>	<b>30.07</b>	<b>151.00</b>
<b>4</b>	<b>272.06</b>	<b>7.5</b>	<b>36.27</b>	<b>37.55</b>	<b>121.09</b>

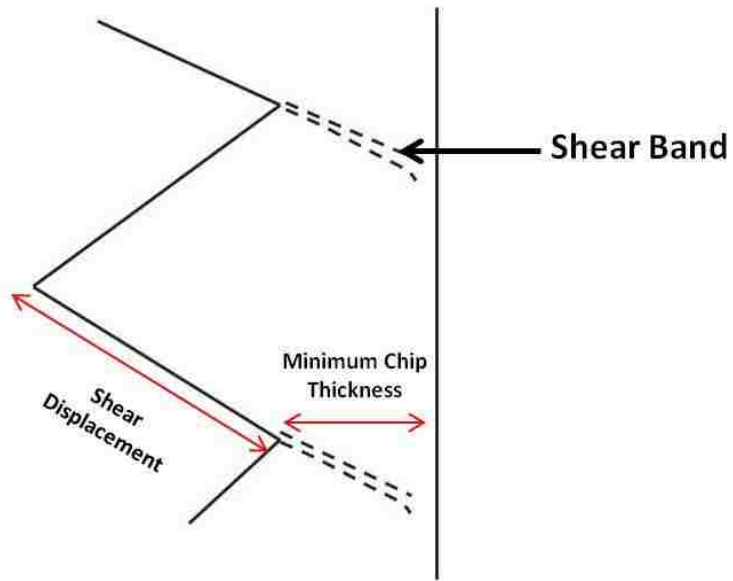
(b)

**Figure 5.7** (a) Optical images of different types of serrated chips formed during dry machining at a cutting speed of 43.2m/min and at a feed rate of 0.38mm/rev and (b) shows the corresponding shear strain in the shear band and the strain rate in the shear plane.



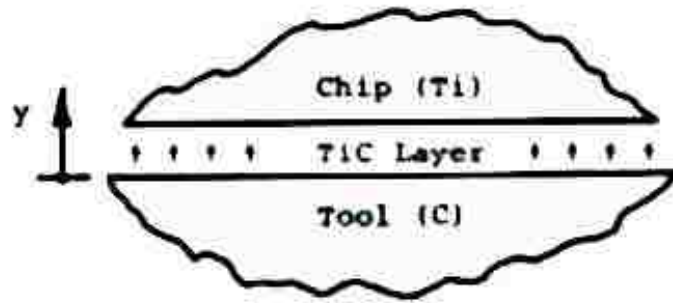


(a)

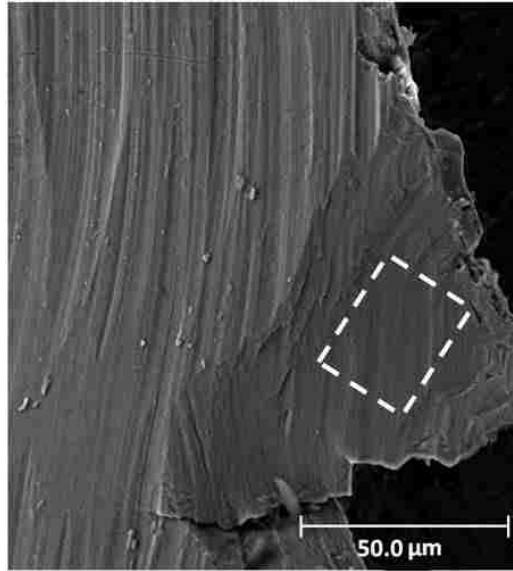


(b)

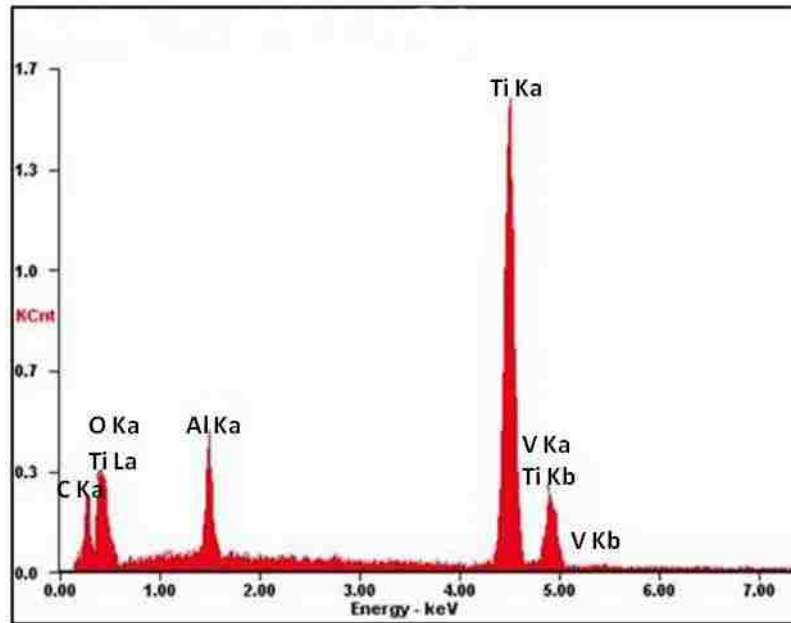
**Figure 5.8** Schematic model of chips based on microstructural quantitative analysis where (a) represents chips of dry condition and (b) of cryogenic condition in between 0.10mm/rev to 0.40mm/rev feed rates.



**Figure 5.9** Model for the wear of diamond by the diffusion of carbon through Titanium Carbide (TiC) reaction layer [47].

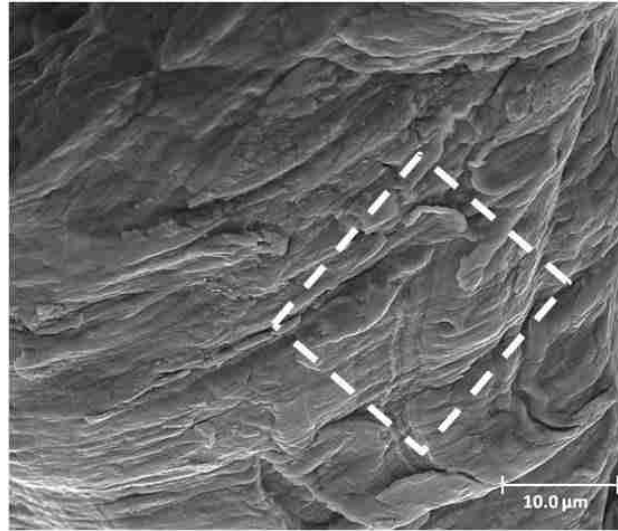


(a)

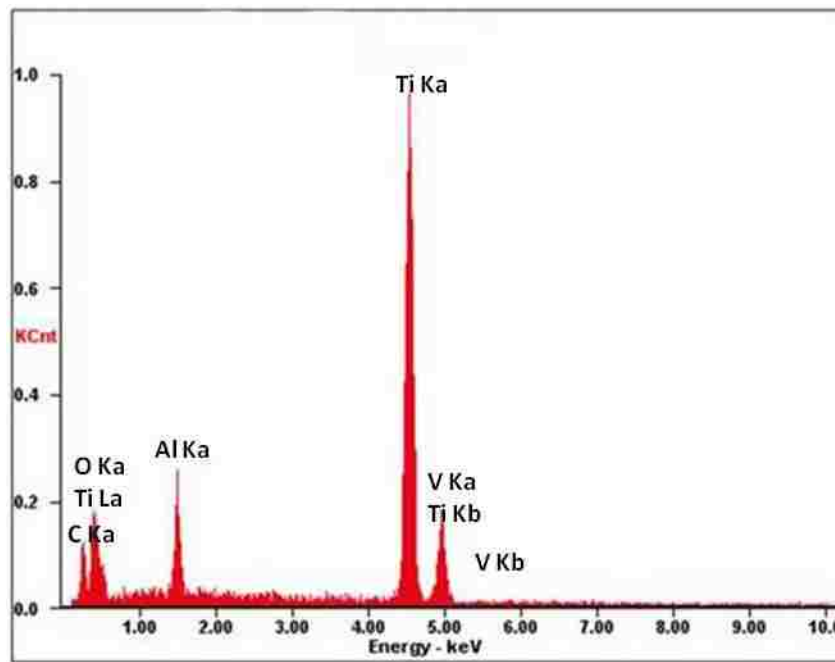


(b)

**Figure 5.10** Diffusion of Carbon from tool to the rake face of the workpiece where (a) shows the SEM image of the rake face and (b) shows the EDS spectra during dry machining at a cutting speed of 43.2 m/min and at a feed rate of 0.22mm/rev.

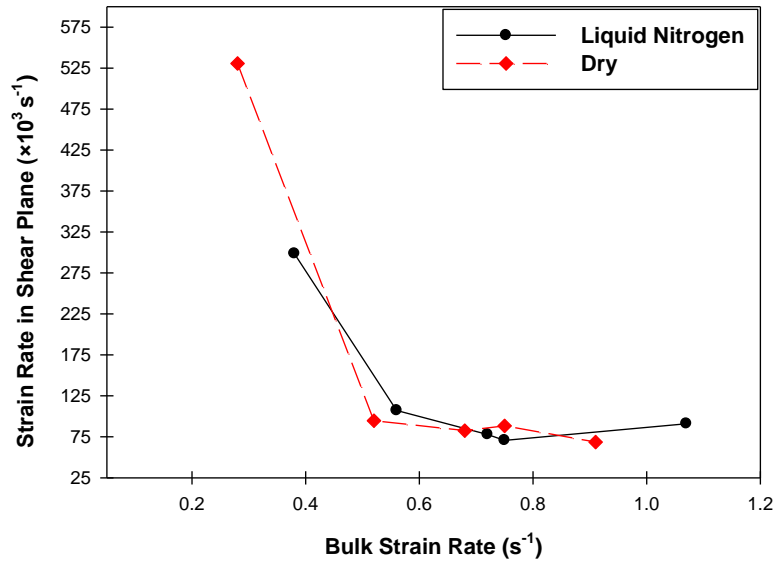


(a)

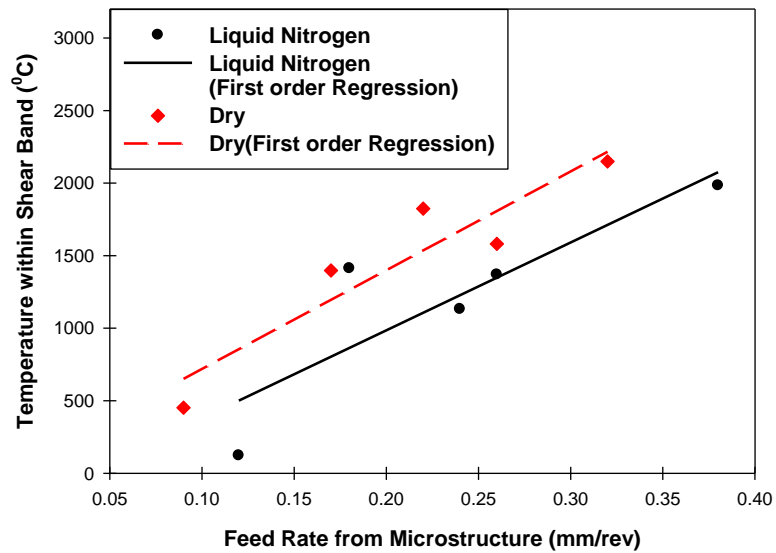


(b)

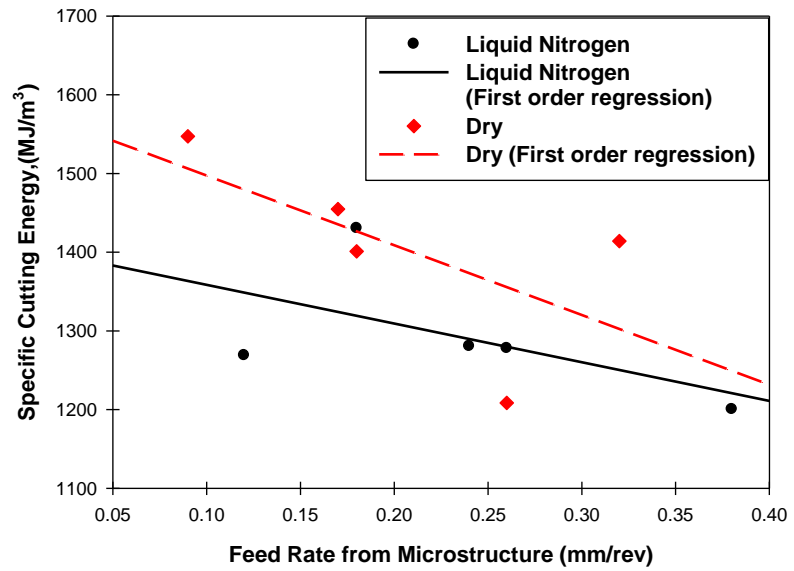
**Figure 5.11** Diffusion of Carbon from the tool to the rake face of the workpiece where (a) shows the SEM image of the rake face and (b) shows the EDS spectra during cryogenic machining at a cutting speed of 43.2 m/min and at a feed rate of 0.24mm/rev.



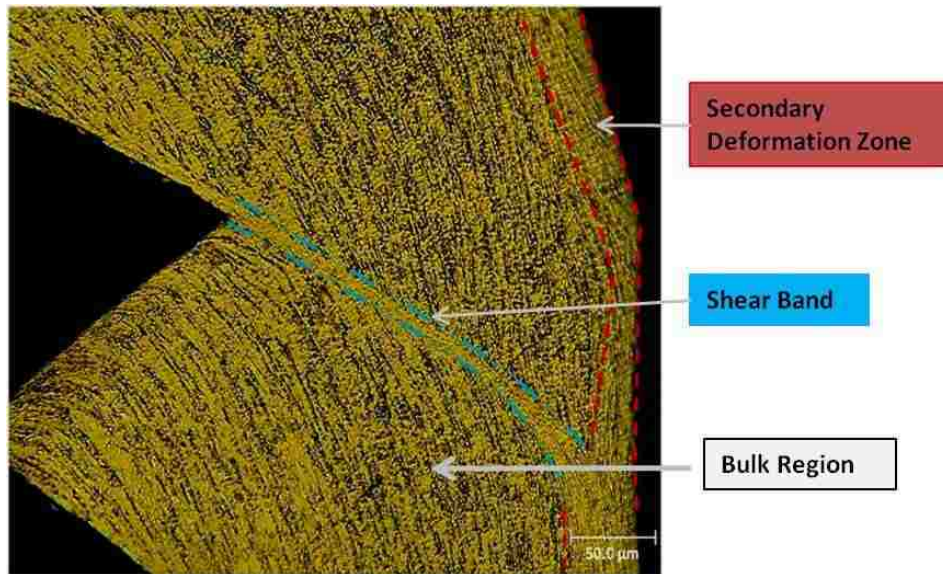
**Figure 5.12** Variation of the strain rate in the shear plane with the bulk strain rate at a cutting speed of 43.2m/min in dry and cryogenic conditions.



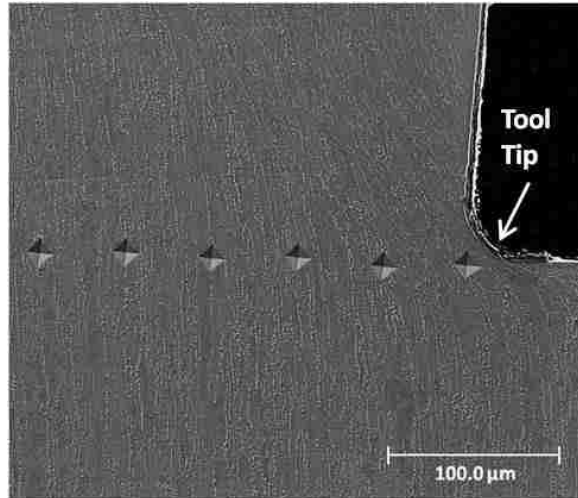
**Figure 5.13** Variation of temperature within the shear band with respect to the feed rate at a cutting speed of 43.2m/min in dry and cryogenic conditions.



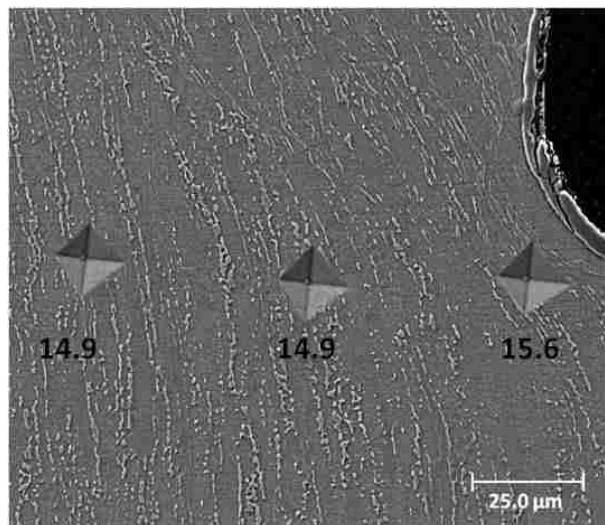
**Figure 5.14** Variation of specific cutting energy with feed rates at a cutting speed of 43.2m/min in dry and cryogenic conditions.



**Figure 5.15** Optical image showing different deformation zones in a serrated chip formed during dry machining at a cutting speed of 43.2m/min and at feed rates of 0.32mm/rev.

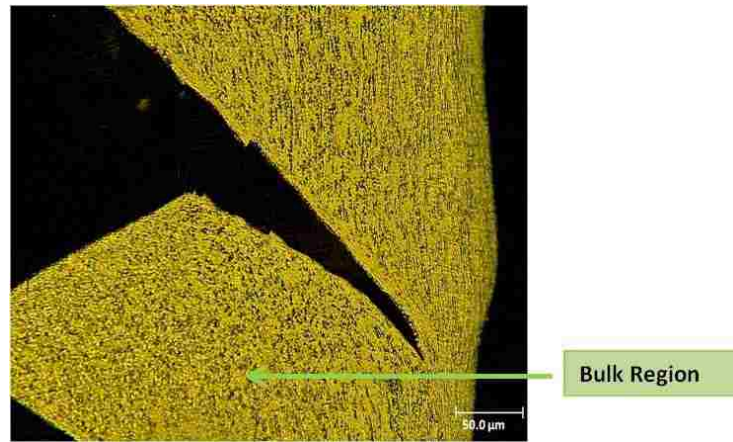


(a)

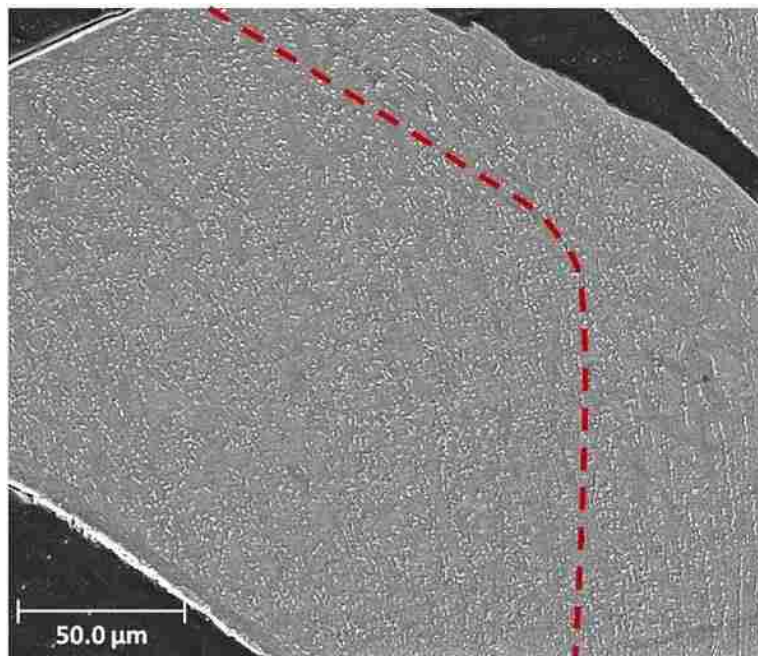


(b)

**Figure 5.16** (a) SEM image of indentation marks in front of the material ahead of the tool tip and (b) shows the same image at higher magnification indicating the average size of the diagonals that clearly depicts lower hardness at the tool tip which corresponds to concentrated deformation.



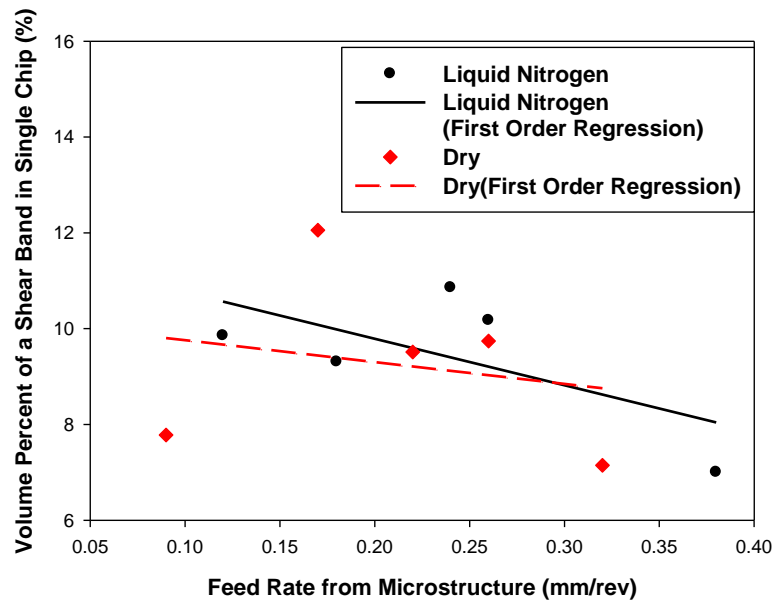
(a)



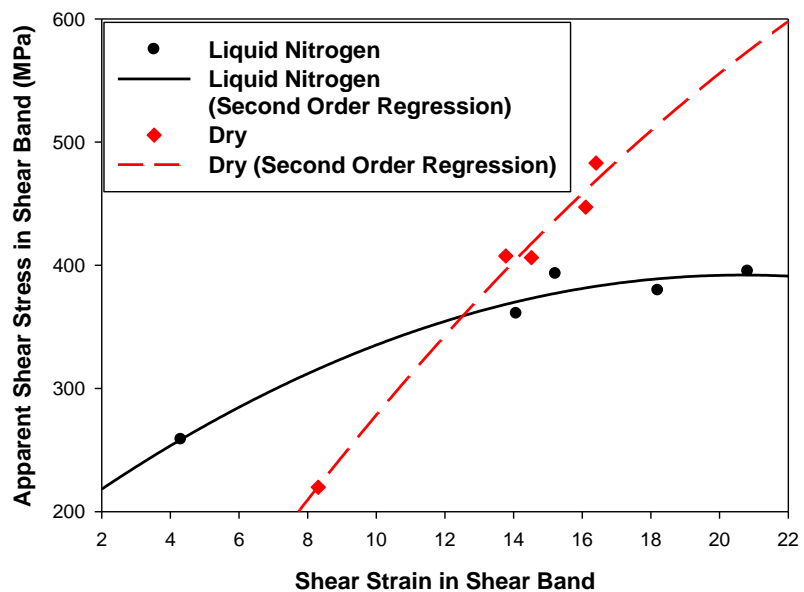
(b)

**Figure 5.17** Optical image of serrated chip showing no deformation in bulk region produced during dry machining at a cutting speed of 43.2m/min and at feed rates of 0.32mm/rev, (b) is a high magnification SEM image of the chips showed in (a) where the secondary deformation zone is separated from the undeformed bulk region.

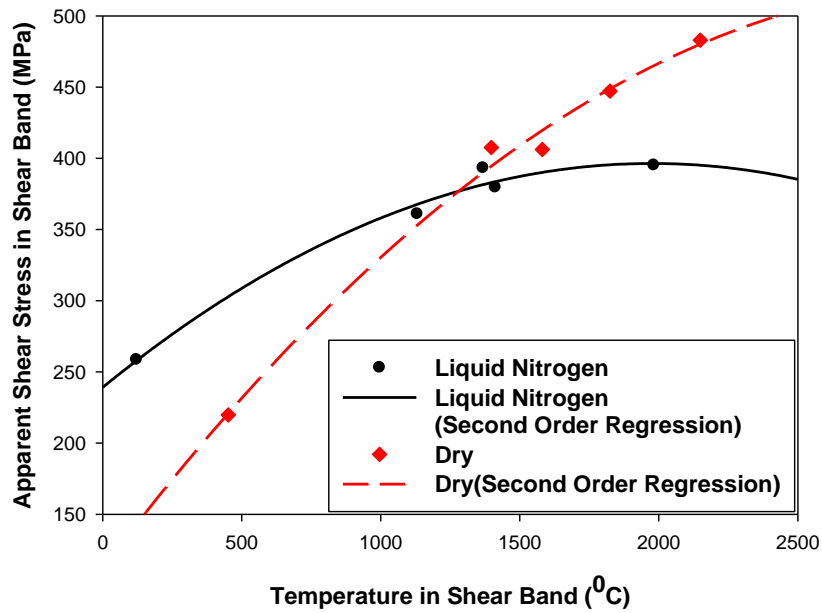




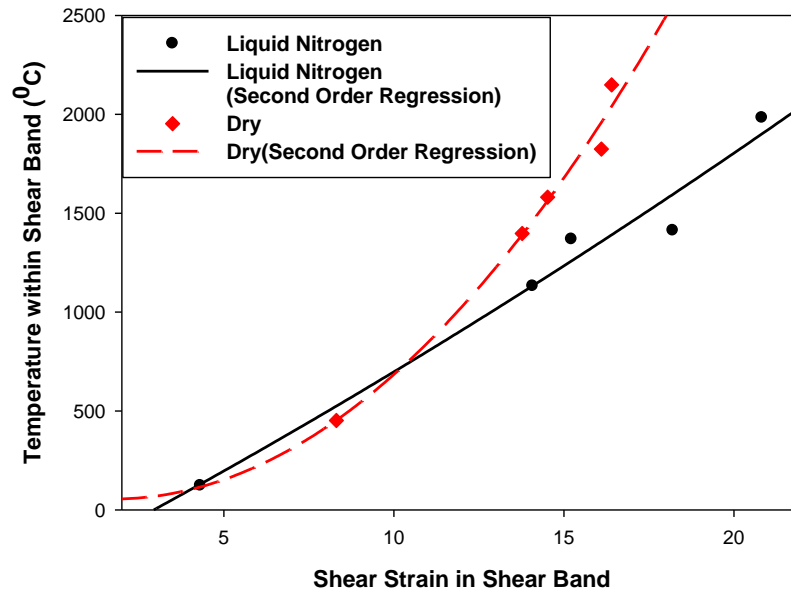
**Figure 5.18** Variation of volume percent of a shear band in a single chip with feed rates at a cutting speed of 43.2m/min in dry and cryogenic conditions.



(a)

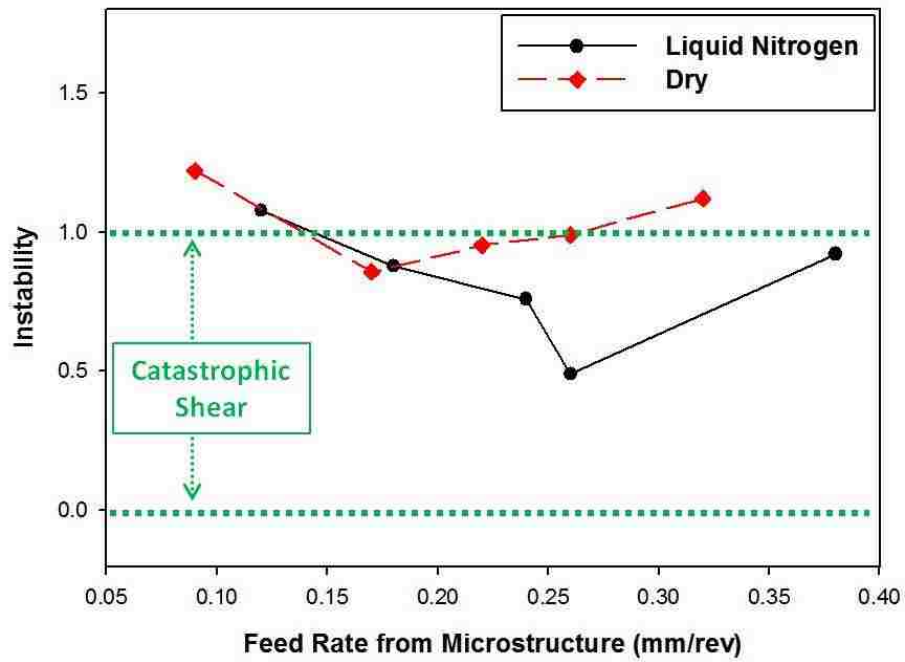


(b)



(c)

**Figure 5.19** Variation of (a) apparent shear stress in the shear band versus the shear strain in the shear band where  $R^2$  value for dry and cryogenic conditions are 0.98 and 0.97 respectively, (b) apparent shear stress in shear band with temperature within shear band where  $R^2$  value for dry and cryogenic conditions are 0.99 and 0.98 respectively and (c) temperature within shear band with shear strain in shear band where  $R^2$  value for dry and cryogenic conditions are 0.98 and 0.97 respectively at a cutting speed of 43.2m/min in dry and cryogenic conditions.



**Figure 5.20** Instability during dry and cryogenic machining at a cutting speed of 43.2m/min at different feed rates.

# CHAPTER 6

## CONCLUSIONS

### 6.1 Conclusions

Ti-6Al-4V alloy were subjected to orthogonal cutting at a cutting speed of 43.2m/min but from very low (0.10mm/rev) to very high (0.40mm/rev) feed rates in dry (ambient) and cryogenic (precooling) conditions. The effects of temperature and strain rate were studied based on microstructural features of chips. The main conclusions are as follows:

1. Real time observation of chip formation at high magnifications through an in-situ machining set-up specifically built for in-situ observations revealed strain localization along a linear path and crack initiation at the tool tip.
2. A Mechanism of serrated chip formation based on microstructural evidences was developed that included the steps of strain localization, crack initiation, stable and unstable crack propagation, as well as crack closure/opening between the two consecutive chips.
3. Serrated chips formed during high speed machining at a cutting speed of 43.2 m/min and at feed rates between 0.10mm/rev and 0.40mm/rev in both dry and cryogenic conditions. The maximum chip thickness, the minimum chip thickness, the distance between shear bands and the shear displacements were measured from microstructures and found to increase with feed rates in both conditions.
4. Differences in crack formation probabilities were observed in chips, during machining at ambient and cryogenic conditions within a feed rate range of 0.10 mm/rev to 0.30mm/rev. At a

particular condition, chips that had higher shear strain in shear band and higher strain rate in shear plane were found to possess narrower and deeper cracks.

5. Fracture surfaces of the chips in both dry and cryogenic conditions revealed elongated dimples along with comparatively smooth regions. At a particular feed rate, surface characteristics and depth of deformed zone in both conditions were comparable.

6. Shear forces were calculated from the measured cutting force, feed force and shear angle. The rate of increase of shear forces was found to vary within the same feed rate range of 0.10 mm/rev to 0.30 mm/rev (for both dry and cryogenic conditions).

7. An empirical model of serrated chip formation was developed. Tool wear, adhesion and diffusion characteristics were described with the help of these models.

8. At a critical feed rate range of 0.10-0.30mm/rev, cryogenic machining (at a cutting speed of 43.2m/min) showed lower adhesion, reduction in pressure on tool by 25%, lower temperature and tool/chip contact time. These factors led to an increase in tool life.

9. A mathematical expression was developed to calculate the instability condition considering shear stress, shear strain and temperature within shear band. It was found that localization was easier during machining at a cutting speed of 43.2 m/min in cryogenic condition, in feed rate range 0.10mm/rev and 0.30mm/rev. This was supported by the observed differences in chip characteristics and measured forces.

## **6.2 Future Work**

1. FIB and TEM analyses of fracture surfaces should be done to understand the effect of phases that exists on titanium alloys on the crack formation tendency and severity.

2. In this study the cutting force in dry and cryogenic condition was constant. Examination of pre-cooled samples machined at different cutting speed will be helpful to clarify the effect of speed and also to find an optimum cutting speed range for industrial applications.

3. Characterization of chips that were produced during continuous cooling should be analysed. These results would be helpful to compare the cryogenic cooling approaches in terms of microstructures.

## REFERENCES

- [1] ME Merchant. Mechanics of the metal cutting process. I. Orthogonal cutting and a type 2 chip, J.Appl.Phys. 16 (1945) 267-275.
- [2] E Lee, B Shaffer, The theory of plasticity applied to a problem of machining, American Society of Mechanical Engineers, Journal of Applied Mechanics ASME Transactions.19 (1952) 234-239.
- [3] P Oxley, M Welsh. Calculating the shear angle in orthogonal metal cutting from fundamental stress-strain- strain rate properties of the work material(Asymptotic angular dependent leakage spectrum of cutting from fundamental stress-strain rate properties), 1964. (1963).
- [4] R Recht. Catastrophic thermoplastic shear, J.appl.Mech. 31 (1964) 186-193.
- [5] M Shaw. The assessment of machinability, ISI Special Repot 94,The Iron and Steel Institute(London)UK,1(1967).
- [6] R Komanduri, B Von Turkovich. New observations on the mechanism of chip formation when machining titanium alloys, Wear. 69 (1981) 179-188.
- [7] A Vyas, M Shaw. Mechanics of saw-tooth chip formation in metal cutting, Journal of manufacturing science and engineering. 121 (1999) 163-172.
- [8] R Komanduri. Some clarifications on the mechanics of chip formation when machining titanium alloys, Wear. 76 (1982) 15-34.
- [9] Z Zhao, S Hong. Cooling strategies for cryogenic machining from a materials viewpoint, Journal of Materials Engineering and Performance. 1 (1992) 669-678.
- [10] MC Shaw, Metal cutting principles, Oxford University Press New York 2005.
- [11] JR Myers, HB Bomberger, FH Froes. Corrosion behavior and use of titanium and its alloys. J.Met. 36 (1984) 50-59.
- [12] H Fujii, K Takahashi, Y Yamashita. Application of titanium and its alloys for automobile parts, Nippon Steel Technical Report. (2003) 70-75.
- [13] G. Lutjering and J.C. Williams., Titanium , Springer – Verlag, Berlin Heiddberg,New York, 2003.
- [14] EW Collings, The physical metallurgy of titanium alloys, ASM Series in Metal Processing, 1-9, 39-50 1984.



- [15] J Mathew Donachie Jr., Titanium a Technical Guide, 2nd Edition ed., ASM International, 2000, 13-24.
- [16] GE Dieter, Mechanical metallurgy, McGraw-Hill New York 1976.
- [17] M Thomas, S Turner, M Jackson. Microstructural damage during high-speed milling of titanium alloys, Scr.Mater. 62 (2010) 250-253.
- [18] J Kim, J Kim, Y Lee, C Park, C Lee. Microstructural analysis on boundary sliding and its accommodation mode during superplastic deformation of Ti-6Al-4V alloy, Materials Science and Engineering: A. 263 (1999) 272-280.
- [19] W Lee, C Lin. Plastic deformation and fracture behaviour of Ti-6Al-4V alloy loaded with high strain rate under various temperatures, Materials Science and Engineering: A. 241 (1998) 48-59.
- [20] E.M. Collings, The physical metallurgy of titanium alloys, , American society for metals, Metal Park ,OH, 1983.
- [21] A Majorell, S Srivatsa, RC Picu. Mechanical behavior of Ti-6Al-4V at high and moderate temperatures-Part I: Experimental results, Materials Science and Engineering A. 326 (2002) 297-305.
- [22] DA Stephenson, JS Agapiou. Metal cutting theory and practice, (1997).
- [23] E Armarego, RH Brown. The machining of metals, Prentice-Hall Inc, Englewood Cliffs, N.J., (1969).
- [24] ME Merchant. Mechanics of the metal cutting process. II. Plasticity conditions in orthogonal cutting, J.Appl.Phys. 16 (1945) 318-324.
- [25] Metals Handbook. vol. 16 Machining,“, ASM International. (1989).
- [26] V Piispanen. Theory of formation of metal chips, J.Appl.Phys. 19 (1948) 876-881.
- [27] R Komanduri, R Brown. On the mechanics of chip segmentation in machining, Journal of Engineering for Industry. 103 (1981) 33-51.
- [28] S Ramalingam, J Black. An electron microscopy study of chip formation, Metallurgical Transactions. 4 (1973) 1103-1112.
- [29] S Ramalingam, AC Bell. A scanning electron microscope stage for the observation of chip formation, Rev.Sci.Instrum. 44 (1973) 573-576.

- [30] H Zhang, A T Alpas. Quantitative evaluation of plastic strain gradients generated during orthogonal cutting of an aluminum alloy, *Materials Science and Engineering: A*. 332 (2002) 249-254.
- [31] H Ni, A T Alpas. Sub-micrometer structures generated during dry machining of copper, *Materials Science and Engineering: A*. 361 (2003) 338-349.
- [32] H Ni, M Elmadagli, A T Alpas. Mechanical properties and microstructures of 1100 aluminum subjected to dry machining, *Materials Science and Engineering: A*. 385 (2004) 267-278.
- [33] M Elmadagli, A T Alpas. Metallographic analysis of the deformation microstructure of copper subjected to orthogonal cutting, *Materials Science and Engineering: A*. 355 (2003) 249-259.
- [34] J Dautzenberg, J Zaat. Quantitative determination of deformation by sliding wear, *Wear*. 23 (1973) 9-19.
- [35] EG Thomsen, CT Yang, S Kobayashi. *Mechanics of plastic deformation in metal processing*, The Macmillan Company, New York, (1965).
- [36] D Tabor. A simple theory of static and dynamic hardness, *Proceedings of the Royal Society of London. Series A. Mathematical and Physical Sciences*. 192 (1948) 247-274.
- [37] R Hill, E Lee, S Tupper. The theory of wedge indentation of ductile materials, *Proceedings of the Royal Society of London. Series A. Mathematical and Physical Sciences*. 188 (1947) 273-289.
- [38] D Marsh. Plastic flow in glass, *Proceedings of the Royal Society of London. Series A. Mathematical and Physical Sciences*. 279 (1964) 420-435.
- [39] E Voce. The relationship between stress and strain for homogeneous deformation, *J Inst Met*. 74 (1948) 537-562.
- [40] P Arrazola, A Garay, L Iriarte, M Armendia, S Marya, F Le Maître. Machinability of titanium alloys (Ti6Al4V and Ti555. 3), *J. Mater. Process. Technol*. 209 (2009) 2223-2230.
- [41] J Kahles, M Field, D Eylon, F Froes. Machining of titanium alloys, *JOM*. 37 (1985) 27-35.
- [42] AD HC Child, *Machining of titanium alloy*, 94 (1968).
- [43] N Narutaki, A Murakoshi, S Motonishi, H Takeyama. Study on machining of titanium alloys, *CIRP Annals-Manufacturing Technology*. 32 (1983) 65-69.
- [44] RM Freeman, PhD Thesis, University of Birmingham, UK(1974).
- [45] S Motonishi, Y Hara, S Isoda, H Itoh, Y Tsumori, Y Terada. Study on machining of titanium and its alloys, *Kobelco technology review*. (1987) 28-31.

- [46] NP Suh, Tribophysics, Prentice-Hall Englewood Cliffs, NJ 1986.
- [47] PD Hartung, B Kramer, B Von Turkovich. Tool wear in titanium machining, CIRP Annals-Manufacturing Technology. 31 (1982) 75-80.
- [48] J Barry, G Byrne, D Lennon. Observations on chip formation and acoustic emission in machining Ti-6Al-4V alloy, Int.J.Mach.Tools Manuf. 41 (2001) 1055-1070.
- [49] R Komanduri, T Schroeder, J Hazra, B Von Turkovich, D Flom. On the catastrophic shear instability in high-speed machining of an AISI 4340 steel, J.Eng.Ind.(Trans.ASME). 104 (1982) 121-131.
- [50] S Semiatin, S Rao. Shear localization during metal cutting, Materials Science and Engineering. 61 (1983) 185-192.
- [51] J Xie, A Bayoumi, H Zbib. Analytical and experimental study of shear localization in chip formation in orthogonal machining, Journal of materials engineering and performance. 4 (1995) 32-39.
- [52] J Xie, A Bayoumi, H Zbib. A study on shear banding in chip formation of orthogonal machining, Int.J.Mach.Tools Manuf. 36 (1996) 835-847.
- [53] ZB Hou, R Komanduri. Modeling of thermomechanical shear instability in machining, Int.J.Mech.Sci. 39 (1997) 1273-1314.
- [54] K Nakayama, The formation of saw-toothed chip in metal cutting, 1 (1974) 572-577.
- [55] N Cook, I Finnie, M Shaw. Discontinuous chip formation, Trans.ASME. 76 (1954) 153.
- [56] M Elbestawi, A Srivastava, T El-Wardany. A model for chip formation during machining of hardened steel, CIRP Annals-Manufacturing Technology. 45 (1996) 71-76.
- [57] G Poulachon, AL Moisan. Hard turning: chip formation mechanisms and metallurgical aspects, Journal of manufacturing science and engineering. 122 (2000) 406-412.
- [58] A Gente, H- Hoffmeister. Chip formation in machining Ti6Al4V at extremely high cutting speeds, CIRP Ann.Manuf.Technol. 50 (2001) 49-52.
- [59] M Cotterell, G Byrne. Dynamics of chip formation during orthogonal cutting of titanium alloy Ti-6Al-4V, CIRP Annals-Manufacturing Technology. 57 (2008) 93-96.
- [60] J Puerta Velásquez, B Bolle, P Chevrier, G Geandier, A Tidu. Metallurgical study on chips obtained by high speed machining of a Ti-6wt.% Al-4wt.% V alloy, Materials Science and Engineering: A. 452 (2007) 469-474.

- [61] J Barry, G Byrne. The mechanisms of chip formation in machining hardened steels, *Journal of manufacturing science and engineering*. 124 (2002) 528-535.
- [62] R Recht. A dynamic analysis of high-speed machining, *High Speed Machining*. (1984) 83-93.
- [63] H Zhen-Bin, R Komanduri. On a thermomechanical model of shear instability in machining, *CIRP Annals-Manufacturing Technology*. 44 (1995) 69-73.
- [64] A Machado, J Wallbank. Machining of titanium and its alloys—a review, *Proc.Inst.Mech.Eng.Pt.B: J.Eng.Manuf*. 204 (1990) 53-60.
- [65] JC Lemaire, W Backofen. Adiabatic instability in the orthogonal cutting of steel, *Metallurgical Transactions*. 3 (1972) 481-485.
- [66] S Semiatin, M Staker, J Jonas. Plastic instability and flow localization in shear at high rates of deformation, *Acta metallurgica*. 32 (1984) 1347-1354.
- [67] S Timothy, I Hutchings. The structure of adiabatic shear bands in a titanium alloy, *Acta Metallurgica*. 33 (1985) 667-676.
- [68] S Timothy. The structure of adiabatic shear bands in metals: a critical review, *Acta Metallurgica*. 35 (1987) 301-306.
- [69] MA Meyers. *Dynamic behaviour of materials*, J.Wiley,(1994) 448-487.
- [70] ME Backman, SA Finnegan, *The propagation of adiabatic shear, Metallurgical Effects at High Strain Rates*, Springer, 1973, pp. 531-543.
- [71] S Semiatin, JJ Jonas, *Formability and workability of metals: plastic instability and flow localization*, American Society for Metals Materials Park, OH 1984.
- [72] A Shahan, AK Taheri. Adiabatic shear bands in titanium and titanium alloys: a critical review, *Mater Des*. 14 (1993) 243-250.
- [73] A Li, J Zhao, Y Zhou, X Chen, D Wang. Experimental investigation on chip morphologies in high-speed dry milling of titanium alloy Ti-6Al-4V, *The International Journal of Advanced Manufacturing Technology*. 62 (2012) 933-942.
- [74] Z Wan, Y Zhu, H Liu, Y Tang. Microstructure evolution of adiabatic shear bands and mechanisms of saw-tooth chip formation in machining Ti6Al4V, *Materials Science and Engineering: A*. 531 (2012) 155-163.
- [75] A Bayoumi, J Xie. Some metallurgical aspects of chip formation in cutting Ti-6wt.% Al-4wt.% V alloy, *Materials Science and Engineering: A*. 190 (1995) 173-180.

- [76] HA Grebe, H Pak, MA Meyers. Adiabatic shear localization in titanium and Ti-6 pct Al-4 pct V alloy, *Metallurgical Transactions A*. 16 (1985) 761-775.
- [77] DS Y Me-Bar. On the adiabatic shear of Ti6Al4V ballistic targets, *Materials Science and Engineering*. 58 (1983) 181-188.
- [78] S Timothy, I Hutchings. Initiation and growth of microfractures along adiabatic shear bands in Ti-6Al-4V, *Materials science and technology*. 1 (1985) 526-530.
- [79] S Timothy, I Hutchings. Adiabatic shear band fracture surfaces in a titanium alloy, *J.Mater.Sci.Lett*. 5 (1986) 453-454.
- [80] RL Woodward. Metallographic features associated with the penetration of titanium alloy targets, *Metallurgical Transactions A*. 10 (1979) 569-573.
- [81] S Liao, J Duffy. Adiabatic shear bands in a Ti-6Al-4V titanium alloy, *J.Mech.Phys.Solids*. 46 (1998) 2201-2231.
- [82] S Ramalingam, JT Black. On the metal physical considerations in the machining of metals, *Journal of Engineering for Industry*. 94 (1972) 1215.
- [83] SY Hong, Y Ding. Cooling approaches and cutting temperatures in cryogenic machining of Ti-6Al-4V, *Int.J.Mach.Tools Manuf*. 41 (2001) 1417-1437.
- [84] S Sun, M Brandt, M Dargusch. Machining Ti-6Al-4V alloy with cryogenic compressed air cooling, *Int.J.Mach.Tools Manuf*. 50 (2010) 933-942.
- [85] M Bermingham, J Kirsch, S Sun, S Palanisamy, M Dargusch. New observations on tool life, cutting forces and chip morphology in cryogenic machining Ti-6Al-4V, *Int.J.Mach.Tools Manuf*. 51 (2011) 500-511.
- [86] M Dhananchezian, M Pradeep Kumar. Cryogenic turning of the Ti-6Al-4V alloy with modified cutting tool inserts, *Cryogenics*. 51 (2011) 34-40.
- [87] A Molinari, C Musquar, G Sutter. Adiabatic shear banding in high speed machining of Ti-6Al-4V: experiments and modeling, *Int.J.Plant*. 18 (2002) 443-459.
- [88] S Subramanian, H Gekonde, G Zhu, X Zhang. Role of microstructural softening events in metal cutting, *Mach.Sci.Technol*. 6 (2002) 353-364.
- [89] W Konig, Applied research on the machinability of titanium and its alloys, *Proceedings of the Forty-Seventh Meeting of AGARD, AGARD Structural and Material*. CP256 ( 1979) 1-10.
- [90] K Venugopal, S Paul, A Chattopadhyay. Growth of tool wear in turning of Ti-6Al-4V alloy under cryogenic cooling, *Wear*. 262 (2007) 1071-1078.

- [91] S Yuan, L Yan, W Liu, Q Liu. Effects of cooling air temperature on cryogenic machining of Ti-6Al-4V alloy, *J.Mater.Process.Technol.* 211 (2011) 356-362.
- [92] ASTM Standard. 3685, Tool-life Testing with Single Point Turning Tools,. (1993).
- [93] GG Ye, SF Xue, W Ma, MQ Jiang, Z Ling, XH Tong, et al. Cutting AISI 1045 steel at very high speeds, *Int.J.Mach.Tools Manuf.* 56 (2012) 1-9.
- [94] M Rogante. Wear characterisation and tool performance of sintered carbide inserts during automatic machining of AISI 1045 steel, *J.Mater.Process.Technol.* 209 (2009) 4776-4783.
- [95] JG Kaufman, Properties of aluminum alloys: tensile, creep, and fatigue data at high and low temperatures, *ASM international* (1999) 11-15.
- [96] JR Davis, Copper and copper alloys, *ASM international* (2001) 35-47.
- [97] AM Handbook-Properties. Selection: Nonferrous Alloys and Special-Purpose Materials, Vol. 2, Metals Park (OH): ASM International. (1990).
- [98] Y Sun, W Zeng, Y Han, Y Zhao, G Wang, MS Dargusch, et al. Modeling the correlation between microstructure and the properties of the Ti-6Al-4V alloy based on an artificial neural network, *Materials Science and Engineering: A.* 528 (2011) 8757-8764.
- [99] BK Kad, SE Schoenfeld, MS Burkins. Through thickness dynamic impact response in textured Ti-6Al-4V plates, *Materials Science and Engineering: A.* 322 (2002) 241-251.
- [100] B De Meester, M Döner, H Conrad. Deformation kinetics of the Ti-6Al-4V alloy at low temperatures, *Metallurgical Transactions A.* 6 (1975) 65-75.
- [101] MA Meyers, G Subhash, BK Kad, L Prasad, Evolution of microstructure and shear-band formation in  $\alpha$ -hcp titanium, *Mechanics of Materials.* 17 (1994) 175-193.
- [102] Y Altintas, Manufacturing automation: metal cutting mechanics, machine tool vibrations, and CNC design, Cambridge university press 2012.
- [103] S Pratibha. Deformation State of Aluminum-6% Silicon Alloy (319 Aluminum) Subjected to Orthogonal Cutting at Different Speeds and Feed Rates, M.A.Sc. University of Windsor (2010).
- [104] AÍS Antonialli, de Andrade Mendes Filho, Anibal, VL Sordi, M Ferrante. The Machinability of Ultrafine-grained Grade 2 Ti Processed by Equal Channel Angular Pressing, *Journal of Materials Research and Technology*,1 (2012)148-153 .
- [105] MA Islam. Determination of the Deformation State of a Ti-6Al-4V Alloy Subjected to Orthogonal Cutting Using Experimental and Numerical Methods., M.A.Sc. University of Windsor (2012).

- [106] J Singh, A T Alpas. High-temperature wear and deformation processes in metal matrix composites, *Metallurgical and Materials Transactions A*. 27 (1996) 3135-3148.
- [107] C Fressengeas. Adiabatic shear morphology at very high strain rates, *Int.J.Impact Eng.* 8 (1989) 141-157.
- [108] G Boothroyd, WA Knight, *Fundamentals of machining and machine tools*, CRC Press 2006.
- [109] R Nakkalil. Formation of adiabatic shear bands in eutectoid steels in high strain rate compression, *Acta metallurgica et materialia*. 39 (1991) 2553-2563.
- [110] FP Incropera, AS Lavine, DP DeWitt, *Fundamentals of Heat and Mass Transfer*, John Wiley & Sons Incorporated 2011.

## APPENDICES

### Appendix A

Rate of heat transfer during the period of submerging the Ti-6Al-4V alloy workpiece in liquid nitrogen was calculated using the following equation [110]:

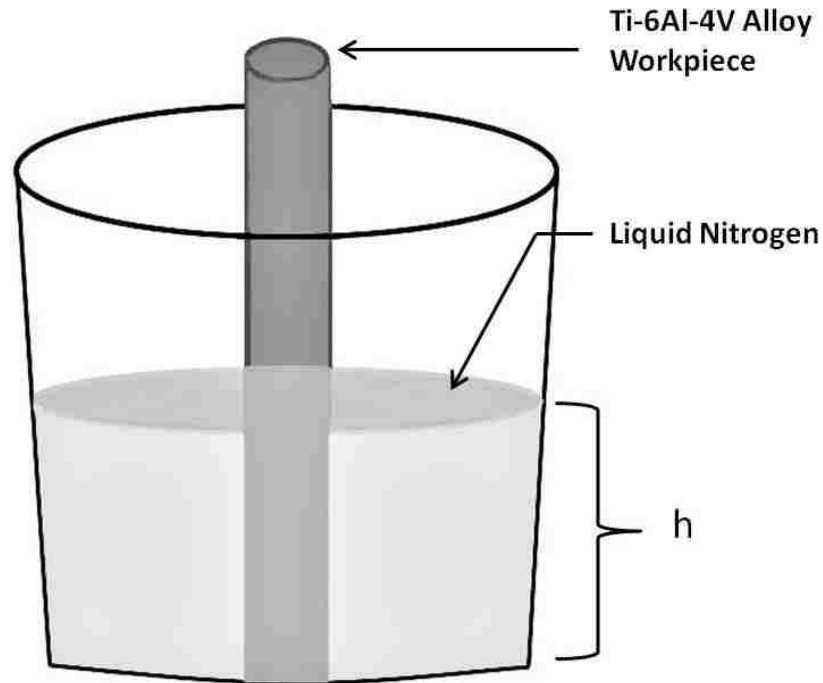
$$\dot{Q}_S = \frac{k_c \times A_S \times (T_o - T_i)}{d} \quad (\text{A.1})$$

where  $\dot{Q}_S$  is the rate of heat transfer,  $k_c$  is the thermal conductivity (for Ti-6Al-4V the value is 6.7 W/m.K),  $T_o$  is temperature of the periphery of the submerged workpiece which is equal to the boiling point of liquid nitrogen (  $-196^{\circ}\text{C}$ ),  $T_i$  is the temperature at the center of the workpiece that is equal to ambient temperature (  $25^{\circ}\text{C}$ ) and  $d$  is the distance of transferred heat which in this case is equal to the radius of the extruded rod workpiece (0.0127m).  $A_S$  is the surface area for the heat transfer which is calculated as:

$$A_S = 2 \times \pi \times r \times h \quad (\text{A.2})$$

where  $r$  is the radius of the workpiece and  $h$  is the height of the workpiece submerged in liquid nitrogen bath as shown in figure A.1. For simplicity, only the peripheral surface area was taken into count where  $h$  was equal to 0.1524m. As can be seen from equation A.1, extra surface area will increase the heat transfer rate faster.





**Figure A.1** Ti-6Al-4V alloy workpiece submerged in liquid nitrogen bath showing the height,  $h$  of the workpiece into the liquid nitrogen bath.

The rate of heat transfer,  $\dot{Q}_S$  was found to be  $-1417.85 \text{ J/s}$  which meant in 1 second  $1417.85 \text{ J}$  heat was taken out of the submerged portion of the workpiece. The following formula [110] was used to calculate the temperature drop in 1 second as a consequent of  $1417.85 \text{ J}$  heat removal.

$$Q_S = m \times C \times \Delta T \quad (\text{A.3})$$

where  $\Delta T$  is the temperature difference and  $m$  is the mass of workpiece submerged in liquid nitrogen which was calculated from the following equation:

$$m = V \times \rho = \pi \times r^2 \times h \times \rho \quad (\text{A.4})$$

where  $V$  is the volume of the submerged workpiece. Using the values and equations A.3 and A.4, it was found that the temperature drop,  $\Delta T$  in each second was  $7.88^\circ\text{C}$ . So, the temperature of

the submerged portion of the workpiece would reach to  $-196^{\circ}\text{C}$  in around 30 seconds. The extra amount of time would ensure the heat loss to be minimum through the rest of the portion of the workpiece.

The workpiece would start to gain heat when taken out of the liquid nitrogen bath. The rate of heat gain through convection was calculated using the following equation [110]:

$$\dot{Q}_G = h_c \times A_s \times (T_{\text{sur}} - T_w) \quad (\text{A.5})$$

where  $\dot{Q}_G$  is the rate of heat gain,  $h_c$  is the coefficient of free convection (for Ti-6Al-4V the value is  $15 \text{ W/m}^2\cdot\text{K}$ ),  $T_{\text{sur}}$  is the temperature of the surroundings which is equal to ambient temperature ( $25^{\circ}\text{C}$ ) and  $T_w$  is the temperature of the workpiece which is  $-196^{\circ}\text{C}$  as calculated. The rate of heat gain was measured to be  $40.31 \text{ W}$ . Using equation A.3 the temperature rise in each second was calculated. It was found that in each second temperature raise around  $0.22^{\circ}\text{C}$ . So in 30 seconds (required time to start machining after workpiece was taken out of the liquid nitrogen bath) increase in temperature was  $6.6^{\circ}\text{C}$ . Temperature of the of the workpiece at the start of the machining was around  $-190^{\circ}\text{C}$ .

## **Appendix B**

A CD that contains the in-situ machining videos of Ti-6Al-4V in dry and cryogenic condition and in-situ machining video of 6061 Aluminum in dry condition is attached with this thesis.

## VITA AUCTORIS

NAME: Md. Fahim Rahman

PLACE OF BIRTH: Dhaka, Bangladesh

YEAR OF BIRTH: 1988

EDUCATION: Bangladesh University of Engineering and Technology  
(BUET), Bangladesh.

Dept. of Materials and Metallurgical Engineering (MME)

B.Sc. Engg. (MME)

January 2006-April 2011

University of Windsor, Windsor, ON.

Dept. of Mechanical, Automotive and Materials Engineering

M.A.Sc. in Engineering Materials

January 2012-December 2013